GENE EXPRESSION AND METABOLISM IN MALIGNANT HYPERTHERMIA SUSCEPTIBLE AND NORMAL SKELETAL MUSCLE

Leon Chang

Submitted in accordance with the requirements for the degree of Doctor of Philosophy

University of Leeds

Faculty of Medicine and Health

September 2020

DECLARATION

The candidate confirms that the work submitted is their own, except where work which has formed part of jointly authored publications has been included. The contribution of the candidate and the other authors to this work has been explicitly indicated below. The candidate confirms that appropriate credit has been given within the thesis where reference has been made to the work of others.

Chapter three includes work featured in the following jointly authored publication:

- CHANG, L., DALY, C., MILLER, D. M., ALLEN, P. D., BOYLE, J. P., HOPKINS, P. M. & SHAW, M. A. 2019. Permeabilised skeletal muscle reveals mitochondrial deficiency in malignant hyperthermia-susceptible individuals. Br J Anaesth, 122, 613-621.

Hopkins, P.M., Shaw, MA., and Boyle, J.P., were responsible for the conception and design of the study.

Chang, L. conducted the experiments and was responsible for data collection.

All authors contributed towards the analysis and interpretation of data.

Chang, L. and Hopkins, P.M., drafted the manuscript.

All authors reviewed drafts of the manuscript and approved the final version.

Chapter four and five include work featured in the following jointly authored publication:

- CHANG, L., LIU, X., DIGGLE, C. P., BOYLE, J. P., HOPKINS, P. M., SHAW, M. A. & ALLEN, P. D. 2020. Bioenergetic defects in muscle fibers of RYR1 mutant knock-in mice associated with malignant hyperthermia. J Biol Chem. DOI: 10.1074/jbc.RA120.013537.

Hopkins, P.M., and Shaw, MA. were responsible for the conception and design of the study.

Chang, L., and Liu, X., conducted the experiments and were responsible for data collection.

All authors contributed towards the analysis and interpretation of data.

Chang, L., and Liu, X., drafted the manuscript.

All authors reviewed drafts of the manuscript and approved the final version.

ACKNOWLEDGEMENTS

I have learnt a great deal working within the Leeds MH Unit and my time here has been thoroughly enjoyable. Firstly, I thank the British Journal of Anaesthesia and the Royal College of Anaesthetists for funding for my PhD. The knowledge and skills I have gained are invaluable towards my development as a scientist, and I would like to acknowledge the amazing individuals who have made this experience possible.

I would like to express my sincere gratitude to my supervisor's Dr Marie-Anne Shaw and Prof Phil Hopkins for their continuous support during my study. Marie-Anne has always been available when I needed advice and her words of encouragement have really helped me through times of stress and uncertainty. Her patience, motivation, and guidance helped me throughout my thesis writing process, and I am truly grateful for her mentorship. Equally, I would like to thank Phil for his excellent guidance during my study and the opportunity to work within his laboratory. I am grateful for his insight into my work, and the opportunities I have received to present my findings at international conferences.

Aside from PhD supervisors, I extend my gratitude to all the staff within the MH Unit (Ms Catherine Daly, Dr Xiaochen Liu, Dr Dorota Miller, Ms Sarah Hobson, and Ms Kirstie Smith) for their technical advice and support during my study. I thank my project collaborators Prof Paul Allen and Dr John Boyle for their expertise, and the valuable opportunities to use RYR1 knock-in mice (Prof Paul Allen) and respirometers (Dr John Boyle) for my research. Additionally, I wish to thank Dr Ian Carr for his guidance with regards to programming and bioinformatics, and Dr Christine Diggle for managing the mouse colonies required for my experiments. All these individuals have contributed towards my PhD experience and I wish them all the best in their future endeavours.

Last but not least, I would like to thank my family, friends, and partner Lisa for their emotional and spiritual support throughout this entire process. My PhD study has been challenging but rewarding, and I am grateful to everyone who supported me on this journey.

ABSTRACT

Malignant hyperthermia (MH) is an autosomal dominant, pharmacogenetic disorder primarily caused by *RYR1* mutations which result in calcium dysregulation within skeletal muscle. Genetically susceptible individuals are at risk of potentially fatal hypermetabolic reactions when exposed to volatile anaesthetics and the muscle relaxant succinylcholine. MH susceptibility is diagnosed through the *in vitro contracture test* (IVCT) by challenging muscle biopsies with triggering agents, or by genetic screening for known familial mutations.

Genome-wide gene expression was compared before and after IVCT, from MH-susceptible (MHS) and non-susceptible (MHN) skeletal muscle by RNA sequencing. A downregulation of genes related to oxidative phosphorylation (OXPHOS) was observed in MHS samples at baseline, suggesting a metabolic defect. Mitochondrial function was assessed by high resolution respirometry, measuring oxygen consumption rates in permeabilised muscle fibres. Results showed evidence of reduced OXPHOS capacity, complex II deficiency and increased mitochondrial content in MHS muscle at baseline. Exposure to halothane triggered a hypermetabolic response in MHS mitochondria which significantly increased oxygen consumption rates in several respiratory states, whilst MHN samples were unaltered.

Genome-wide gene expression and mitochondrial function was also studied at baseline and after halothane challenge, using transgenic mouse models of MH to investigate RYR1 variant-specific effects. At baseline, fatty acid oxidation and mitochondria-related gene expression was downregulated in mice homozygous (HOM) for G2435R-RYR1 and heterozygous (HET) for T4826I-RYR1. In comparison to wild-type, mitochondria from G2435R-RYR1 HOM mice showed an increase in complex I-facilitated OXPHOS and reduced mitochondrial content at baseline. Mitochondria from transgenic mice also showed evidence of increased sensitivity to both halothane and calcium in comparison to wild-type.

This study presents evidence of mitochondrial dysfunction in human and mouse MHS skeletal muscle, which is correlated with gene expression changes associated with oxidative metabolism. Functional defects in mitochondria are therefore potential contributors to phenotypic variability observed in MH.

TABLE OF CONTENTS

ABBREVIATIONS

$[Ca^{2+}]$	Calcium concentration
$[Ca^{2+}]_{rest}$	Resting calcium concentration
ADP	Adenosine diphosphate
ANOVA	Analysis of variance
ATP	Adenosine triphosphate
BIOPS	Buffer solution for respirometry
BLEB	Blebbistatin
BLVRB	Biliverdin reductase B
Ca^{2+}	Calcium
CACNA1S	Calcium Voltage-Gated Channel Subunit Alpha1 S gene
$CaCO_3$	Calcium carbonate
CASQ	Calsequestrin
cis-eQTL	Expression quantitative trait loci local to target gene
CO_2	Carbon dioxide
CoA	Coenzyme A
COPD	Chronic obstructive pulmonary disease
CoQ10	Coenzyme Q10
CoQ6	Coenzyme Q6
CPT1B	Carnitine palmitoyltransferases 1b
CPT2	Carnitine palmitoyltransferases 2
CRU	Calcium release unit
Cryo-EM	Cryo-electron microscopy

Cyt c	Cytochrome c
DAPIT	Diabetes-associated protein in insulin-sensitive tissue
DHPR	Dihydropyridine receptor
DMSO	Dimethyl sulphoxide
EHI	Exertional heat illness
EMHG	European malignant hyperthermia group
eQTL	Expression quantitative trait loci
ER	Endoplasmic reticulum
ETC	Electron transport chain
ETS	Electron transport system
$FADH_2$	Flavin adenine dinucleotide
FAOD	Fatty acid oxidation disorder
FCCP	carbonyl cyanide 4-(trifluoromethoxy)-phenylhydrazone
FCR	Flux control ratio
FDR	False discovery rate
FFA	Free fatty acid
GA	General anaesthesia
GO	Gene ontology
GTEx	Genotype-tissue Expression
GWAS	Genome wide association study
HET	Heterozygous
HOM	Homozygous
IFC	Integrated fluidic circuit
IVCT	*In vitro* contracture test

LCAD	Long-chain acyl-CoA dehydrogenase
LD	Linkage disequilibrium
Log2FC	Log2 Fold Change
MAM	Mitochondria associated membranes
MCAD	Medium-chain acyl-CoA dehydrogenase
MCU	Mitochondrial calcium uniporter
Mg^{2+}	Magnesium
MH	Malignant hyperthermia
MHS	Malignant hyperthermia susceptible
MHS_c	Malignant hyperthermia susceptible (abnormal IVCT to caffeine only)
MHS_h	Malignant hyperthermia susceptible (abnormal IVCT to halothane only)
MHS_{hc}	Malignant hyperthermia susceptible (abnormal IVCT to both halothane and caffeine)
Mir05	Assay media for respirometry
MPTP	Mitochondrial permeability transition pore
mRNA	Messenger RNA
mtDNA	Mitochondrial DNA
NADH	Nicotinamide adenine dinucleotide
NCX	The sodium-calcium exchanger
NOX2	NADPH oxidase 2
OXPHOS	Oxidative phosphorylation
PCA	Principle component analysis
PGM1	Phosphoglucomutase-1

Q	Ubiquinone
RaM	Rapid mode of uptake
RNASeq	RNA sequencing
ROS	Reactive oxygen species
ROX	Residual oxygen flux
RT-PCR	Real-time polymerase chain reaction
RyR	Ryanodine receptor
RyR1	Ryanodine receptor isoform 1
RyR2	Ryanodine receptor isoform 2
RyR3	Ryanodine receptor isoform 3
SERCA	Sarcoplasmic/endoplasmic reticulum calcium ATPase pumps
SITraN	Sheffield Institute for Translational Neuroscience
SNP	Single nucleotide polymorphism
SOCE	Store operated calcium entry
SOD	Superoxide dismutase
SOD1	Superoxide dismutase 1
SOD2	Superoxide dismutase 2
SR	Sarcoplasmic reticulum
STIM1	Stromal interaction molecule 1
SUIT	Substrate-uncoupler-inhibitor-titration
T2DM	Type 2 diabetes mellitus
TEM	Transmission electron microscopy
TF	Transcription factors
TMPD	N,N,N′,N′-tetramethyl-p-phenylenediamine

trans-eQTL	Expression quantitative trait loci distant to target gene
TSS	Transcription start site
VLCAD	Very long-chain acyl-CoA dehydrogenase
WT	Wild-type

LIST OF FIGURES

LIST OF TABLES

1 GENERAL INTRODUCTION

In modern day medicine, the application of general anaesthesia (GA) using gaseous substances or intravenous medicine, alleviates distress in patients undergoing invasive and painful medical procedures. GA is usually considered as a safe process, but complications can occur, ranging from milder symptoms such as dizziness and vomiting, to more serious complications which are potentially fatal (NHS, 2018). GA-associated deaths are very rare and difficult to quantify as they are usually multifactorial (Gottschalk et al., 2011). An example of a potentially fatal complication is the pharmacogenetic disorder malignant hyperthermia (MH), which has a mortality rate of 4% within the UK (Gupta and Hopkins, 2017). This thesis will explore skeletal muscle gene expression and metabolic function in the context of MH. The general introduction will provide the relevant background on skeletal muscle function, Ca^{2+} regulation, excitation-contraction coupling, muscle metabolism and MH genetics - all of which are key areas related to MH pathology.

1.1 SKELETAL MUSCLE STRUCTURE AND FUNCTION

Skeletal muscle occupies approximately 40% of human body weight, composed of water (~75%), protein (~20%) and a mixture of fat and carbohydrates (~5%) (Frontera and Ochala, 2015). The main function of skeletal muscle is to convert chemical energy into mechanical energy for movement, posture maintenance and general applications of force (Trovato et al., 2016). Additional functions include protecting inner organs, acting as a storage site for carbohydrates and amino acids, and the maintenance of core body temperature through muscle contraction. Amino acids, carbohydrates and fats stored in skeletal muscle also contribute to the maintenance of blood glucose levels during periods of starvation (Frontera and Ochala, 2015). The structure of skeletal muscle is highly organized, containing muscle fibre bundles (fascicles) separated by three layers of connective tissue which maintain its integrity (epimysium, perimysium, and endomysium) (Figure 1.1).

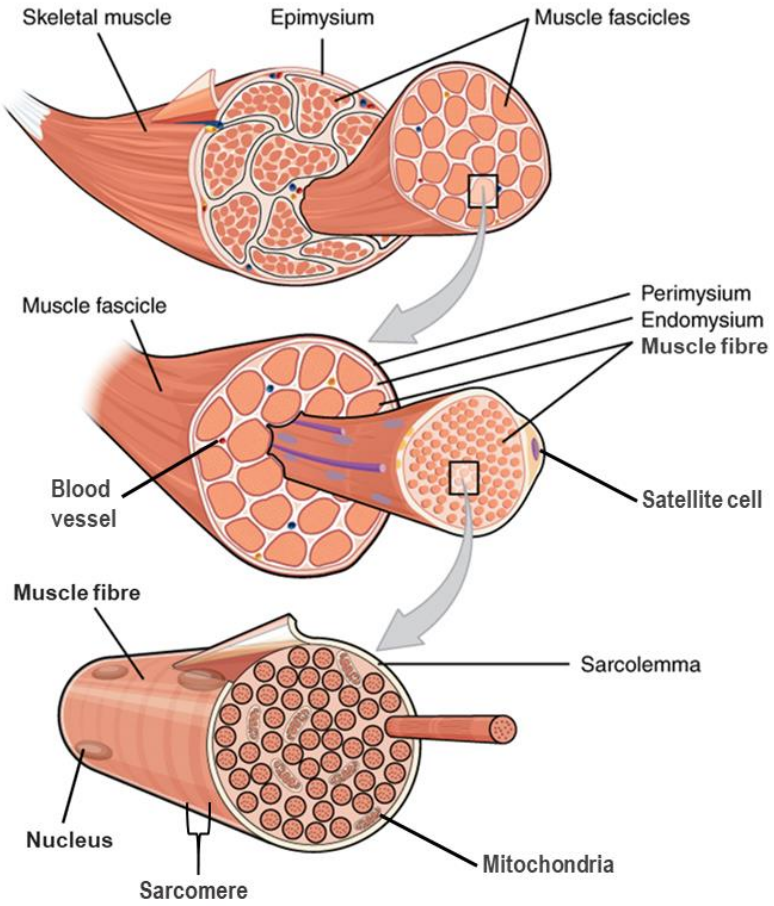

Figure 1.1. An overview of skeletal muscle structure. In brief, the epimysium surrounds the outer layer of the muscle, in which numerous muscle fibre bundles reside, known as fascicles. Fascicles are surrounded by the perimysium and muscle fibres are separated by the endomysium. Each individual muscle fibre is surrounded by a plasma membrane called the sarcolemma (Frontera and Ochala, 2015). Muscle fibres are composed of actin and myosin myofibrils which are organised and repeated as sarcomeres, the basic functional unit of skeletal muscle. This image is an adaptation from (OpenStax, 2013), which is made available under the terms of the Creative Commons Attribution 4.0 international license (https://creativecommons.org/licenses/by/4.0/deed.en).

Individual muscle fibres contain repetitive functional units called sarcomeres, which contain actin (thin) and myosin (thick) myofilaments. There can be thousands of sarcomeres within a single muscle cell and the myofilament arrangements give skeletal muscle a striated appearance (Krans, 2010). Skeletal muscle contraction is described by the sliding filament theory, which involves the shortening of sarcomeres through a molecular interaction known as cross bridge cycling (Squire, 2016; Huxley and Hanson, 1954; Huxley and Niedergerke, 1954). A cross bridge is formed when the head of a myosin myofilaments binds onto actin and pulls it along using the energy supplied by adenosine triphosphate (ATP) hydrolysis (Figure 1.2).

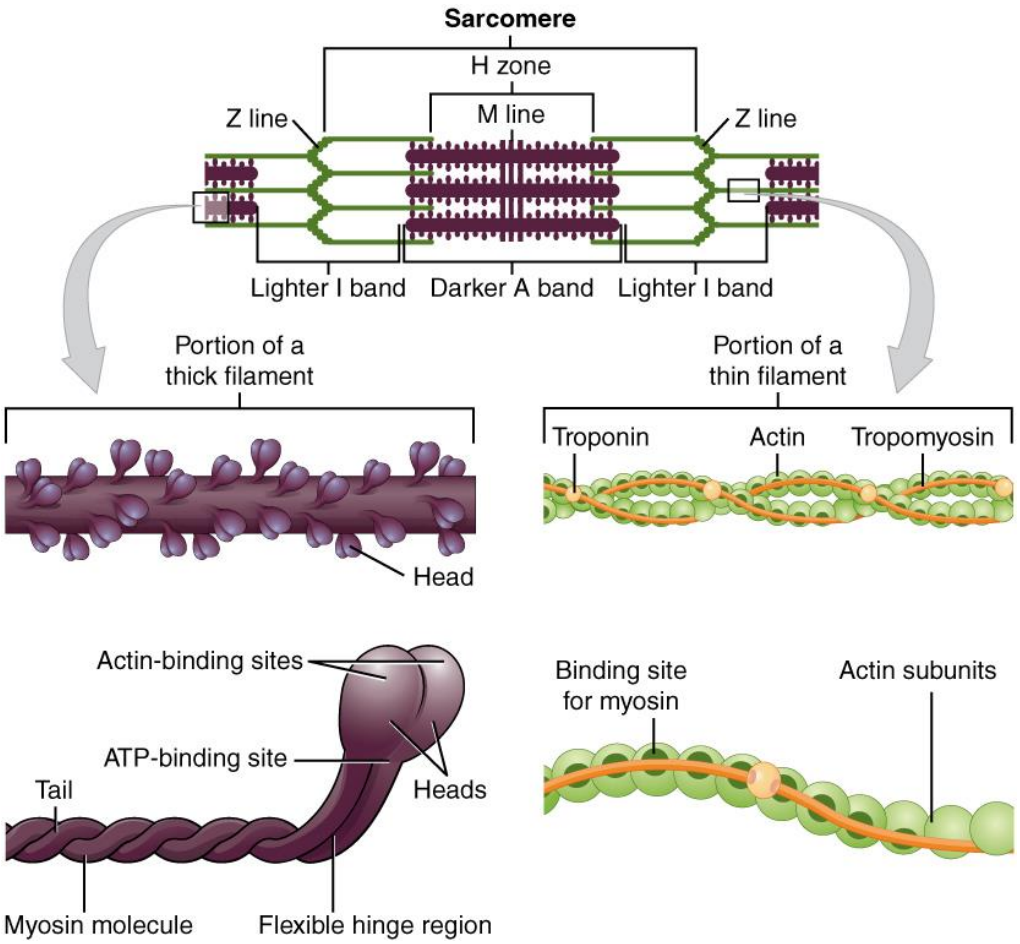

Figure 1.2. Schematic representation of sarcomere structure. The darker A band contains myosin, whilst the lighter I band contains actin. The binding of myosin to actin is regulated by the two proteins troponin and tropomyosin. At rest, tropomyosin blocks the myosin binding site, preventing contraction. For binding to occur, Ca^{2+} must bind to troponin, which in turn shifts the position of tropomyosin away from the myosin binding site. Successful binding of the myosin head onto actin, initiates cross bridge cycling. The actin myofilaments are tethered to structures located at the lateral ends of each sarcomere (Z lines), and subsequent cross bridging results in the entire sarcomere shortening. This image was taken from (OpenStax, 2013), which is made available under the terms of the Creative Commons Attribution 4.0 international license (https://creativecommons.org/licenses/by/4.0/deed.en).

Mammalian skeletal muscle can be categorised into different fibre types which allow functional adaptation to different scenarios. The most basic classification broadly divides muscle fibres into slow-twitch type I and fast-twitch type II fibres which are specialised for oxidative and glycolytic metabolism, respectively. This classification of type II fibres can be further divided into fast-twitch oxidative type IIA and fast-twitch glycolytic type IIX and IIB, due to the heterogeneity within type II muscle fibres (Schiaffino and Reggiani, 2011; Talbot and Maves, 2016). Type I muscle fibres are defined by a red appearance (high myoglobin

content), slow contraction times, high resistance to fatigue and high oxidative capacity due to high mitochondrial content - suitable for sustained aerobic activity requiring low-level force production such as walking (Scott et al., 2001). Type IIA muscle fibres function as a hybrid between type I and type II, with a red appearance, strong contractures, intermediate resistance to fatigue and a high capacity for both oxidative and glycolytic metabolism. Finally, both IIX and type IIB have a white appearance due to low levels of myoglobin and mitochondria. These fibres favour anaerobic metabolism and are highly sensitive to fatigue, best for short anaerobic activities requiring strong contractions such as sprinting and jumping (Schiaffino and Reggiani, 2011).

Mature muscle fibres are post-mitotic but have a high capacity for regeneration due to adult muscle stem cells known as satellite cells, which reside between the basal lamina and the sarcolemma (Nguyen et al., 2019). In the event of muscle damage (i.e. through exercise), satellite cells activate to regenerate new muscle fibres for growth and repair (Yin et al., 2013). Activated satellite cells proliferate and undergo differentiation to form myoblasts, defined as embryonic precursors of muscle cells. These myoblasts can then differentiate further and merge into multinucleated muscle fibres *in vitro* (myotubes), a process governed by a network of transcription factors (Yin et al., 2013; Mukund and Subramaniam, 2020).

1.1.1 Calcium signalling in skeletal muscle

Ca^{2+} is a ubiquitous messenger, responsible for the regulation of many cellular processes including skeletal muscle function. Ca^{2+} in skeletal muscle is stored within the sarcoplasmic reticulum (SR), at an estimated concentration of 0.3 mM (Rudolf et al., 2006). In contrast, the resting Ca^{2+} concentration ($[Ca^{2+}]_{rest}$) within the cytosol is much lower (~100 nM) and acute alterations in $[Ca^{2+}]_{rest}$ are required to regulate muscle contraction and relaxation mechanisms (Calderon et al., 2014; Kuo and Ehrlich, 2015). Rapid changes in $[Ca^{2+}]_{rest}$ are a result of Ca^{2+} efflux from the SR which is triggered by the propagation of action potentials across the sarcolemma (Gehlert et al., 2015). The efflux of Ca^{2+} from the SR is dependent on the molecular interactions between the L-type voltage-gated Ca^{2+} channel, dihydropyridine receptors (DHPR), and the isoform 1 Ca^{2+} release channel ryanodine receptors (RyR1). The process in which an electrical stimulus is converted into a mechanical response is known as excitation-contraction coupling (1.3) (Sandow, 1952).

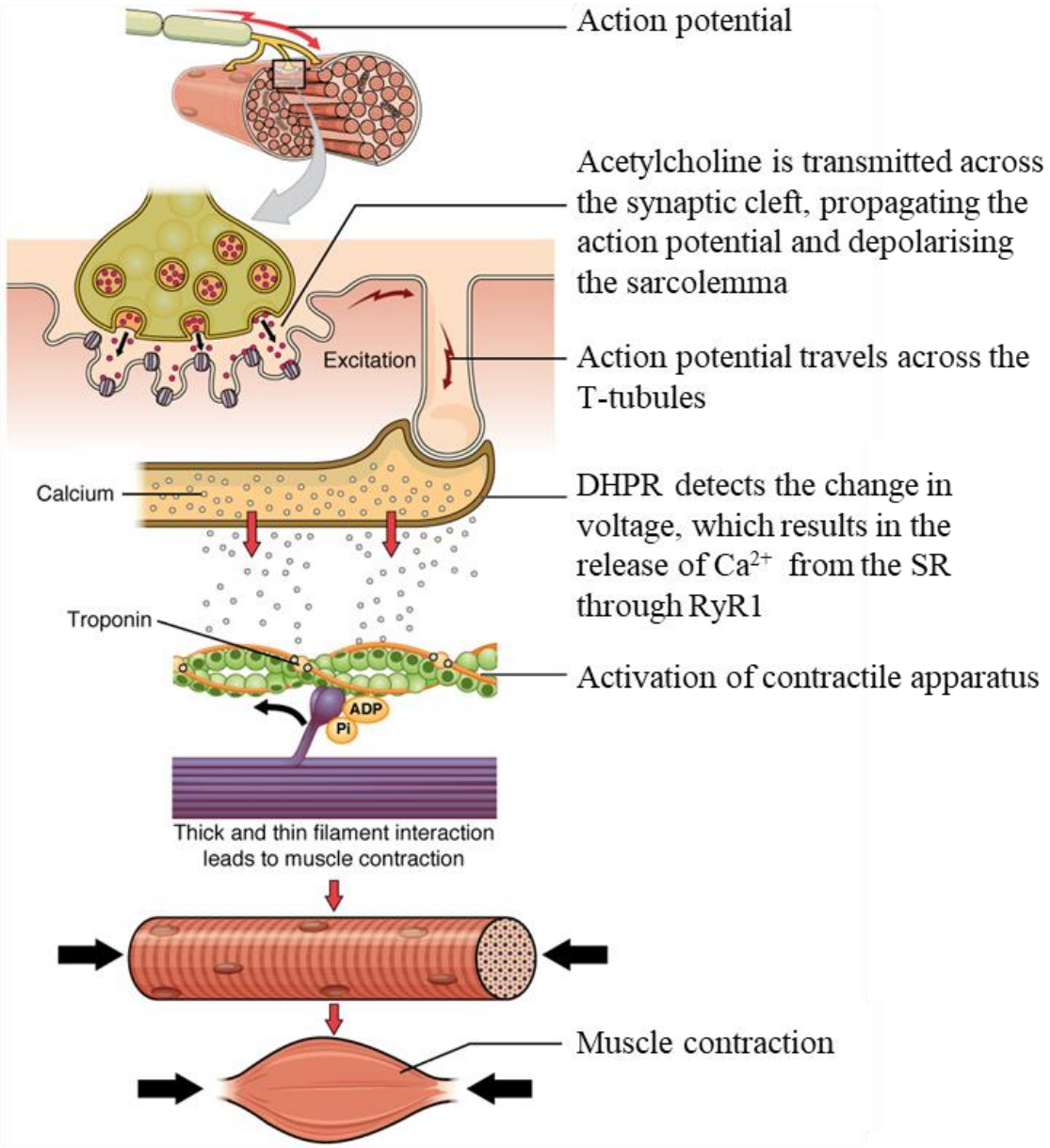

Figure 1.3. An overview of excitation-contraction coupling. In brief, when an action potential has been initiated and reaches the neuromuscular junction, vesicles of acetylcholine are released which bind to receptors on the motor end plate. This results in the activation of sodium ion channels and the depolarisation of the sarcolemma, creating another action potential. This action potential travels across invaginations in the sarcolemma called the t-tubules, and the voltage change is detected by the voltage-gated Ca^{2+} channel DHPR. DHPR then interacts with RyR1 which results in Ca^{2+} efflux from the SR. Elevations in $[Ca^{2+}]_{rest}$ activates the contractile apparatus and the subsequent interactions between myofilaments, lead to muscle contraction through the shortening of sarcomeres. This image is an adaptation taken from (OpenStax, 2013), which is made available under the terms of the Creative Commons Attribution 4.0 international license (https://creativecommons.org/licenses/by/4.0/deed.en).

Following muscle contraction, $[Ca^{2+}]_{rest}$ is returned to basal level primarily though SR replenishment and extracellular Ca^{2+} entry. The reuptake of Ca^{2+} back into the SR is facilitated by ATP-dependent sarcoplasmic/endoplasmic reticulum calcium ATPase pumps (SERCA) on the SR membrane (Stammers et al., 2015). The Ca^{2+} within the SR is buffered by the luminal protein calsequestrin (CASQ), which prevents the SR from swelling in the presence of high $[Ca^{2+}]$ (Murphy et al., 2009a). Alongside SERCA, the replenishing of SR Ca^{2+} is assisted by store operated Ca^{2+} entry (SOCE), which facilitates the transport of extracellular Ca^{2+} into the cytosol (Trebak et al., 2013).

SOCE is dependent on the interactions between the Ca^{2+} channel Orai1 (present on the sarcolemma) and the Ca^{2+} sensor stromal interaction molecule 1 (STIM1) (present on the SR membrane), both of which activate in response to the depletion of Ca^{2+} from the SR (Cho et al., 2017) (Figure 1.4). The entry of extracellular Ca^{2+} from SOCE is important for Ca^{2+} homeostasis and assists the maintenance (but not initiation) of muscle contraction in addition to muscle differentiation and growth, through the activation of Ca^{2+}-dependent pathways (Kiviluoto et al., 2011; Cho et al., 2017).

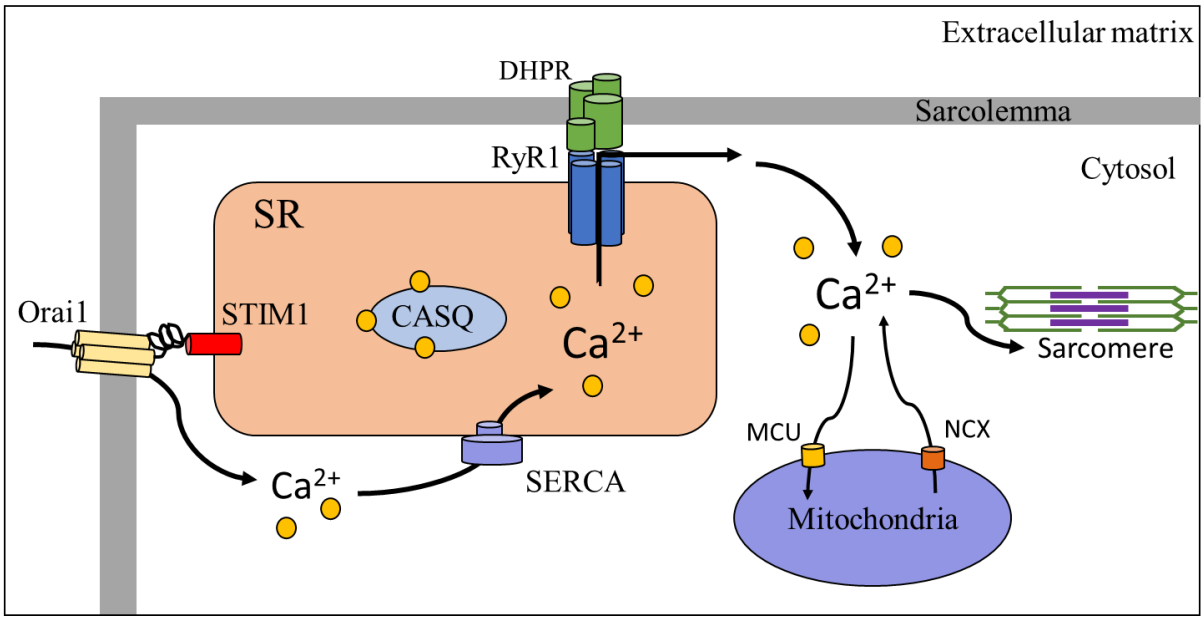

Figure 1.4. Modes of Ca^{2+} homeostasis in skeletal muscle. A schematic diagram outlining the different modes of Ca^{2+} transport within skeletal muscle. This image was drawn based on information from (Gehlert et al., 2015; Cho et al., 2017; Contreras et al., 2010).

1.1.2 Mitochondrial function

Ca^{2+} handling by mitochondria is important for energy production, $[Ca^{2+}]_{rest}$ maintenance and determining cell fate (Contreras et al., 2010). Mitochondria are known as the powerhouses of the cell and provide the ATP required for muscle contraction and Ca^{2+} homeostasis through oxidative phosphorylation (OXPHOS). Physical training through repeated bouts of endurance exercise promotes mitochondrial biogenesis in skeletal muscle, which reflects an increase in mitochondrial content and/or a change in mitochondrial composition (Ljubicic et al., 2010). This remodelling of skeletal muscle mitochondria helps the muscle to adapt and serve different functions more efficiently and reduce its sensitivity to fatigue.

In addition to the activity of SERCA and SOCE, studies have shown that mitochondria also act as Ca^{2+} buffers and secondary Ca^{2+} stores to help regulate $[Ca^{2+}]_{rest}$ (Contreras et al., 2010). Ca^{2+} signalling regulates mitochondrial function by altering the activity of dehydrogenase enzymes which are sensitive to changes in cytosolic and mitochondrial $[Ca^{2+}]$ (Denton, 2009). The uptake of Ca^{2+} in mitochondria is facilitated by the mitochondrial Ca^{2+} uniporter (MCU) and expelled from the organelle through sodium (Na^+)/Ca^{2+} antiporters (NCX) (Figure 1.4) (Mishra et al., 2017; Palty et al., 2010). During pathological instances of mitochondrial Ca^{2+} overload, the mitochondrial permeability transition pore (MPTP) can activate which causes mitochondrial swelling and initiates apoptotic mechanisms (Rasola and Bernardi, 2007).

1.1.3 Oxidative phosphorylation

Most of the energy production in skeletal muscle occurs through OXPHOS, where electrons and oxygen are converted into energy in the form of ATP (Mitchell and Moyle, 1967). This process takes place in the inner mitochondrial membrane through the electron transport system (ETS), which consists of several multi-subunit enzymes: NADH dehydrogenase (complex I), Succinate dehydrogenase (complex II), cytochrome c oxidoreductase (complex III), cytochrome c oxidase (complex IV) and ATP synthase (complex V) (Chaban et al., 2014). OXPHOS requires the donation of electrons from nicotinamide adenine dinucleotide (NADH) and flavin adenine dinucleotide ($FADH_2$), produced by fatty acid oxidation and the citric acid cycle within the mitochondrial matrix, and by glycolysis within the cytosol. The ETS utilizes

the energy from electron transport to transfer protons across the inner mitochondrial membrane which generates a proton gradient. The ETS is known to as a 'coupled' system as transfer of protons is dependent on the transport of electrons. The proton gradient generated is used by ATP synthase to generate ATP from adenosine diphosphate (ADP) (Figure 1.5) (Berg et al., 2002).

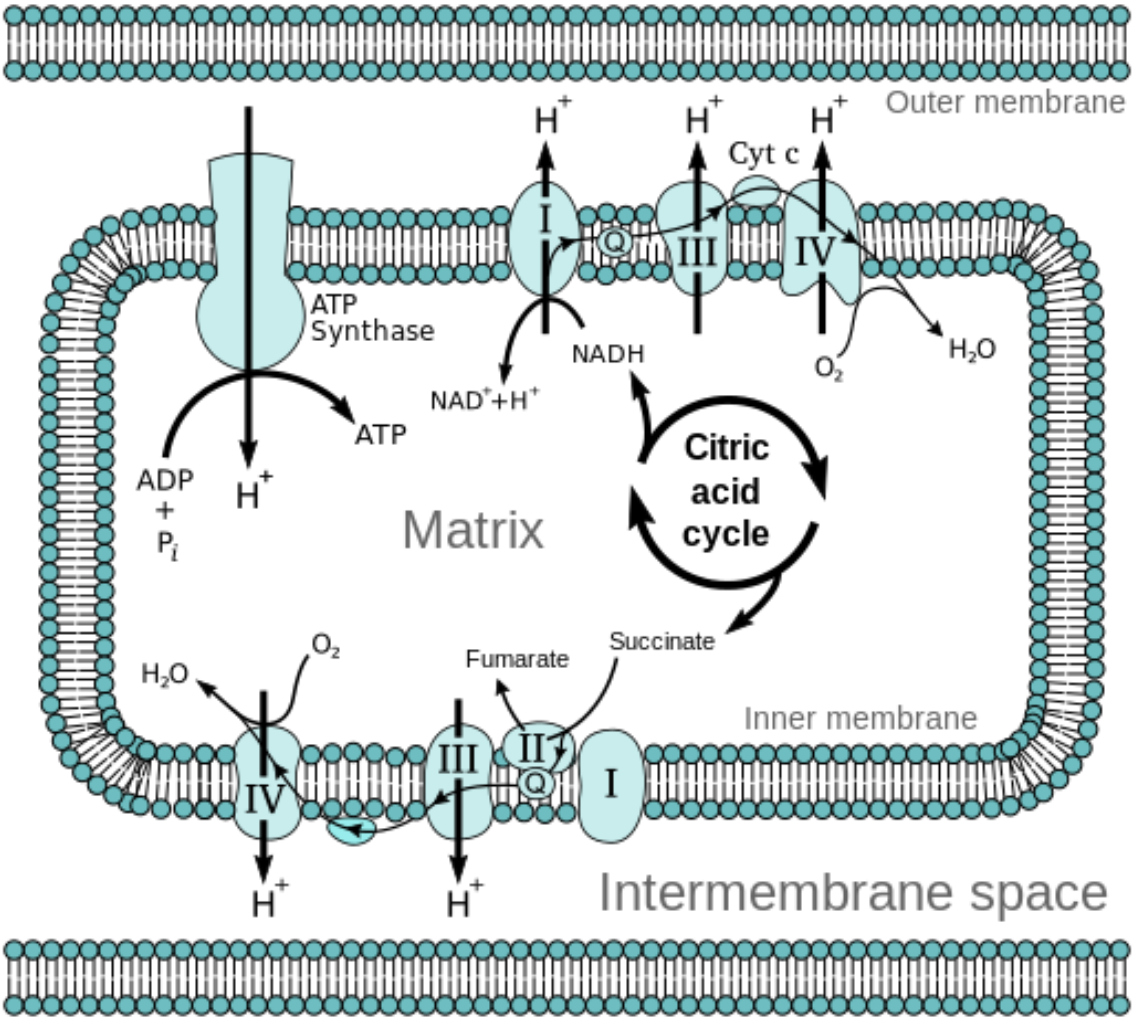

Figure 1.5. Schematic representation of the mitochondrial electron transport system. In brief, OXPHOS is initiated by the transfer of electrons from NADH to complex I and $FADH_2$ to complex II. NADH and $FADH_2$ are the first electron donors generated through glycolysis, fatty acid oxidation and the citric acid cycle. These electrons are then transferred to complex III and complex IV by the mobile electron carriers, ubiquinone (Q) and cytochrome c (Cyt c), respectively. Finally, these electrons are donated to the final electron acceptor, molecular oxygen, to generate water. The energy released from the transfer of electrons is used to pump protons through the inner mitochondrial membrane and into the intermembrane space to generate a proton gradient. The movement of protons occur at complexes I, III and IV. Complex V (ATP Synthase) uses this proton gradient to drive the conversion of ADP to ATP (Berg et al., 2002; Chaban et al., 2014). Image was taken from the public domain and adapted.

1.1.4 Ryanodine receptors

The ryanodine receptor (RyR) is a type of intracellular Ca^{2+} channel, responsible for the release of Ca^{2+} from the endoplasmic reticulum (ER)/SR. In humans, there are three RyR isoforms (RyR1, RyR2, RyR3), which are expressed in a wide range of cell types (Lanner et al., 2010). The first isoform RyR1 was cloned in 1990 and is localized primarily in skeletal muscle (Zorzato et al., 1990). The second isoform RyR2 is found in cardiac cells (Otsu et al., 1990). RyR3, formally known as the brain isoform, was first identified in brain tissue (Hakamata et al., 1992). The function of RyRs are vital for excitation-contraction coupling in skeletal/cardiac muscle and Ca^{2+} homeostasis.

For this thesis, RyR1 will be the primary focus and will be discussed in greater detail. The RyR1 is a large channel with a molecular mass of ~2.3 MDa and a homotetrameric structure consisting of four protomers, each containing ~5000 amino acid residues (Imagawa et al., 1987; Inui et al., 1987). Cryo-electron microscopy (Cryo-EM) reports have revealed that these protomers are built on an extended α-solenoid scaffold surrounding a transmembrane pore with a general structure belonging to the six-transmembrane ion channel superfamily (Zalk et al., 2015; Yan et al., 2015).

Binding sites for Ca^{2+}, ATP, caffeine and ryanodine have been identified in RyR1 (des Georges et al., 2016). The binding sites for Ca^{2+}, caffeine and ATP are located at interdomain interfaces of the C-terminal domain and successful binding of these activating ligands result in conformational changes that lead to the opening of RyR1 (Figure 1.6). The Ca^{2+} binding sites on RyR1 are divided into high affinity activating sites and low affinity inactivating sites which regulate RyR1 in a concentration-dependent manner (des Georges et al., 2016). The activity of RyR1 is also modulated through interactions with the DHPR, intracellular molecules (e.g. Ca^{2+}, Mg^{2+}, ATP), and Ca^{2+}-handling proteins (e.g. CASQ and Calmodulin) and through post-translational modifications (e.g. oxidation, phosphorylation) (Lanner et al., 2010; Hernandez-Ochoa et al., 2015).

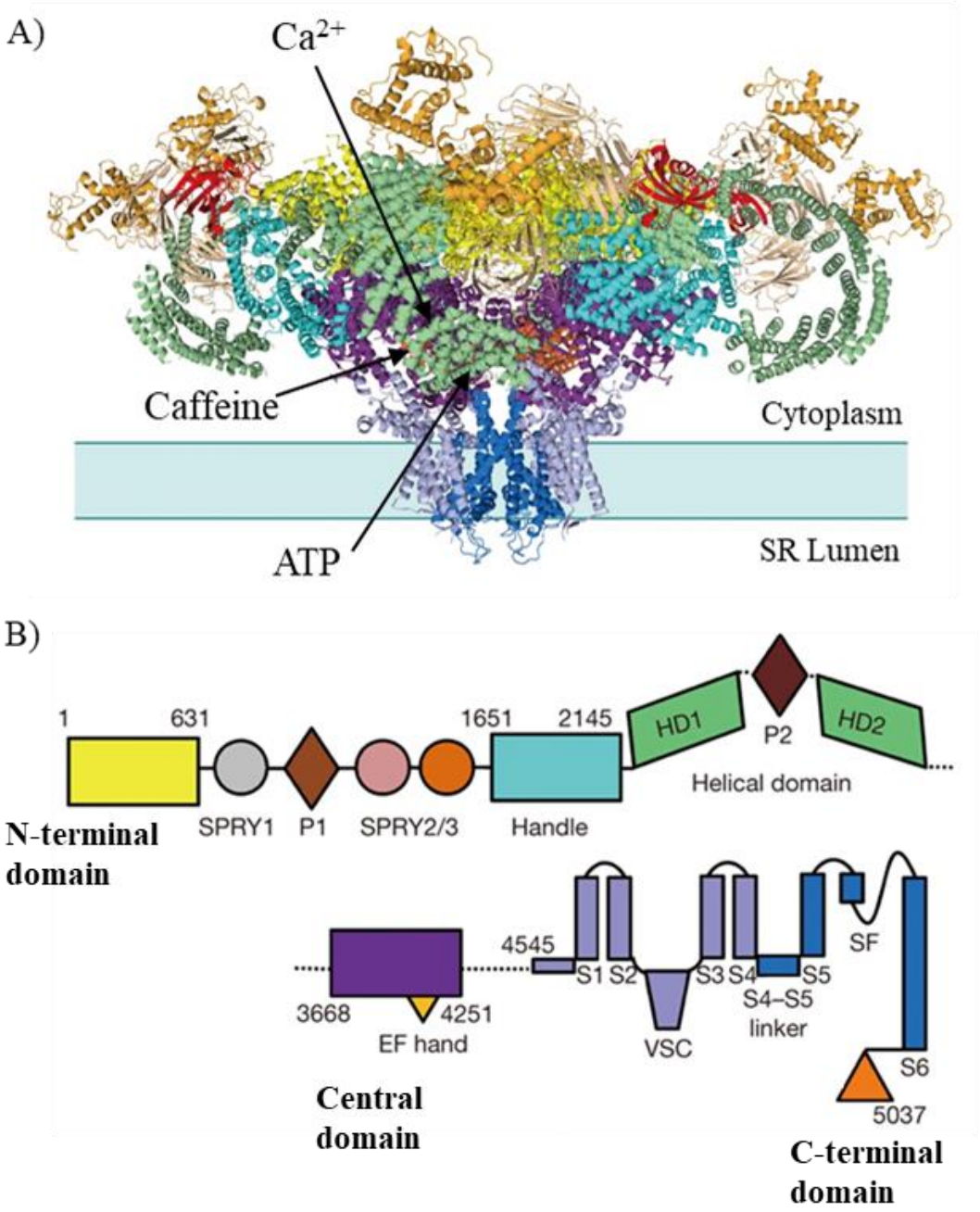

Figure 1.6. Structure of RyR1. A) Tetrameric structure of RyR1 and its orientation on the SR membrane. The binding sites for Ca2+, caffeine and ATP are located at interdomain interfaces of the C-terminal domain their approximate locations are indicated by the arrows. **B)** Schematic diagram of RyR1 domain organisation. This image is adapted from (Yan et al., 2015).

The gene encoding RyR1 (*RYR1*) is located on chromosome 19q13.2, and *RYR1* mutations have been associated with several inherited skeletal muscle disorders with both dominant and recessive modes of inheritance (Kushnir et al., 2018). Examples of these include MH, central core disease, multi-minicore disease, nemaline myopathy and centronuclear myopathy (Kushnir et al., 2018; Robinson et al., 2006). These conditions all feature RyR1-related Ca^{2+} dysregulation which impairs excitation-contraction coupling and general skeletal muscle function.

1.1.5 The Dihydropyridine receptor

The DHPR is an L-type voltage-gated Ca^{2+} channel situated in the sarcolemma at t-tubules. The DHPR has a molecular mass of 450 kDa, consisting of five subunits (α1, α2, δ, β and γ) and is essential for excitation-contraction coupling and Ca^{2+} homeostasis (Hu et al., 2015; Sandow, 1952). DHPRs are mechanically coupled to RyR1 at sites known as calcium release units (CRU), referring to junctions where the sarcolemma and SR membrane are in proximity (Franzini-Armstrong and Jorgensen, 1994). In response to membrane depolarisation (via action potentials), DHPRs undergo conformational changes which in turn triggers the activation of RyR1, resulting in the rapid release of Ca^{2+} from the SR into the cytosol (Calderon et al., 2014). The α1 subunit of DHPR is encoded by the *CACNA1S* gene (also known as *CACNL1A3*) which is mapped to chromosome 1q32.1, and mutations within this gene have been associated with MH and hypokalemic periodic paralysis type 1 (Monnier et al., 1997; Ptacek et al., 1994).

1.2 MALIGNANT HYPERTHERMIA

MH (MIM# 145600) is a potentially fatal, pharmacogenetic disorder which affects Ca^{2+} homeostasis in skeletal muscle. Individuals susceptible to MH (MHS) undergo hypermetabolic reactions when exposed to volatile anaesthetics (e.g. halothane, sevoflurane, isoflurane) and the muscle relaxant succinylcholine (Hopkins, 2011). The first case of human MH susceptibility was described in 1960, featuring a family in which 10 out of 38 members died after exposure to GA (Denborough et al., 1962). MH is known to be inherited in an autosomal dominant mendelian fashion, but there is increasing evidence which supports a threshold (non-

mendelian) genetic model with genetic modifiers of phenotype (Robinson et al., 2000; Monnier et al., 2002; Robinson et al., 2003a; Carpenter et al., 2009b; Miller et al., 2018). MH susceptibility is associated with mutations in *RYR1*, *CACNA1S* and *STAC3*, all of which encode proteins directly involved with excitation-contraction coupling (Robinson et al., 2006; Monnier et al., 1997; Horstick et al., 2013).

Clinical features of an MH reaction include an increase in carbon dioxide (CO_2) production and oxygen consumption, followed by tachycardia, hyperthermia, sustained muscle contracture and progressive muscle rigidity (Rosenberg et al., 2015; Larach et al., 2008). Without intervention, prolonged MH reactions progress to respiratory and metabolic acidosis due to skeletal muscle ATP depletion. Life-threatening complications include rhabdomyolysis, acute renal failure, heart failure, and disseminated intravascular coagulation (Rosenberg et al., 2015; Gupta and Hopkins, 2017). The only drug specifically used to treat MH is Dantrolene, which acts as an RyR1 agonist and halts the Ca^{2+} efflux from the SR thereby interrupting muscle contraction (Glahn et al., 2010; Bannister, 2013).

1.2.1 Epidemiology

In the UK population, the incidence of MH reactions occurring under anaesthesia has been estimated to be within the range of 1:50,000 to 1:70,000 anaesthetic procedures (Gupta and Hopkins, 2017). However, these estimations do not reflect the true prevalence of MH within the population, as there is incomplete penetrance of the genetic trait. Many individuals who were later found to be MHS, did not have MH reactions upon first exposure to triggering agents (Ibarra Moreno et al., 2019). Some may also never experience procedures requiring anaesthesia, which contributes towards an underestimation of prevalence. It is therefore accepted that the genetic traits for MH may require the contributions of additional genetic or non-genetic factors to manifest, which makes it difficult to estimate disease penetrance (Shaw and Hopkins, 2019). Despite these difficulties, the estimated prevalence for carrying a pathogenic *RYR1* mutation was estimated to be as high as 1:1500 (Shaw and Hopkins, 2019), which accounts for approximately 76% of MH families within the UK (Miller et al., 2018). MH can affect all ethnicities but there is evidence of higher incidence in males (2:1) and those who are of a younger age demographic (Riazi et al., 2014; Rosenberg et al., 2015).

1.2.2 Diagnosis

The diagnosis of MH susceptibility can be achieved through the *in vitro* contracture test (IVCT), which involves challenging a muscle biopsy with halothane and caffeine (EMHG, 1984). The IVCT is standardised across Europe by the European Malignant Hyperthermia Group (EMHG) and is known to have a high sensitivity (99%) and specificity (94%) (Hopkins et al., 2015). It remains as the only definitive method used to confirm MH susceptibility, but some individuals can be diagnosed through genetic testing if they are from families with a known causative MH mutation (Hopkins et al., 2015; Urwyler et al., 2001). The first individual to have an MH reaction within a family (proband/index case) and relatives from MH families without known causative mutations are always referred for the IVCT (Hopkins et al., 2015). The only exclusion criteria are children under the age of 10, due to lack of sensitivity data below that age, and children who weigh less than 30 kg, due to sample length requirements (Gupta and Hopkins, 2017). Muscle biopsies for the IVCT are taken from the *vastus medialis* (one of the four muscles that make up the quadriceps) and they are exposed to incremental concentrations of halothane (0.5, 1.0, 2.0 Vol%) (Figure 1.7) and caffeine (0.5; 1.0; 1.5; 2.0; 3.0; 4.0; and 32 mmol L-1) (EMHG, 1984).

The force of muscle contracture in response to each drug is measured at each concentration and the diagnosis is dependent on whether it meets the required diagnostic threshold (Hopkins et al., 2015). A more detailed description of this procedure can be found in chapter 2, section 2.2.2. The outcome of the IVCT assigns everyone to one of four IVCT phenotypes: MH non-susceptible (MHN), MHS_h (abnormal reaction to halothane only), MHS_{hc} (abnormal reaction to both halothane and caffeine) and MHS_c (abnormal response to caffeine only). People with an IVCT phenotype corresponding to an abnormal response to either halothane, caffeine, or both, are managed as individuals clinically at risk of MH (Hopkins et al., 2015).

Genetic screening is an alternative, less invasive means for MH diagnosis using blood samples. The relatives of MHS individuals with known causative mutations are usually referred for genotyping to screen for familial variants (Urwyler et al., 2001). If the familial variant is identified, MHS diagnosis in these cases can be based on the results of genetic screening alone. Relatives who are genotyped and are absent for the familial mutation are subsequently referred to IVCT for diagnosis (Hopkins et al., 2015). At present, the prospective genetic screening for MH susceptibility involves a panel of 50 functionally characterised mutations (48 variants in

RYR1 and two variants in *CACNA1S*), recognised by the EMHG (www.emhg.org, 2020). This list is constantly updated as more genetic variants are discovered and functionally characterised.

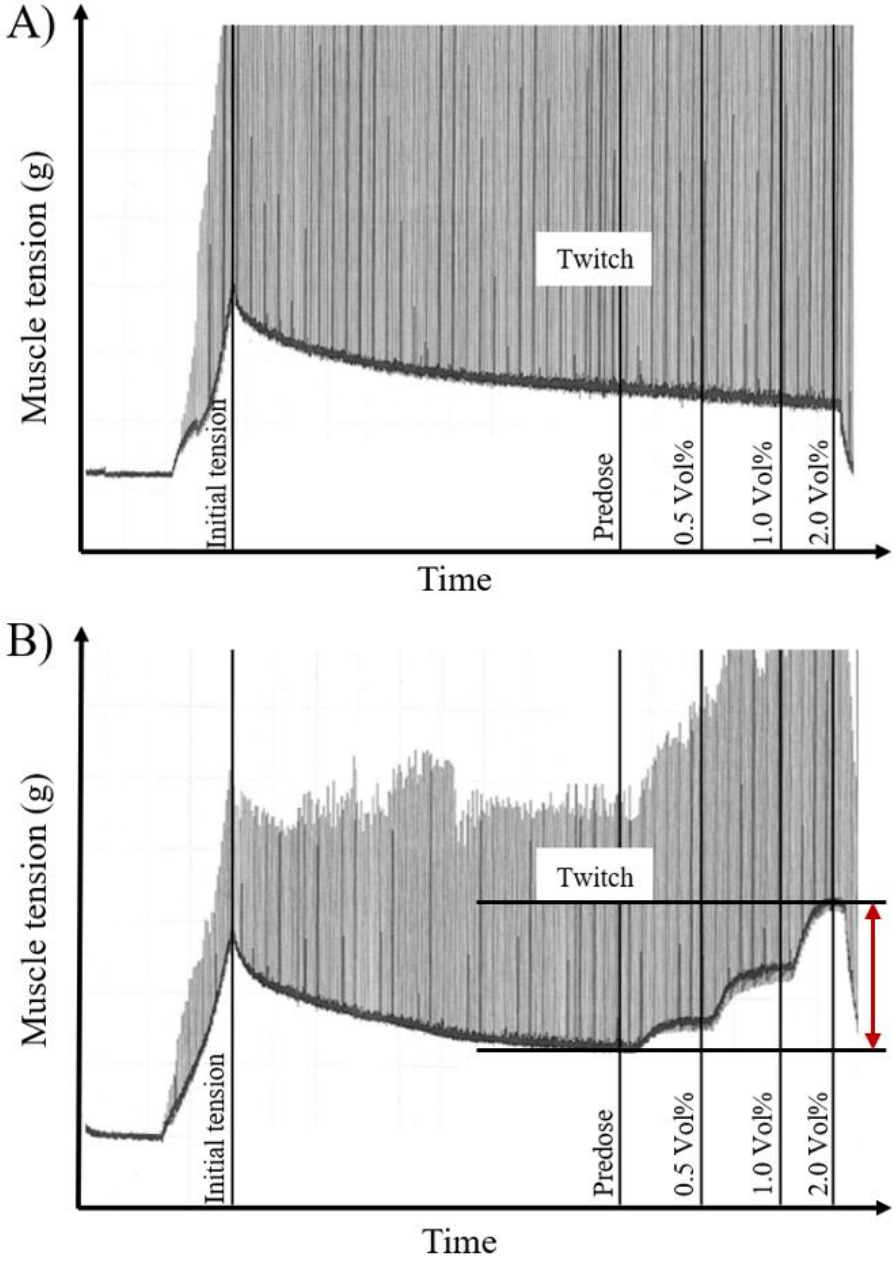

Figure 1.7. *In vitro* contracture test using halothane. These are representative IVCT traces using for an **A)** MHN and **B)** MHS individual using incremental concentrations of halothane (Predose, 0.5, 1.0, 2.0 Vol%). The muscle biopsy viability is dependent on the quality of the muscle twitch. The initial tension is measured after applying electrical stimulation and this is used as a reference to scale the measurement made at 2.0 Vol% halothane (indicated by the red arrow). Muscle tension (g) is measured over time and a positive (abnormal) response to halothane corresponds to a contracture strength of 0.2g at 2.0 Vol% (EMHG, 1984; Hopkins et al., 2015).

1.2.3 Causative mutations

Mutations in *RYR1* account for the majority of MHS individuals (~70%), whilst *CACNA1S* and *STAC3* account for <2% of cases (Robinson et al., 2006; Monnier et al., 1997; Horstick et al., 2013; Carpenter et al., 2009a). A significant proportion (~30%) of the MHS population still do not have pathogenic mutations assigned, which highlights the need for further investigation. RyR mutations were first identified as a candidate for human MH through a linkage study with MH families, where co-segregation of the MH phenotype was observed with *RYR* markers (MacLennan et al., 1990). Since then, hundreds of *RYR1* mutations have been associated with MH but only a small proportion is used for diagnostic genetic testing. The most prevalent mutation within the UK is the *RYR1* c.7300G>A variant which accounts for 16% of MHS families (Miller et al., 2018). Mutations in *RYR1* cause a gain-of-function effect in skeletal muscle which increases RyR1 sensitivity to activation. This results in Ca^{2+} dysregulation, impaired excitation-contraction coupling and the involuntary opening of RyR1 when exposed to MH triggering agents. Although rare, some cases of human MH have also been reported with homozygous and compound heterozygous RyR1 mutation carriers (Lynch et al., 1997; Rueffert et al., 2001; Monnier et al., 2002).

Mutations in *CACNA1S* were first associated with MH after its identification in a large French pedigree (Monnier et al., 1997). Functional analysis of *CACNA1S* mutations have shown to cause a similar gain-of-function effect in skeletal muscle which results in Ca^{2+} dysregulation and heightened RyR1 sensitivity (Weiss et al., 2004). The third candidate gene for human MH, *STAC3*, encodes a muscle-specific adaptor protein, which has been shown to modulate SR Ca^{2+} release and the conformational coupling between RyR1 and DHPR (Nelson et al., 2013; Polster et al., 2016). It is associated with native American myopathy and mutations in *STAC3* were found to decrease excitation-contraction coupling (Horstick et al., 2013).

1.2.4 Discordance

The main challenge in the diagnosis of MH is the high degree of genotype-phenotype discordance observed in this disorder (Miller et al., 2018). Discordance in the context of MH, refers to MHS individuals (diagnosed through IVCT) who lack the familial mutation, or individuals who are MHN (diagnosed through IVCT) and have been confirmed to carry the

familial variant (Robinson et al., 2003b). There have been many reports of discordance within MH families in the past (Deufel et al., 1995; Fagerlund et al., 1997; Fortunato et al., 1999; Heytens, 2007) and two of the largest studies were reported within the UK population (Robinson et al., 2002; Miller et al., 2018). In 2002, a study observed genotype-phenotype discordance in nine out of 297 individuals within the UK, in which five individuals were false-positive and four were false-negative (Robinson et al., 2002). A more recent study reported higher rates of discordance having found genotype-phenotype discrepancies in 86 out of 328 MH families (Miller et al., 2018). These results show that reliable diagnoses of MH cannot be based on genetic testing alone. All discordant individuals who are mutation negative but IVCT positive are therefore still managed as clinically at risk of MH and relatives who lack the familial variant, are always referred to IVCT to minimise the chance of false-negative diagnoses (Hopkins et al., 2015; Robinson et al., 2003b). The discordance observed in MH indicates further genetic complexity and may be due to a combination of genetic and environmental modifiers of phenotype yet to be discovered.

1.2.5 Disorders associated with malignant hyperthermia

As MH is predominantly caused by mutations in *RYR1*, it is associated with several RyR1-related myopathies such as central core disease and multi-minicore disease (Litman et al., 2018). Central core disease (MIM# 117000) is defined as an inherited neuromuscular disorder characterised by central cores in skeletal muscle and clinical features of congenital myopathy. Central cores refer to regions devoid of mitochondria, predominantly in type I fibres and are consequently deficient in oxidative metabolism (Jungbluth, 2007). Central core disease can be inherited in an autosomal dominant and recessive fashion (Manzur et al., 1998), and often manifests in infancy, with variable clinical features ranging from asymptomatic to mild/severe muscle stiffness, weakness, muscle atrophy and skeletal deformities such as scoliosis (Jungbluth, 2007).

Multi-minicore disease (MIM# 255320) is also a neuromuscular disorder, defined by ‘minicores’ which refer to areas of sarcomeric disorganisation and diminished oxidative activity due to lack of mitochondria. Multi-minicore disease is another early onset congenital myopathy but features an autosomal recessive mode of inheritance (Wei and Dirksen, 2010). Typical clinical features include: hypotonia, developmental delay, muscle weakness and

scoliosis. Both central core disease and multi-minicore disease are rare congenital myopathies which share an overlap in *RYR1* mutations also associated with MH, making those conditions a significant risk factor (Robinson et al., 2006). Individuals who have central core disease were also reported to have more severe MH phenotypes based on IVCT data (Robinson et al., 2002).

1.2.6 Animal models for malignant hyperthermia

MH susceptibility is not specific to humans, and has also been reported in dogs, horses, giraffes, pigs and genetically engineered mice (Roberts et al., 2001; Aleman et al., 2004; Citino et al., 1984; Harrison, 1975; Chelu et al., 2006). A lot of early MH research involved MHS pigs, but unlike humans, MH susceptibility in pigs arises from autosomal recessive inheritance of *RYR1* mutations which also predisposes them to an overt sensitivity to stress (Fujii et al., 1991; Fletcher et al., 1991a). These stress-induced MH reactions in pigs mimic those triggered by GA in MHS humans, characterised by muscle rigidity, tachycardia, metabolic acidosis, hyperthermia, and death (Mitchell and Heffron, 1982). Human MH is typically triggered by anaesthetic means but there have been cases of 'awake' MH episodes triggered by heat stress, similar to those experienced in MHS pigs, in the absence of anaesthesia (Gronert et al., 1980; Groom et al., 2011; Nishio et al., 2009; Carsana, 2013).

Modern MH research has now adopted the use of transgenic mice after the first RYR1 knock-in mouse model of MH was developed (Chelu et al., 2006). There are currently four MH mouse models available, created using different *RYR1* mutations associated with MH susceptibility in humans (Table 1.1). RYR1-knock in mice typically feature elevated $[Ca^{2+}]_{rest}$, increased oxidative stress and increased sensitivity to temperature, caffeine, and volatile anaesthetics. Mice with homozygous expression of the RYR1 mutation often have increased phenotype severity, or result in non-viable offspring, depending on the variant used to create it (Chelu et al., 2006; Yang et al., 2006; Yuen et al., 2012; Lopez et al., 2018). Skeletal muscle from porcine and murine models of MH, both have higher $[Ca^{2+}]_{rest}$ (approximately three-fold greater) in comparison to non-susceptible muscle (Yang et al., 2006; Lopez et al., 1986), and exposure to clinically relevant doses of volatile anaesthetics has been shown to further elevate $[Ca^{2+}]_{rest}$ by several fold (Barrientos et al., 2012; Lopez et al., 1988).

RYR1 mutation	Exon	Mutation position (Amino acid change)	Disease	Reference
Y522S	14	1565A>C (Tyrosine to Serine)	MH/central core disease	Chelu *et al.*, 2006
R163C	6	487C>T (Arginine to Cysteine)	MH/central core disease	Yang *et al.*, 2006
T4826I	100	14477C>T (Threonine to Isoleucine)	MH	Yuen *et al.*, 2012
G2435R	45	7300G>A (Glycine to Arginine)	MH	Lopez *et al.*, 2018

Table 1.1. RYR1 knock-in mouse models of malignant hyperthermia. A summary of the RYR1 knock-in mouse models that have been developed based on human *RYR1* mutations associated with MH and central core disease (Chelu et al., 2006; Yang et al., 2006; Yuen et al., 2012; Lopez et al., 2018).

1.3 THESIS AIMS AND RESULT CHAPTER SUMMARIES

This thesis aims to identify potential modifiers of the MH phenotype by comparing genome-wide gene expression and mitochondrial function between MHS and MHN skeletal muscle, before and after drug challenge. This project is divided into four separate results chapters, each with chapter-specific introductions, followed by methods, results and discussion. A summary of each chapter is described below.

- Chapter two describes a next generation RNA sequencing (RNAseq) experiment to investigate differential gene expression between MHN and MHS skeletal muscle. mRNA was extracted from MHN and MHS human muscle biopsies, and gene expression profiles were compared at baseline and after IVCT. Lists of differentially expressed genes were functionally annotated, and genes of interest were validated using real-time polymerase chain reactions (RT-PCR). Bioinformatic tools were then used to

investigate genes of interest for regulatory elements which may contribute to MH phenotype variability.

- Chapter three describes a high-resolution respirometry experiment using human muscle biopsies. This chapter aimed to identify differences in mitochondrial function between MH phenotypes which may contribute towards phenotypic variability and the muscle-related symptoms experienced by MHS individuals in absence of triggering agents. Mitochondrial function was assessed by measuring oxygen consumption rates in permeabilized muscle fibres using the Oroboros respiratory analyser (Oroboros Instruments, Innsbruk, Austria). Differences in functional capacity between phenotypes were compared at baseline and in response to IVCT.

- Chapter four describes an RNAseq experiment, using the G2435R-RYR1 knock-in mouse model of MH. This mouse model carries an *RYR1* mutation equivalent to the most common human MH mutation within the UK (c.7300G>A). The aim of this chapter was to provide the first analysis of gene expression in the new RYR1 knock-in mouse model by exploring gene expression differences between mouse genotypes. *Soleus* muscles taken from wild-type and RYR1 knock-in mice were exposed to halothane for 30 minutes before mRNA was extracted. RNAseq was performed using these samples and the gene expression profiles were compared with and without exposure to halothane. Lists of differentially expressed genes were functionally annotated to identify pathways and biological processes of interest in relation to MH.

- Chapter five describes a high-resolution respirometry experiment aimed to assess mitochondrial function in the G2435R-RYR1 knock-in mouse model for the first time. Oxygen consumption rates were measured in permeabilized muscle fibres using the Oroboros respiratory analyser and these were compared between wild-type and RYR1 knock-in genotypes. Mitochondrial function was also assessed in the same manner, in response to halothane treatment and elevated [Ca^{2+}].

2 IDENTIFICATION OF GENES ASSOCIATED WITH MALIGNANT HYPERTHERMIA AND RELATED PHENOTYPES

2.1 INTRODUCTION

The early diagnosis of an MH reaction is crucial to reduce rates of morbidity and mortality, but this can be difficult due to the variable nature of the MH phenotype. Consistent monitoring of clinical signs after anaesthesia is important as MHS probands can not only have reactions promptly after application but can also have slow response times causing delayed management (Carpenter et al., 2009b). In addition, some MHS probands are also known to have had previous anaesthetic history without triggering MH reactions which lead to underestimations of disease prevalence. Aside from clinical observations, muscle biopsies taken for IVCT also exhibit variability in the laboratory phenotype, with some MHS samples responding only to one or both muscle stimulants (halothane and caffeine)(Carpenter et al., 2009b; Robinson et al., 2002).

A few studies have attempted to make genotype-phenotype correlations by comparing IVCT contracture data between individuals carrying a range of *RYR1* variants associated with MH (Manning et al., 1998; Fiege et al., 2002; Carpenter et al., 2009b; Robinson et al., 2002). Fiege et al. found that IVCT data from MHS individuals carrying the C487-T *RYR1* mutation had lower halothane and caffeine threshold concentrations compared to those with other variants, indicating differences in RYR1 sensitivity (Fiege et al., 2002). Carpenter et al., also showed that individuals with certain *RYR1* variants had increased muscle contracture strengths and shorter response times to IVCT, introducing the concept of weak and strong MH mutations based on laboratory phenotype (Carpenter et al., 2009b). Other observations of disparity include sex-related analyses showing increased IVCT contracture strengths and shorter response times in male MHS individuals (Robinson et al., 2002) and epigenetic studies showing a parent-of-origin effect with children of affected mothers having increased chances of having MH (Robinson et al., 2009).

The cause of phenotype variability in MH is still a subject of debate. MH is traditionally seen as a genetic condition with an autosomal dominant mode of inheritance but increasing evidence supports a multifactorial model. The high rates of genotype-phenotype discordancy remain as the largest problem associated with genetic diagnosis of MH susceptibility. A significant number of individuals diagnosed as MHS, do not have causative mutations assigned, indicating the presence of unidentified variants, genes or factors contributing to MH

yet to be discovered. Throughout the years there have been many novel variants in *RYR1* and *CACNA1S* associated with MH, but only a small number have been functionally characterised for predictive diagnostic DNA screening (Brandom et al., 2013; Kim et al., 2013; Fiszer et al., 2015; Levano et al., 2017). Excluding *RYR1* and *CACNA1S*, the only other gene found to be causative of MH is *STAC3*, responsible for Native American myopathy (Horstick et al., 2013). Other gene loci of interest include *CASQ1* encoding calsequestrin (Capacchione et al., 2010) and *JSRP1* encoding JP-45, another integral SR protein (Yasuda et al., 2013). Despite modern advances, MH susceptibility caused by non-RYR1/CACNA1S/STAC3 variants is still estimated to occur in 14-23% of MH families (Miller et al., 2018). On that basis, there is still a lot to be achieved before comprehensive genetic screening is available for MH. Ongoing research aims to reduce this population of unaccounted families by functionally characterising new mutations and by exploring potential modifiers of phenotype.

One approach used to investigate disease phenotype variability is through identifying genetic variants in regions that can alter gene expression and contribute to disease. Researchers investigating different disease models have found that certain disease traits are associated with variants in modifier genes. Modifier genes are defined as genes which can influence the expression of other genes and alters disease penetrance, dominance, expressivity, and pleiotropy (Haldane, 1941; Nadeau, 2001). An example of this would be the disease model for cystic fibrosis. Cystic fibrosis is caused by mutations in the cystic fibrosis transmembrane conductance regulator (*CFTR*) gene but a range of modifier genes have been associated with variable phenotypic traits such as liver disease (*SERPINA1*), diabetes (*TCF7L2*) and pulmonary function (*EDNRA*, *IFRD1*, *IL8*) (Bartlett et al., 2009; Blackman et al., 2009; Darrah et al., 2010; Gu et al., 2009; Hillian et al., 2008).

On a broader scale, this concept is also applied to expression quantitative trait loci (eQTL), which refer to larger genomic regions containing single nucleotide polymorphisms (SNPs) that have the potential to influence mRNA expression levels. These eQTLs can either be local within 1 Mb of the transcription start site (TSS) (cis-eQTL), or distant at over 5 Mb away from the TSS or on a different chromosome (trans-eQTL) (Nica and Dermitzakis, 2013). Identification of eQTLs is often achieved through direct associations made between genotype data through genome wide association studies (GWAS) and gene expression data from transcriptome analyses (Sun, 2012). The largest available resource for eQTL data is currently the Genotype-Tissue Expression (GTEx) consortium, which is a publicly available database

containing information on over 1000 individuals across 54 types of non-diseased tissue (Consortium, 2013).

Studies indicate that most of the regulatory control takes place locally near the genes of interest, having identified many more cis-eQTLs than trans-eQTLs (Dixon et al., 2007). This may be attributed to eQTLs being enriched in enhancer elements - defined as cis-acting DNA sequences which regulation gene expression by increasing transcription levels (Garieri et al., 2017). Enhancers contain binding sites for transcription factors (TF) and are situated remotely from promoter regions, upstream or downstream of their associated gene targets (Figure 2.1). The method at which enhancers interact with gene promoters is thought to be through mechanisms of DNA looping, which bring the enhancers within proximity of target genes (Ong and Corces, 2011). Genetic variation within enhancers have shown to result in phenotypic variation. An example being the malformation of limbs due to mutations within enhancers that regulate limb-specific *SHH* expression, which is vital for distal limb development (Sagai et al., 2005). Information on known human enhancers can be found on GeneHancer, an open access database which has compiled enhancer-gene associations from four different genome-wide databases (Fishilevich et al., 2017).

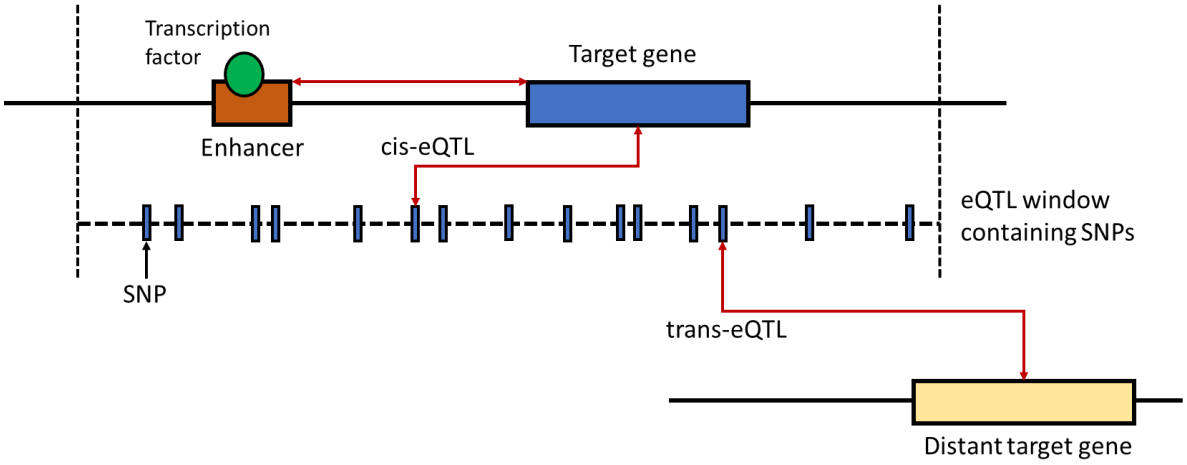

Figure 2.1. A schematic diagram of gene expression regulatory mechanisms. The eQTL window contains candidate SNPs which are associated with regulating the expression target genes. SNPs which are in proximity of the target gene (within 1 Mb of TSS) are referred to as cis-eQTLs whilst SNPs which modify distant gene expression are trans-eQTLs (>5 Mb of TSS). Enhancers activated through TF binding interact with the promoters of target genes to promote gene expression.

Due to the complexities of MH genetics, the concept of gene expression modifiers is an area of interest and thought to contribute towards the genotype-phenotype variability seen in MHS individuals. This chapter presents an investigation into gene expression modifiers aimed to identify candidate modifier loci containing regulatory elements capable of influencing the MH phenotype. This will be achieved by addressing the following research questions:

- What genes are differentially expressed in skeletal muscle at baseline, between MHN and MHS phenotypes?
- What genes are differentially expressed in skeletal muscle after exposure to halothane and caffeine?
- Do these differentially expressed genes have similar functional properties?
- Using bioinformatic resources, what regulatory elements modulate the expression of these differentially expressed genes?

Finally, any eQTLs found associated with genes of interest are presented as potential contributors to MH phenotype diversity which will need to be confirmed in larger cohorts of MHN and MHS individuals through SNP genotyping.

2.2 MATERIALS AND METHODS

2.2.1 Human muscle samples

The samples used to study human MH were provided by the Leeds MH Unit, where skeletal muscle biopsies are routinely collected for the IVCT. Patients gave written informed consent to the study that was approved by Leeds (East) Research Ethics Committee (reference 10/H1306/70). Each individual had six muscle fascicles (typical dimensions 25 mm x 4 mm x 3mm) excised from the *vastus medialis* under femoral nerve block and immediately placed in oxygenated Krebs-Ringer solution (118.1 mM NaCl, 3.4 mM KCl, 0.8 mM $MgSO_4$, 1.2 mM KH_2PO_4, 11.1 mM Glucose, 25.0 mM $NaHCO_3$, 2.5 mM $CaCl_2$, pH 7.4) at room temperature

and taken to the MH laboratory. The samples were then kept at room temperature in the Krebs-Ringer solution, which was perfused continuously with carbogen (95% O_2, 5% CO_2), until used for IVCT. Biopsy samples are frozen in RNAlater for long term storage at -80 ^oC once IVCT is complete. Muscle samples which did not undergo IVCT were used as control samples for subsequent experiments. Further details regarding the choice of control sample can be found in section 2.2.5.

2.2.2 In vitro contracture test

IVCTs were conducted by Ms Catherine Daly (Laboratory Manager of the MH Unit) and Dr Dorota Miller (Postdoctoral Researcher at the MH Unit), according to the protocol outlined by the EMHG (Hopkins et al., 2015). Muscle biopsies weighing between 100-200 mg are sutured and suspended in a tissue bath for five minutes whilst optimal tissue length is determined. The initial length of tissue is measured between sutures and held for four minutes before electrically stimulated (1-2 ms supramaximal stimulus at a frequency of 0.2 Hz) and slowly stretched at a force of 2mN (0.2g) to achieve optimal twitch readings (2-3g or 120-150% of initial length). This new length is referred to as the optimal tissue length and is held for 15 minutes for stabilisation.

Caffeine treatment was applied through perfusing the tissue bath with incremental increases of caffeine concentration at 0.5; 1.0; 1.5; 2.0; 3.0; 4.0; and 32 mmol L-1. Each increment was applied after three minutes of exposure with the previous concentration. The muscle contracture strength in response to drug treatment was measured and a contracture of 2 mN (0.2g) at 2 mmol L-1 corresponds to a positive caffeine result. Likewise, halothane treatment was applied through perfusing the tissue bath with incremental increases of halothane concentration through a serviced and calibrated vaporizer. Incremental concentrations of 0.11; 0.22; and 0.44 mmol L-1 were used, equivalent to 0.5, 1.0, 2.0 Vol%. A contracture threshold of 2 mN (0.2g) at 2.0 Vol% halothane corresponds to a positive halothane result. The results of IVCT generate phenotype groupings, individuals with a positive test are referred to as MHS and those with negative results are deemed MHN. The umbrella term MHS is further split into three categories: MHS_{hc} (positive response to halothane and caffeine), MHS_h (positive response to halothane only), and MHS_c (positive response to caffeine only). All MHS groups are managed as individuals clinically at risk of MH.

2.2.3 Total RNA extraction and clean up

All muscle samples selected for gene expression studies (Microarray, RNAseq, Biomark™, QuantiStudio™ 7) had total RNA extracted using a chloroform/isopropanol extraction method, followed by a clean-up procedure to remove contaminants. These muscle samples were first placed in 1ml TRIzol® before being processed using an IKA T-10 basic ULTRA-TURRAX® homogeniser and left at room temperature for five minutes. Each sample was then transferred into a clean 1.5 ml Eppendorf tube with 200 µl of chloroform. This was thoroughly mixed and placed in a micro-centrifuge for 10 minutes at 13,000 rpm (4 ^{o}C) to create two distinct phases. The upper aqueous layer (containing the total RNA) was carefully extracted and transferred into a new clean 1.5 ml Eppendorf tube and mixed with 1:1 ratio isopropanol (approximately 600 µl) to precipitate the RNA overnight at -80 ^{o}C.

The following day, the samples were spun down in a micro-centrifuge for 30 minutes at 13,000 rpm (4 ^{o}C) and the supernatant was then removed. The remaining RNA pellet is then washed with 500 µl 75% ethanol and micro-centrifuged again for 10 min at 13,000 rpm (4 ^{o}C). This washing procedure is repeated twice before the pellet is air-dried to remove residual ethanol and dissolved in nuclease-free water for further cleaning using the RNAeasy microkit (QIAGEN) with on-column DNase treatment, according to manufacturer's instructions.

2.2.4 RNA sample quality check

The quality control check for all RNA samples was done on the Agilent 4200 Tapestation which uses electrophoresis to generate RIN^{e} numbers representing RNA integrity. RNA samples with integrity scores of RIN^{e} >7.0 were classed as good quality and acceptable for further use. The gel images and electropherograms were visually inspected to ensure no significant DNA or chemical contamination remained which could interfere with downstream processes (Figure 2.2).

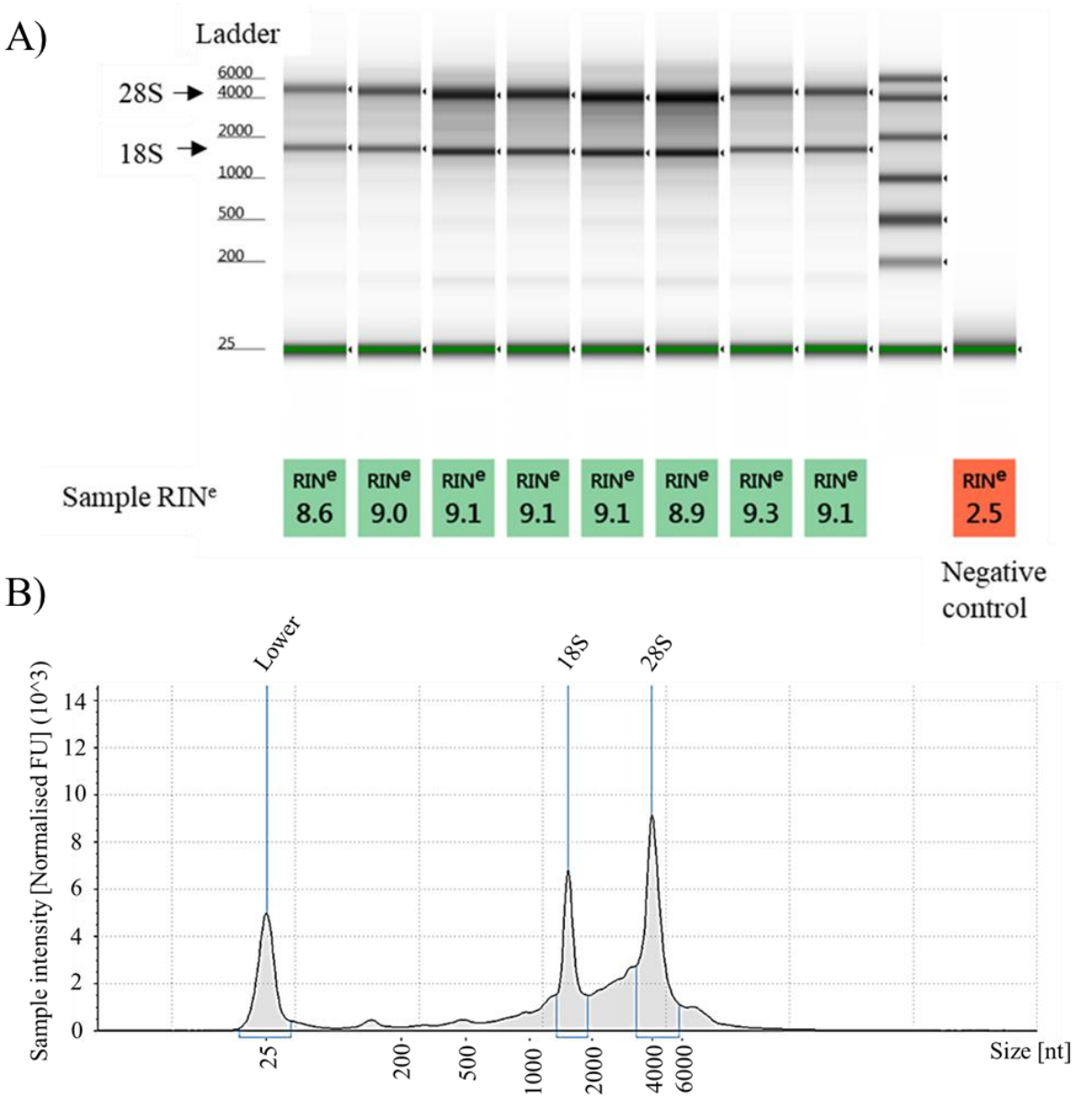

Figure 2.2. Tapestation: Quality assessment of RNA samples. A) Example of electrophoresis gel and **B)** electropherogram generated from Tapestation (Agilent) showing the quality assessment of a batch of RNA samples (RIN^e) with clear bands and peaks representing 18S and 28s rRNA with no other signs of prominent banding or peaks indicating DNA or chemical contamination.

2.2.5 Affymetrix Clariom S Microarray

Each individual undergoing IVCT had four different types of muscle biopsy collected and frozen at -80 ^oC, all of which were utilized in different experiments. In addition to a halothane-

treated and caffeine-treated sample, two untreated samples were used as controls. These being the snap frozen tissue, frozen immediately in RNAlater at -80 ^{o}C upon receipt and the re-oxygenated tissue, kept re-oxygenated at room temperature whilst the rest of the tissue was undergoing IVCT. To assess which untreated sample type was most appropriate for gene expression study, RNA from one snap frozen muscle sample and one re-oxygenated muscle sample was extracted from each MHN individuals (n=10) and sent to the Sheffield Institute for Translational Neuroscience (SITraN) to process on two Affymetrix Clariom S microarrays.

Samples were diluted down to a concentration of 70 ng/µl, quality checked for an RIN^{e} value of >7.0, before being pooled together into two different sample groups and investigated on separate chips. One chip had 10 RNA samples extracted from snap frozen muscle and the other had 10 RNA samples from re-oxygenated muscle. The Clariom S microarray screened for 21448 probe sets, each representing a gene based on the GRCh38.p7 annotation of the human genome. CEL expression files were imported into Expression Console (Affymetrix) for gene-level normalization (*GAPDH*, *ACTB*) and signal summarization. Resulting CHP files were then imported into the Transcriptome Analysis Console TAC 4.0 (Affymetrix) for result summary and visualisation. Gene expression signals were converted into relative logs and the differences between two chips were compared as expression fold changes.

2.2.6 RNAseq experimental design

12 individuals (four MHN, four MHS_h and four MHS_{hc}) who previously had IVCT at the Leeds MH Unit (Table 2.1), were chosen for RNAseq and RNA was extracted from *vastus medialis* muscle biopsies taken from long term -80 ^{o}C storage. All RNA samples were prepared as described in section 2.2.3 and 2.2.4. The purpose of this experiment was to investigate differential gene expression between MHN and MHS muscle, both at baseline and after drug exposure through the IVCT. Only male individuals were selected to remove gender variability and all participants were unrelated to each other. The control samples selected were re-oxygenated tissue biopsies taken from MHN individuals with negative IVCT results for both halothane and caffeine. The sample selection for the MHS phenotype had several criteria: all MHS samples required a unique familial *RYR1* variant confirmed through genotyping and a strong positive contracture response to halothane (0.5g contracture at 2 Vol% halothane). Additionally, MHS_{hc} samples required a strong response of 0.5g contracture strength at 2 Vol%

halothane and a 0.2g contracture strength response to 2mmol L-1 caffeine. The majority of MHS individuals met these criteria aside from two MHS_h individuals (Patient 6 and 8) which had lower contractures at 2 Vol% halothane, one of which also did not have a confirmed familial *RYR1* variant (Patient 6). This was due to limitations in MHS_h sample availability but were still included and taken into consideration when interpreting results.

Patient	Gender	Age at time of biopsy	MH status	Contracture at 2% halothane	Contracture at 2 mM caffeine	*RYR1* Family variant
1	M	13	MHN	0	0	c.7361G>A (negative)
2	M	11	MHN	0	0	c.1840C>T (negative)
3	M	19	MHN	0	0	c.7361G>A (negative)
4	M	19	MHN	0	0	c.6617C>T (negative)
5	M	12	MHS_h	1.169g	0	c.7007G>A
6	M	39	MHS_h	0.236g	0	No familial variant
7	M	30	MHS_h	0.728g	0	c.4293G>A, c.7879G>A
8	M	12	MHS_h	0.234g	0	c.5183C>T
9	M	18	MHS_{hc}	0.644g	2.094g	c.12700G>C
10	M	11	MHS_{hc}	1.785g	0.605g	c.7292A>T
11	M	16	MHS_{hc}	1.607g	0.387g	c.14201G>A
12	M	14	MHS_{hc}	0.905g	0.602g	c.6617C>T

Table 2.1. Summary of patient details selected for RNAseq. This table summarises the gender, biopsy age, MH status, IVCT contracture strengths (halothane and caffeine) and familial *RYR1* variant for everyone selected for RNAseq.

2.2.7 Truseq® Stranded mRNA library preparation

The polyA selected mRNA libraries were created by Ms Catherine Daly (Laboratory Manager of the MH Unit). RNA samples were first quantified using the Qubit™ RNA HS Assay Kit, before used to create libraries using the Truseq Stranded mRNA library preparation kit (Illumina®), according to manufacturer's guidelines. All cDNA libraries were quality checked using the Agilent D1000 screentape and quantified using the Quant-iT™ PicoGreen® dsDNA assay according to manufacturer's guidelines.

2.2.8 Illumina® HiSeq® NGS

Illumina NGS sequencing is comprised of four steps: library preparation, cluster generation, sequencing, and data analysis. In brief, library preparation involves fragmenting cDNA samples and ligating specialised adapters to both fragment ends. These single stranded fragments are distributed across flow cells (glass slide with lanes) which contain a dense lawn of primers that hybridize to the two types of adapter on the DNA fragments. Unlabelled nucleotides are then added along with DNA polymerase to initiate clonal bridge amplification. In this process, the DNA strand folds over attaching the second adapter to the alternative primer on the flow cell. Polymerases generate the complementary strand resulting in a double stranded bridge which gets denatured, forming two single stranded molecules (forward strand and reverse stand). This is repeated for all the fragments simultaneously creating clusters of clonally amplified fragments (Figure 2.3).

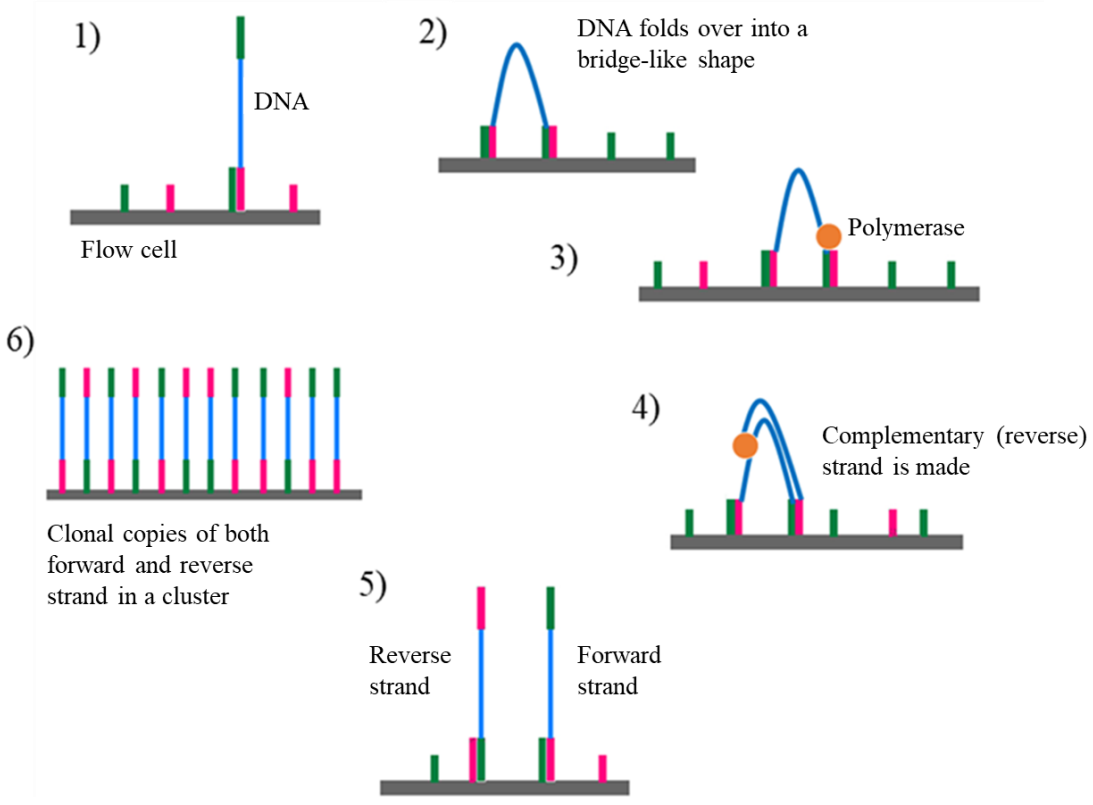

Figure 2.3. Schematic diagram of clonal bridge amplification. This process involves **1)** DNA fragment hybridization, **2)** DNA folding, **3)** polymerase initiating amplification, **4)** complementary strand formation, **5)** denaturing of double stranded bridge and the **6)** clustering of clonal copies. This image is adapted from a graphic produced by DMLapato, made available under the terms of the Creative Commons Attribution 4.0 international license (https://creativecommons.org/licenses/by/4.0/deed.en).

Sequencing of both forward and reverse strands occurs through fragment extension using fluorescent nucleotides that excite the clusters with a light source, emitting a characteristic fluorescent signal. This process is also known as sequencing by synthesis. Sequences from pooled libraries are separated based on the unique indices introduced during sample preparation. These reads are then aligned to a reference genome, quantified, and annotated using bioinformatic tools.

In this study, all 36 mRNA-enriched cDNA libraries were sequenced by the NGS facility using Illumina's HiSeq® 3000 platform. Libraries were indexed and compiled into a singular pool at equimolar concentrations, which was then distributed across three HiSeq 3000 150-bp paired-end lanes, achieving an average of 25M reads per sample. Sequencing generated raw data in the form of a forward and reverse FASTQ file for each sample on each lane which was exported for analysis.

2.2.9 Differential gene expression analysis

Raw sequencing data (FASTQ files) were initially processed using the Medical Advanced Research Computer (MARC1) - a high-performance computer cluster at the University of Leeds. The FASTQ files for each technical replicate across HiSeq lanes were combined and trimmed using the command-line tool Cutadapt to remove all adapter sequences and bad quality base calls from each read (<10) (Martin, 2011). Quality assessment of data was then compared before and after Cutadapt trimming using the quality control application FastQC (Figure 2.4) (https://www.bioinformatics.babraham.ac.uk/projects/fastqc/), designed for high throughput sequence data (Cock et al., 2010).

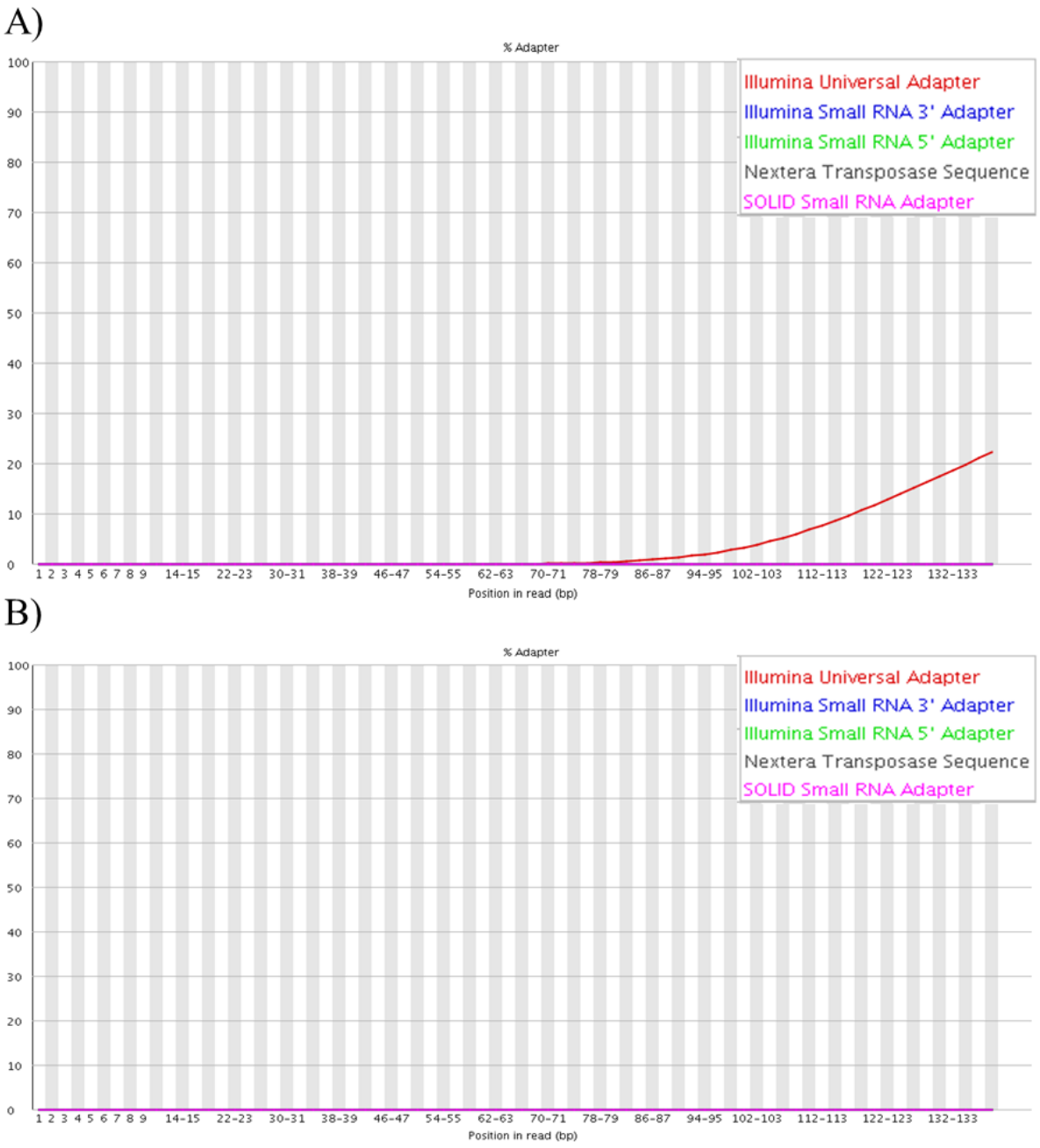

Figure 2.4. FastQC: Adapter content removal from sequencing data. FASTQC report showing "Adapter content" in the sequencing data. The top figure **A)** shows evidence of Illumina Universal Adapter contamination towards the higher base-pair read positions (red line), **B)** this contamination is removed after trimming with Cutadapt as seen in the bottom image.

All 36 samples generated good quality libraries for sequencing (Figure 2.5, 2.6) and aligned to the human reference genome GRCh38.p13 using the STAR aligner (Dobin et al., 2013) before being quantified using featureCounts (Liao et al., 2014). Processed count data was then imported into RStudio (RStudio Team, 2015). RStudio is an open-source integrated

development environment for R, a programming language for statistical computing and graphics. The RStudio package DESeq2 was used to analyse gene count data and generate lists of differential expressed genes (Love et al., 2014). In brief, DESeq2 achieves this by fitting generalised linear models to each gene assuming negative binomial distribution. Dispersion estimates are calculated using maximum likelihoods which weigh log2 fold changes (log2FC) relative to gene-wise variation and the mean-dispersion relationship (Love et al., 2014). The p-values generated from DESeq2 were adjusted for multiple testing using the Benjamini-Hochberg (BH) adjustment (Benjamini and Hochberg, 1995). The R package ggplot2 was used to create MA plots and principle component analysis (PCA) plots for the visualisation of global gene expression between phenotypes (Wickham, 2016).

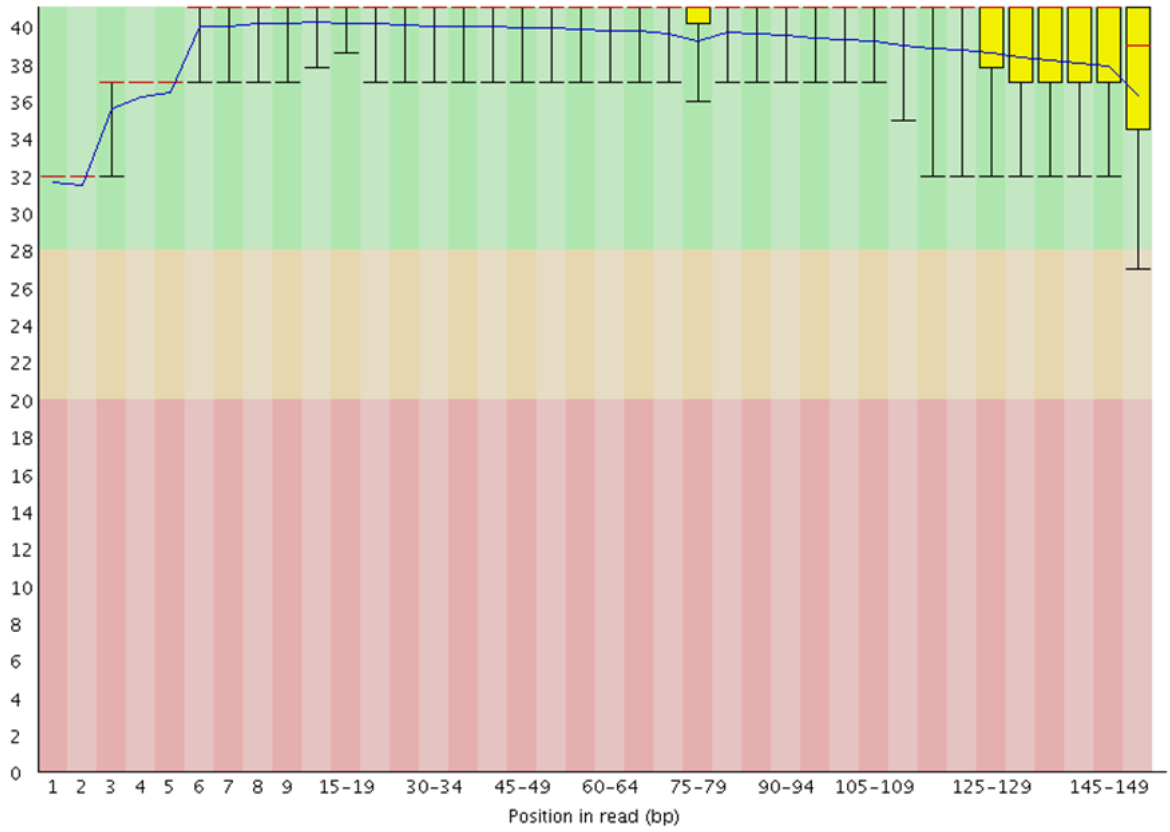

Figure 2.5. FastQC Quality scores across all bases. Box-Whisker type plot generated by FastQC showing an overview of the range of quality values across all bases at each position in the FASTQ file. The quality scores (y-axis) at each read position (x-axis) is drawn with the graph background dividing the y axis base calls into very good quality (green), reasonable quality (orange) and poor quality (red). The central red line is the median value and the yellow box represents the inter-quartile range. The whiskers shown represent the 10% and 90% points and the blue line represents the mean quality.

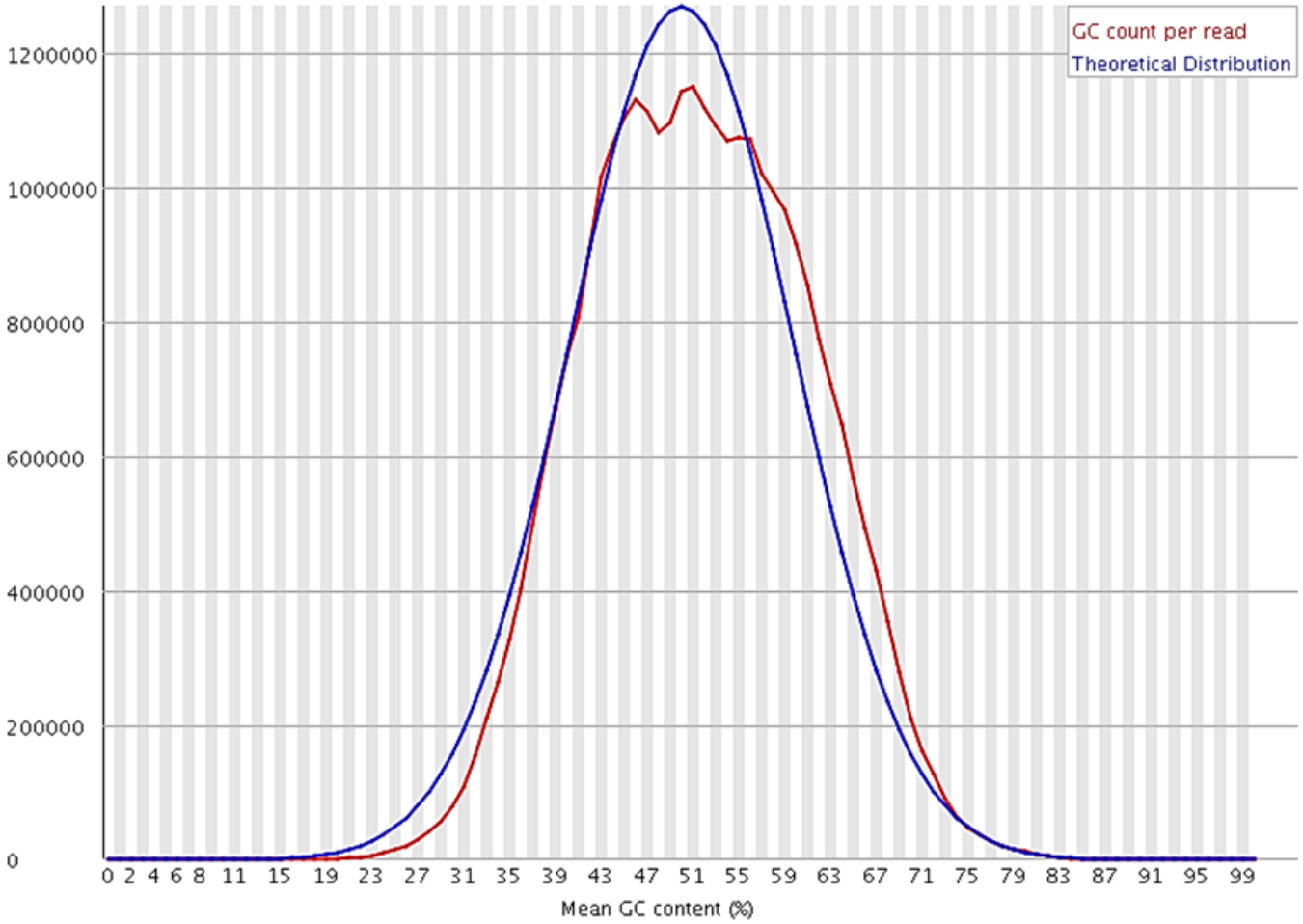

Figure 2.6. FastQC GC distribution over all sequences. The 'per sequence GC content' module measures the GC content across the whole length of each sequence in a file and compares it to a modelled normal distribution of GC content. The theoretical distribution (blue line) of GC content is compared to the GC count for reads (red line). The red curve did not exhibit an irregular shape and did not appear to shift, indicating no systemic bias or library contamination.

An overview of all the computational steps required to process sequencing data for differential gene expression analysis is presented in Figure 2.7.

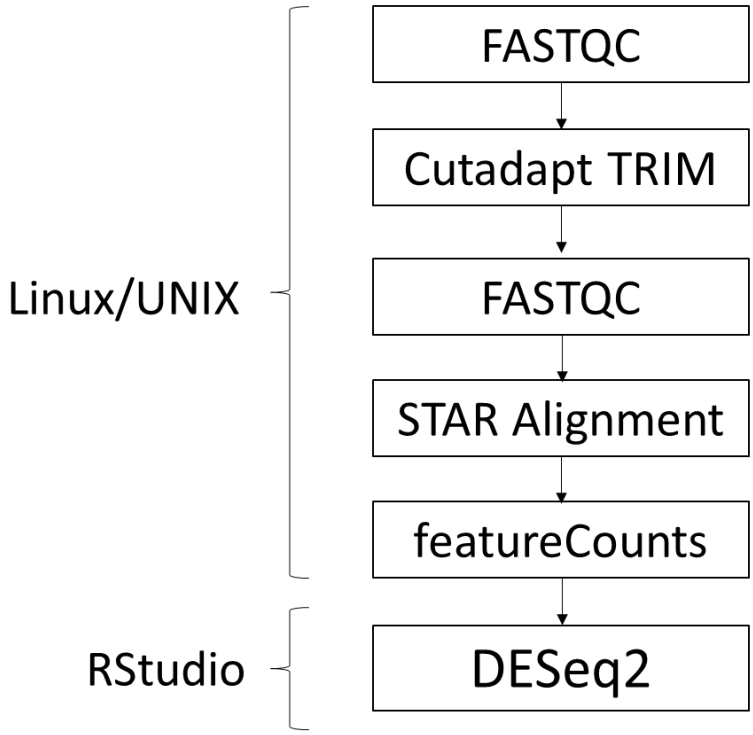

Figure 2.7. RNAseq experimental pipeline. Flow chart outlining the pipeline used for differential gene expression analysis.

2.2.10 Gene ontology and pathway analysis

Functional classification of differentially expressed genes involved inputting DESeq2 gene lists into the online enrichment analysis tool Enrichr (Chen et al., 2013; Kuleshov et al., 2016). Enrichr calculates enrichment scores using statistics based off the Fisher's exact test, used to assess the significance of overlap between inputted gene lists and the chosen gene-set library (Chen et al., 2013). Significantly enriched terms are defined as those with an adjusted p-value <0.05. Gene lists were initially compared to 472 pathway terms in the "WikiPathways_2019_Human" library with a gene coverage of 6201 genes, before further enrichment analysis of gene ontology terms utilising libraries: "GO_Biological_Process_2018" (5103 terms, 14433 gene coverage), "GO_Molecular_Function_2018" (1151 terms, 11459 gene coverage) and "GO_Cellular_Component_2018" (446 terms, 8655 gene coverage).

2.2.11 Biomark™ HD Real-Time PCR system

Validation of RNAseq data was done using the Biomark™ HD RT-PCR system which detects gene expression levels using high throughput microfluidic technology. Three 48.48 Dynamic Array™ integrated fluidic circuits (IFC) were used with TaqMan® primers to assess gene expression in *vastus medialis* biopsies, taken from a cohort of MHN (n=36) and MHS (n=36, MHS_h (18), MHS_{hc} (18)) individuals (before and after halothane-treatment, total of 72 samples). The sample selection for the MHS phenotype was based on the IVCT halothane response which required at least 0.2g contracture at 2 Vol% halothane. Each phenotype had a 1:1 ratio of males to females. 10X assay mixture and sample pre-mix for 17 assays (including three housekeeping) were prepared (Table 2.2), with each assay performed in duplicate.

Each 10X assay consisted of 2.5 µl 20X TaqMan® gene expression assay (Applied Biosystems) and 2.5 µl 2X Assay Loading Reagent (Fluidigm, PN 85000736). The final concentration (at 10X) for each primer was 9 µM and 2 µM for the probe. Each sample pre-mix was made up of 2.5µl TaqMan® Universal PCR Master Mix (2X) (Applied Biosystems, PN 4304437), 0.25 µl 20X GE Sample Loading Reagent (Fluidigm, PN 85000746) and 2.25 µl pre-amplified cDNA, making a total of 5µl volume in each inlet. The IFC controller MX was used to prime 48.48 Dynamic Arrays™ IFC Chips (Fluidigm) with control line fluid by running the Prime (113x) script.

Once primed, 5 µL of each assay and sample mix was then transferred into the appropriate inlets of the primed chip and reloaded into the IFC controller MX to run the Load Mix (113x) script. Once the script finished, the chips were then placed in the Biomark™ instrument to run the RT-PCR protocol starting with 95 °C for 10 minutes followed by 40 cycles at 95 °C for 15 seconds and 60 °C for one minute. The data was imported into the Fluidigm Real-Time PCR Analysis Software and the differences in gene expression (pre – post halothane) were normalised against three housekeeping genes (*B2M*, *TBP* and *RPLP0*) and converted into log2FC using the ΔΔCt method (Vandesompele 2002, Livak 2001). The comparison of datasets between Biomark™ RT-PCR and RNAseq data was achieved by linear regression analysis to identify correlations.

2.2.12 QuantiStudio™ 7 Real-Time PCR system

The investigation of five OXPHOS genes were selected (Table 2.2) based off the differential gene expression analysis at baseline (MHN vs MHS) using RNA-seq data. These genes were investigated using the QuantiStudio ™ 7 RT-PCR sytem set up on multiple 384-well plates. TaqMan® primers were used for assays and genes of interest were normalised against three housekeeping genes: *TBP*, *B2M* and *RPLP0* (Table 2.2) (Vandesompele et al., 2002). Each assay was conducted in triplicate, using a sample population of MHN (n=36) and MHS (n=36, MHS_h (18), MHS_{hc} (18)) individuals. The sample selection for the MHS phenotype was based on the IVCT halothane response which required at least 0.2g contracture at 2 Vol% halothane. Each phenotype had a 1:1 ratio of males to females. Each reaction contained a total volume of 10 µl, consisting of 0.5 µl 20X TaqMan® gene expression assay, 5 µl 2X TaqMan® gene expression master mix, 2 µl cDNA and 2.5 µl RNase-free water. The standard thermocycling program consisted of a 95 °C denaturation for 10 min, followed by 40 cycles of 95 °C for 15 seconds and 60°C for 60 seconds. The CT values from each triplicate assay were averaged for each sample and gene expression was expressed as log2FC using the ΔΔCt method (Livak and Schmittgen, 2001). Normality of the datasets were assessed using the Shapiro-Wilk test. Differences between phenotypes were analysed using Mann-Whitney U tests and median tests due to non-parametric distributions.

	Gene symbol	Applied Biosystems Assay ID
Housekeeping genes	*B2M*	Hs00187842_m1
	RPLP0	Hs00420895_gH
	TBP	Hs00427620_m1
(Biomark™ RT-PCR) Genes for RNAseq validation	*INSIG1*	Hs01650979_m1
	NR4A2	Hs01118813_m1
	DNAJA1	Hs00266011_m1
	SOCS1	Hs00864158_g1
	TNFRSF10D	Hs00388742_m1
	IRF1	Hs00971965_m1
	PPP1R10	Hs00160391_m1
	HSPA1A	Hs00359163_s1
	CNOT11	Hs00213916_m1
	VMA21	Hs01595025_m1
	SNX3	Hs00601001_m1
	NDFIP1	Hs00228968_m1
	PYURF	Hs00430939_g1
	UBE2N	Hs03046007_gH
(QuantiStudio™ RT-PCR) OXPHOS genes	*ATP5MD (USMG5)*	Hs00910071_g1
	MALSU1	Hs00370770_m1
	NDUFC2	Hs00190012_m1
	COQ6	Hs05050186_s1
	MPC2	Hs00967250_m1

Table 2.2. Genes selection for RT-PCR. TaqMan® gene primers selected for Biomark™ HD RT-PCR and QuantiStudio™ 7 RT-PCR systems with corresponding Applied Biosystems assay IDs.

2.2.13 GeneHancer

The bioinformatic database GeneHancer was utilised to identify regulatory enhancer elements for genes of interest. Genehancer is a database containing information on human enhancers and their inferred target genes, accessed in the framework of GeneCards (Fishilevich et al., 2017). Data on enhancer elements and genomic locations are compiled from four different information sources (ENCODE, VISTA, FANTOM and Ensembl). Candidate enhancers with confidence scores supported by multiple evidence sources are classed as elite enhancers. The enhancers which have gene-enhancer associations reported from multiple evidence sources are also flagged with elite association scores. Enhancers that achieve both criteria, are classed as 'double elite enhancers' and those associated with the genes of interest were investigated further in this study (Fishilevich et al., 2017).

2.2.14 GTEx consortium

The eQTLs associated with genes of interest were explored using the publicly available tissue-specific eQTL data on the GTEx consortium, generated from 706 skeletal muscle samples (Consortium, 2013). Each gene of interest was used as a search term to identify genomic regions containing SNPs associated with modifying gene expression. These genomic regions were then compared with the double elite enchancers identified from GeneHancer to observe whether there was overlap.

2.3 RESULTS

2.3.1 Microarray: Snap frozen vs Re-oxygenated muscle comparison

Gene expression profiles from snap frozen and re-oxygenated muscle were compared using two Affymetrix Clariom S microarray chips to decide which sample type was the most appropriate to act as control in the RNAseq experiment. The expression levels of 21448 genes were investigated and a total of 798 genes were found to be differentially expressed at over 2-fold difference (3.72% of all gene probe sets). Within this gene set, 447 genes were expressed at a higher level in re-oxygenated muscle and 351 genes had reduced expression in comparison to snap frozen muscle. An overview of global gene expression differences can be viewed in Figure 2.8.

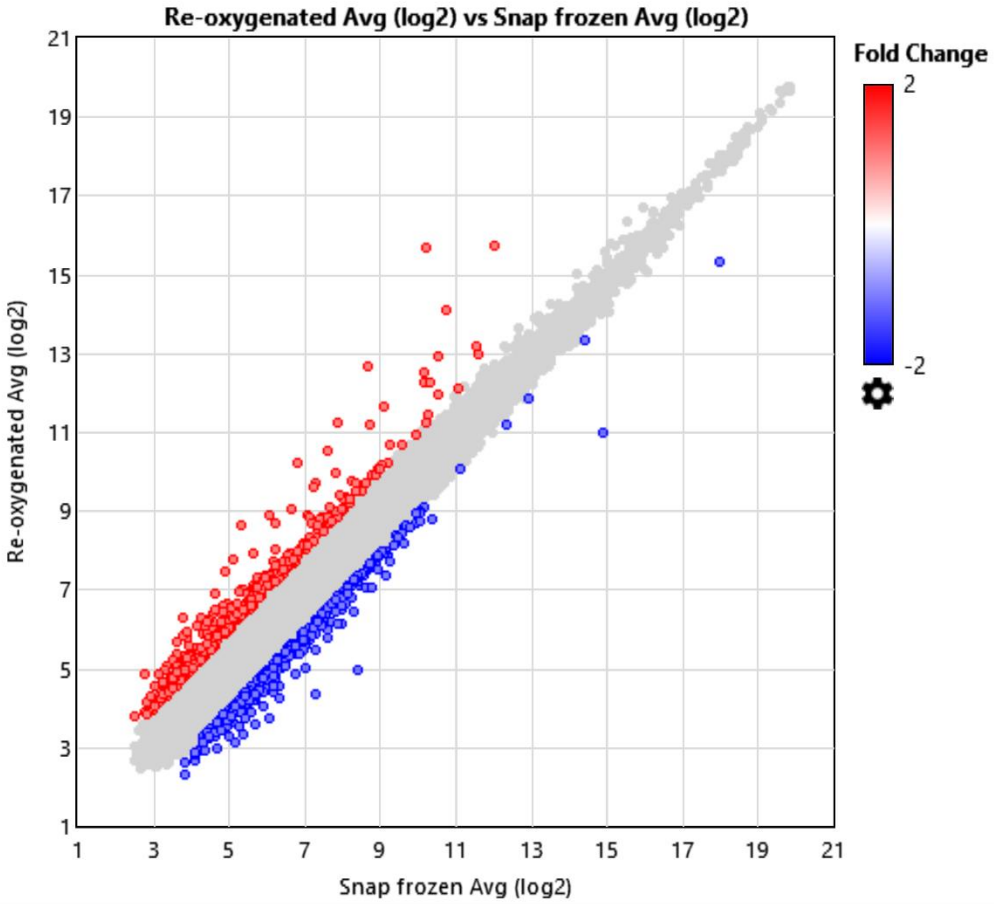

Figure 2.8. Microarray data - Scatter plot presenting global gene expression signals (log2FC) between re-oxygenated muscle and snap frozen muscle. Genes found to be expressed at ≥2 fold-change greater in re-oxygenated muscle are highlighted in red (447) whilst negatively expressed genes at ≤-2 fold-change are highlighted in blue (351).

Both upregulated and downregulated gene sets were subsequently grouped to identify the proportion of coding and non-coding genes (Figure 2.9). The TAC 4.0.2 software assigns each transcript with a locus type and each gene is assigned a locus type based on the locus types from individual transcripts. If more than one locus type is reported, then the locus type is assigned as "multiple complex". Upregulated and downregulated gene sets showed 94 (21.03%) and 51 (14.53%) protein-coding transcripts respectively, whilst non-coding and unassigned genes occupied ~14-16% of each set. Many genes (>60%) were classified as 'multiple complex' indicating more than one locus type.

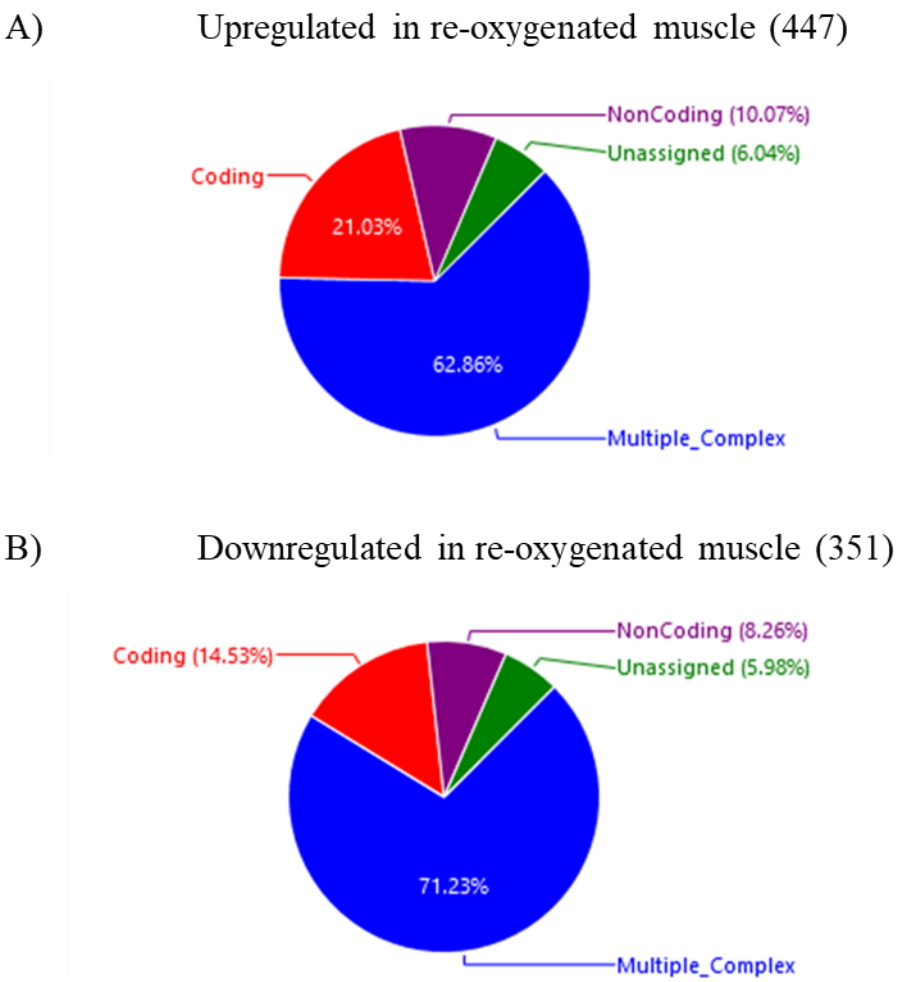

Figure 2.9. Microarray data - Grouping of differentially expressed genes in re-oxygenated muscle. Pie chart illustrations summarizing the gene groupings: Multiple complex (blue), coding (red), non-coding (purple) and unassigned (green). The proportion of each group within **A)** upregulated and **B)** downregulated gene sets in re-oxygenated muscle are represented as a percentage.

Exploration of the most differentially expressed genes revealed seven out of 447 genes were upregulated in re-oxygenated muscle at over 10-fold-change in comparison to snap frozen muscle (*OTUD1, FOS, EGR1, JUNB, FOSB, ZFP36* and *LOC100130705*). In contrast, the smaller cohort of 351 genes more highly expressed in snap frozen biopsies only had two genes expressed at over 10-fold difference (*HBB, HBG2*) (Figure 2.10).

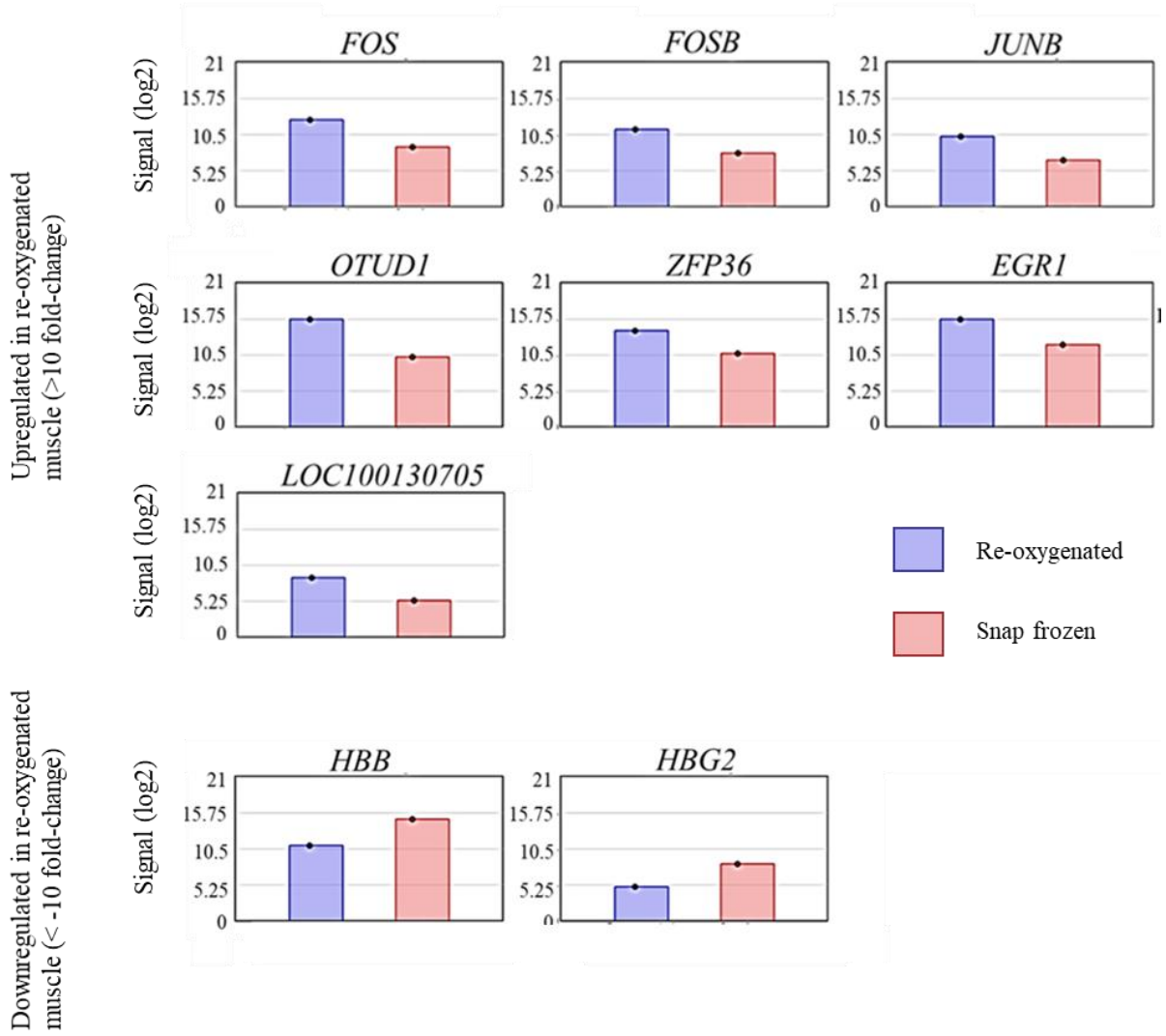

Figure 2.10. Microarray data - Bar charts illustrating differences in gene expression between re-oxygenated and snap frozen muscle. The average gene expression signals are presented for the seven most upregulated (> 10 fold-change) and 2 most downregulated (< -10 fold-change) genes in re-oxygenated muscle (n=10, blue) vs snap frozen muscle (n=10, red).

A more detailed summary of all genes expressed between >2-10 fold-change difference in re-oxygenated muscle is displayed in Table 2.3.

Fold difference / % total genes	Upregulated in re-oxygenated muscle	Downregulated in re-oxygenated muscle
>10 / 0.04%	***OTUD1*** *- OTU Deubiquitinase 1* ***FOS*** *- Fos Proto-Oncogene, AP-1 Transcription Factor Subunit* ***EGR1*** *- Early Growth Response 1* ***JUNB*** *- JunB Proto-Oncogene, AP-1 Transcription Factor Subunit* ***FOSB*** *- FosB Proto-Oncogene, AP-1 Transcription Factor Subunit* ***ZFP36*** *- ZFP36 Ring Finger Protein* ***LOC100130705*** *– Histone Deacetylase 6 also known as HDAC6GADD45B*	***HBB*** *- Hemoglobin Subunit Beta* ***HBG2*** *- Hemoglobin Subunit Gamma 2IL7R*
>6 / 0.07%	***IER2*** *- Immediate Early Response 2* ***MYC*** *- V-Myc Avian Myelocytomatosis Viral Oncogene Homolog* ***IL6*** *- Interleukin 6* ***SLC2A14*** *- Solute Carrier Family 2 Member 14*	***HBA2*** *- Hemoglobin Subunit Alpha 2* ***HBA1*** *- Hemoglobin Subunit Alpha 1*
>5 / 0.11%	***KLF4*** *- Kruppel Like Factor 4* ***KIAA1683*** *- KIAA1683* ***ADAMTS1*** *- ADAM Metallopeptidase With Thrombospondin Type 1 Motif 1* ***SLC2A3*** *- Solute Carrier Family 2 Member 3* ***CYR61*** *- Cysteine Rich Angiogenic Inducer 61* ***JUN*** *- Jun Proto-Oncogene, AP-1 Transcription Factor Subunit* ***CCL2*** *- C-C Motif Chemokine Ligand 2* ***DUSP1*** *- Dual Specificity Phosphatase 1* ***IRF1*** *- Interferon Regulatory Factor 1*	
>4 / 0.18%	***ATF3*** *- Activating Transcription Factor 3* ***NR4A3*** *- Nuclear Receptor Subfamily 4 Group A Member 3* ***BTG2*** *- BTG Anti-Proliferation Factor 2* ***C9orf84*** *- Chromosome 9 Open Reading Frame 84* ***SHC4*** *- SHC Adaptor Protein 4* ***C10orf13*** *- Fibroblast Growth Factor Binding Protein 3, also known as FGFBP3* ***MAP2K1*** *- Mitogen-Activated Protein Kinase Kinase 1* ***OR5T1*** *- Olfactory Receptor Family 5 Subfamily T Member 1*	***RBM26*** *- RNA Binding Motif Protein 26* ***DBF4*** *- DBF4 Zinc Finger* ***ALAS2*** *- 5'-Aminolevulinate Synthase 2* ***SLCO4C1*** *- Solute Carrier Organic Anion Transporter Family Member 4C1* ***SMIM8*** *- Small Integral Membrane Protein 8*
>2 / 3.72%	**419 additional genes**	**342 additional genes**

Table 2.3. Microarray data - Differentially expressed genes in re-oxygenated muscle vs snap frozen muscle. List of upregulated and downregulated genes (>2-10-fold change) in re-oxygenated muscle (n=10) , split into divided according to the degree of fold-change difference in comparison to snap frozen muscle (n=10).

Subsequent functional grouping of genes upregulated in re-oxygenated muscle was performed using bioinformatic tool Enrichr (described in section 2.2.10) which showed significant enrichment of four molecular function terms involved in TF activity and DNA binding. Four enriched pathway terms were also upregulated, but these terms were unrelated to each other and deemed to be of low physiological relevance. In contrast, no significant gene ontology (GO) terms in the 'biological process' and 'cellular component' categories were found. No significant pathway and ontology terms were found using the list of genes downregulated in re-oxygenated muscle (Table 2.4).

Overall, the results showed a 3.72% difference in global expression (>2 fold-change) between the two sample types. Re-oxygenated muscle showed significant upregulation in genes involved with TF activity and binding which may be a natural shift in gene expression due to time under *ex vivo* conditions. This feature of *ex vivo* degradation was likely to be present in post IVCT samples selected for the subsequent RNAseq experiment and on that basis, re-oxygenated muscle was chosen as the more appropriate control type to minimise experimental noise.

	Upregulated in re-oxygenated muscle	Adjusted p value	Genes
(GO_BP) Biological Process			n/a
(GO_MF) Molecular Function	RNA polymerase II core promoter proximal region sequence-specific DNA binding (GO:0000978)	1.03E-02	*ATF3, DLX5, ELF1, FOS, FOSB, FUBP3, IRF1, JUN, JUNB, KLF6, MYC, MYEF2, NR4A1, NR4A3, RFX3, RFX8, SMARCA4, TOX2*
	transcription factor activity, RNA polymerase II core promoter proximal region sequence-specific binding (GO:0000982)	1.10E-02	*ATF3, BHLHE40, DLX5, ELF1, FOS, FOSB, FOXC2, FUBP3, IRF1, JUN, KLF4, KLF6, MYC, MYEF2, NFIL3, NR4A1, NR4A3, RCOR1, TOX2,*
	core promoter proximal region sequence-specific DNA binding (GO:0000987)	1.99E-02	*ATF3, DLX5, ELF1, FOS, FOSB, FUBP3, IRF1, JUN, JUNB, KLF4, KLF6, MYC, MYEF2, NR4A1, NR4A3, RFX3, RFX8, SMARCA4, TOX2*
	RNA polymerase II transcription factor binding (GO:0001085)	2.58E-02	*BBS4, BHLHE40, DACT1, FOS, HCLS1, ID1, ID2, JUN, KLF4, TCERG1, WWP2*
(GO_CC) Cellular Component			n/a
Pathways	Spinal Cord Injury WP2431	1.09E-03	*BTG2, CCL2, CHST11, EGR1, FOS, IL6, LTB4R, MYC, NOS2, NR4A1, PTGS2, RHOB, ZFP36*
	Prolactin Signaling Pathway WP2037	1.11E-02	*FOS, IRF1, IRS2, JUN, MAP2K1, MYC, NOS2, PTK2, SOCS3*
	let-7 inhibition of ES cell reprogramming WP3299	3.28E-02	*EGR1, KLF4, MYC*
	Preimplantation Embryo WP3527	3.43E-02	*EGR1, FOSB, KLF4, SMARCA, TPRX1, ZAR1, ZFP36*
	Downregulated in re-oxygenated muscle	**Adjusted p value**	**Genes**
(GO_BP) Biological Process			n/a
(GO_MF) Molecular Function			n/a
(GO_CC) Cellular Component			n/a
Pathways			n/a

Table 2.4. Microarray data - Gene ontology and enriched pathway terms (Snap frozen vs re-oxygenated muscle). Gene ontology analyses of microarray data highlighting significantly enriched biological process, molecular function, cellular component, and pathway terms using both upregulated and downregulated genes lists from the snap frozen vs re-oxygenated muscle comparison. Gene ontology terms with >0.05 adjusted p-value were omitted from the table.

2.3.2 RNAseq: MHN vs MHS (baseline)

RNAseq analysis of differential gene expression was first conducted at baseline comparing MHS and MHN phenotypes without IVCT treatment. References to the 'MHS' phenotype in this section refers to both MHS_h and MHS_{hc} samples combined. Differentially expressed genes were defined as those with a significant adjusted p-value of <0.1, generated by DESeq2. Baseline comparisons generated a cohort of 822 differentially expressed genes (false discovery rate (FDR) 10%), of which 38 transcripts were novel. Compared to MHN controls, the MHS group showed increased gene expression in 203 genes and decreased gene expression in 619 genes. The effect size of upregulated genes ranged from 0.22 to 5.17 log2FC, whereas the larger list of downregulated genes showed a smaller range in effect size (-0.19 to -2.06 log2FC).

To extract biological information from this data, pathway analysis was carried out on each gene list using Enrichr (described in section 2.2.10). Amongst the top 10 pathway terms downregulated in MHS samples, five terms were significantly enriched (adjusted p-value <0.05), three of which were related to mitochondria. These being 'Electron transport chain WP111', 'Oxidative phosphorylation WP623' and 'Mitochondrial complex I assembly model OXPHOS system WP4324'. Pathways enriched from upregulated genes featured a range of terms with no central theme, which makes interpretation difficult (Table 2.5).

Index	Upregulated pathway terms	P-value	Adjusted p-value	Odds Ratio	Combined score
1	Overview of nanoparticle effects WP3287	3.09E-05	7.29E-03	21.48	223.09
2	Photodynamic therapy-induced NF-kB survival signaling WP3617	3.69E-04	4.36E-02	11.66	92.18
3	TLR4 Signaling and Tolerance WP3851	2.54E-03	1.99E-01	10.93	65.35
4	Deregulation of Rab and Rab Effector Genes in Bladder Cancer WP2291	1.05E-02	5.49E-01	12.76	58.15
5	TNF alpha Signaling Pathway WP231	2.91E-04	4.58E-02	6.65	54.19
6	Cells and Molecules involved in local acute inflammatory response WP4493	1.18E-02	5.57E-01	12	53.3
7	VEGFA-VEGFR2 Signaling Pathway WP3888	2.23E-05	1.05E-02	4.76	50.95
8	let-7 inhibition of ES cell reprogramming WP3299	5.74E-02	8.74E-01	17.01	48.61
9	DDX1 as a regulatory component of the Drosha microprocessor WP2942	6.66E-02	9.25E-01	14.58	39.49
10	EV release from cardiac cells and their functional effects WP3297	6.66E-02	8.99E-01	14.58	39.49

Index	Downregulated pathway terms	P-value	Adjusted p-value	Odds Ratio	Combined score
1	Electron Transport Chain (OXPHOS system in mitochondria) WP111	1.14E-26	5.40E-24	11.17	667.26
2	Oxidative phosphorylation WP623	3.67E-20	8.66E-18	12.97	580.53
3	Nonalcoholic fatty liver disease WP4396	2.71E-19	4.26E-17	7.2	308.04
4	Mitochondrial complex I assembly model OXPHOS system WP4324	6.76E-08	7.97E-06	7.25	119.73
5	Proteasome Degradation WP183	8.11E-05	7.66E-03	4.91	46.27
6	Fatty Acid Beta Oxidation WP143	3.03E-03	2.05E-01	4.98	28.86
7	Heme Biosynthesis WP561	2.73E-02	1.00E+00	7.52	27.07
8	Selenium Metabolism and Selenoproteins WP28	2.23E-03	1.75E-01	4.41	26.96
9	Selenium Micronutrient Network WP15	3.90E-03	2.30E-01	3.15	17.46
10	Triacylglyceride Synthesis WP325	3.28E-02	1.00E+00	4.23	14.46

Table 2.5. Pathway enrichment analysis for MHN vs MHS (baseline). This table contains a list of the top 10 upregulated (orange) and downregulated (blue) pathway terms generated by Enrichr are displayed in combined score order (log of p-value from Fisher's exact test multiplied by z score of deviation from expected rank). The 196 genes upregulated, and 591 genes downregulated in the MHN vs MHS baseline comparison were used as input. Significantly enriched pathway terms (adjusted p-value < 0.05) are highlighted in grey.

Following pathway analysis, functional classification was performed using GO libraries on Enrichr (described in section 2.2.10). Analysis of downregulated genes from the MHN vs MHS (baseline) comparison, revealed 10 significantly downregulated biological processes, all of which were involved in mitochondria and the ETS (Table 2.6). Further GO analysis of molecular function yielded similar results to biological processes and enriched cellular component terms were also based largely in mitochondria. On the other hand, analysis of upregulated genes showed no significant gene ontology terms. All gene ontology results for the MHN vs MHS baseline comparison are available in the appendices (see Appendix 1).

GO Biological process term	Overlap	P-value	Adjusted P-value	Odds Ratio	Combined Score
mitochondrial ATP synthesis coupled electron transport (GO:0042775)	26/85	9.84E-20	5.02E-16	10.35	453.03
respiratory electron transport chain (GO:0022904)	27/94	1.21E-19	3.10E-16	9.72	423.37
NADH dehydrogenase complex assembly (GO:0010257)	18/64	2.32E-13	2.97E-10	9.52	276.87
mitochondrial respiratory chain complex I biogenesis (GO:0097031)	18/64	2.32E-13	2.37E-10	9.52	276.87
mitochondrial respiratory chain complex I assembly (GO:0032981)	18/64	2.32E-13	1.98E-10	9.52	276.87
mitochondrial respiratory chain complex assembly (GO:0033108)	23/97	6.36E-15	1.08E-11	8.02	262.31
mitochondrial electron transport, NADH to ubiquinone (GO:0006120)	14/46	3.34E-11	2.43E-08	10.30	248.46
mitochondrial electron transport, ubiquinol to cytochrome c (GO:0006122)	06/14	1.59E-06	5.08E-04	14.50	193.62
mitochondrial translational elongation (GO:0070125)	18/87	6.60E-11	4.21E-08	7.00	164.13
mitochondrial translational termination (GO:0070126)	18/89	9.84E-11	5.58E-08	6.84	157.70

Table 2.6. Top 10 downregulated biological processes in the MHN vs MHS baseline comparison. Top 10 GO terms for downregulated biological processes comparing MHS controls against MHN controls at baseline. GO terms are displayed in combined score order (log of p-value from Fisher's exact test multiplied by z score of deviation from expected rank).

Multiple GO terms corresponded to mitochondrial complex I assembly, and information on the genes involved were subsequently extracted from the DESeq2 gene list for further investigation. A total of 18 complex I-encoding genes were found downregulated in MHS muscle with an effect size ranging from -0.52 to -0.82 log2FC (Table 2.7).

ID	log2FC	lfcSE	Adjusted p-value	hgnc_symbol	Gene name
ENSG00000151366	-0.72	0.18	3.53E-02	*NDUFC2*	NADH:Ubiquinone Oxidoreductase Subunit C2[a]
ENSG00000259112	-0.75	0.20	5.30E-02	*NDUFC2-KCTD14*	NDUFC2-KCTD14 Readthrough (*NDUFC2* paralog)[a]
ENSG00000174886	-0.82	0.24	6.27E-02	*NDUFA11*	NADH:Ubiquinone Oxidoreductase Subunit A11[a]
ENSG00000165264	-0.60	0.18	6.63E-02	*NDUFB6*	NADH:Ubiquinone Oxidoreductase Subunit B6[a]
ENSG00000004779	-0.66	0.21	7.53E-02	*NDUFAB1*	NADH:Ubiquinone Oxidoreductase Subunit AB1[a]
ENSG00000189043	-0.53	0.17	7.71E-02	*NDUFA4*	NDUFA4 Mitochondrial Complex Associated[a]
ENSG00000110717	-0.81	0.27	8.20E-02	*NDUFS8*	NADH:Ubiquinone Oxidoreductase Core Subunit S8[b]
ENSG00000178057	-0.73	0.24	8.21E-02	*NDUFAF3*	NADH:Ubiquinone Oxidoreductase Complex Assembly Factor 3[c]
ENSG00000186010	-0.73	0.24	8.21E-02	*NDUFA13*	NADH:Ubiquinone Oxidoreductase Subunit A13[a]
ENSG00000131495	-0.74	0.25	8.48E-02	*NDUFA2*	NADH:Ubiquinone Oxidoreductase Subunit A2[a]
ENSG00000213619	-0.72	0.25	8.50E-02	*NDUFS3*	NADH:Ubiquinone Oxidoreductase Core Subunit S3[b]
ENSG00000139180	-0.52	0.18	8.56E-02	*NDUFA9*	NADH:Ubiquinone Oxidoreductase Subunit A9[a]
ENSG00000267855	-0.67	0.23	8.71E-02	*NDUFA7*	NADH:Ubiquinone Oxidoreductase Subunit A7[a]
ENSG00000115286	-0.67	0.23	8.83E-02	*NDUFS7*	NADH:Ubiquinone Oxidoreductase Core Subunit S7[b]
ENSG00000167792	-0.62	0.22	8.98E-02	*NDUFV1*	NADH:Ubiquinone Oxidoreductase Core Subunit V1[b]
ENSG00000224877	-0.68	0.24	8.98E-02	*NDUFAF8*	NADH:Ubiquinone Oxidoreductase Complex Assembly Factor 8[c]
ENSG00000099795	-0.73	0.26	9.00E-02	*NDUFB7*	NADH:Ubiquinone Oxidoreductase Subunit B7[a]
ENSG00000185633	-0.69	0.25	9.73E-02	*NDUFA4L2*	NDUFA4 Mitochondrial Complex Associated Like 2[a]

Table 2.7. Differentially expressed genes associated with complex I in the MHN vs MHS (baseline) comparison. The list of differentially expressed genes encoding proteins associated with mitochondrial complex I, generated from DESeq2 comparing MHN (n=4) and MHS (n=8) controls at baseline, displayed in order of adjusted p-value. Gene names are annotated using superscript letters based on function, a. Encodes accessory subunit of the mitochondrial membrane respiratory chain NADH dehydrogenase, b. Encodes a core subunit for mitochondrial complex I, and c. Encodes a mitochondrial complex I assembly protein that interacts with complex I subunits.

2.3.3 RNAseq: MHN vs MHSh (baseline)

Following the MHN vs MHS comparison, differential gene expression at baseline was performed with the MHS phenotype split into subgroups MHS_h and MHS_{hc}. Comparisons showed that MHS_h vs MHN muscle featured a large set of 1654 differentially expressed genes (FDR 10%), 73 of which were novel. This may be partly due to the variability in individuals chosen to represent the MHS_h phenotype in terms of biopsy age (12-39) and *RYR1* genetics (one individual with no *RYR1* variant and one compound heterozygous) (Table 2.1).

A large proportion of genes were downregulated in MHS_h (1281/1654, 74.5%), with an effect size ranging from -0.25 to -2.37 log2FC. Genes upregulated in MHS_h made up the remaining 25.5% of the set (373/1654) with an effect size between 0.3 to 4.09 log2FC. Pathway analysis results showed two pathway terms 'mRNA Processing WP411' and 'Translation Factors WP107' upregulated in MHS_h and nine pathways downregulated in MHS_h including the three mitochondria-related terms previously found in the previous MHN vs MHS comparison (see Appendix 2). Similarly, GO analyses showed that the MHS_h phenotype had significant downregulation of biological processes, molecular function, and cellular component terms heavily involved with mitochondria and OXPHOS (see Appendix 3). In contrast, functional grouping of upregulated genes presented with several GO terms involved with mRNA splicing and processing, the most significant being 'RNA splicing, via transesterification reactions with bulged adenosine as nucleophile (GO:0000377)', 'mRNA splicing, via spliceosome (GO:0000398)' and 'mRNA processing (GO:0006397)'.

2.3.4 RNAseq: MHN vs MHS_{hc} (baseline)

Compared to the differences between MHN vs MHS_h at baseline, the MHS_{hc} vs MHN comparison only presented with 68 differentially expressed genes (FDR 10%), nine of which were novel. Out of 68 genes, there were 42 genes upregulated in MHS_{hc}, covering an effect size range between 0.54 to 5.79 log2FC. In contrast, 26 genes were found downregulated in MHS_{hc}, expressed in the range of -0.47 to -2.80 log2FC. Pathway analysis revealed eight terms significantly upregulated in MHS_{hc}, majority of which are involved with fatty acid metabolism: 'SREBF and miR33 in cholesterol and lipid homeostasis WP2011', 'Adipogenesis WP236', 'Transcription factor regulation in adipogenesis WP3599' and 'Eicosanoid Synthesis WP167'

(see Appendix 4). In contrast, several energy metabolism-related pathways were downregulated in MHS_{hc} such as 'Oxidative phosphorylation WP623', 'Electron Transport Chain (OXPHOS system in mitochondria) WP111' and 'Glycolysis and Gluconeogenesis WP534'. These however were not statistically significant, likely due to the small number of genes used for analysis. In contrast to pathway analysis, no significant GO terms were found using both upregulated and downregulated gene sets (see Appendix 5).

2.3.5 MA plot and volcano plot

Global gene expression changes were visualised using MA plots and volcano plots, illustrating the differences described in section 2.3.3 and 2.3.4. MA plots present gene expression changes between two conditions as two-dimensional scatter plots in terms of log2FC (M) on the y-axis and the mean of normalised gene expression counts (A) on the x-axis. The MA plot for MHS_h against MHN show a large sum of differentially expressed genes with the majority in the range of -1 and 1 log2FC. In contrast, the plot for MHS_{hc} against MHN show a much smaller number of differentially expressed genes but are expressed at a greater range in effect size (Figure 2.11).

Likewise, this can also be seen in the volcano plots (Figure 2.12) in addition to the overall distribution of p-values across all genes. Despite having many more statistically significant genes in the MHN vs MHS_h comparison, the majority of these genes (1653/1654) had adjusted p-values between 0.1 and 0.05. In contrast, the MHN vs MHS_{hc} volcano plot showed that the majority of differentially expressed genes (42/68) had lower p-values (adjusted p-value <0.05) which reflect more significant changes in gene expression.

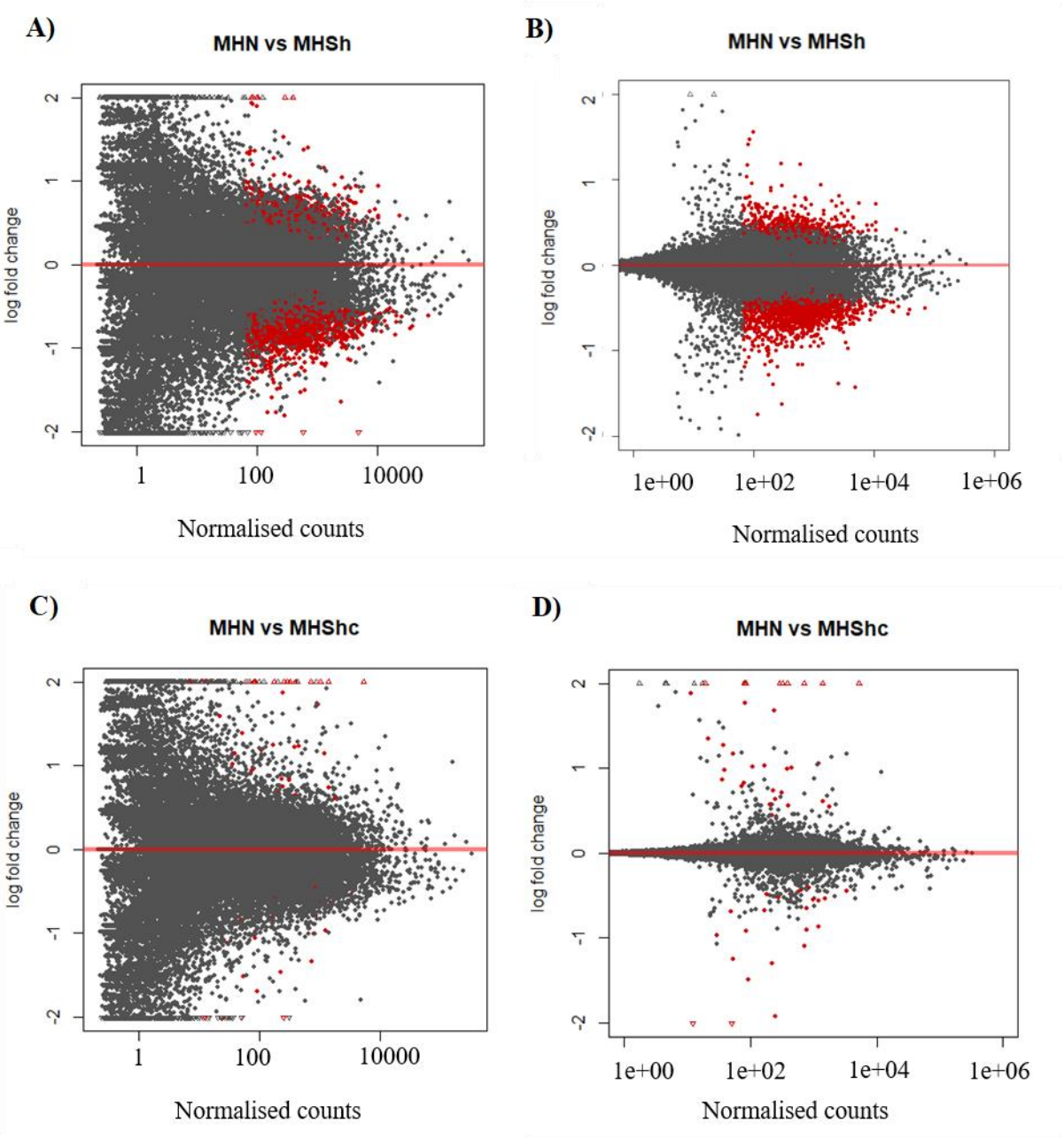

Figure 2.11. MA plots visualising gene expression changes between MH phenotypes. Log2FC (y-axis) is plot against mean of normalised gene expression counts (x-axis). Plots **A)** and **B)** feature the same MHN vs MHS_h comparison but plot **B)** has shrunken log2FC, which removes the noise from genes with low counts (Zhu et al., 2019). Plots **C)** and **D)** feature the MHN vs MHS_{hc} comparison but plot **D)** also has shrunken log2FC. Genes which are differentially expressed adjusted p-value < 0.1 are highlighted in red. The triangles indicate genes which are expressed at a log2FC that exceeds the y-axis limits.

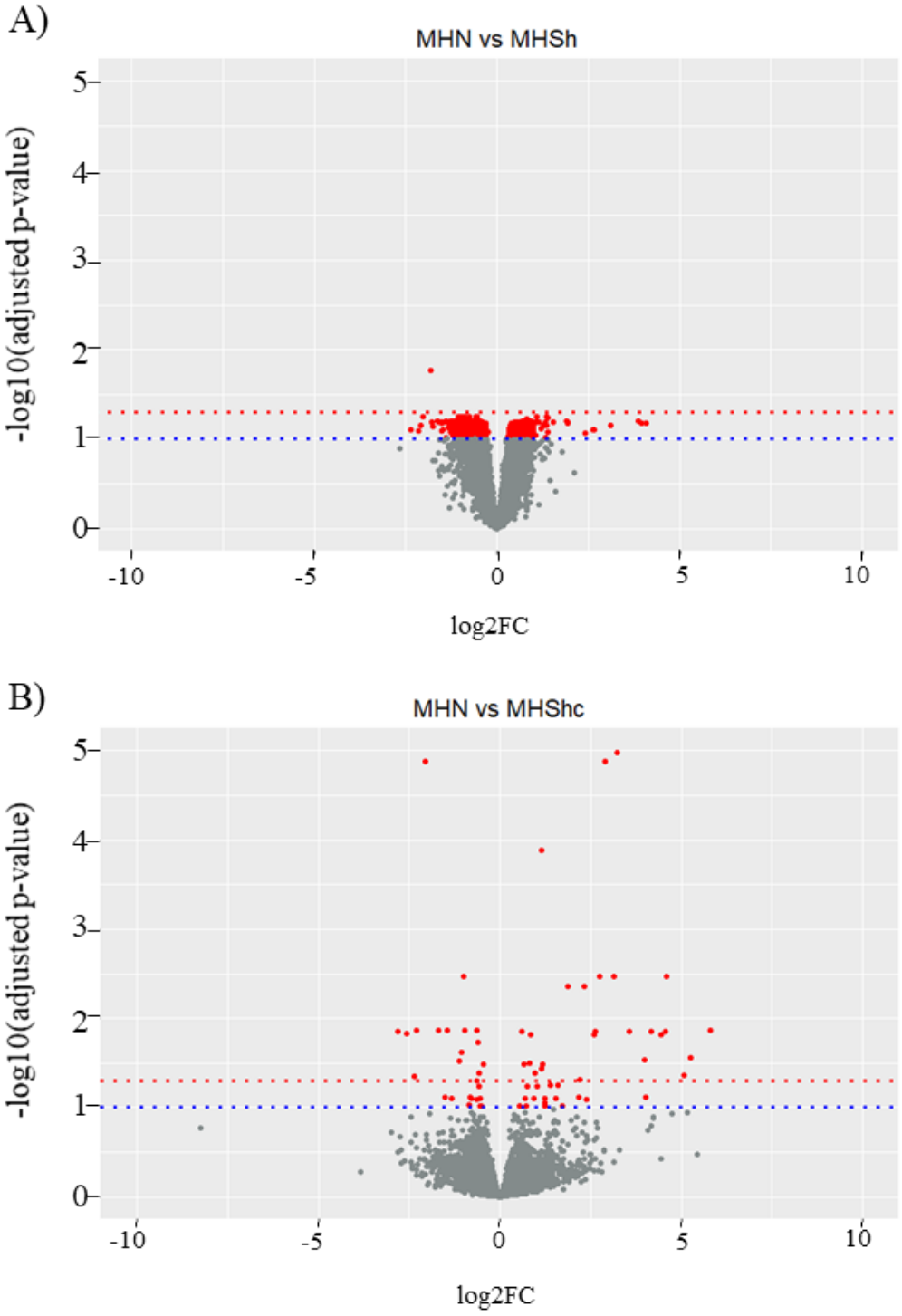

Figure 2.12. Volcano plots visualising p-value and fold-change distribution across genes. Log2FC (x-axis) is plot against the -log10(adjusted p-value) (y-axis). Plot **A)** Features data from the MHN vs MHS_h comparison and plot **B)** features data from the MHN vs MHS_{hc} comparison. The threshold for statistical significance was adjusted p-value <0.1 which corresponds to a -log10(adjusted p-value) of >1, indicated by the horizontal blue line. All statistically significant genes above this threshold are highlighted in red. An addition red line has been added at -log10(adjusted p-value) 1.3 which reflects an adjusted p-value of 0.05.

2.3.6 RNAseq: Effects of halothane treatment on gene expression

Analysis of gene expression pre vs post halothane IVCT, showed that MHN muscle was the most heavily influenced. A total of 2905 genes (212 novel) were differentially expressed in this phenotype after IVCT halothane exposure. Among these genes, 1350 were upregulated (0.22 to 7.27 log2FC) and 1555 genes were downregulated (-0.22 to -3.32 log2FC). In comparison to MHN, the MHS phenotype showed much less gene expression change with only 325 differentially expressed genes (66 novel) after halothane exposure. References to the 'MHS' phenotype in this section refers to both MHS_h and MHS_{hc} samples combined. In this gene set, 248 genes were upregulated, with an effect size between 0.31 and 5.20 log2FC whilst 77 genes were downregulated between -0.24 and -3.83 log2FC.

Pathway analysis on the MHN (pre vs post halothane) gene set showed significant downregulation of five OXPHOS-related terms after halothane exposure (Table 2.8). However, this same observation was not seen in the MHS phenotype where no pathway terms were found significantly downregulated. Analysis of upregulated pathways in both MHN and MHS gene sets generated a wide range of signalling and regulation pathways terms with no area of focus making interpretation difficult (Table 2.9).

GO analyses on the MHN phenotype also revealed significant downregulation of many mitochondria and OXPHOS-related terms in biological process, molecular function, and cellular component (see Appendix 6). Once again, these observations were not apparent in the MHS pre vs post halothane response, aside from one biological process term 'mitochondrial electron transport, NADH to ubiquinone (GO:0006120)' (see Appendix 7). GO analysis of upregulated genes in both MHN and MHS phenotypes were similar to the results observed in the pathway analysis (see Appendix 6, 7).

MHN (pre vs post halothane)

Index	Name	P-value	Adjusted p-value	Odds Ratio	Combined score
1	Electron Transport Chain (OXPHOS system in mitochondria) WP111	1.03E-25	4.85E-23	6.21	357.39
2	Cytoplasmic Ribosomal Proteins WP477	1.25E-20	2.95E-18	5.94	272.14
3	Oxidative phosphorylation WP623	6.89E-18	1.08E-15	6.72	265.64
4	Nonalcoholic fatty liver disease WP4396	1.96E-16	2.31E-14	4.04	146.04
5	Mitochondrial complex I assembly model OXPHOS system WP4324	3.62E-08	3.42E-06	4.47	76.6
6	Heme Biosynthesis WP561	2.50E-03	1.69E-01	6.18	37.04
7	miRNA Biogenesis WP2338	6.29E-03	2.70E-01	6.95	35.25
8	Cerebral Organic Acidurias, including diseases WP4519	1.04E-02	3.78E-01	5.96	27.2
9	Target Of Rapamycin (TOR) Signaling WP1471	7.98E-04	6.28E-02	3.48	24.8
10	IL-9 Signaling Pathway WP22	5.69E-03	2.68E-01	4.09	21.15

MHS (pre vs post halothane)

Index	Name	P-value	Adjusted p-value	Odds Ratio	Combined score
1	miR-517 relationship with ARCN1 and USP1 WP3596	1.76E-02	1	56.34	227.51
2	Robo4 and VEGF Signaling Pathways Crosstalk WP3943	2.11E-02	1	46.95	181.12
3	Hfe effect on hepcidin production WP3924	2.46E-02	1	40.24	149.11
4	Type 2 papillary renal cell carcinoma WP4241	6.48E-03	1	16.57	83.5
5	Gene regulatory network modelling somitogenesis WP2854	3.84E-02	1	25.61	83.49
6	Osteoblast Signaling WP322	4.86E-02	1	20.12	60.85
7	Osteoclast Signaling WP12	5.53E-02	1	17.61	50.96
8	ID signaling pathway WP53	5.53E-02	1	17.61	50.96
9	ACE Inhibitor Pathway WP554	5.87E-02	1	16.57	46.98
10	NOTCH1 regulation of human endothelial cell calcification WP3413	5.87E-02	1	16.57	46.98

Table 2.8. Top 10 downregulated pathway terms pre vs post IVCT (halothane). A list of the top 10 downregulated pathway terms generated from Enrichr comparing the pre vs post effects of halothane on both phenotypes (MHN and MHS). Terms are displayed in combined score order (log of p-value from Fisher's exact test multiplied by z score of deviation from expected rank). Significantly enriched pathway terms (adjusted p-value < 0.05) are highlighted in grey.

MHN (pre vs post halothane)

Index	Name	P-value	Adjusted p-value	Odds Ratio	Combined score
1	Photodynamic therapy-induced NF-kB survival signaling WP3617	7.56E-10	1.79E-07	6.88	144.48
2	mRNA Processing WP411	2.75E-14	1.30E-11	4.46	139.23
3	Cells and Molecules involved in local acute inflammatory response WP4493	3.25E-06	2.19E-04	7.55	95.45
4	Photodynamic therapy-induced unfolded protein response WP3613	2.70E-06	2.12E-04	5.94	76.24
5	Spinal Cord Injury WP2431	1.27E-08	2.00E-06	3.54	64.31
6	Hepatitis C and Hepatocellular Carcinoma WP3646	1.06E-06	1.25E-04	4.59	63.09
7	Overview of nanoparticle effects WP3287	9.29E-05	2.31E-03	5.91	54.91
8	Prion disease pathway WP3995	2.10E-05	7.62E-04	4.86	52.4
9	Hypertrophy Model WP516	1.35E-04	3.04E-03	5.62	50.05
10	Aryl Hydrocarbon Receptor WP2586	1.74E-05	7.47E-04	4.19	45.89

MHS (pre vs post halothane)

Index	Name	P-value	Adjusted p-value	Odds Ratio	Combined score
1	Platelet-mediated interactions with vascular and circulating cells WP4462	1.50E-05	2.36E-03	25.58	284.03
2	miRNAs involvement in the immune response in sepsis WP4329	1.03E-06	4.84E-04	17.63	243.08
3	EV release from cardiac cells and their functional effects WP3297	1.72E-03	3.11E-02	31.06	197.78
4	Photodynamic therapy-induced NF-kB survival signaling WP3617	1.62E-05	1.91E-03	15.53	171.28
5	Role Altered Glycolysation of MUC1 in Tumour Microenvironment WP4480	2.90E-03	4.90E-02	24.15	141.1
6	Oligodendrocyte Specification and differentiation(including remyelination), leading to Myelin Components for CNS WP4304	1.58E-04	8.26E-03	14.49	126.89
7	Bone Morphogenic Protein (BMP) Signalling and Regulation WP1425	5.23E-03	7.05E-02	18.12	95.17
8	Type II interferon signaling (IFNG) WP619	3.61E-04	1.42E-02	11.75	93.14
9	IL1 and megakaryocytes in obesity WP2865	1.35E-03	3.02E-02	13.59	89.83
10	TNF alpha Signaling Pathway WP231	2.26E-05	2.13E-03	8.27	88.49

Table 2.9. Top 10 upregulated pathway terms pre vs post IVCT (halothane). A list of the top 10 upregulated pathway terms generated from Enrichr comparing the pre vs post effects of caffeine on both phenotypes (MHN and MHS). Terms are displayed in combined score order (log of p-value from Fisher's exact test multiplied by z score of deviation from expected rank). Significantly enriched pathway terms (adjusted p-value < 0.05) are highlighted in grey.

2.3.7 RNAseq: Effects of caffeine treatment on gene expression

The gene expression change in response to caffeine resembled the pattern observed in response to halothane, with most differentially expressed genes occurring in the MHN phenotype. A total of 1554 genes (159 novel) differentially expressed, 943 genes upregulated (0.16 to 7.90 log2FC) and 611 genes downregulated (-0.22 to -4.38 log2FC). The MHS gene set after caffeine exposure featured a much smaller gene set with 583 genes (95 novel). Out of 583 genes 451 were upregulated (0.26 to 5.71 log2FC) and 132 genes were downregulated (-0.23 to -4.00 log2FC) after caffeine exposure.

Pathway analysis on the MHN (pre vs post caffeine) gene set showed significant downregulation in the 'Electron Transport Chain (OXPHOS system in mitochondria) WP111' and 'Oxidative phosphorylation WP623' pathway terms which were also featured in the MHN pre vs post halothane comparison. Likewise, no pathways were significantly downregulated in the MHS (pre vs post caffeine) phenotype. Upregulated gene sets from both MHN and MHS pre vs post caffeine comparisons generated a wide range of signalling and regulatory pathways terms which were difficult to interpret like the effects seen with halothane (see Appendix 8). Results from GO analysis also resembled those observed in the pre vs post halothane response, with many mitochondria and OXPHOS-related terms downregulated in MHN samples following caffeine exposure. These observations were not seen in MHS samples. All upregulated gene ontology terms in both phenotypes consisted of a wide range of biological functions similar to the pathway analysis (see Appendix 9,10).

2.3.8 Similarities in halothane and caffeine response between MHS phenotypes

Cross comparison of pre vs post IVCT gene lists highlighted differentially expressed genes shared between multiple phenotypes (see Appendix 11). DESeq2 was used to generate additional pre vs post halothane and caffeine gene lists with the MHS phenotype split into MHS_h and MHS_{hc} subsets. The MHS_h phenotype had 230 genes differentially expressed in response to halothane and 449 genes in response in caffeine. A similar number of genes were differentially expressed in MHS_{hc} samples with 256 and 363 genes differentially expressed post-halothane and caffeine, respectively. All MHS_h and MHS_{hc} responses to both halothane

and caffeine were compared to identify similarities in gene expression and a total of 89 genes were shared between all treatment responses (Figure 2.13).

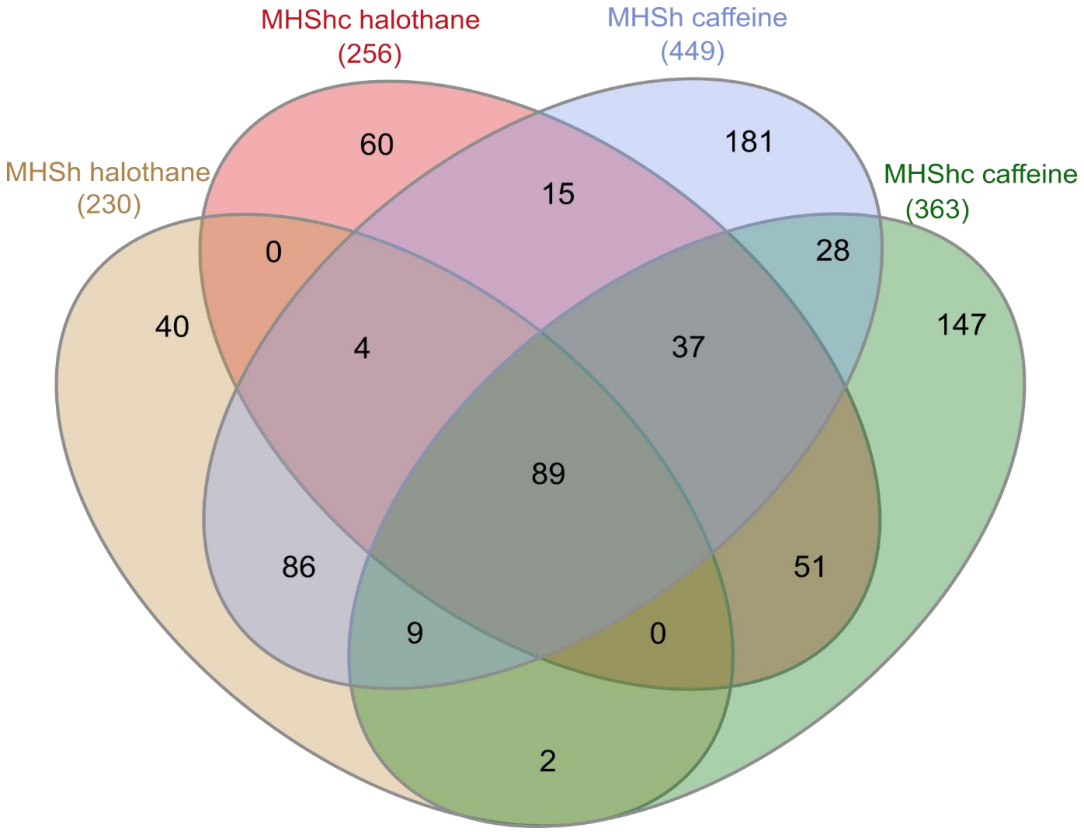

Figure 2.13. Cross comparison of gene expression changes in response to halothane and caffeine. Differentially expressed gene lists for both MHS_h and MHS_{hc} phenotypes are displayed as a Venn diagram showing the overlap between treatment responses. The gene lists for each segment can be found in Appendix 11. This image was generated using InteractiVenn (Heberle et al., 2015).

This set of 89 genes was compared against the MHN treatment responses to see if they were unique to MHS phenotypes. This comparison revealed that most of these genes were also differentially expressed in the MHN phenotype after halothane and caffeine treatments, indicative of a gene set associated with normal physiological response. Only three out of 89 genes (*GIMAP8*, *MT-TM* and *PECAM1*) were unique to the MHS responses, all of which were downregulated after halothane and caffeine exposure.

2.3.9 Principal component analysis

Relationships between each sample were examined and visualised using a PCA plot (Figure 2.14). The gene expression count data for all 36 samples were plotted and most of the untreated control samples cluster on the right side of the plot whilst post-IVCT samples cluster on the left. There is no obvious outlier based off visual assessment but there appears to be a greater variability in the baseline pre-IVCT samples in all phenotypes, based off the loose clustering seen. Both the post-IVCT halothane and post-IVCT caffeine clusters overlap containing a mixture of all three phenotypes indicating a close relationship between samples. This suggests that both halothane and caffeine exposure have similar effects on gene expression across all phenotypes.

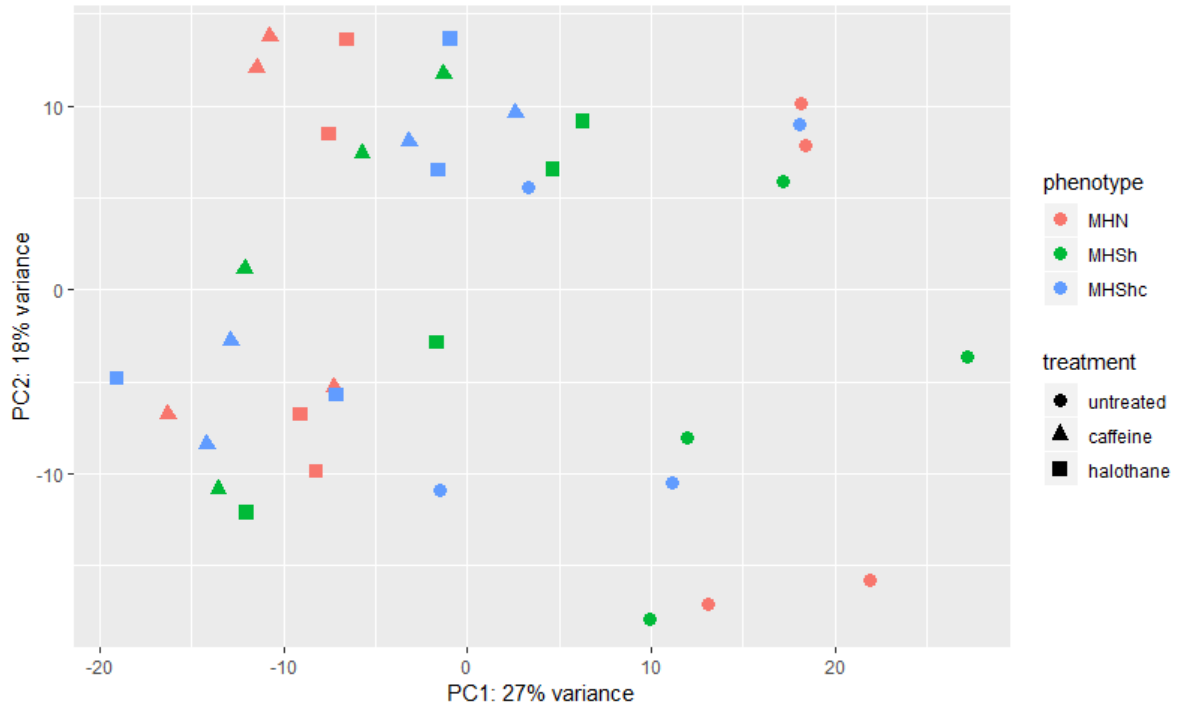

Figure 2.14. Principal component analysis plot examining relationships between human MH samples. The variance between samples is represented by a percentage (%) on PC1 (x-axis) and PC2 (y-axis). All 36 samples are plotted with PC1 against PC2 and their respective phenotype (MHN: Red, MHSh: Green, MHShc: Blue) and treatment groups (untreated: circle, caffeine: triangle, halothane: square).

2.3.10 RNAseq validation (Biomark™ RT-PCR)

The data generated from RNAseq was validated using genes selected from the MHN and MHS (MHS_h and MHS_{hc} combined) pre vs post halothane comparison. A cohort of paired pre vs post halothane samples from MHN (n=36) and MHS (n=36) individuals were used to assess the directional changes in gene expression. A selection of 14 genes with adjusted p-value <0.05 were chosen based on their up or downregulation in specific phenotypes, outlined in Table 2.10.

Gene	Full name	Rationale
NR4A2	Nuclear Receptor Subfamily 4 Group A Member 2	Genes found upregulated solely in the MHN (pre vs post halothane) comparison and not in the MHS (pre vs post halothane) comparison
INSIG1	Insulin Induced Gene 1	Genes upregulated in both MHN and MHS (pre vs post halothane) comparisons
DNAJA1	DnaJ Heat Shock Protein Family (Hsp40) Member A1	
SOCS1	Suppressor of cytokine signaling 1	
TNFRSF10D	TNF Receptor Superfamily Member 10d	
IRF1	Interferon Regulatory Factor 1	
PPP1R10	Protein Phosphatase 1 Regulatory Subunit 10	
HSPA1A	Heat Shock Protein Family A (Hsp70) Member 1A	
CNOT11	CCR4-NOT Transcription Complex Subunit 4	Genes found downregulated solely in the MHN (pre vs post halothane) comparison and not found in the MHS (pre vs post halothane) comparison
VMA21	Vacuolar ATPase Assembly Factor	
SNX3	Sorting Nexin 3	
NDFIP1	Nedd4 Family Interacting Protein 1	
PYURF	PIGY Upstream Reading Frame	
UBE2N	Ubiquitin Conjugating Enzyme E2 N	

Table 2.10. Genes selected for RNAseq validation with rationale.

The changes in gene expression were quantified using Biomark™ RT-PCR, with each gene assay ran in duplicate (described in section 2.2.11). The differences in log2FC from RT-PCR were calculated and compared to the log2FC results generated from DESeq2 analyses and visualised using bar charts (Figure 2.15). Visual inspection of bar charts shows good general correlation in most genes selected aside from *NR4A2* in the MHS samples. RNASeq results show that *NR4A2* was significantly upregulated in only MHN samples, but RT-PCR data contradict these findings showing similar levels of upregulation in both phenotypes. Furthermore, genes found to be downregulated in RNAseq results (*CNOT11*, *VMA21*, *SNX3*. *NDFIP1*, *PYURF*, *UBE2N*) showed very little gene expression change in RT-PCR.

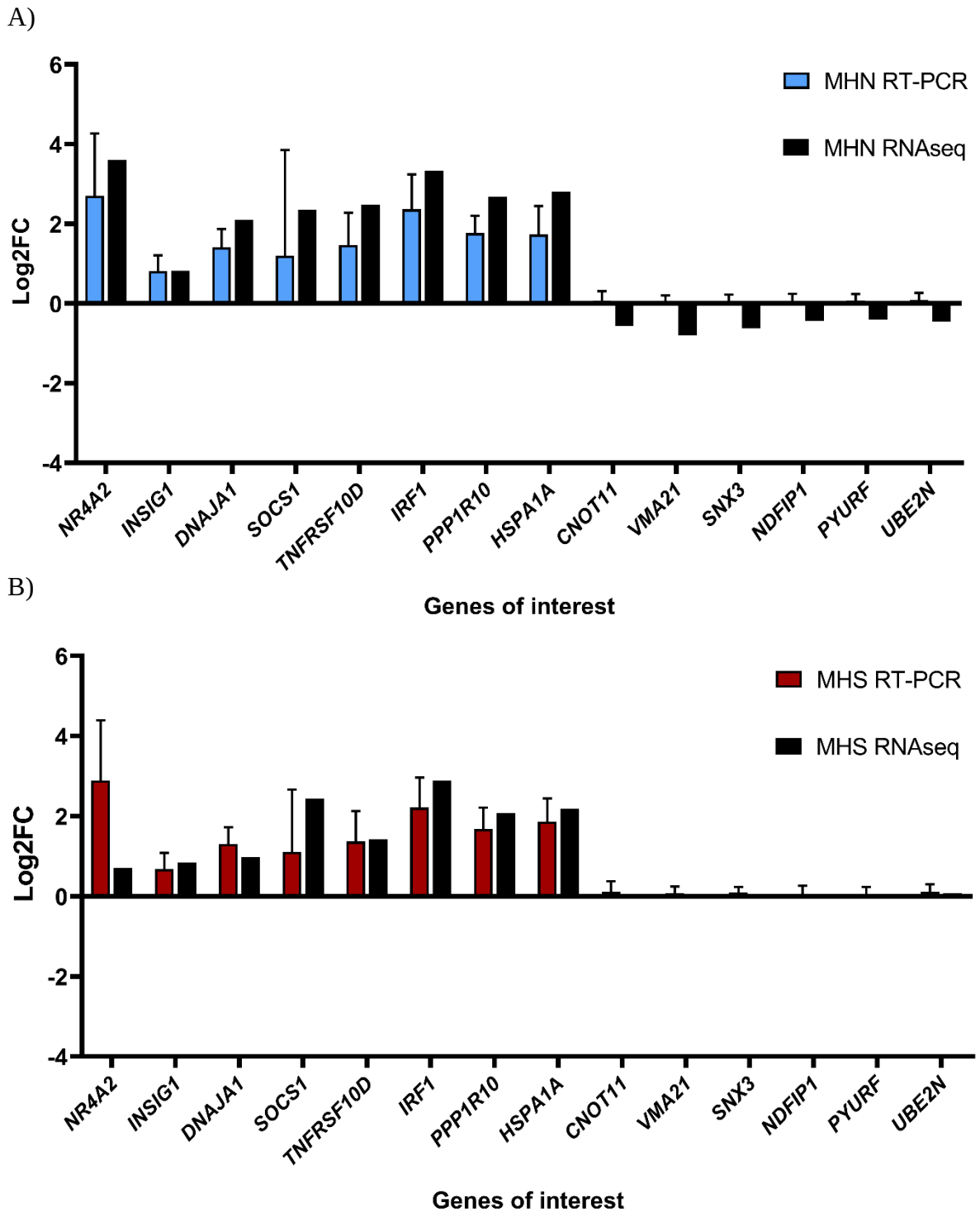

Figure 2.15. RNAseq validation. The gene expression changes comparing the mean log2FC (with standard deviation) from RT-PCR to the log2FC generated from DESeq2. Presented as bar charts for the **A)** MHN (n=36) phenotype and **B)** the MHS (n=36) phenotype.

Following visual inspection of bar charts, the correlation between RNAseq and RT-PCR data was assessed using linear regression analyses. The outcome of this showed strong positive correlation in both MHN (R^2 = 0.96, p<0.0001) and MHS (R^2 = 0.52, p=0.0037) phenotypes. The log2FC results from RNAseq and RT-PCR were plotted against each other and visualised on a scatter graph (Figure 2.16). Visual inspection of the scatter graph reinforces that the MHS *NR4A2* result appears to be an outlier in the overall trend. Despite this outlier, this experiment was successful in validating the RNAseq data overall.

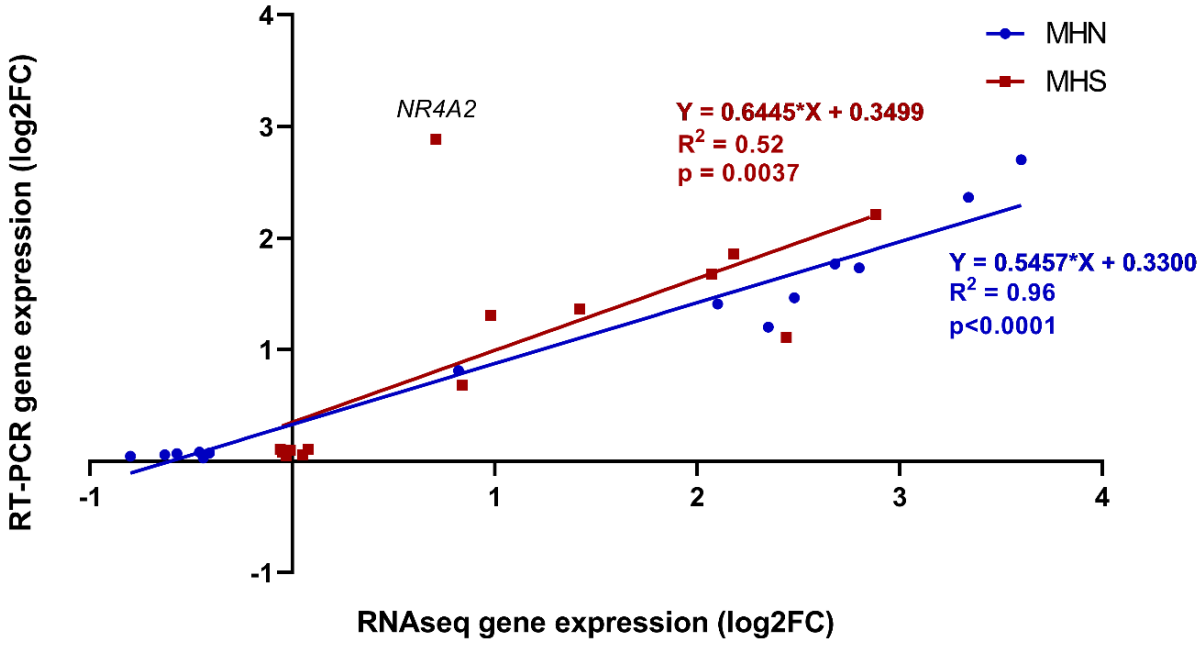

Figure 2.16. Scatter graph and linear regression analyses for RNAseq validation. The log2FC results from RNAseq and RT-PCR are plotted against each other, featuring both the MHN (blue) and MHS (red) phenotypes.

2.3.11 Genes of interest (Mitochondria-related)

Given the prominent feature of OXPHOS/mitochondria-related genes in multiple RNAseq comparisons, further investigation was conducted at the baseline level using five genes (*ATP5MD* (also known as *USMG5*), *MALSU1*, *NDUFC2*, *COQ6* and *MPC2*) selected from the MHN vs MHS (MHS_h + MHS_{hc}) baseline comparison (described in section 2.3.2). RNAseq results show that all five genes were downregulated in the MHS phenotype when compared to MHN, and this was reassessed by QuantiStudio™ 7 RT-PCR, in a larger sample size (described in section 2.2.6). The expression levels of these genes were quantified, and relative FC data are displayed as boxplots (Figure 2.17).

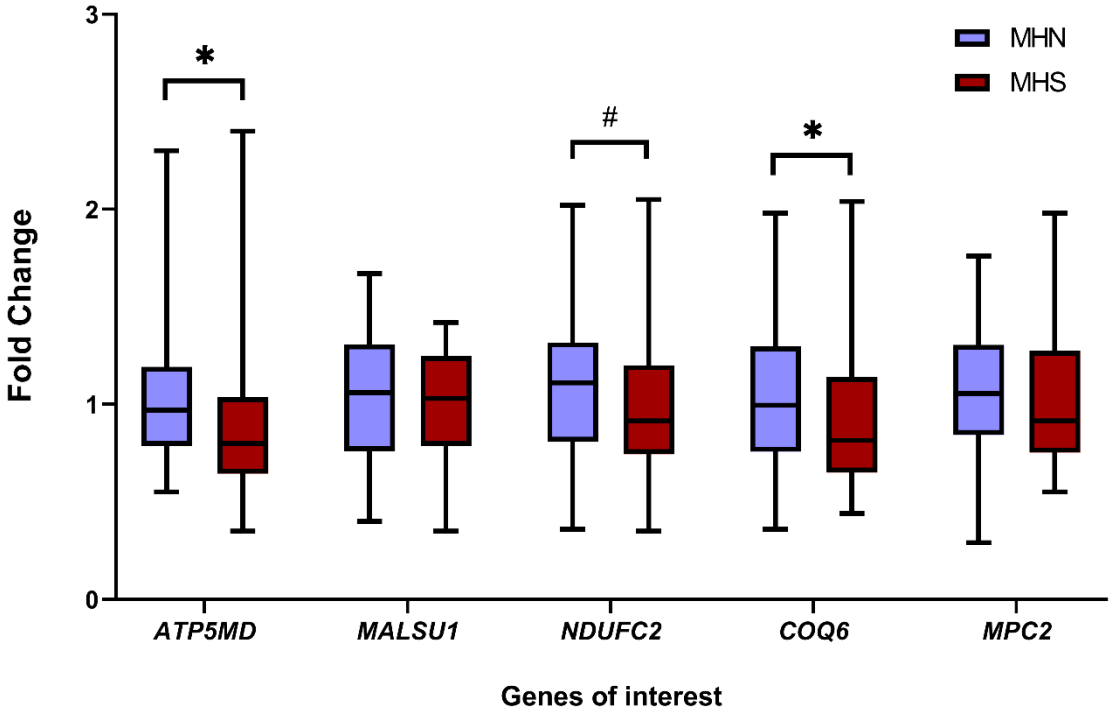

Figure 2.17. Baseline MHN vs MHS comparison in five genes of interest. Box plots comparing relative gene expression (FC) between MHN (n=36) and MHS (n=36) phenotypes. Significant Mann-Whitney U tests ($p < 0.05$) are annotated with an asterisk and significant independent sample median tests ($p < 0.05$) are annotated with #.

The gene expression FC data generated was not normally distributed (assessed by Shapiro-Wilk test, p>0.05) and was therefore analysed using non-parametric independent sample Mann-Whitney U (comparing distributions) and median tests. All five genes of interest were downregulated in the MHS phenotype, but only *ATP5MD* (p=0.022) and *COQ6* (p=0.049) showed a statistically significant difference in distribution (Figure 2.18) and only *NDUFC2* showed a statistically significant reduction in median (p=0.01).

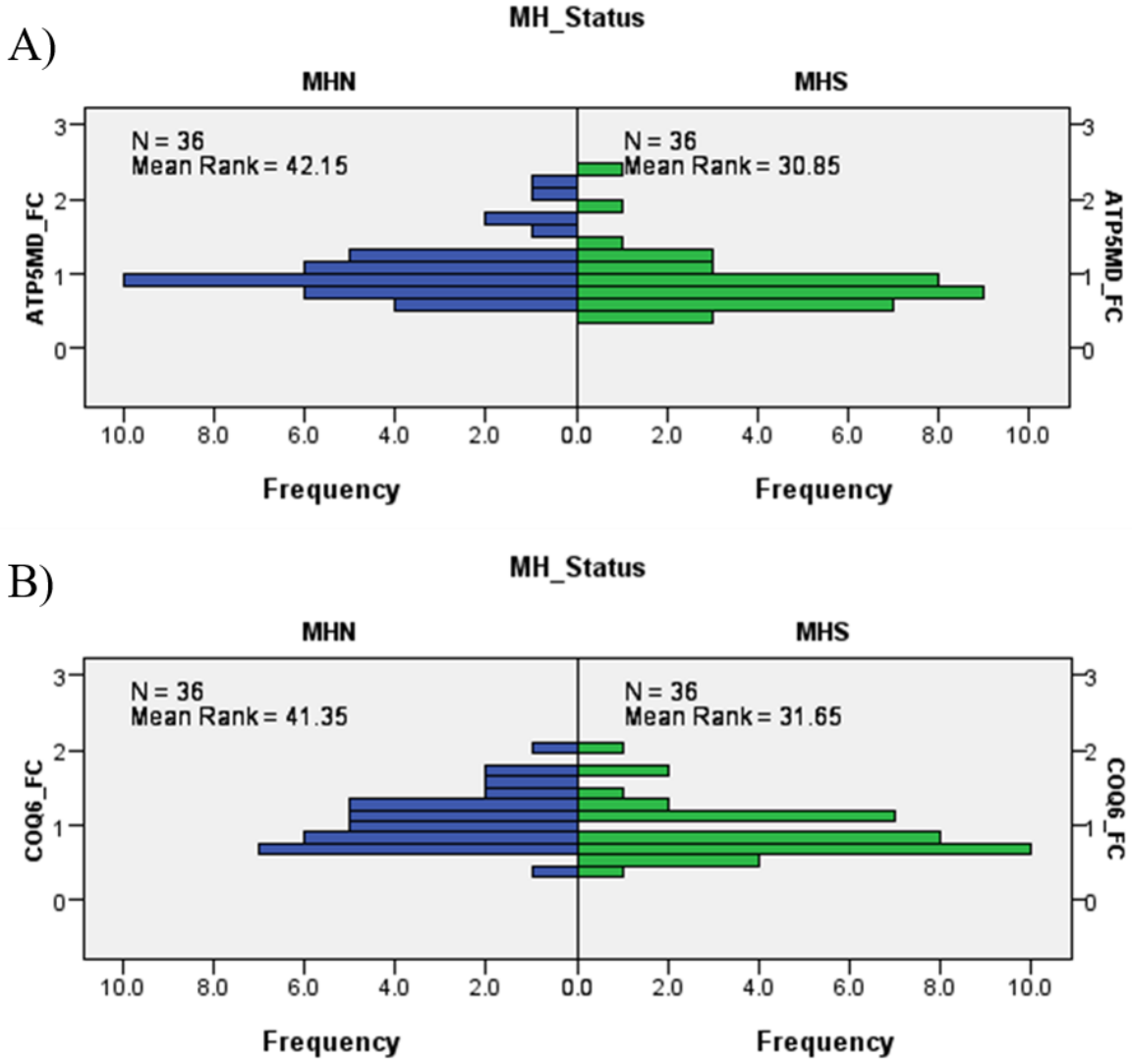

Figure 2.18. Comparison of gene expression fold change data distribution. Bar charts illustrating overall distribution of FC data for **A)** *ATP5MD* and **B)** *COQ6* in both MHN (n=36) and MHS (n=36) phenotypes.

2.3.12 Gene expression enhancers and eQTLs

Regulatory elements for *ATP5MD*, *NDUFC2* and *COQ6* were identified using information available on GeneHancer and the GTEx consortium (Consortium, 2013; Fishilevich et al., 2017). The three genes of interest *USMG5* (*ATP5MD*), *NDUFC2* and *COQ6* were supplied to the GTEx consortium as search terms under the tissue filter 'Muscle -Skeletal'. This search identified regions containing SNPs considered to be cis-eQTLs for each gene of interest.

A total of 184 SNPs were found for *USMG5* (*ATP5MD*) in the region between chr10: 102831425-104339678, where 22 other protein-coding genes reside. GeneHancer identified 10 enhancer elements associated with *ATP5MD*, of which one is a double elite enhancer (GH10J103394) containing 249 TF binding sites, located at chr10: 103394884-103398147. The GTEx consortium shows there are two SNPs within this double elite enhancer flagged as significant cis-eQTLs (Table 2.11).

220 SNPs for *NDUFC2* have been found in the region chr11: 78018473-78389198 where eight other protein-coding genes reside. GeneHancer shows 25 enhancer elements associated with *NDUFC2* and one double elite enhancer (GH11J078077) within this region containing 407 TF binding sites, located at chr11: 78077847-78082082. The GTEx consortium highlights 6 SNPs within this enhancer as cis-eQTLs (Table 2.11).

581 SNPs for COQ6 reside at chr14: 73788853-74220793 along with seven other protein-coding genes. 14 enhancers were associated with COQ6 with one double enhancer (GH14J073949) within this region containing 263 TF binding sites, located at chr14: 73949296-73951373. Seven SNPs within this enhancer are flagged as cis-eQTLs (Table 2.11). The GTEx database contained no information on trans-eQTLs being found for any of these genes.

Gene	Variant ID (cis-eQTL)	SNP ID
ATP5MD	chr10_103395309_C_A_b38	rs11191676
	chr10_103395888_T_C_b38	rs2292807
NDUFC2	chr11_78078508_T_C_b38	rs636141
	chr11_78078585_A_G_b38	rs595133
	chr11_78079607_T_C_b38	rs534418
	chr11_78079817_C_G_b38	rs499799
	chr11_78080263_T_A_b38	rs637124
	chr11_78080403_G_C_b38	rs607199
COQ6	chr14_73949296_G_A_b38	rs62006128
	chr14_73949536_A_T_b38	rs7400918
	chr14_73949700_TTTCTC_T_b38	rs148549829
	chr14_73949897_T_C_b38	rs11621743
	chr14_73950242_G_C_b38	rs17552038
	chr14_73950852_T_G_b38	rs112218167
	chr14_73951095_G_C_b38	rs8013496

Table 2.11. A summary of cis-eQTL SNPs identified within enhancer regions.

TFs known to interact with each double enhancer were cross compared with the MHN vs MHS baseline gene list to identify shared observations. This comparison identified 171 TFs shared between all three enhancers and six TFs (ATF3, CHD2, CTBP1, ESRRA, NFKBIZ, TEAD4) were shared between all four datasets (Figure 2.19). In the MHN vs MHS baseline comparison the genes encoding ATF3, CHD2 and NFKBIZ are upregulated in MHS individuals at 2.26, 0.62 and 1.35 log2FC, respectively. In contrast, CTBP1, ESRRA and TEAD4 are downregulated in MHS samples at -0.53, -0.64 and -0.90 log2FC, respectively. These six TFs all bind to the double elite enhancers identified in each gene of interest and their activities are potentially responsible for the differential gene expression of *NDUFC2*, *COQ6* and *ATP5MD*.

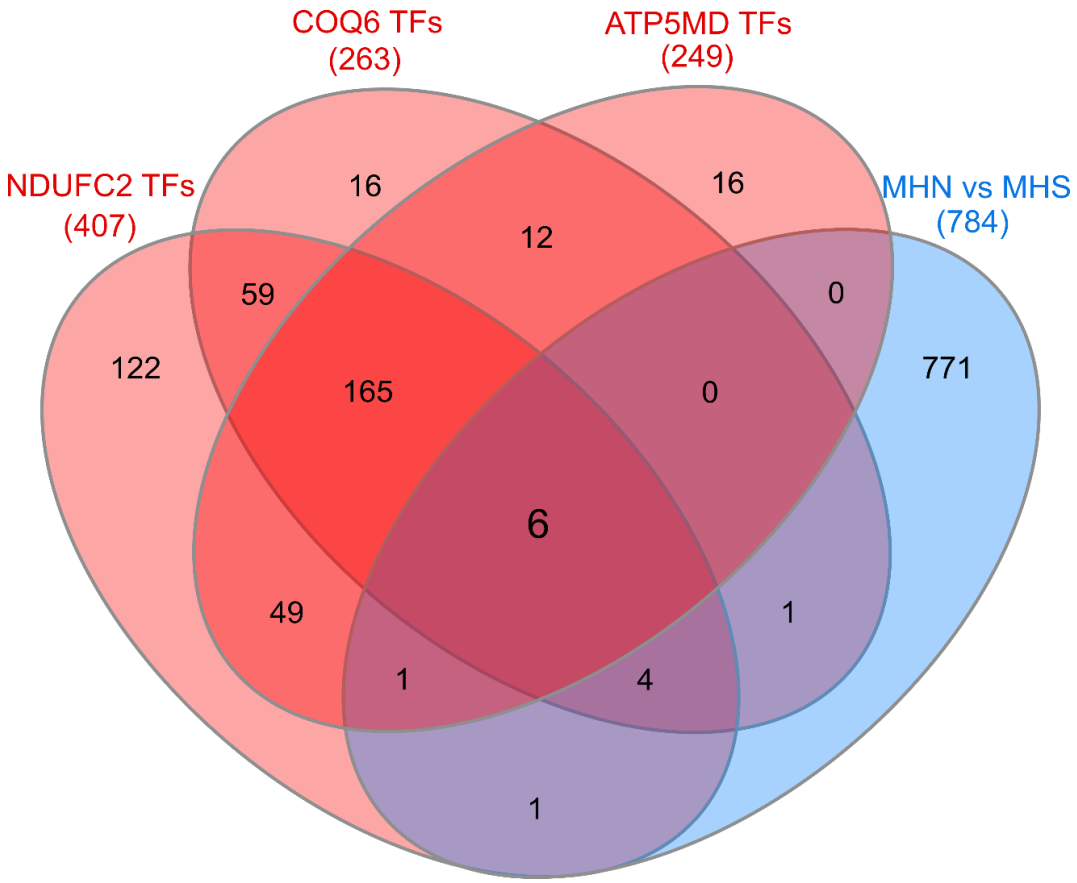

Figure 2.19. Cross comparison of transcription factors associated with enhancer regulatory elements. The TFs associated with each double enhancer for *NDUFC2*, *ATP5MD* and *COQ6* (red) were cross compared with the MHN vs MHS baseline gene list (Blue). This image was generated using InteractiVenn (Heberle et al., 2015).

Follow up work using this information would involve genotyping a large cohort of MHN and MHS individuals for the SNPs found within the enhancers of each gene of interest (Table 2.11). Alternatively, identifying tag-SNPs spanning each eQTL region of interest using information from linkage disequilibrium (LD) data can also be achieved using computational methods to confirm whether any contribute to the MHS susceptibility.

2.4 DISCUSSION

The aim of this study was to identify potential MH modifier loci using bioinformatic tools and differential gene expression data between MH phenotypes, both at baseline and after IVCT. As outlined in the methods, the IVCT is a lengthy procedure which utilises muscle biopsies over a period of ~30 minutes after surgical excision. The length of time the sample spends outside the human body can potentially cause changes in gene expression, resulting from external stressors such as temperature, oxygen availability and lack of blood supply. To address this concern, a comparison of gene expression was conducted prior to sequencing using snap frozen and re-oxygenated muscle. This experiment explored possible alterations in gene expression caused by *ex vivo* stressors prior to IVCT. This information was then used to inform which muscle sample was the most appropriate choice to act as control for the subsequent RNAseq experiment.

The gene expression profiles comparing re-oxygenated muscle to snap frozen muscle revealed a significant 10 fold-change upregulation in several genes, three of which (*FOS, FOSB, JUNB*) were known as AP-1 TF subunits. Other members of this group found highly expressed include *JUN* upregulated in re-oxygenated muscle at >5 fold-change and *ATF3* at >4 fold-change. This group of TFs is known to modulate gene expression with diverse functional properties, associated with cell proliferation, differentiation, apoptosis and oncogenesis (Shaulian and Karin, 2002). The roles of AP-1 TFs in skeletal muscle are complex, as their function can be dependent on specific subunit compositions (Chinenov and Kerppola, 2001).

Structurally, AP-1 TFs are heterodimers formed by a combination of proteins from the FOS (FOS, FOSB, FRA-1, FRA-2), JUN (JUN, JUNB and JUND), ATF and MAF protein families which are widely expressed in a variety of cell types (Garces de Los Fayos Alonso et al., 2018). JUN proteins can form homodimers with other JUN proteins as well as heterodimers with FOS proteins, whereas FOS proteins can only form heterodimers in order to bind DNA (Halazonetis et al., 1988; O'Shea et al., 1992). Following dimerization, they act as TFs which bind to regulatory sites called TPA-responsive elements and cAMP response elements in promoter and enhancer regions of target genes (Chinenov and Kerppola, 2001).

A study investigating mRNA expression in human skeletal muscle found that almost all members of the *JUN* and *FOS* gene family (aside from *FRA-2*) were significantly

upregulated after 30 minutes of exercise, ranging from 1.5 to 20 fold-change (Puntschart et al., 1998). Likewise, a similar observation was made when mRNA and protein levels in the JUN and FOS family were overexpressed in skeletal muscle after denervation, which has also been linked with the induction of apoptosis during times of cellular stress (Weis, 1994; Shaulian and Karin, 2001). These findings from literature support the notion that the *JUN* and *FOS* genes were likely upregulated due to the sample stress and degradation from *ex vivo* conditions. Gene expression of *FOS* and *JUN* was much lower in snap frozen muscle since they were frozen and kept at -80 °C shortly after surgery. As a result, the gene expression profile from snap frozen muscle, is thought to be the most accurate representation of basal gene expression within skeletal muscle. However, given that the IVCT is conducted *ex vivo*, natural degradation of the sample cannot be avoided, so re-oxygenated muscle was therefore chosen to serve as the RNAseq control to reduce the noise caused by non-IVCT stressors.

Initial interrogation of RNAseq data compared differential gene expression at baseline, showing a large set of genes downregulated in MHS (MHS_h + MHS_{hc}) samples, many of which were functionally grouped into the OXPHOS system and mitochondria. Baseline analyses with MHS phenotype subsets showed surprisingly few differentially expressed genes in MHS_{hc} individuals in comparison to MHS_h, despite the former being responsive to both halothane and caffeine. This may be due to the MHS_h sample group being more diverse than both MHN and MHS_{hc} groups with regards to age range. The MHS_h sample group age range was between 12-39 years which was significantly greater than the MHN (13-19 years) and MHS_{hc} (11-18 years).

Several studies have shown that age can have a profound effect on skeletal muscle gene expression, showing increased expression of pathways regulating cell growth and immune response with age, whilst gene expression for energy metabolism and mitochondrial OXPHOS decreases (Zahn et al., 2006; Bua et al., 2006; de Magalhaes et al., 2009). The higher age range in MHS_h samples may have contributed in the overestimation of baseline differences between MHN and MHS_h phenotypes. Differentially expressed genes in the MHS_{hc} vs MHN comparison, although few, have a greater effect size than those seen in MHS_h. This may reflect the differences in IVCT phenotype with MHS_{hc} individuals being associated with stronger responses (Robinson et al., 2002).

Mitochondrial dysfunction is speculated to be a downstream consequence of RyR1 dysfunction in MH, since MH events result in sustained muscle contractures which depend on ATP. Amongst differentially expressed genes at baseline, a large percentage downregulated in

MHS were responsible for encoding mitochondrial complex I. Complex I is the first enzyme of the electron transport chain (ETC) and its primary function is to oxidize NADH (generated by the Krebs cycle) and to transfer these electrons along the ETC reducing ubiquinone to ubiquinol. The energy released from this process is then used to transfer protons from the mitochondrial matrix into the intermembrane space, contributing to a proton gradient which is later used by ATP synthase to synthesize ATP (Sharma et al., 2009). Disruption of complex I function therefore negatively impacts OXPHOS resulting in metabolic conditions.

Complex I is the largest and most complicated component of the ETC, composed of 44 subunits, 37 of which are encoded by nuclear genes and 7 by mitochondrial genes (Sanchez-Caballero et al., 2016). Comparison of MHN vs MHS at baseline identified 18 complex I-encoded nuclear genes downregulated in MHS skeletal muscle. This significant number of downregulated genes suggests MHS individuals may have a degree of complex I deficiency. The prevalence of adults suffering from mitochondrial disease is estimated at 1 in 8000 individuals and complex I deficiency is the most common single enzyme deficiency responsible for mitochondrial disorders (Schaefer et al., 2008; Rodenburg, 2016). Many of the complex I and OXPHOS genes downregulated in MHS muscle, have been associated with metabolic conditions such as type 2 diabetes (T2DM) (Sreekumar et al., 2002; Mootha et al., 2003; Patti et al., 2003; Ling et al., 2007). Downregulation of OXPHOS genes are thought to contribute towards mechanisms leading to insulin-resistance, increasing the risk of T2DM (Patti and Corvera, 2010).

A past study found that MHS individuals had elevated plasma insulin levels in comparison to controls after intravenous glucose tolerance tests, leading to suggestions of impaired Ca^{2+} handling in pancreatic beta cells (Denborough et al., 1974). Individuals with T2DM are also frequently associated with deficiencies in extracellular and intracellular Mg^{2+} which is a known RyR1 inhibitor (Barbagallo and Dominguez, 2015). RyRs in muscle are sensitive to intracellular and luminal Mg^{2+} which act to inhibit Ca^{2+} release from the SR by competing with intracellular Ca^{2+} for RyR1 binding sites (Laver et al., 2004). If MH susceptibility is indeed linked to mechanisms which cause T2DM, then the associated Mg^{2+} deficits would help explain the hypersensitivity of RyR1 due to lower levels of inhibition.

A study using complex I (NDUFV1) knock-down C2C12 myoblasts found evidence of enhanced skeletal myogenesis and insulin signalling, suggesting a mechanism whereby NDUFV1 knock-down reduces NAD^{+}/NADH ratio which inactivates SIRT1 (Hong et al.,

2014). The protein SIRT1 is a NAD^+-dependent histone deacetylase and has been shown to regulate skeletal muscle gene expression and differentiation (Fulco et al., 2003). In the model proposed by Hong and colleagues, the inactivation of SIRT1 leaves myogenic transcription factors such as MyoD acetylated and activated, resulting in myogenic enhancement (Hong et al., 2014). This is interesting in the context of MH, as a study on >300 MHS patients found that individuals with muscular body types had a significantly higher rate of recrudescence (defined as the development of MH signs 2 hours after the initial MH event) (Burkman et al., 2007). This indicates a possible correlation between complex I, muscle mass and MH susceptibility.

Increased muscle mass is typically correlated with increased mitochondrial biogenesis - an adaptation from physical training. Physical training not only promotes mitochondrial biogenesis but can also alter the muscle fibre type distribution in skeletal muscle, a variable which was difficult to account for in this study. Studies have shown that the muscle fibre type distribution in the quadriceps of untrained individuals is in the range of ~40% type I, ~60% type II (Staron et al., 2000). The amount and type of physical training experienced by an individual can alter the proportion of type I and type II fibres present within the muscle biopsy and this may influence gene expression since they prefer different modes of energy metabolism (Wilson et al., 2012).

Furthermore, certain health conditions such as chronic obstructive pulmonary disease (COPD) have also been known to shift muscle fibre type distributions (Debigare et al., 2003; Gosker et al., 2007). Studies have found that individuals with COPD had less type I slow-oxidative fibres in comparison to controls, in addition to a reciprocal increase in type IIB fast-glycolytic fibres, possibly as a compensation mechanism (Debigare et al., 2003; Gosker et al., 2007). Detailed information on physical training and medical history was not factored into the analysis for this study and may account for some of the variability seen between datasets. If OXPHOS deficiency is truly present in MHS muscle, then individuals who possess higher proportions of type I slow-oxidative fibres may be more susceptible to myopathic traits and a more severe MH phenotype.

In addition to baseline differences, OXPHOS genes were also found to be downregulated in MHN samples after exposure to both halothane and caffeine. Surprisingly, halothane and caffeine had a much larger effect on MHN muscle gene expression in comparison to MHS. Pathway analysis on MHN gene lists highlighted the downregulation of

OXPHOS and ETS pathway terms after both halothane and caffeine exposure, but these findings were not observed in the MHS phenotype. The absence of OXPHOS gene downregulation in the MHS treatment response may be due to OXPHOS gene expression already being reduced at baseline. Many complex I-encoding genes were downregulated in MHN and this negative shift in complex I gene expression may reflect a relationship between complex I and muscle stimulants. A study on complex I *gas-1* mutant *Caenorhabditis elegans (C.elegans)*, showed that halothane had an inhibitory effect on complex I-dependent respiration whilst complex II-dependent respiration was increased, possibly as a way of compensation (Kayser et al., 2004). This observation was also supported in a study involving cardiac mitochondria taken from guinea-pigs, showing reversible inhibition of complex I activity using halothane, isoflurane and sevoflurane (Hanley et al., 2002).

Evidence has shown that halothane can induce Ca^{2+} release from the SR resulting in muscle contracture (Palade et al., 1989). This can occur in both wild-type and MHS skeletal muscle but the activation of RyR1 is regulated by several cytosolic modulators (Ca^{2+}, ATP, Mg^{2+}) (Diaz-Sylvester et al., 2008). As previously mentioned, cytosolic Mg^{2+} is an important inhibitor of RyR1 and the resting Mg^{2+} concentration in MHN muscle is higher than MHS, reducing the sensitivity of RyR1. The downregulation of OXPHOS genes in MHN muscle after halothane and caffeine stimulants may also be an adaptation to lower cytosolic ATP levels which reduce the sensitivity of RyR1 further and prevent Ca^{2+} release from the SR. These inhibitory mechanisms are possibly weaker in MHS muscle, given the cytosolic Mg^{2+} deficits and passive Ca^{2+} leak from the SR raising cytosolic Ca^{2+}.

Comparison of halothane and caffeine responses across MHS phenotypes identified only three genes in common (*GIMAP8*, *MT-TM*, *PECAM1*), all of which were downregulated after drug exposure. The gene *GIMP8* is a member of the GTPase of immunity-associated protein (GIMAP) family, which aids the regulation of lymphocyte survival and homeostasis (Schwefel et al., 2013). One study has also described a reduction in *GIMAP8* expression after exercise (McLean et al., 2015). *PECAM1* similarly encodes, platelet and endothelial cell adhesion molecule 1, a protein which is found on the surface of a range of immune cells (Gumina), whilst *MT-TM* is an RNA gene for the mitochondrially encoded the tRNA for methionine (Anderson et al., 1981). The downregulation of these genes may be due to an inflammatory response caused by the stress of drug exposure.

The comparatively weak effect of halothane and caffeine seen on MHS gene expression might be explained by limitations in experimental design. One concern for the RNAseq design was whether the length of time exposed to halothane/caffeine was appropriate to detect gene expression changes reflective of an MH reaction. The IVCT is a diagnostic test with fixed guidelines on drug exposure time and concentrations, limiting the experiment to a singular time point and predefined drug concentrations. Optimisation of experimental factors was therefore not possible since the IVCT was used as the means of applying drug treatment. Multiple studies have shown that skeletal muscle gene expression can change significantly with time, differing in orders of magnitude over a 24-hour period (Neubauer et al., 2014; Liu et al., 2010). On that basis, it is possible that the time point used to assess treatment effect in this experiment failed to capture changes which reflect the hypermetabolic response of interest.

Ideally, this experimental design could be refined by using cultured myotubes to help optimise for experimental factors. The first advantage to culturing myotubes, is the ability to overcome the limitations with the muscle biopsy control samples (*ex vivo* stressors and degradation over time) described in this section. Secondly, instead of using the IVCT to apply drug treatment, drugs can be incorporated into culture media in a plate format to allow more flexibility over drug exposure time and drug concentrations. One approach would be to use a microplate reader to measure Ca^{2+} flux in myotubes using a Ca^{2+}-sensitive fluorescent dye. With this technique, a dose response experiment can be conducted with a range of halothane and caffeine concentrations to identify the concentration which elicits a maximum response, indicated by Ca^{2+} flux. Using this information, the ideal drug concentration can then be applied to myotubes at several time points spanning 0 to 24-hours. RNA can then be extracted from myotubes at each time point and prepared for RNAseq. This setup design should provide the maximal drug response in myotubes and allow the assessment of gene expression change over time in all MH phenotypes. Furthermore, myotubes cultured for such experiments should ideally be sourced from individuals who are of similar age, fitness level and *RYR1* variant to reduce variability associated with those factors.

Due to the concerns regarding the efficacy of drug treatments, follow up work from RNAseq data was done on baseline MHN and MHS comparisons only, using the QuantiStudio RT-PCR system. Five genes of interest were selected from baseline MHN vs MHS comparisons, three directly involved with the ETC (*USMG5*, *NDUFC2* and *COQ6*) and two involved in closely related external processes (*MPC2* and *MALSU1*). All five genes were found to be downregulated in MHS samples based on the results from RNAseq, but this was not

entirely consistent with the follow up RT-PCR. Only three of the five mitochondria-related genes showed statistically significant downregulation (*USMG5*, *NDUFC2* and *COQ6*). Directional changes in gene expression were consistent between RNAseq and RT-PCR, but it appeared as though these differences were overestimated in the RNAseq data. The MHS individuals selected for RNAseq had strong IVCT responses (majority >0.5g contracture at 2 Vol% halothane) as opposed to the much more lenient criteria (>0.2g contracture at 2 Vol% halothane) used for RT-PCR. The more stringent criteria was adopted for RNAseq to maximize the chance of identifying differential gene expression between phenotypes and this could not be applied to RT-PCR due to limitations in sample population. On that basis, the RT-PCR findings are a more accurate representation of the overall MHS population, as the overtly strong IVCT responses selected for RNAseq may have exaggerated the baseline findings.

Consequently, the two genes *MPC2* and *MALSU1* which were not significantly downregulated using RT-PCR, also had the smallest effect sizes out of the five genes selected. This may reflect a need to consider a FC threshold in future when considering genes of interest. The gene expression difference between MHS and MHN samples at baseline were less than -1 log2FC in all five genes selected. These effect sizes may be too small for RT-PCR detection if there is indeed an overestimation of baseline differences as previously discussed. This observation appears to be supported by the data generated on the Biomark RT-PCR system used for RNAseq validation. The six genes assessed for their downregulation in MHN samples after halothane exposure (*CNOT11, VMA21, SNX3, NDFIP1, PYURF, UBE2N*) also had less than -1 log2FC effect size from RNAseq data and this corresponded to very little gene expression on the Biomark system. In contrast, the genes assessed for their upregulation after halothane treatment (*NR4A2*, *INSIG1*, *DNAJA1*, *SOCS1*, *TNFRSF10D*, *IRF1*, *PPP1R10* and *HSPA1A*) had larger effect sizes (majority >2 log2FC) and these differences resembled those detected on the Biomark. In hindsight, it would have been more appropriate to follow up genes of interest showing > 1 log2FC effect size to account for overestimations in the RNAseq data.

With regards to biological function, *MPC2* encodes mitochondrial pyruvate carrier 2, responsible for importing pyruvate across the inner mitochondrial membrane. Deficiency in MPC2 has been shown to result in elevated blood glucose levels as a result of reduced glucose-stimulated insulin secretion (Vigueira et al., 2014). In contrast, *MALSU1* (mitochondrial assembly of ribosomal large subunit 1), is required for assembly and stability of the large ribosomal subunit (Rorbach et al., 2012). These two genes did not appear to be downregulated in the wider MHS sample population assessed by RT-PCR which may indicate that

bioenergetic defect in MHS muscle is caused by damage to ETC components as opposed to deficiencies in external factors such as substrate transport or mitochondrial ribosome formation.

USMG5 (*ATP5MD*) encodes the diabetes-associated protein in insulin-sensitive tissue (DAPIT) and was first described as a novel protein downregulated in the insulin-sensitive tissues found in diabetic rats (Paivarinne and Kainulainen, 2001). It is associated with ATP synthase (complex V) and is thought to have a role in maintaining complex V population in mitochondria (Meyer et al., 2007; Ohsakaya et al., 2011). Histological reports have shown increased localisation of DAPIT in cells with high aerobic metabolism, favouring oxidative fibres in skeletal muscle (Kontro et al., 2012). Mutations in *USMG5* are associated with complex V deficiency, reduced ATP production and Leigh's syndrome (Barca et al., 2018). Leigh's syndrome is a condition which can be caused by mutations in all mitochondrial complexes, characterised by progressive loss of mental capacity and motor function, often resulting in death 2-3 years after disease onset (Ruhoy and Saneto, 2014).

The complex I-encoding *NDUFC2* has been associated with stroke, diabetes and cardiovascular disease (Rubattu et al., 2016; Raffa et al., 2017; Madonna et al., 2019). It has been shown that NDUFC2 deficiency can result in a variety of mitochondrial defects such as reduced ATP production, reduced mitochondrial membrane potential, ultra-structural impairments and increased reactive oxygen species (ROS) production (Rubattu et al., 2016; Raffa et al., 2017; Raffa et al., 2019; Madonna et al., 2019). Mitochondria are a main source of ROS, generated primarily from complex I, complex III and the more recently suggested complex II (Murphy, 2009b; Quinlan et al., 2012). ROS are important signalling molecules for organelle crosstalk, and dysregulation can lead to mitochondrial dysfunction and induction of apoptosis through excessive oxidative damage. The reduced expression of complex I subunits may lead to higher levels of oxidative stress in MHS muscle, resulting in functional defects. These findings suggest inherent bioenergetic defect in MHS muscle, which may contribute to some of the muscle-related symptoms (cramps, weakness etc) described in MHS patients.

Coenzyme Q6 monooxygenase (CoQ6) encoded by *COQ6* is an essential component to the ETC and takes part in the production of coenzyme Q10 (CoQ10). CoQ10 is responsible for several functions which include acting as an antioxidant, a cofactor for mitochondrial dehydrogenases and an apoptotic regulator. Mutations in *COQ6* cause CoQ10 deficiency, often associated with steroid-resistant nephrotic syndrome (SRNS), deafness and a range of muscle-

related manifestations such as hypotonia, dystonia, myopathy, exercise intolerance and elevated CK levels (Heeringa et al., 2011; Salviati et al., 2017). The bioenergetic consequences of CoQ10 deficiency appears to be complex as severe deficiency has been associated with reduced ATP production and normal ROS production, whilst minor CoQ10 deficiency has been observed with high ROS production and no change to ATP levels (Quinzii and Hirano, 2010). Consequences to reduced CoQ6 expression include increased apoptosis and mitochondrial depolarisation, both of which were observed in CoQ6 knockdown cells carrying pathogenic mutations (Salviati et al., 2017).

Exploration of regulatory elements for *ATP5MD*, *NDUFC2* and *COQ6* showed that many common TFs regulate the gene expression for all three genes. Among this selection, the genes encoding six of these TFs (*ATF3*, *CHD2*, *NFKBIZ*, *CTBP1*, *ESRRA* and *TEAD4*) were also found differentially expressed in the MHS phenotype at baseline. Gene expression levels of *ATF3*, *CHD2* and *NFKBIZ* were upregulated in MHS skeletal muscle whilst *CTBP1*, *ESRRA* and *TEAD4* were downregulated in comparison to MHN. Dysregulation of these TFs in MHS muscle may contribute to the MH phenotype by modifying OXPHOS gene expression resulting in functional consequences.

Activating transcription factor 3 (ATF3), encoded by *ATF3*, is a member of the ATF/CREB family of TFs and is upregulated in response to a range of stressors including: exercise, ER-stress, oxidative stress and hypoxia (Hai et al., 1999; Hai and Hartman, 2001). Exercise-induced *ATF3* expression in skeletal muscle has shown to regulate the mRNA expression of inflammatory chemokines and cytokine, performing a homeostatic function for recovery (Fernandez-Verdejo et al., 2017). The increase of *ATF3* expression in MHS skeletal muscle indicates a state of elevated cellular stress at baseline. This is further supported by the increased gene expression of *CHD2*, encoding chromodomain helicase DNA-binding domain 2 (CHD2), which has been shown to localise at sites of DNA damage and promotes repair (Luijsterburg et al., 2016). One source of increased cellular stress could be increased ROS production as previously mentioned, given the number of OXPHOS-related genes downregulated in MHS muscle.

Furthermore, studies have shown that *CTBP1*, encoding the c-terminal binding protein (CTBP1), can function as a metabolic sensor through interactions with NAD^+/NADH and helps maintain mitochondrial activity (Fjeld et al., 2003). Mitochondrial elongation, swelling, reduced ATP levels and reduced oxygen consumption has been observed in CTBP1 knock-out

HeLa cells (Kim and Youn, 2009). Likewise, downregulation of *ESRRA* in skeletal muscle, encoding estrogen-related receptor-α (ERRα), has also been shown to impair muscle regeneration and mitochondrial biogenesis (LaBarge et al., 2014). Many of these features have been reported in MH studies which supports a link between mitochondrial abnormality and differential gene expression (Lavorato et al., 2016; Durham et al., 2008; Yuen et al., 2012; Giulivi et al., 2011).

In summary, transcriptome comparisons between MHN and MHS skeletal muscle, has highlighted a downregulation of OXPHOS-related gene expression at baseline in MHS individuals. RNAseq resulted were successfully validated using the Biomark RT-PCR system, and three OXPHOS genes of interest, *ATP5MD*, *NDUFC2* and *COQ6* were followed up using bioinformatic resources. Many common TFs were found to regulate all three genes, six of which were also differentially expressed at baseline between MHN and MHS samples. Since these OXPHOS genes and their TFs appear to be associated with the MHS phenotype, the regulatory mechanisms of these genes have become an area of interest. It is possible that variants within the enhancer regions of *ATP5MD*, *NDUFC2* and *COQ6* interfere with TF binding properties which modify transcriptional activity, causing variation in MH phenotypes.

One approach to further this investigation would be to study the eQTLs identified for *ATP5MD*, *NDUFC2* and *COQ6*, by SNP genotyping a large cohort of MHN and MHS individuals. A focal point for genotyping could be the SNPs identified in each enhancer for the three genes of interest, or alternatively a broader tag-SNP genotyping approach could be adopted across the eQTL region of interest. A tag-SNP is a representative SNP in a region of the genome in high LD that represents a haplotype. Programs containing tag-SNP algorithms can be used to select tag-SNPs from haplotype blocks containing SNPs in high LD across the candidate loci (Halperin et al., 2005; Sicotte et al., 2011; Ao et al., 2005). This makes it possible to investigate genetic variation and association between phenotypes without genotyping every SNP in the region. Successful identification of these SNPs in MHS individuals, will provide evidence of these loci contributing towards the MH phenotype and provide new insights into the pathophysiology surrounding MH.

3 ASSESSMENT OF MITOCHONDRIAL FUNCTION IN MALIGNANT HYPERTHERMIA-SUSCEPTIBLE INDIVIDUALS

3.1 INTRODUCTION

MHS individuals, in the absence of anaesthetic triggers, do not have obvious clinical phenotypes but there have been reports of some experiencing muscle-related traits, such as exercise intolerance, muscle weakness, cramping and exercise-induced rhabdomyolysis (Timmins et al., 2015; Wappler et al., 2001; Litman et al., 2018). These features are often observed in MH-associated congenital myopathies such as central core disease and multi-minicore disease, which have impaired oxidative metabolism (Jungbluth, 2007; Robinson et al., 2006). Mitochondria are the primary drivers of cellular metabolism and their involvement in MH susceptibility was speculated prior to the discovery of any genetic factors. Over fifty years ago, researchers hypothesised that MH triggering events lead to mitochondrial uncoupling, which contribute to the increase in body temperature, CO_2 production and lactate formation observed in MH reactions (Wilson et al., 1966; Gatz and Jones, 1969). However, the literature surrounding mitochondrial dysfunction in MH has been conflicting, with differing observations reported in both human and animal MH models.

In 1975, Isaacs & Heffron used electron microscopy to examine four human MHS muscle biopsies, taken from the quadriceps, and each sample had sub-populations of swollen mitochondria with damaged cristae (Isaacs and Heffron, 1975). These observations were supported in a more recent study by Lavorato et al., who were investigating chronic alterations in MHS skeletal muscle ultrastructure (Lavorato et al., 2016). In that study, they observed a higher frequency of mitochondrial abnormalities within MHS skeletal muscle, referring to sub-populations of round, swollen mitochondria, with reduced matrix density and variable distributions of cristae (Lavorato et al., 2016). These reports of structural abnormality within MHS mitochondria suggest some form of chronic muscle damage associated with MH susceptibility which may be difficult to detect clinically.

Two studies reported normal OXPHOS and respiratory control in human MHS mitochondria, but a higher sensitivity to Ca^{2+}-induced uncoupling was observed (Britt et al., 1973; Cheah et al., 1989). These findings appear to contradict the recent study by Thompson and colleagues, who reported evidence of impaired OXPHOS and ATP production after bouts of training in MHS individuals, indicating a functional defect in MHS mitochondria

(Thompson et al., 2017). It was also noted that skeletal muscle homogenates from MHS humans and MHS pigs had higher rates of fatty acid production which may indicate a defect in mitochondrial lipid metabolism (Cheah et al., 1989; Fletcher et al., 1991a; Fletcher et al., 1991b; Fletcher et al., 1990).

Early observations on MHS mitochondria were based primarily on skeletal muscle taken from MHS pigs. In contrast to MHS humans, MH susceptibility in pigs is autosomal recessive and they are predisposed to an overt sensitivity towards stress (Fujii et al., 1991; Fletcher et al., 1993). Although rare, heat-stress induced MH reactions have been reported in humans which may reflect a degree of similarity between species in the absence of anaesthesia (Gronert et al., 1980; Groom et al., 2011; Nishio et al., 2009; Carsana, 2013). MHS pigs have been reported to have respiratory states over three times higher than MHN pigs, alongside reduced Ca^{2+} accumulation in MHS mitochondria (Britt et al., 1975). This study contradicted other reports which have shown either no significant difference or reduced mitochondrial function in MHS mitochondria in comparison to MHN pigs (Denborough et al., 1973; Eikelenboom and van den Bergh, 1973; Gronert and Heffron, 1979). These conflicting claims are likely due to differences in methodology, but one consistent observation shared between all studies was the halothane-induced inhibition of mitochondrial respiration (Britt et al., 1975; Britt et al., 1973; Gronert and Heffron, 1979).

Research on RYR1 knock-in mouse models of MH have also reported various degrees of mitochondrial abnormality depending on the *Ryr1* variant. On a structural level, mitochondrial deformity has been observed in the skeletal muscle from the Y522S-RYR1 and T4826I-RYR1 mouse models which is an indication of damage (Durham et al., 2008; Boncompagni et al., 2009; Yuen et al., 2012). These reports often denote a loss of cristae organization and mitochondrial swelling which suggests there may be metabolic dysfunction and altered OXPHOS in muscles from both MHS mice (Durham et al., 2008; Boncompagni et al., 2009; Yuen et al., 2012) and humans (Isaacs and Heffron, 1975; Lavorato et al., 2016). Other notable observations found in MHS mice include reduced oxygen consumption rates in T4826I-RYR1 knock-ins (Yuen et al., 2012), increased oxidative stress in Y522S-RYR1 knock-ins (Durham et al., 2008) and evidence of R163C-RYR1 mutants having both those features with reduced mitochondrial protein expression (Giulivi et al., 2011).

The purpose of this study was to investigate mitochondrial function in skeletal muscle biopsies taken from human MHS individuals. This was achieved by using high-resolution

respirometry to measure oxygen consumption rates in permeabilised muscle fibres. Experiments were designed and carried out to address the following research questions:

- Is there evidence of altered mitochondrial content between MHN and MHS skeletal muscle?
- Does mitochondrial function differ between MHN and MHS skeletal muscle at baseline?
- How does exposure to IVCT halothane alter mitochondrial function in both MH phenotypes?

3.2 METHODS

3.2.1 Patients

Patients samples were collected from individuals who were referred for IVCT on suspicion of their susceptibility to MH. Most index case patients had been found not to harbour a pathogenic variant in *RYR1* and *CACNA1S* (www.emhg.org, 2020) prior to attending. Family members were either from families where no pathogenic variant had been found or who had been found not to carry a familial variant. Patients gave written informed consent to the study that was approved by Leeds (East) Research Ethics Committee (reference 10/H1306/70). Patients were diagnosed using the IVCT as either MHS_h, MHS_{hc} or MHN according to the protocol of the EMHG (Hopkins et al., 2015).

3.2.2 Muscle samples

Diagnostic muscle biopsies and IVCTs were conducted by Ms Catherine Daly (Laboratory Manager of the MH Unit) and Dr Dorota Miller (Postdoctoral Researcher at the MH Unit), according to the protocol of the EMHG (Hopkins et al., 2015). In brief, six muscle fascicles (typical dimensions 25 mm x 4 mm x 3mm) were excised from *vastus medialis* under femoral nerve block and immediately placed in oxygenated Krebs-Ringer solution (118.1 mM NaCl, 3.4 mM KCl, 0.8 mM $MgSO_4$, 1.2 mM KH_2PO_4, 11.1 mM Glucose, 25.0 mM $NaHCO_3$, 2.5 mM $CaCl_2$, pH 7.4) at room temperature and taken to the MH laboratory. There, the samples were kept at room temperature in the Krebs-Ringer solution, which was gassed continuously with carbogen (95% O_2, 5% CO_2), until being used for the IVCT tests.

This study required both a muscle fascicle that had not been used for the diagnostic challenge tests (baseline) and a fascicle that had been used in the static halothane test (halothane-exposed). At the end of the halothane test procedure both the halothane-exposed and baseline samples were each placed into 1 ml of ice-cold biopsy preservation buffer, BIOPS (2.77 mM CaK_2EGTA, 7.23 mM K_2EGTA, 5.77 mM Na_2ATP, 6.56 mM $MgCl_2 \cdot 6H2O$, 20 mM taurine, 15 mM Na_2Phosphocreatine, 20 mM imidazole, 0.5 mM dithiothreitol, and 50 mM MES hydrate, pH 7.1, adjusted with 5 N KOH at 0 °C). The samples were then placed in a petri dish with ice cold BIOPS and separated using forceps to obtain small muscle fibre bundles containing approximately 4-5 fibres each.

These samples then underwent chemical permeabilization in BIOPS containing saponin (50 $\mu g \cdot ml^{-1}$) for 30 min, before being washed with 1 ml respiration medium, Mir05 (0.5 mM EGTA, 3 mM $MgCl_2 \cdot 6H2O$, 60 mM lactobionic acid, 20 mM taurine, 10 mM KH_2PO_4, 20 mM HEPES adjusted to pH 7.1 with KOH at 37 °C, 110 mM D-sucrose, and 1 $g \cdot L^{-1}$ essentially fatty acid free BSA) to remove residual saponin. The sample was then taken out of solution and blot-dried for 5 seconds before being weighed and loaded into the respirometer chambers (5-10 mg in each chamber) containing 2 ml of Mir05. The time between biopsy collection and assay time was approximately 90 – 120 minutes. This sample preparation procedure was adapted from previously described protocols (Kuznetsov et al., 2008; Pesta and Gnaiger, 2012; Chang et al., 2019).

3.2.3 High Resolution Respirometry

Oxygen consumption over time was measured using Oroboros respiratory analysers (Oroboros Instruments, Innsbruk, Austria) at 2 second intervals with polarographic oxygen sensors and expressed as mass-specific oxygen flux (pmol/s*mg). The analyser was calibrated daily in air saturated solution before experimentation. Assays were initiated by injecting oxygen into each chamber to raise the oxygen concentration to >400 nmol/mL prior to starting a substrate-uncoupler-inhibitor titration (SUIT) protocol. Re-oxygenation of the chambers was performed to maintain oxygen concentration between 200-500 nmol/mL to prevent limitation due to oxygen diffusion (Kuznetsov et al., 2008) each assay was performed at 37 °C, with chamber stirrers set at 750 rpm.

3.2.4 Substrate-uncoupler-inhibitor titration protocol

An adapted SUIT protocol (Figure 3.1) was used to investigate the OXPHOS capacity of individual complexes and respiratory states (Kuznetsov et al., 2008; Pesta and Gnaiger, 2012; Chang et al., 2019). The procedure was initiated with the addition of 5 μM blebbistatin (BLEB) to prevent spontaneous contraction of muscle fibres (Perry et al., 2012; Perry et al., 2011). Glutamate (10 mM), malate (0.5 mM) and pyruvate (5 mM) were then applied to facilitate measurements of the complex I respiration in the absence of ADP (LEAK). ADP (2.5 mM) is

then added next to allow the measurement of maximal complex I-supported OXPHOS ($CI_{(OXPHOS)}$). At this point, the outer mitochondrial membrane integrity was assessed by the addition of 10 μM cytochrome c. An increased respiration rate after addition of cytochrome c indicates outer mitochondrial membrane damage: samples that showed an increased respiration rate after cytochrome c of >10% were excluded from data analysis.

Once membrane integrity has been assessed, the maximal activity of complex II is stimulated with the addition of succinate (10 mM). The oxygen flux at this stage ($CI+CII_{(OXPHOS)}$) reflects the combined activities of complex I and complex II together and is also regarded as the maximum OXPHOS capacity in the coupled state. Next, step-wise additions of carbonyl cyanide 4-(trifluoromethoxy)-phenylhydrazone (FCCP) (0.5 μM) are made until there is no further increase in oxygen flux. This step-wise addition of FCCP uncouples the ETS by collapsing the proton gradient between the intermembrane space and the mitochondrial matrix providing the maximum ETS capacity ($CI+CII_{(ETS)}$). Then, after uncoupling the system, electron flow through complex I is inhibited using rotenone (0.5 μM), providing maximum complex II activity alone ($CII_{(ETS)}$). Finally, antimycin A is introduced to inhibit complex III. Complex III activity is technically contributing to all data points aside from the Complex IV assay. However, its activity is not measured directly in this protocol as it obtains electrons downstream of complex I and II. Residual oxygen flux (ROX) present after the addition of antimycin A is a result of non-mitochondrial respiration which is then subtracted from each respiratory state reading before analysis.

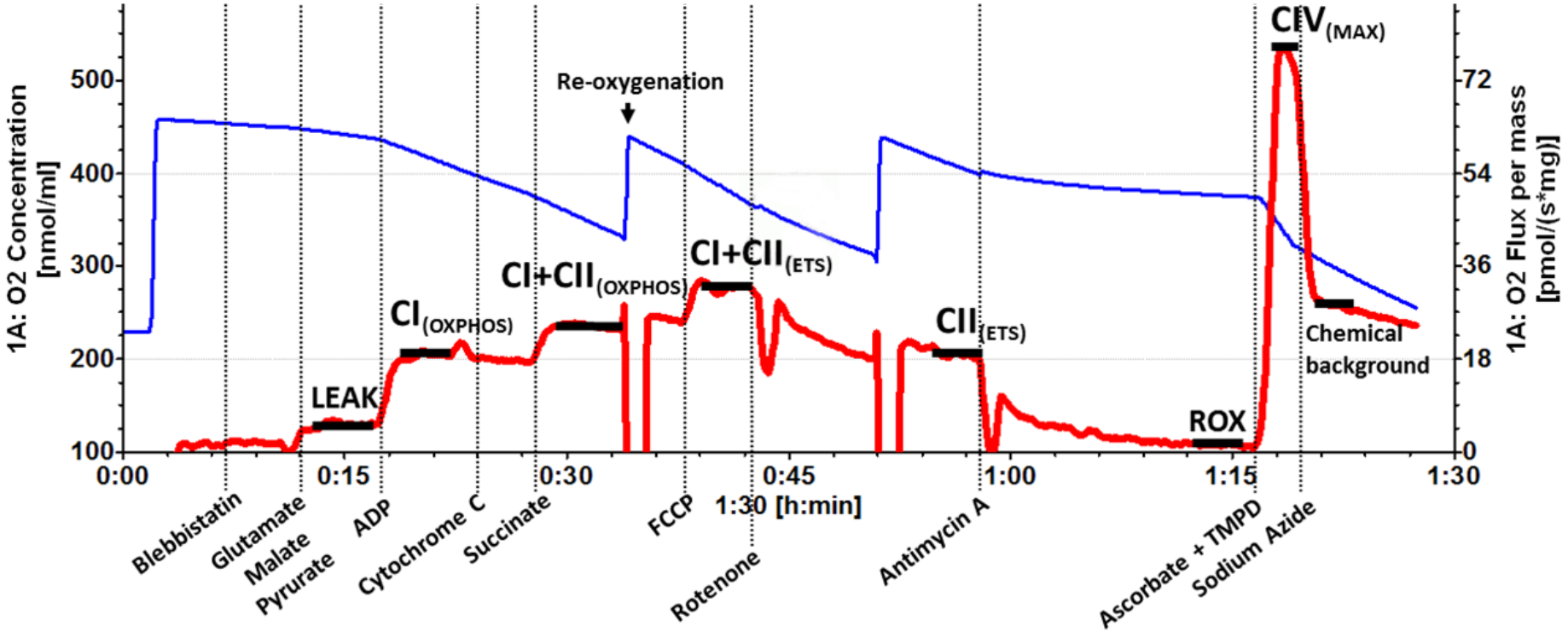

Figure 3.1. High resolution respirometry trace. This trace shows the rate of oxygen flux (red line) over time after sequential titration of substrates and inhibitors, expressed as pmol/s*mg. An overview of the SUIT protocol and CIV assay can be seen, with each vertical line representing the timepoint at which substrates/inhibitors were added. The blue line represents oxygen levels within the chamber (nmol/ml). The horizontal black lines which overlay the red line plateaus indicate the position of data points, Residual oxygen flux (ROX) present after the addition of antimycin A reflects non-mitochondrial respiration.

3.2.5 Complex IV Assay

Measurement of mass-specific complex IV oxygen flux was used as an alternative proxy marker for estimations of mitochondrial content. Ascorbate (2 mM) and N,N,N′,N′-tetramethyl-p-phenylenediamine (TMPD) (0.5 mM) was applied to each sample at the end of the standard SUIT protocol. The measurement of complex IV flux is taken at the peak of the corresponding trace and residual chemical background is finally removed from this value by applying sodium azide (10 mM) to the sample (Larsen et al., 2012).

3.2.6 Data handling and analysis

Raw data output is in the form of oxygen flux per muscle mass (pmol/s*mg) which includes the confounding effects of both mitochondrial quality and quantity. The data in this study were internally normalised to the common reference state, $CI+CII_{(ETS)}$ (maximum uncoupled respiration). Normalised oxygen flux per mass is presented as flux control ratios (FCR) which highlight differences in mitochondrial function, as a proportion of the reference state, which is independent of mitochondrial content.

Oxygen flux readings recorded from each sample trace were exported from proprietary software DatLab5 (Oroboros Instruments, Innsbruk, Austria) into Microsoft Excel before analysis using IBM SPSS statistics v21. Pairwise comparisons were performed using a combination of Wilcoxon signed-rank tests to assess the effects of halothane-exposure and Mann-Whitney U tests to assess differences between baseline controls. Mann-Whitney U tests were also used to compare the magnitude of FCR differences (pre vs post halothane) between MH phenotypes (MHN vs MHS). Further analysis using MHS subgroups involved a Kruskal-Wallis test and post hoc Dunn's procedure to identify differences between patients classified as MHN, MHS_h and MHS_{hc}. Data were summarised as boxplots using GraphPad Prism 8.

3.3 RESULTS

3.3.1 Patient characteristics

A summary of patient characteristics is presented in Table 3.1. We included 59 individuals (MHN n=36, MHS n=23) from 52 families: the maximum number from any family was two individuals. 18 of the 23 MHS individuals were subsequently found to carry at least one variant in the *RYR1* gene, of which only the c.1021G>A mutation has been functionally characterised (www.emhg.org, 2020). None of the patients had clinical or histopathological features suggestive of a mitochondrial myopathy.

***In vitro* contracture test result**	**MHN (n = 36)**	**MHS (n = 23)**					
		MHS_h (n = 12)			**MHS_{hc} (n = 11)**		
Male / Female	16 / 20	05 / 07			07 / 04		
Age at biopsy (years)	(11 – 68)	(12 – 64)			(12 – 57)		
Individuals with at least one *RYR1* variant	-	8			10		
***RYR1* variants found**	-	**Nucleotide change**	**Amino acid change**	**Accession number**	**Nucleotide change**	**Amino acid change**	**Accession number**
		c.251C>T[b]	p.Thr84Met	rs186983396	c.455C>A[b]	p.Ala152Asp	-
		c.4178A>G[a]	p.Lys1393Arg	rs137933390	c.1202G>A[c]	p.Arg401His	rs193922766
		c.5183C>T[c]	p.Ser1728Phe	rs193922781	c.8729C>T[b]	p.Tyr2910Met	-
		c.6670C>T[b]	p.Arg2224Cys	rs199870223	c.10357C>T[b]	p.Arg3453Cys	rs1482429489
		c.6785G>A[b]	p.Gly2262Asp	-	c.11132C>T[c]	p.Thr3711Met	rs375915752
		c.7879G>A[c]	p.Val2627Met	-	c.11958C>G[c]	p.Asp3986Glu	rs193922842
		c.12860C>T[b]	p.Ala4287Val	-	c.12700G>C[c]	p.Val4234Leu	rs193922852
		c.14210G>A[c]	p.Arg4737Gln	rs193922868	c.7879G>A[c]	p.Val2627Met	-
		c.4293G>A	p.Thr1431=	rs727504130	c.1021G>A[d]	p.Gly341Arg	rs121918592

Table 3.1. Summary of patient characteristics contributing to the respirometry study. The *RYR1* variants are annotated for their likely pathogenicity using the criteria of Miller *et al* as: a. Unlikely pathogenic; b. Potentially pathogenic; c. Likely pathogenic; d. pathogenic (Miller et al., 2018).

The contracture strengths of each MHS individual are summarised in Table 3.2. The threshold for positive IVCT halothane response is 0.2g at 2 Vol% halothane and a positive caffeine response was 0.2g at 2 mM caffeine.

Patient number	IVCT classification	Contracture at 2% halothane (g)	Contracture at 2mM caffeine (g)
1	MHS_h	0.6	0
2	MHS_h	0.4	0
3	MHS_h	1.05	0
4	MHS_h	0.3	0
5	MHS_h	0.35	0
6	MHS_h	0.2	0
7	MHS_h	0.2	0
8	MHS_h	0.3	0
9	MHS_h	0.2	0.05
10	MHS_h	0.3	0
11	MHS_h	0.2	0.1
12	MHS_h	0.2	0.1
13	MHS_{hc}	0.7	0.2
14	MHS_{hc}	0.7	2
15	MHS_{hc}	1.8	1
16	MHS_{hc}	1.05	0.5
17	MHS_{hc}	0.9	0.2
18	MHS_{hc}	1.05	0.75
19	MHS_{hc}	2.55	0.9
20	MHS_{hc}	0.4	0.25
21	MHS_{hc}	1.6	0.4
22	MHS_{hc}	0.9	0.2
23	MHS_{hc}	0.45	0.3

Table 3.2. *In vitro* contracture test responses for all MHS samples used in respirometry. Contracture responses at 2 Vol% halothane and 2 mM caffeine for all 23 MHS patient samples used for high resolution respirometry. The MHN patients all had 0 g responses at 2 Vol% halothane and 2 mM caffeine.

3.3.2 Mass-specific oxygen flux comparisons

Oxygen flux per milligram of muscle was compared between MHN and MHS samples, with and without exposure to halothane (Figure 3.2). Baseline comparison of samples without halothane exposure showed no differences between the two phenotypes aside from $CIV_{(MAX)}$. A statistically significant increase in mass-specific $CIV_{(MAX)}$ was observed in the MHS phenotype ($p=0.021$) which suggests that MHS samples had greater mitochondrial content in comparison to MHN. The effects of halothane were assessed using pairwise comparisons within phenotype, which showed that oxygen flux was significantly elevated in MHS samples after halothane exposure in several respiratory states: $CI_{(OXPHOS)}$, $CI+CII_{(OXPHOS)}$, $CI+CII_{(ETS)}$ and $CII_{(ETS)}$. This change in oxygen flux was not observed in MHN samples, showing no significant alteration after exposure to halothane.

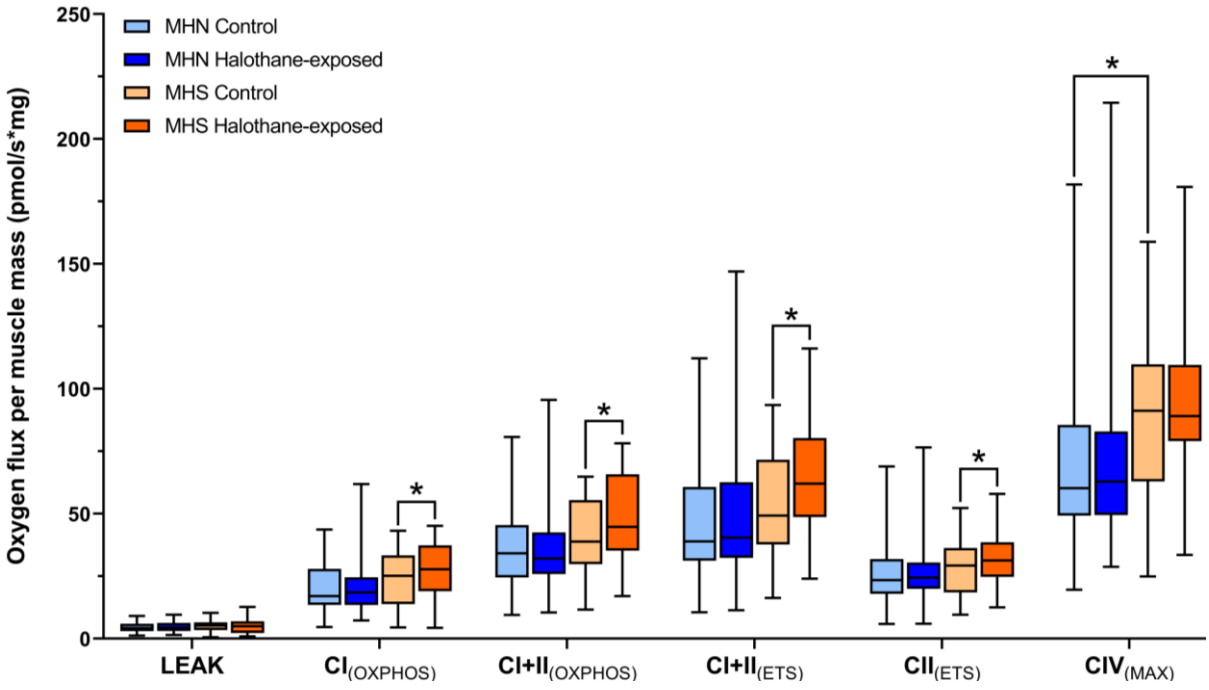

Figure 3.2. High resolution respirometry of permeabilised *vastus medialis* biopsies from MHN and MHS individuals. Boxplots show median, IQR and min-max range for MHN (n= 36) and MHS (n=23) individuals in control and halothane-exposed samples. Statistically significant pairwise comparisons ($p<0.05$) are labelled with an asterisk (refer to table 3.3 for exact p-values).

3.3.3 Flux control ratios (normalised oxygen flux)

Mass-specific oxygen flux was normalised to a common reference state (control $CI+CII_{(ETS)}$) to generate FCR, which provides a measure of mitochondrial function as a proportion of the max ETS capacity. This removes the confounding effects of mitochondrial content differences between samples and gives a more accurate representation of inherent function (Figure 3.3). Comparisons of FCR at baseline revealed that $CI+CII_{(OXPHOS)}$ and $CII_{(ETS)}$ were significantly lower in MHS samples when compared to MHN ($p=0.033$ and 0.005, respectively), suggesting functional deficiency. Normalised $CIV_{(MAX)}$ showed no significant differences between MHS and MHN controls indicating similar functional capacity of complex IV. The pairwise comparisons of FCR between control and halothane-exposed samples support the findings seen in the mass-specific dataset, with statistically significant findings in several of the same respiratory states (Table 3.3). However, one exception was found in MHN $CII_{(ETS)}$ which increased after halothane-exposure ($p=0.041$).

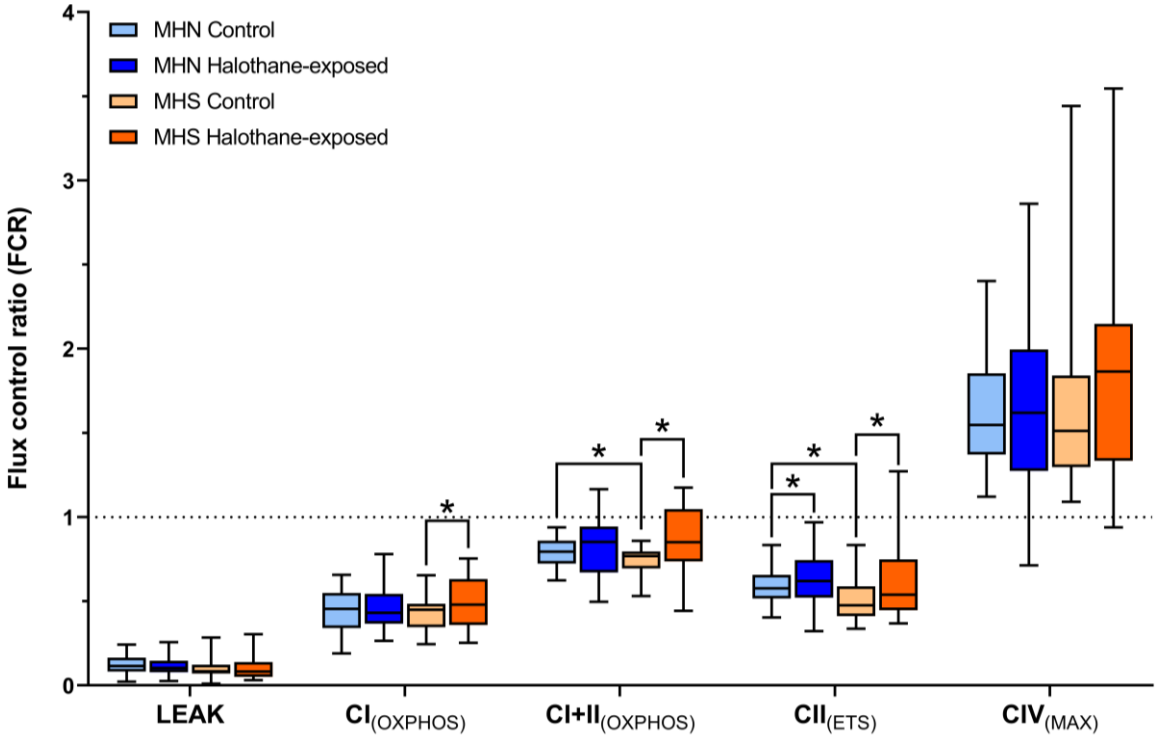

Figure 3.3. Boxplot comparison of flux control ratios from MHN and MHS individuals. FCR are generated by internally normalizing oxygen flux per muscle mass to the non-halothane-exposed control $CI+CII_{(ETS)}$ (indicated by the horizontal dashed line). Boxplots show median, IQR and min-max range for MHN (n=36) and MHS (n=23) individuals in control and halothane-exposed samples. Statistically significant pairwise comparisons ($p<0.05$) are labelled with an asterisk (refer to table 3.3 for exact p-values).

Respiratory State	Oxygen consumption rate (pmol/s*mg)		
	MHN	MHS	MHN vs MHS
	Control vs halothane-exposure (p-value)		Control comparisons (p-value)
LEAK	0.944	0.429	0.732
$CI_{(OXPHOS)}$	0.593	0.012	0.113
$CI+CII_{(OXPHOS)}$	0.789	0.005	0.071
$CI+CII_{(ETS)}$	0.157	0.003	0.05
$CII_{(ETS)}$	0.057	0.001	0.376
$CIV_{(MAX)}$	0.718	0.101	0.021

Respiratory State	Flux control ratio (FCR)		
	MHN	MHS	MHN vs MHS
	Control vs halothane-exposure (p-value)		Control comparisons (p-value)
LEAK	0.753	0.362	0.074
$CI_{(OXPHOS)}$	0.48	0.007	0.534
$CI+CII_{(OXPHOS)}$	0.47	0.003	0.033
$CI+CII_{(ETS)}$			
$CII_{(ETS)}$	0.041	0.001	0.005
$CIV_{(MAX)}$	0.307	0.052	0.913

Table 3.3. Summary of all statistical comparisons for each data set (Human respirometry). An overview of the specific p-values for each pairwise comparison between and within phenotype for the mass-specific oxygen flux (pmol/s*mg) and FCR readings are displayed. The p-values for FCR differences between MHS subgroups are also included with post hoc statistics for each comparison.

3.3.4 FCR changes within subdivided MHS phenotypes

To assess whether halothane effects differed within the MHS sub-phenotypes (MHS_h and MHS_{hc}), FCR data was used for further analysis. Prior to splitting the MHS phenotype into subgroups, the magnitude of change before and after halothane exposure (FCR difference) was calculated and compared between MHN and MHS phenotypes (MHS_h + MHS_{hc}) (Figure 3.4). Mann-Whitney U tests were used to compare FCR differences in six respiratory states and a statistically significant difference was found in $CI+CII_{(OXPHOS)}$ ($p=0.045$) and $CI+CII_{(ETS)}$ ($p=0.03$).

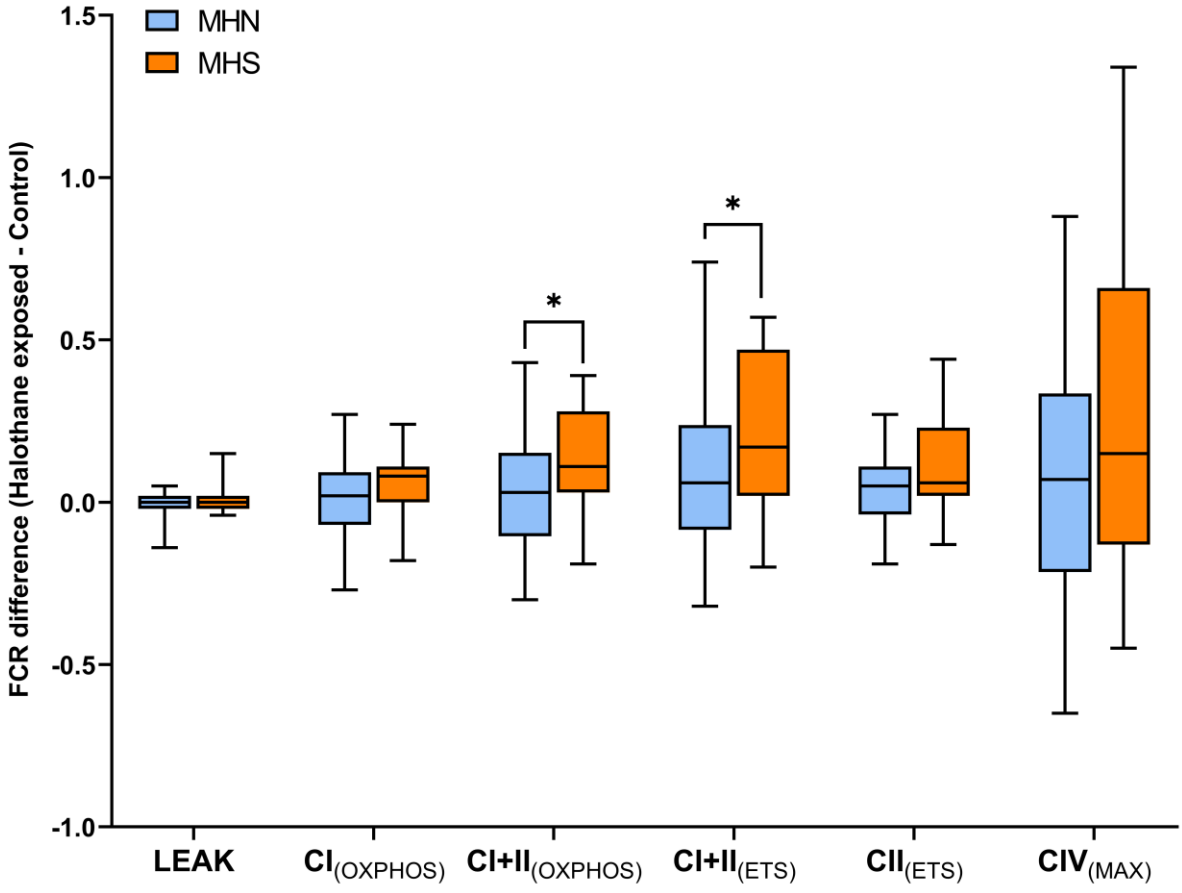

Figure 3.4. Boxplots comparing FCR difference (in response to halothane) between MHN and MHS phenotypes. The magnitude of change in FCRs (before and after IVCT halothane exposure) are compared between MHN (n = 36) and MHS samples (n = 23). Data is displayed as boxplots, which show median, IQR and min-max response range for each phenotype. Comparisons labelled with an asterisk show statistically significant comparisons ($p<0.05$).

Next, FCR differences were calculated and compared between MHN and MHS samples subdivided into MHS_h and MHS_{hc} subgroups (Figure 3.5) – there were no patients in this study categorized as MHS_c. Results from the Kruskal-Wallis test showed that $CI+CII_{(OXPHOS)}$ responses differed significantly between MH phenotypes after halothane exposure ($p=0.043$). Post hoc analysis showed that FCR differences in $CI+CII_{(OXPHOS)}$ were significantly different between MHN and MHS_{hc} phenotypes ($p=0.036$). The differences in response between MHN and MHS groups is largely attributable to responses from the MHS_{hc} subgroup because significant differences in response between the MHN and MHS_h groups were not found.

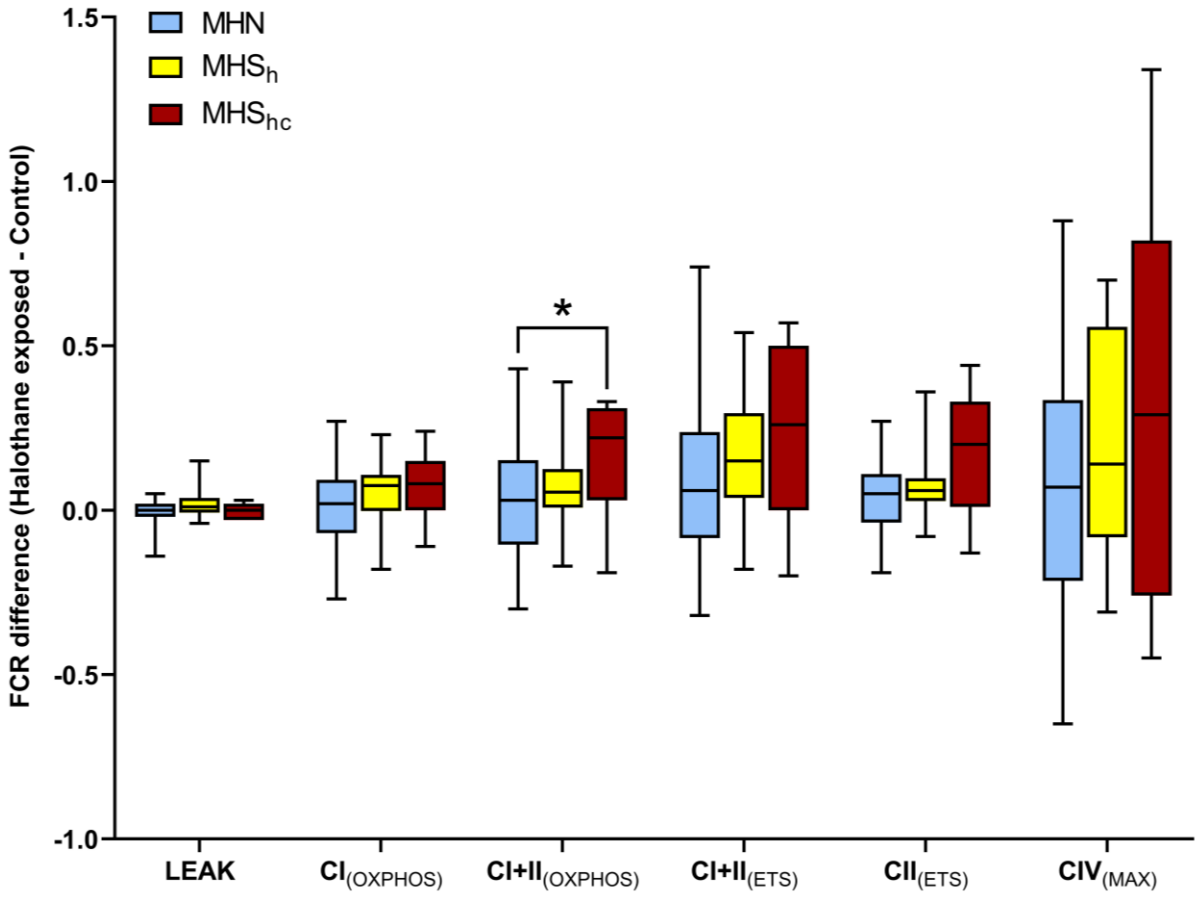

Figure 3.5. Boxplots comparing FCR difference (in response to halothane) between MHN, MHSh and MHShc phenotypes. MHN samples (n = 36) were plotted with MHS samples (n = 23) - further split into MHS_h (n = 12) and MHS_{hc} (n = 11) subgroups. Boxplots show median, IQR and min-max response range for each phenotype. Comparisons labelled with an asterisk show statistically significant post hoc pairwise comparisons ($p<0.05$).

3.4 DISCUSSION

The aim of this study was to provide insight into the relationship between mitochondrial function and MH susceptibility using human skeletal muscle as opposed to MH animal models. Mass-specific oxygen consumption rates (pmol/s*mg) was first compared between MH phenotypes at the baseline level before halothane treatment. This comparison showed that the mass-specific oxygen consumption rates was not significantly different between MHN and MHS samples, aside from the $CIV_{(MAX)}$ state, which was significantly elevated in the MHS phenotype. This observation suggests that there was increased mitochondrial content in the MHS sample population, which was somewhat surprising since other MH studies have reported either no significant difference or the opposite effect in MHS muscle (Lavorato et al., 2016; Boncompagni et al., 2009; Giulivi et al., 2011; Barrientos et al., 2012).

The report by Lavorato et al. observed human MHN and MHS muscle composition using electron microscopy and they reported slightly less mitochondrial content in MHS samples, but this was not found to be statistically significant (Lavorato et al., 2016). Other reports commenting on this feature were based on muscle from the Y522S-RYR1, T4826I-RYR1 and R163C-RYR1 knock-in mouse models, all of which presented evidence of reduced mitochondrial content (Boncompagni et al., 2009; Giulivi et al., 2011; Barrientos et al., 2012). Despite the $CIV_{(MAX)}$ oxygen consumption rates data suggesting increased mitochondrial content in human MHS samples, it is difficult to claim that this observation is representative of the overall MHS population due to the variable nature of human skeletal muscle. Mitochondrial content and OXPHOS capacity in humans can be significantly altered based on muscle fibre type distribution and different types of physical training. The *vastus medialis* biopsies used for IVCT, are a part of the quadriceps muscle group, which typically have a fibre type distribution around ~40% slow-twitch type I and ~60% fast-twitch type II (Staron et al., 2000; Edgerton et al., 1975). Slow-twitch oxidative muscle fibres are rich in mitochondria and can be developed from sustained exercises with increased time under tension. Both variables were not accounted for in this experimental design which in hindsight could be improved by incorporating data from an exercise questionnaire to group individuals into levels of fitness for sub-analysis.

The use of alternative mitochondrial biomarkers such as citrate synthase and mitochondrial DNA (mtDNA) were considered but the complex IV assay was ultimately

chosen for several reasons. The complex IV assay can be easily prepared and applied immediately after the SUIT protocol, which allows an assessment of mitochondrial content on the same exact sample to avoiding issues with sample degradation. Its usage was also supported by the study conducted by Larsen et al. which compared commonly used mitochondrial biomarkers to the gold standard transmission electron microscopy (TEM) (Larsen et al., 2012). The outcome of that study showed that the complex IV assay (TMPD + Ascorbate) had strong correlations with the mitochondrial content measurements made by TEM, serving as a good functional biomarker. This contrasts with their findings comparing mtDNA with TEM, which showed poor correlation between the two assays (Larsen et al., 2012). The use of mtDNA as a marker for mitochondrial content is very common and the lack of correlation observed in that study was surprising. However, there have been reports of mtDNA not increasing significantly after training despite other biomarkers increasing, which seem to support this claim (Menshikova et al., 2005; Pesta et al., 2011). Furthermore, mtDNA copy number can vary considerably between individuals which also adds additional variability to its usage (Wiesner et al., 1992).

To identify functional differences between MHN and MHS mitochondria specifically, mass-specific oxygen consumption rates were normalised against a common respiratory state ($CI+CII_{(ETS)}$) within each sample to generate FCR data, which is corrected for mitochondrial content. Baseline comparison of FCR between phenotypes, showed significantly reduced $CI+CII_{(OXPHOS)}$ and $CII_{(ETS)}$ FCRs in MHS samples - indicating a functional deficit. The reduction of $CI+CII_{(OXPHOS)}$ FCR reflects a lower OXPHOS capacity and implies that there is uncoupling of MHS mitochondria in addition to complex II deficiency (reduced $CII_{(ETS)}$) under normal untriggered conditions. As previously mentioned, MHS individuals do not typically present with a phenotype in the absence of MH triggers, but some individuals in past reports have shown signs of myopathy such as exercise intolerance, weakness and cramping (Timmins et al., 2015; Wappler et al., 2001; Litman et al., 2018). It is possible that the baseline deficiencies detected here in MHS mitochondria are a downstream consequence of RyR dysfunction, which contribute to some of those issues.

A lower OXPHOS capacity and MHS mitochondrial uncoupling likely limits the rate of ATP production and is potentially due to the mitochondrial swelling and structural abnormalities reported in both human (Lavorato et al., 2016; Isaacs and Heffron, 1975) and MH animal models (Durham et al., 2008; Boncompagni et al., 2009; Yuen et al., 2012). The structural damage seen in MHS mitochondria is speculated to be the result of oxidative damage

accumulated over time which is promoted by the chronically elevated $[Ca^{2+}]_{rest}$ present in MHS muscle (Lopez et al., 1985; Lopez et al., 1986; Lopez et al., 2018; Giulivi et al., 2011; Yuen et al., 2012). Studies have shown that mitochondria, Ca^{2+} and ROS interact closely to regulate cellular processes and increases in $[Ca^{2+}]$ is known to stimulate mitochondrial activity which in turn increases the rates of ROS production through the ETS (Gorlach et al., 2015).

The main sites of ROS production in mitochondria are complex I and III but some reports have also shown significant ROS generation at complex II under special circumstances (Guzy et al., 2008; Quinlan et al., 2012; Zorov et al., 2014). Studies on MH RYR1 knock-in mouse models have reported an increase in ROS production and it is possible that this feature also translates into human MHS muscle (Durham et al., 2008; Giulivi et al., 2011). ROS have traditionally been associated with negative consequences (contributing to oxidative stress, pathogenesis and cell death) but research has now shown that ROS also contributes to the regulation of normal physiological processes, at the appropriate concentrations (Barbieri and Sestili, 2012). Oxidative stress in mitochondria is usually regulated by antioxidative mechanisms involving superoxide dismutases (SOD) that act to convert superoxide into H_2O_2, which in turn is further decomposed by glutathione peroxidase (Turrens, 2003). Elevations in mitochondrial ROS and Ca^{2+} have also been shown to trigger the activation of mitochondrial uncoupling proteins and the MPTP, which may account for the mitochondrial uncoupling observed in MHS samples (Mailloux and Harper, 2011; Briston et al., 2017). The inability of antioxidative mechanisms to compensate for increased ROS production can lead to pathogenesis in skeletal muscle and may warrant further research in the context of MH.

With regards to complex-specific deficiency, the lack of difference observed in complex I between MH phenotypes at baseline indicates that complex II is the major component responsible for the reduced OXPHOS capacity observed in MHS muscle. Complex II, also known as succinate dehydrogenase, is encoded entirely by nuclear genes and functions in both OXPHOS and the Kreb's cycle (Bezawork-Geleta et al., 2017). There has not been any previous literature connecting complex II involvement with MH susceptibility and this is the first study to provide evidence of its deficiency in MHS muscle. Collectively these findings suggest a potential compensation mechanism, in which human MHS muscle upregulates mitochondrial numbers to counteract deficiencies in mitochondrial function, hence similar baseline oxygen flux per unit of muscle mass.

Literature surrounding mitochondrial function in MH is conflicting, but the overall concept of mitochondrial deficiency in MHS muscle is supported by several other studies having also shown functional deficiencies (Gronert and Heffron, 1979; Barrientos et al., 2012; Yuen et al., 2012; Rouviere et al., 2012; Thompson et al., 2017). One study of interest was the recent publication by Thompson et al. who also studied MH in humans. In this study they reported significant reductions in aerobic and anaerobic capacity in MHS individuals after bouts of exercise which they suspect is the reason for MHS-related exercise intolerance (Thompson et al., 2017). Despite evidence of OXPHOS deficiency being reported across multiple studies, some of the features detailed in our human study conflict with the those generated using the MH mouse models.

One example of this comparison is the Giulivi et al. study using R163C-RYR1 knock-in mice (Giulivi et al., 2011). R163C-RYR1 knock-in mice were shown to have reduced mitochondrial content, reduced oxygen uptake using malate-glutamate and succinate, in addition to reduced complex I, III and IV activity when compared to wild-type mice (Giulivi et al., 2011). These aspects conflict with the data from this present human study on several accounts, having shown evidence suggesting higher mitochondrial content, deficiency in succinate-facilitated oxygen flux and deficiency in only complex II. These conflicting observations may reflect a combination of interspecies variation between human and mice, and technical differences in methodology.

The present study utilised permeabilised muscle fibres extracted from the *vastus medialis* whilst Giulivi et al. used isolated mitochondria in their assessment of mitochondrial function and content. A limitation of using isolated mitochondria is that it does not allow interaction between organelles within the cell. Studies have identified tethers between mitochondria and the SR creating close contact sites called mitochondria-associated membranes (MAMs) (Eisner et al., 2013). The passive Ca^{2+} leak from mutant RYR1 in MHS muscle would expose mitochondrial subpopulations to higher concentrations of Ca^{2+} which may alter mitochondrial Ca^{2+} intake through MCU channels. This interaction can be important for the accurate reflection of mitochondrial function in MH since its pathology is caused by Ca^{2+} dysregulation. The use of muscle fibres permeabilised with saponin is advantageous in this regard, as it allows the assessment of mitochondrial function with cellular components intact and maintains the crosstalk ability between organelles (Saks et al., 1998).

In addition to sample type, another significant difference in protocol is the temperature used between studies. The oxygen uptake assay in the Giulivi et al. mouse study was conducted at 22 °C, whereas this present study was performed at 37 °C (Giulivi et al., 2011). A study by Lemieux et al. used high resolution respirometry to assess mitochondrial respiratory control across a temperature range (4 °C - 40 °C) using permeabilised mouse myocardial fibres and showed significant alterations in OXPHOS capacity at different temperatures (Lemieux et al., 2017). This factor, together with sample type and interspecies variation, can change mitochondrial bioenergetics and should be taken into consideration before drawing comparisons.

Following baseline observations, the effect of halothane on mitochondrial function was assessed by analysing oxygen consumption rates and FCR data before and after halothane exposure between phenotypes. Results showed that halothane exposure triggered an increase in oxygen consumption in the MHS phenotype – indicative of a hypermetabolic response. This response to halothane is thought to be due to an increase in Ca^{2+} uptake in MHS mitochondria following Ca^{2+} efflux from the SR, through activated RyR1 channels. Increases in mitochondrial [Ca^{2+}] is known upregulate oxidative metabolism by stimulating dehydrogenase enzymes, increasing the rates of NADH and ATP production (Griffiths and Rutter, 2009; McCormack and Denton, 1979; Denton, 2009). An overload of Ca^{2+} in mitochondria is known to induce the opening of the MPTP and activate apoptotic mechanisms - a potential cause of the rhabdomyolysis and cell death which occur in a fulminant MH reaction. In contrast, MHN samples were largely unaltered by halothane exposure, aside from the $CII_{(ETS)}$ FCR result which was also elevated. This increase in $CII_{(ETS)}$ was unexpected but suggests that there is a non-RyR1 mediated halothane effect on mitochondria.

Several reports studying the effects of halothane have noted an interaction which causes the inhibition of complex I activity in mitochondria. In the context of MH, complex I activity was shown to be reduced by halothane exposure in MHS swine (Britt et al., 1975; Gronert and Heffron, 1979), but this effect was also demonstrated in research outside of MH, showing that the two traits are not dependent. Hanley et al. studied the effects of anaesthetics on porcine heart mitochondria and demonstrated reversible dose-dependent inhibition of complex I after exposure to isoflurane, sevoflurane, and halothane – the latter of which had the strongest effect (Hanley et al., 2002). This observation was supported by research on the complex I mutant *gas-1 C.elegans* model which also presented with evidence of decreased complex I function and increased sensitivity to inhalation anaesthetics (Falk et al., 2006; Kayser et al., 2004).

Surprisingly, this halothane-induced complex I inhibition was also not observed in this study in either phenotype. This disparity may be due differences in methodology, as previously explained, in addition to the limitations in this protocol. In this present study, there was a time delay between halothane exposure and oxygen consumption measurements (~90 - 120 minutes) due to sample preparation and transport. Since the halothane-induced complex I inhibition is reversible (Hanley et al., 2002), it is possible that complex I function was given enough time to recover before the assay was conducted.

The magnitude of FCR change, before and after halothane exposure, was compared between MH phenotypes and the maximum OXPHOS ($CI+CII_{(OXPHOS)}$) and ETS ($CI+CII_{(ETS)}$) capacities were significantly upregulated in MHS samples. Within this dataset, sub-analysis of the MHS phenotype was performed to identify any differences between MHS_h and MHS_{hc} samples. There was a significant difference in maximum OXPHOS capacity between MHS_{hc} and MHN phenotypes, but this was absent in MHS_h comparisons, indicating a heightened sensitivity in MHS_{hc} samples. This was not surprising as the MHS_{hc} classification has been associated with stronger phenotypes based on IVCT contracture data (Robinson et al., 2002) and this was supported by the results of this present study. The MHS_h classification in contrast is often associated with weaker phenotypes and the FCR changes were coincidently not significantly different from MHN responses after halothane exposure.

The only study which has reported a conflicting pattern in MHS_h and MHS_{hc} responses was a recent study on Canadian MHS individuals which identified a higher index of calcium-related changes in muscle cells cultured from MHS_h individuals in comparison to MHS_{hc} (Figueroa et al., 2019). This discrepancy might be explained by their use of cultured myotubes as opposed to the adult muscle fibres used in this present study. The reason behind why some MHS individuals have increased sensitivity to caffeine is unknown and the differences between MHS_h and MHS_{hc} skeletal muscle is unclear from a physiological viewpoint. The RyR1 architecture is known to have a putative binding site for caffeine next to the Ca^{2+} binding site in the central domain (des Georges et al., 2016). Caffeine is a potent activator of RyR1, and its binding causes a conformational change which significantly increases RyR1 sensitivity to Ca^{2+} activation (Murayama et al., 2018). One possible explanation may be that certain MH-associated *RYR1* mutations interfere with the caffeine binding sites on RyR1 which consequently raises its affinity and sensitivity to caffeine.

Despite identifying differences in mitochondrial function after halothane exposure, a potential confounding factor needs to be taken into consideration when interpreting results. The issue stems from the method of halothane administration through the IVCT, which is a complex test encompassing several other interventions. Samples that undergo IVCT are held at an approximate physiological length and tension before being electrically stimulated prior to halothane exposure. This adjustment of sample length and exposure to electric stimulus were not applied to the baseline control samples due to limitations of the IVCT rig not allowing multiple tests to occur simultaneously. Ideally the experiment could have been improved by applying these additional treatments to all baseline samples in the absence of halothane to rule out any effects not related to halothane exposure. Alternatively, it may have been possible to avoid all IVCT-related confounding factors if halothane were applied directly into the respirometry chambers by dissolving it into a solvent.

In conclusion, the results from this study have demonstrated evidence of impaired mitochondrial function in permeabilised human MHS skeletal muscle at baseline. These findings may be a contributor towards some of the myopathic symptoms (exercise intolerance, cramping, weakness) reported by MHS individuals in absence of MH triggering agents. This feature is believed to be a downstream consequence of oxidative stress facilitated by the chronic elevation of cytoplasmic Ca^{2+} described in MHS muscle. Furthermore, exposure to 2 Vol% halothane also significantly increased OXPHOS and ETS capacity in MHS muscle which is indicative of a hypermetabolic response associated with the MH phenotype.

4 DIFFERENTIAL GENE EXPRESSION BETWEEN WILD-TYPE AND RYR1 KNOCK-IN MICE

4.1 INTRODUCTION

Many studies on MH have adopted the use of RYR1 knock-in mouse models which offer several advantages with regards to experimental design. Firstly, skeletal muscle is easily attainable from knock-in mice as they can be captive bred for experimentation. This breeding process can control for genetic variability and other factors which significantly alter muscle function, such as muscle fibre distribution and muscle mass which vary considerably in humans due to lifestyle. Other advantages of using mouse models include a greater degree of control over variables such as age and sex, which can be investigated within experimental designs. In the last two decades, four RYR1 knock-in mouse models have been developed based on variants of interest (Y522S-RYR1, R163C-RYR1, T4826I-RYR1, G2435R-RYR1), to further our understanding of MH pathophysiology (Chelu et al., 2006; Yang et al., 2006; Yuen et al., 2012; Lopez et al., 2018). *Ryr1* variants associated with MH, can occur across all regions of the gene but research in knock-in mouse models of MH has focussed on variants within the N-terminal, C-terminal and central regions of the RYR1 protein (Lopez et al., 2018).

The first murine model of MH developed was the Y522S-RYR1, corresponding to an *Ryr1* mutation of tyrosine to serine at position 522 of N-terminal region (Chelu et al., 2006). This mutation was identified in three individuals of a French family, following the death of a proband due to an MH crisis (Quane et al., 1994). Functional characterisation of this model showed Y522S-RYR1 HET mice to have increased sensitivity to temperature, voltage, and caffeine exposure, resulting in rhabdomyolysis and temperature-induced death (Chelu et al., 2006). A mild bleeding phenotype was also observed in Y522S-RYR1 HET mice, with bleeding scores two-three times greater than wild-type (WT) mice, attributed to alterations in smooth muscle Ca^{2+} homeostasis (Lopez et al., 2016). Additional phenotypic traits include a range of mitochondrial defects with regards to damage, structure and oxidative/nitrosative stress - to be explored further in chapter 5 (Durham et al., 2008; Boncompagni et al., 2009; Michelucci et al., 2017; Canato et al., 2019).

The second murine model of MH (R163C-RYR1) was reported in the same year, carrying another mutation found in the N-terminal region of RYR1 (Yang et al., 2006). The

R163C-RYR1 HET mice were found to undergo fulminant MH reactions in response to halothane and high ambient temperatures. Characterised by increased rectal temperatures, increased respiratory rate, metabolic acidosis, and acute rigor mortis upon death (Yang et al., 2006). Whole cell patch clamp studies found that DHPR channel activity was also altered due to the R163C-RYR1 variant, and this was speculated to contribute towards MH episodes (Bannister et al., 2010). Cultured myotubes from this model demonstrated several aspects of Ca^{2+} dysregulation featuring elevated intracellular Ca^{2+} (Feng et al., 2011; Yang et al., 2006), enhanced Ca^{2+} entry rates (Cherednichenko et al., 2008) and slower decay of Ca^{2+} transients in response to membrane depolarisation (Esteve et al., 2010). Furthermore, mitochondrial defects were also observed in R163C-RYR1 mice with reduced OXPHOS and increased oxidative stress, similar to that seen in the Y522S-RYR1 model (Giulivi et al., 2011; Durham et al., 2008).

In contrast to the first two knock-in murine models, the third RYR1-knock in mouse model (T4826I-RYR1) was developed carrying a variant in C-terminal region of RYR1 (Yuen et al., 2012). This mutation resides between the S4-S5 cytoplasmic linker of RYR1 and was associated with MH after being first described in a New Zealand Maori pedigree (Brown et al., 2000). Both heterozygous (HET) and homozygous (HOM) mice with this mutation were fully viable, whilst HOM mice from the first two models showed developmental defects and did not survive past the embryonic stage (Yuen et al., 2012; Chelu et al., 2006; Yang et al., 2006). Consistent with the other MH mouse models, T4826I-RYR1 mice have elevated intracellular Ca^{2+}, evidence of mitochondrial defect and fulminant MH reactions in response to high temperatures and anaesthetic treatment (Barrientos et al., 2012; Yuen et al., 2012). Interestingly, mice with this mutation also exhibit a gene-dose and sex-dependent susceptibility to MH, which may be a feature of *Ryr1* variants within the C-terminal region (Yuen et al., 2012).

Among the several hundred human *RYR1* mutations associated with MH, the missense point mutation c.7300G>A on exon 44, is the most common cause of human MH within the UK (Carpenter et al., 2009b; Miller et al., 2018; Robinson et al., 2002). This mutation causes a p.Gly2434Arg amino acid change and resides in the central region of RYR1. It is present in approximately 16% of MHS families in the UK and despite its prevalence, is associated with a weak clinical phenotype based off IVCT contracture data (Carpenter et al., 2009b; Miller et al., 2018). Due to its significance in the UK MHS population, a fourth RYR1 knock-in mouse model (G2435R-RYR1) equivalent to the human *RYR1* c.7300G>A mutation was created,

representing the only MH mouse model with a variant in central region (Lopez et al., 2018). Consistent with previously reported RYR1 knock-in mice models, G2435R-RYR1 HET and HOM mice were functionally characterised showing elevated $[Ca^{2+}]_{rest}$ and increased sensitivity to caffeine, halothane, and elevated ambient temperatures (Lopez et al., 2018). These features have a gene-dose dependent effect reflected by the differences in $[Ca^{2+}]_{rest}$ (mean (SD): HET-156nM (16), HOM-265nM (32)), death times for halothane-induced (mean: HET–65.2 minutes, HOM-18 minutes) and temperature-induced MH reactions (mean: HET-68.6 minutes, HOM-17.9 minutes) (Lopez et al., 2018).

To date there has not been an in-depth report on the gene expression profiles for any of these RYR1 knock-in mouse models. This information may help explain the functional variation observed in MH phenotypes and provide insight into how different *Ryr1* variants affect skeletal muscle function. This chapter presents the first study of transcriptomic changes in the skeletal muscle of G2435R-RYR1 mice both under baseline conditions and after treatment with halothane. This will be achieved using RNAseq and bioinformatic resources to functionally categorise gene sets. The use of this mouse model allowed more control over experimental design which accounts for some of the limitations (age, treatment, fibre composition) previously described in the human RNAseq experiment (Chapter 2). In addition, T4826I-RYR1 HET mice were also included in this study to see how gene expression differs between these two mouse models.

This chapter aims to address the following research questions:

- What genes are differentially expressed between WT, G2435R-RYR1 and T4826I-RYR1 knock-in mice at baseline?
- How does halothane exposure alter gene expression in WT, G2435R-RYR1 and T4826I-RYR1 knock-in mice?
- Which biological functions and pathways are enriched at baseline and in response to halothane exposure?

4.2 METHODS

4.2.1 Animals

All RYR1 knock-in mice were housed in pathogen-free conditions with free access to food, water, and 12-hour light-and-dark cycles. All mice used for transcriptomics were eight weeks of age and experiments were undertaken with UK Home Office approval (Licence number PB2FB5E94).

4.2.2 RNAseq experimental design

A total of 12 mice were selected for sequencing comprised of four genotypes: WT, G2435R-RYR1 HET, G2435R-RYR1 HOM and T4826I-RYR1 HET. All RYR1 knock-in mice (n=3 of each genotype) were eight weeks of age and male. The purpose of this experiment was to explore differential gene expression between the different RYR1 knock-in mouse genotypes both at baseline and after exposure to halothane. Paired samples were collected from each mouse (before and after halothane exposure) and all WT mice used in next generation sequencing were created within the G2435R-RYR1 colony through HET x HET breeding.

4.2.3 Preparation of samples for RNA sequencing

RYR1 knock-in mice were killed by cervical dislocation before both hind limbs were removed from each mouse and dissected to expose the *Soleus* muscles on the surface. One limb was designated as the baseline sample (without halothane exposure) and the other limb was designated as the halothane-treated sample. The baseline samples for each genotype were kept suspended in oxygenated Krebs-Ringer solution for 30 minutes at 37 ^{o}C before *Soleus* muscles were removed from the limb and transferred into RNAlater (INVITROGEN) at -80 ^{o}C until further processing.

Halothane-treated samples were given the same treatment, with the addition of 2 Vol% halothane perfused into the Krebs-Ringer solution for 30 minutes at 37 ^{o}C. Both baseline and halothane-treated *Soleus* muscles were homogenised in 1 ml TRIzol© using an IKA T-10 basic

ULTRA-TURRAX® homogeniser before RNA was extracted using a chloroform/isopropanol extraction method (described in chapter 2, section 2.2.3), followed by an RNA clean up step using the RNAeasy microkit (QIAGEN) with on-column DNase treatment, according to manufacturer's instructions. Quality assessment of RNA samples was performed on the Agilent 4200 Tapestation (described in chapter 2, section 2.2.4) and samples with integrity scores of RIN^e >7.0 were considered acceptable for sequencing.

4.2.4 Truseq® Stranded mRNA library preparation

PolyA selected mRNA libraries were created from the isolated RNA by the Next Generation Sequencing Facility at St James's University Hospital, Leeds. RNA samples were first quantified using the Qubit™ RNA BR Assay Kit (Invitrogen™), before being used to create libraries using the Truseq Stranded mRNA library preparation kit (Illumina®), according to manufacturer's guidelines. All cDNA libraries were quality checked and quantified by Ms Catherine Daly (Laboratory Manager of the MH Unit) using the Agilent D1000 screentape and the Quant-iT™ PicoGreen® dsDNA assay.

4.2.5 Illumina® HiSeq® NGS

A total of 24 mRNA-enriched libraries (12 before and 12 after halothane exposure) were indexed and compiled into a single pool at equimolar concentrations. This library pool was then distributed across two HiSeq 3000 150-bp paired-end lanes, achieving an average of 25M reads per sample. A forward and reverse FASTQ file was generated for each sample on each lane. Further details on the sequencing technology can be found in chapter 2, section 2.2.8.

4.2.6 Differential gene expression analysis

Raw sequencing data (FASTQ files) were initially processed using the Medical Advanced Research Computer (MARC1) - a high-performance computer cluster at the University of Leeds. The FASTQ files for each technical replicate across HiSeq lanes were combined and

trimmed using “Cutadapt” to remove adapters and bad quality base calls (<10) (Martin, 2011). Quality assessment before and after trimming was performed using FastQC (https://www.bioinformatics.babraham.ac.uk/projects/fastqc/) (Cock et al., 2010). All samples were aligned a reference genome (GRCm38.p6) using the STAR aligner and quantified using featureCounts (Dobin et al., 2013; Liao et al., 2014). Processed sequencing data was then imported into RStudio and analysed using the DESeq2 package for differential gene expression (RStudio Team, 2015; Love et al., 2014). DESeq2 generates gene lists with p-values adjusted for multiple testing using the BH adjustment (Benjamini and Hochberg, 1995). The default setting in DESeq2 uses a cut-off of padj <0.1 for differentially expressed genes, but in this study, a more stringent cut-off of padj <0.05 was used to classify statistically significant findings. Visualisations of data through MA plots, PCA plots and heatmaps were created using the R package “ggplot2” (Wickham, 2016).

4.2.7 Pathway and gene ontology

Differentially expressed gene lists generated from DESeq2 were functionally characterised using the online enrichment analysis tool Enrichr (Chen et al., 2013; Kuleshov et al., 2016). Enrichr calculates enrichment scores using statistics based off the Fisher’s exact test, used to assess the significance of overlap between inputted gene lists and the chosen gene-set library (Chen et al., 2013). Gene lists were initially examined for enriched pathway terms by comparing the genes to 176 pathway terms in the “WikiPathways_2019_Mouse” database with a gene coverage of 4558 genes. Bar chart visualisation of pathway enrichment analysis was produced through the Enrichr webtool and modified. Pathway map visualisation was generated through MetaCore™ from Thomson Reuters.

Further enrichment analysis of GO terms involved comparing gene sets to the following gene-set libraries from Enrichr:

“GO_Biological_Process_2018” (5103 terms, 14433 gene coverage),
“GO_Molecular_Function_2018” (1151 terms, 11459 gene coverage),
“GO_Cellular_Component_2018” (446 terms, 8655 gene coverage).

4.3 RESULTS

4.3.1 Differential gene expression at baseline

The transcriptome profiles from each RYR1 knock-in mouse genotype was compared to WT to identify genes differentially expressed at baseline (Adjusted p-value <0.05). The WT vs G2435R-RYR1 HET comparison showed only one gene, *Blvrb* (log2FC 0.88), upregulated in G2435R-RYR1 HET muscle. In contrast, a much larger set of 393 genes were differentially expressed in the WT vs G2435R-RYR1 HOM comparison with 98 genes upregulated (0.19 to 1.47 log2FC) and 295 downregulated (-0.16 to -7.14 log2FC) in G2435R-RYR1 HOM. Likewise, the WT vs T4826I-RYR1 HET comparisons featured 206 differentially expressed genes with 82 upregulated (0.24 to 6.96 log2FC) and 124 downregulated (-0.16 to -5.06 log2FC) in T4826I-RYR1 HET. These three gene sets were cross compared on a Venn diagram to identify genes in common (Figure 4.1).

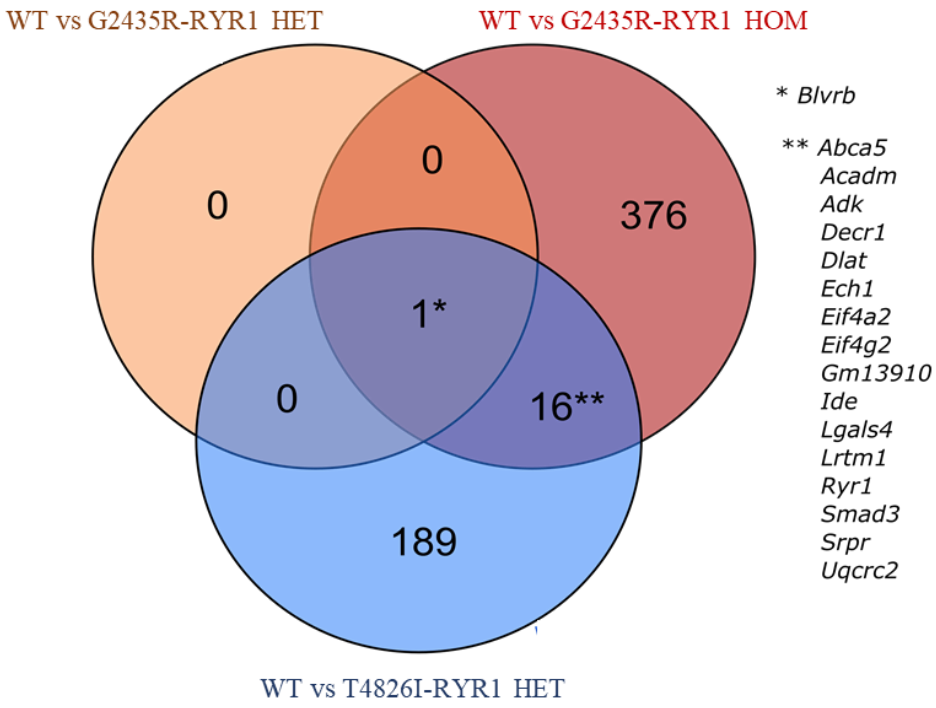

Figure 4.1. Cross comparison of differential gene expression between RYR1 knock-in mice at baseline. The WT vs G2435R-RYR1 HET (1 gene, orange), WT vs G2435R-RYR1 HOM (393 genes, red) and WT vs T4826I-RYR1 HET (206 genes, blue) gene sets were compared and overlapping genes are highlighted with an asterisk.

Only *Blvrb* was found differentially expressed (upregulated) in all three WT vs RYR1 knock-in comparisons, whilst 16 genes were exclusively shared between the WT vs G2435-RYR1 HOM and WT vs T4826I-RYR1 HET gene sets (Figure 4.1). The expression levels of these 16 genes in both RYR1 knock-in genotypes followed the same directionality in comparison to WT, aside from *Ide* which was upregulated in T4826I-RYR1 HETs (0.59 log2FC) and downregulated in G2435R-RYR1 HOMs (-0.31 log2FC). Within this short list of genes, another noteworthy finding was the gene expression of *Ryr1* which was significantly reduced in both G2435R-RYR1 HOM (-0.78 log2FC) and T4826I-RYR1 HET (-0.93 log2FC) mice in comparison to WT (Table 4.1).

	G2435R-RYR1 HET		**G2435R-RYR1 HOM**		**T4826I-RYR1 HET**	
Gene	Log2FC	padj	Log2FC	padj	Log2FC	padj
Abca5			-0.35	1.97E-02	-0.50	8.00E-05
Acadm			-0.30	6.43E-03	-0.27	3.01E-02
Adk			-0.25	3.98E-02	-0.35	1.63E-03
Blvrb	0.88	3.91E-03	1.47	2.82E-15	0.87	8.63E-05
Decr1			-0.33	1.41E-02	-0.31	3.69E-02
Dlat			-0.27	9.87E-03	-0.24	4.77E-02
Ech1			-0.87	1.50E-13	-0.46	1.36E-03
Eif4a2			-0.16	1.46E-02	-0.16	1.68E-02
Eif4g2			-0.17	6.66E-03	-0.16	2.67E-02
Gm13910			-0.42	1.12E-03	-0.37	7.69E-03
Ide			-0.31	3.33E-02	0.59	1.08E-07
Lgals4			-1.58	2.09E-09	-0.88	6.02E-03
Lrtm1			-0.45	2.57E-02	-0.60	1.22E-03
Ryr1			-0.78	5.28E-08	-0.93	7.20E-13
Smad3			-0.40	1.41E-02	-0.37	4.98E-02
Srpr			-0.28	1.44E-02	-0.29	1.57E-02
Uqcrc2			-0.22	1.51E-02	-0.22	2.07E-02

Table 4.1. A summary of all data associated with differentially expressed genes found in common across multiple RYR1 knock-in genotypes. Genes of interest are displayed in alphabetical order and the directionality of change in comparison to WT mice is represented by log2FC values (negative = downregulated, positive = upregulated) alongside their respective adjusted p-values (padj).

4.3.2 MA plots

Global gene expression differences at baseline were visualised using MA plots which display the comparisons between G2435R-RYR1 HET, HOM and T4826I-RYR1 HET mice against WT mice (Figure 4.2). MA plots present gene expression changes between two conditions as two-dimensional scatter plots in terms of log2FC (M) on the y-axis and the mean of normalised gene expression counts (A) on the x-axis. The MA plot for G2435R-RYR1 HETs against WT show very little difference between genotypes as only one gene was differentially expressed. In contrast, both the plots for G2435R-RYR1 HOM and T4826I-RYR1 HETs against WT show many differentially expressed genes (adjusted p-value <0.05) but the gene expression in T4826I-RYR1 HETs appear more spread out along the y axis indicating greater range in effect sizes overall.

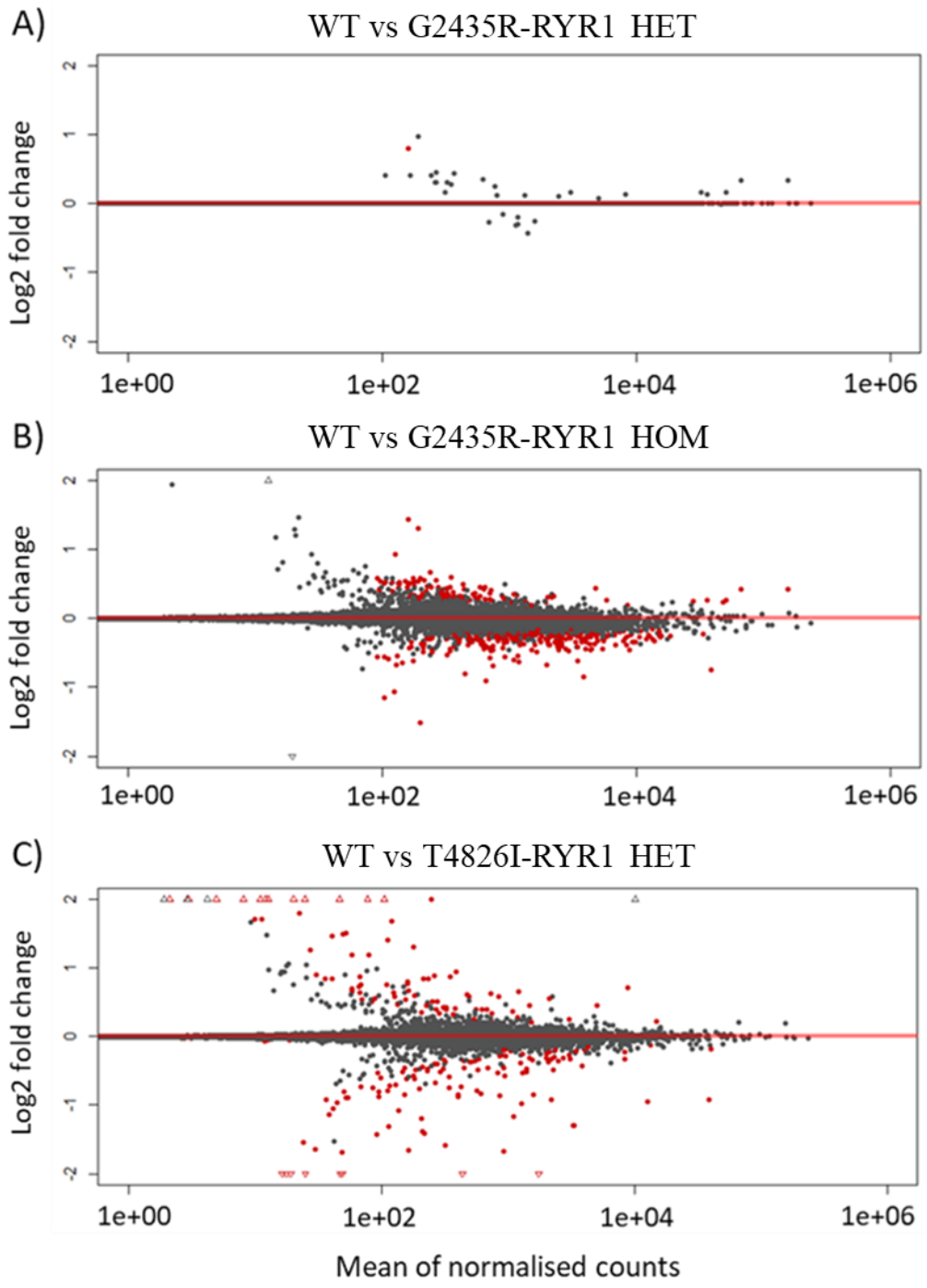

Figure 4.2. MA plots visualising global gene expression changes between RYR1 knock-in mouse genotypes. The log2FC were shrunken (Zhu et al., 2019) to remove the noise associated with log2FC from low count genes. These shrunken log2FC (y-axis) are plot against mean of normalised gene expression counts (x-axis). Plots **A)**, **B)** and **C)** reflect the global gene expression changes in the WT vs G2435R-RYR1 HET, WT vs G2435R-RYR1 HOM and WT vs T4826I-RYR1 HET comparisons, respectively. Genes which are differentially expressed adjusted p-value < 0.05 are highlighted in red. The triangles indicate genes which are expressed at a log2 fold change that exceeds the y-axis limits.

4.3.3 Pathway enrichment analysis

The lists of differentially expressed genes (adjusted p-value < 0.05) from the WT vs G2435R-RYR1 HOM and WT vs T4826I-RYR1 HET comparisons were divided into up/downregulated subgroups and used as inputs for pathway enrichment analysis through Enrichr. The WT vs G2435R-RYR1 HET comparison was not used as there was only one differentially expressed gene. The top 10 upregulated pathways output for WT vs G2435R-RYR1 HOM only contained one statistically significant term (adjusted p-value < 0.05) 'MAPK signalling pathway WP493' upregulated in G2435R-RYR1 HOM muscle (see Appendix 12). Likewise, there was also a lack of observations in the WT vs T4826I-RYR1 HET comparison, which had no significantly upregulated pathways (see Appendix 13).

In contrast, many downregulated genes in the WT vs G2435R-RYR1 HOM comparison were successfully grouped, featuring seven significantly enriched pathway terms, all of which were related to cellular energy production (Figure 4.3). In particular, the top four downregulated pathways: 'Fatty Acid Beta Oxidation WP1269', 'Mitochondrial LC-Fatty Acid Beta-Oxidation WP401', 'Fatty Acid Biosynthesis WP336' and 'Fatty acid oxidation WP2318' were all involved with fatty acid oxidation. Likewise, a similar feature was also found in the WT vs T4826I-RYR1 HET comparison. The top three significantly downregulated pathways were all related to fatty acid oxidation, but only 'Fatty acid oxidation WP2318' was statistically significant (Figure 4.3).

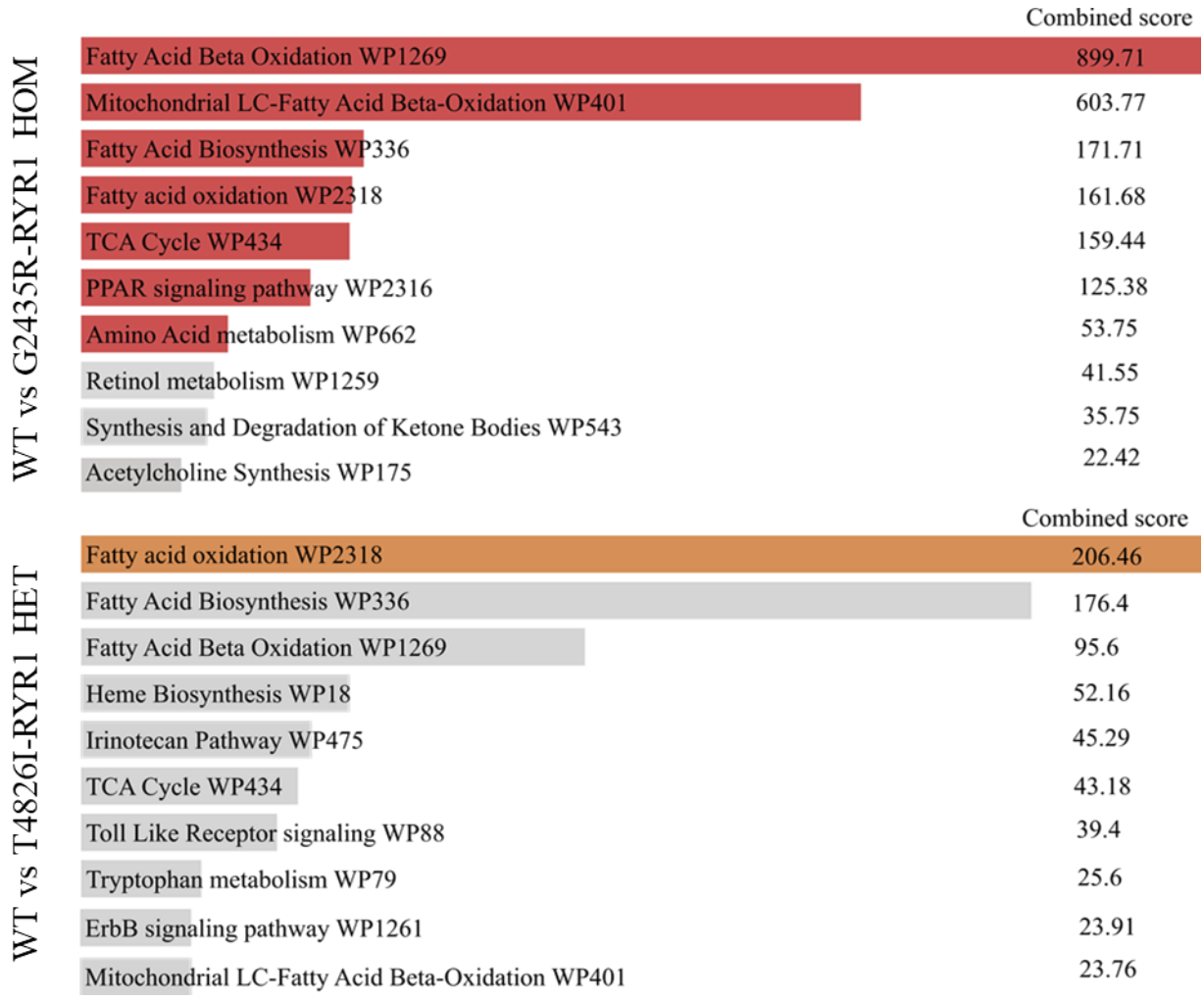

Figure 4.3. Bar chart visualisation of pathway analysis generated by Enrichr. The top 10 downregulated pathways are shown for the WT vs G2435R-RYR1 HOM (red) and WT vs T4826I-RYR1 HET (orange) comparisons, in combined score order (log of p-value from Fisher's exact test multiplied by z score of deviation from expected rank). Significantly downregulated genes generated from DESeq2 analysis were used as input. Coloured bars represent statistically significant terms (adjusted p-value < 0.05).

Following pathway enrichment analysis, a fatty acid β-oxidation pathway map was then created to visualise the genes found downregulated in both G2435R-RYR1 HOM and T4826I-RYR1 HET genotypes (Figure 4.4).

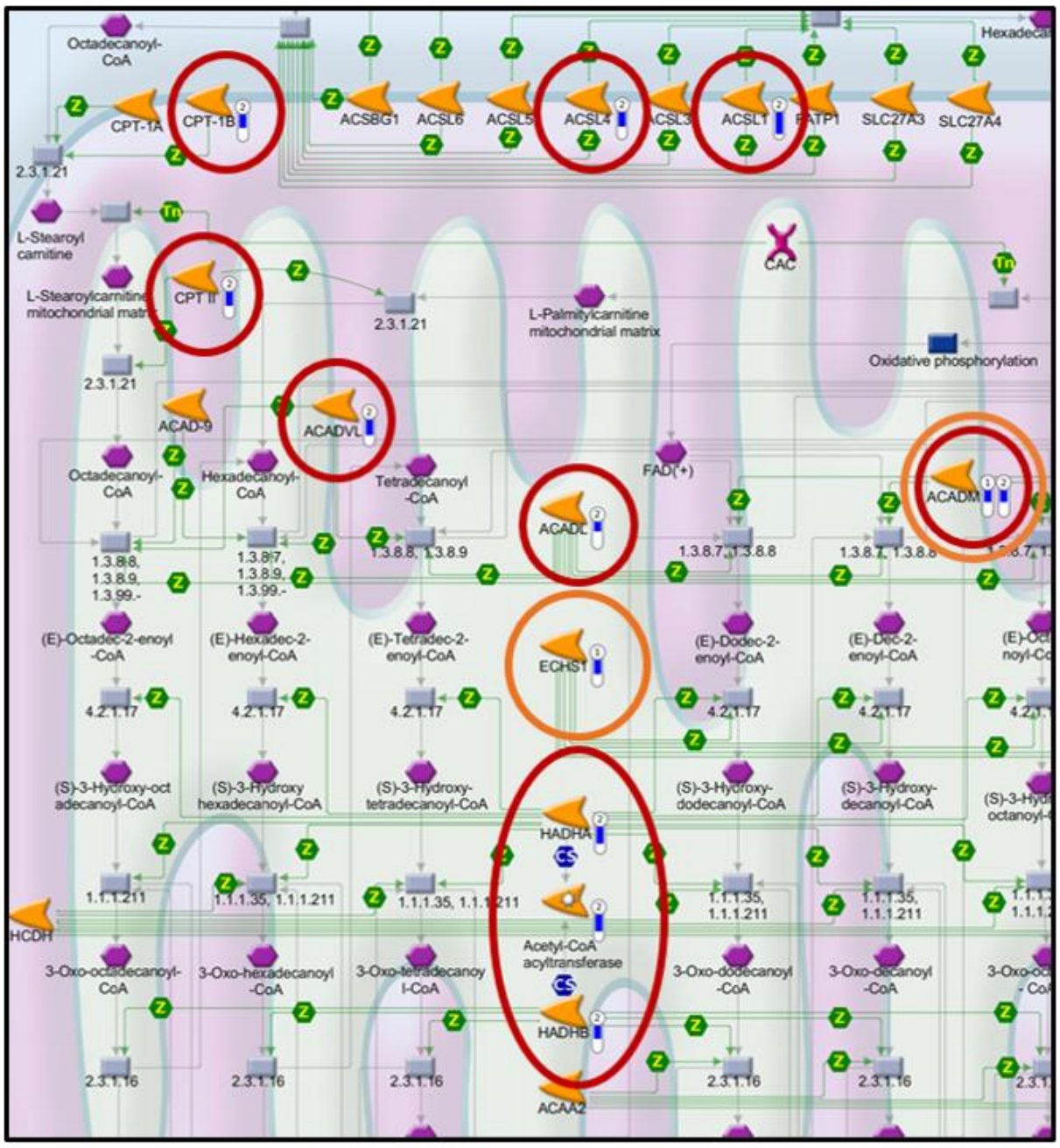

Figure 4.4. Schematic diagram of the mitochondrial fatty acid β-oxidation pathway. This diagram was generated using MetaCore™ and provides an overview of the proteins involved with fatty acid β-oxidation within mitochondria. Proteins encoded by genes found under the pathway term 'Mitochondrial LC-Fatty Acid Beta-Oxidation WP401' by Enrichr are highlighted by coloured circles (red = downregulated in G2435R-RYR1 HOM, orange = downregulated in T4826I-RYR1 HET).

4.3.4 Gene ontology analysis

Up and downregulated genes (adjusted p-value < 0.05) were functionally grouped based on biological processes, molecular function, and cellular component ontology terms. Most of the statistically significant observations came from using the downregulated gene set in the WT vs G2435R-RYR1 HOM comparison. The top 10 downregulated biological processes in G2435R-RYR1 HOM mice were all involved in either fatty acid oxidation or fatty acid transport into mitochondria (Table 4.1) and only one molecular function term 'Acetyl-CoA C-acyltransferase activity (GO:0003988)' was significantly downregulated.

Many genes encoding proteins localised in the mitochondria also appear to be downregulated in G2435R-RYR1 HOM, as 'Mitochondrion (GO:0005739)', 'Mitochondrial matrix (GO:0005759)' and 'Mitochondrial inner membrane (GO:0005743)' were among the top three enriched cellular component terms. The 'Mitochondrion (GO:0005739)' contained the highest number of differentially expressed genes, including some genes of interest '*Ndufs1*', '*Ndufs2*', '*Sdha*' and '*Uqcrc2*' which encode for mitochondrial complexes I, II and III of the electron transport chain (Table 4.1). Analysis of upregulated genes for the WT vs G2435R-RYR1 HOM comparison showed no significant enrichment of biological process or molecular function terms, and the only statistically significant finding was in the cellular component terms: 'Cytoskeleton (GO:0005856)', 'Cell cortex part (GO:0044448)', 'Secretory granule lumen (GO:0034774)', 'Caveola (GO:0005901)', 'Focal adhesion (GO:0005925)'(see Appendix 14).

In comparison, the same analysis using downregulated genes in the WT vs T4826I-RYR1 HET gene set shared several of the same biological process terms surrounding fatty acid metabolism, but these were not found to be statistically significant (see Appendix 15). The only shared observation between the two WT vs G2435R-RYR1 HOM and the WT vs T4826I-RYR1 HET comparisons was an enrichment of genes in the cellular component terms 'Mitochondrion (GO:0005739)' and 'Mitochondrial matrix (GO:0005759)'.

Gene Ontology analyses for WT vs G2435R-RYR1 HOM comparison (downregulated)

	Downregulated	Adjusted p-value	Genes
(GO_BP) Biological Process	1. Fatty acid beta-oxidation (GO:0006635)	8.84E-08	*Abcd3, Acad11, Acadl, Acadm, Acadvl, Acat1, Decr1, Etfa, Etfdh, Hadha, Hadhb, Hsd17b4*
	2. Fatty acid catabolic process (GO:0009062)	1.05E-05	*Abcd3, Acad11, Acadl, Acadm, Acadvl, Acat1, Decr1, Hadha, Hadhb, Hsd17b4, Mut*
	3. Fatty acid oxidation (GO:0019395)	1.50E-05	*Abcd3, Acad11, Acadl, Acadm, Acadvl, Acat1, Decr1, Hadha, Hadhb, Hsd17b4*
	4. Fatty acid beta-oxidation using acyl-CoA dehydrogenase (GO:0033539)	8.25E-05	*Acad11, Acadl, Acadm, Acadvl, Etfa, Etfdh*
	5. Long-chain fatty acid transport (GO:0015909)	2.62E-03	*Acacb, Acsl1, Cd36, Cpt1b, Cpt2, Prkaa2*
	6. Mitochondrial transmembrane transport (GO:1990542)	9.58E-03	*Acacb, Afg3l2, Cpt1b, Cpt2, Prkaa2, Timm29*
	7. Fatty acid transmembrane transport (GO:1902001)	1.17E-02	*Acacb, Cpt1b, Cpt2, Prkaa2*
	8. Carnitine shuttle (GO:0006853)	1.33E-02	*Acacb, Cpt1b, Cpt2, Prkaa2*
	9. Regulation of fatty acid oxidation (GO:0046320)	1.97E-02	*Acadl, Acadvl, Lonp2, Mlycd*
	10. Regulation of acyl-CoA biosynthetic process (GO:0050812)	2.19E-02	*Dlat, Dld, Pdha1, Pdpr*
(GO_MF) Molecular Function	1. Acetyl-CoA C-acyltransferase activity (GO:0003988)	4.30E-02	*Acat1, Hadha, Hadhb*
	2. 3-hydroxyacyl-CoA dehydrogenase activity (GO:0003857)	7.84E-02	*Hadha, Hadhb, Hsd17b4*
	3. Acyl-CoA dehydrogenase activity (GO:0003995)	8.27E-02	*Acad11, Acadl, Acadm, Acadvl*
	4. Aminoacyl-tRNA ligase activity (GO:0004812)	9.50E-02	*Eprs, Iars, Iars2, Lars, Tarsl2*
	5. Nucleoside-triphosphatase activity (GO:0017111)	1.02E-01	*Abcd3, Ddx6, Dnajc27, Eif4a2, Gfm1, Hspa9, Hspd1, Kif1b, Kif16b, Kif21a, Myh8, Mut, Rab10, Rhou, Rragd, Tsr1, Vwa8*
	6. Adenylate cyclase binding (GO:0008179)	1.23E-01	*Adcy2, Akap6, Cap2*
	7. RNA binding (GO:0003723)	1.53E-01	*Adk, Akap1, Atxn2, Cd, Cefl1, Cluh, Ddx21, Ddx6, Eif4A2, Eif4G2, Eprs, Fastkd2, G2Bp2, Gfm1, Gpatch1, Hadhb, Hdlbp, Hspa9, Hspd1, Immt, Larp18, Lrpprc, Map3K20, Map4, Mrps12, Msi2, Mtif2, Mtdh, Nap1L4, Otud4, Polr2B, Ptcd3, Rrp12, Sf3B2, Smad3, Uso1, Tsr1*
	8. Voltage-gated cation channel activity (GO:0022843)	1.57E-01	*Cacna1s, Cacna2d1, Itgav, Kcnq5, Kcnma1, Lrrc38, Ryr1*
	9. Flavin adenine dinucleotide binding (GO:0050660)	1.67E-01	*Acad11, Acadl, Etfa, Etfdh, Oxnad1*
	10. Protein transporter activity (GO:0008565)	2.02E-01	*Cse1l, Ipo7, Kpna3, Kpna6, Uso1, Vps35*

Table 4.2. Gene ontology analyses (downregulated genes) for the WT vs G2435R-RYR1 HOM comparison. The significantly downregulated gene list from the WT vs G2435R-RYR1 HOM comparison was used as input for Enrichr and the top 10 terms for biological process, molecular function and cellular component are presented, in p-value ascending order. Continued on next page.

	Downregulated	Adjusted p value	Genes
(GO_CC) Cellular Component	1. Mitochondrion (GO:0005739)	3.09E-11	*Acacb, Acadl, Acadm, Acadvl, Acat1, Acsl1, Afg3l2, Akap1, Alas1, Bcl2l13, Coq3, Cpt1b, Cpt2, Cs, Decr1, Dlat, Dld, Dnaja3, Ech1, Etfa, Fastkd2, Gfm1, Hadha, Hadhb, Hsdl2, Hspa9, Hspd1, Iars2, Ide, Immt, Lrpprc, Mlycd, Mrs2, Msrb3, Mtif2, Mut, Ndufs1, Ndufs2, Ogdh, Oxnad1, Pdha1, Pdpr, Pptc7, Ptcd3, Sdha, Slc25a12, Taco1, Timm44, Uqcrc2, Vps35, Vwa8, Yme1l1*
	2. Mitochondrial matrix (GO:0005759)	9.04E-10	*Acadl, Acadm, Acadvl, Acat1, Alas1, Coq3, Cs, Decr1, Dlat, Dld, Dnaja3, Etfa, Etfdh, Gfm1, Hspa9, Hspd1, Iars2, Mlycd, Mut, Ndufs1, Ndufs2, Nsun4, Ogdh, Pdha1, Pdpr, Timm44*
	3. Mitochondrial inner membrane (GO:0005743)	4.89E-03	*Acad11, Abcb7, Afg3l2, Cpt2, Hadha, Hadhb, Hspd1, Immt, Mrps12, Mrs2, Ptcd2, Sdha, Slc25a12, Timm29, Timm44, Uqcrc2, Yme1l1*
	4. Microbody (GO:0042579)	9.86E-03	*Abcd3, Acad11, Ech1, Hsd17b4, Hsdl2, Ide, Lonp2, Mlycd*
	5. Peroxisome (GO:0005777)	1.23E-02	*Abcd3, Acad11, Ech1, Hsd17b4, Hsdl2, Ide, Lonp2, Mlycd*
	6. Peroxisomal matrix (GO:0005782)	3.53E-02	*Abcd3, Hsd17b4, Ide, Lonp2, Mlycd*
	7. Microbody lumen (GO:0031907)	4.11E-02	*Abcd3, Hsd17b4, Ide, Lonp2, Mlycd*
	8. Endoplasmic reticulum subcompartment (GO:0098827)	6.90E-02	*Rab10, Rab3gap1, Ryr1*
	9. Endoplasmic reticulum tubular network (GO:0071782)	1.11E-01	*Rab10, Rab3gap1, Stim1*
	10. Early endosome (GO:0005769)	1.30E-01	*Hspd1, Igf2r, Kif16b, Lmtkz, Mmgt1, Snx12, Snx27, Tbc1d16, Vps33a, Vps35*

4.3.5 Differential gene expression in response to halothane

No differentially expressed genes were identified in WT mice after halothane exposure and only one, zero and 23 genes were differentially expressed in G2435R-RYR1 HET, HOM and T4826I-RYR1 HET genotypes, respectively. The single gene differentially expressed in G2435R-RYR1 HET was *Gm46620*, a non-characterised long non-coding RNA gene and is thought to be of low physiological significance. Out of the 23 genes differentially expressed in T4826I-RYR1 HETs, 21 were downregulated with an effect size between -0.20 and -3.65 log2FC. Genes of interest within this list include *Pygm* (-0.36 log2FC), *Pgm1* (-0.33 log2FC) and *Atp2a1* (-0.26 log2FC) implicated in metabolic deficiencies and Ca^{2+} dysregulation. The minor effects of halothane exposure within all four RYR1 genotypes suggest that the halothane treatment was not effective and failed to trigger a physiologically relevant response.

4.3.6 Relationships between samples

The relationships between samples were examined and visualised using a PCA plot (Figure 4.5). The gene expression count data for all 24 samples was plotted together and the highest degrees of variability occurs between the T4826I-RYR1 HET and G2435R-RYR1 HOM sample genotypes as shown by the distant clustering on the horizontal PC1 axis. The WT and G2435R-RYR1 HET samples in comparison are loosely clustered together in the centre, showing similar global gene expression, as expected from the results previously described. Likewise, the halothane-treated samples within each genotype are clustered with the baseline control samples showing a close relationship. Variability on the vertical PC2 axis is the greatest within the G2435R-RYR1 HOM genotype as two samples does not seem to cluster effectively.

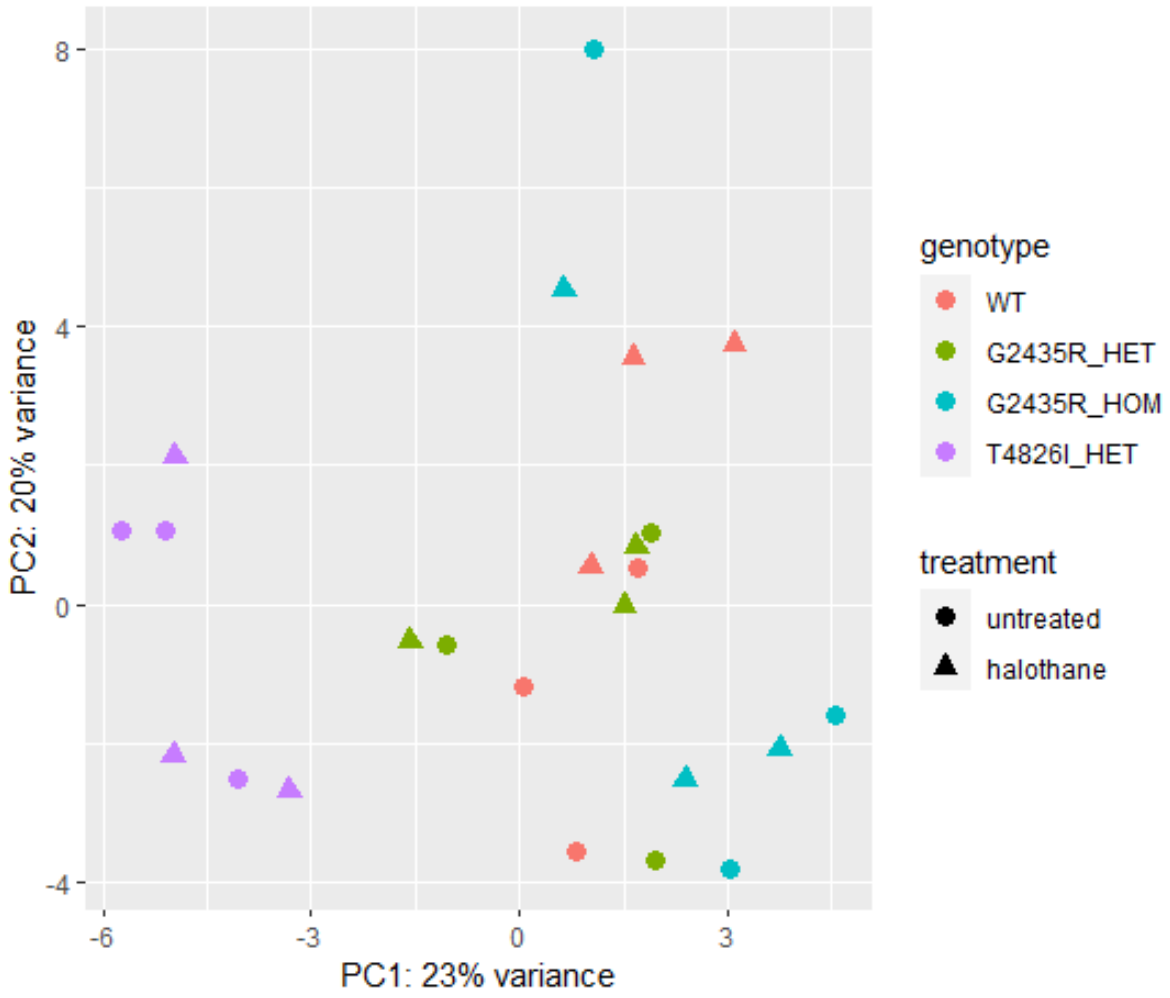

Figure 4.5. Principle component analysis plot examining the relationships between all mouse samples. The variance between samples is represented by a percentage (%) on PC1 (x-axis) and PC2 (y-axis). All 24 mouse samples are plotted with PC1 against PC2 and their respective genotype (WT: Red, G2435R-RYR1 HET: Green, G2435R-RYR1 HET: Blue and G2435R-RYR1 HET: Purple) and treatment groups (untreated: circle, halothane: triangle).

A sample-sample distance heatmap (Figure 4.6) was also used as an alternative visualisation for the overall gene expression differences between samples. Using the dendrogram we can see clustering of all WT and G2435R-RYR1 HET samples showing a close relationship between these two genotypes. In contrast, the T4826I-RYR1 HET samples formed their own distinct cluster in the top left whilst all G2435R-RYR1 HOM samples clustered to the bottom right which support the notion that these two genotypes have more divergent transcriptome profiles in comparison to G2435R-RYR1 HETs and WT mice. Halothane-treated samples clustered together with their respective untreated counterparts highlighting the lack of effect from the halothane treatment.

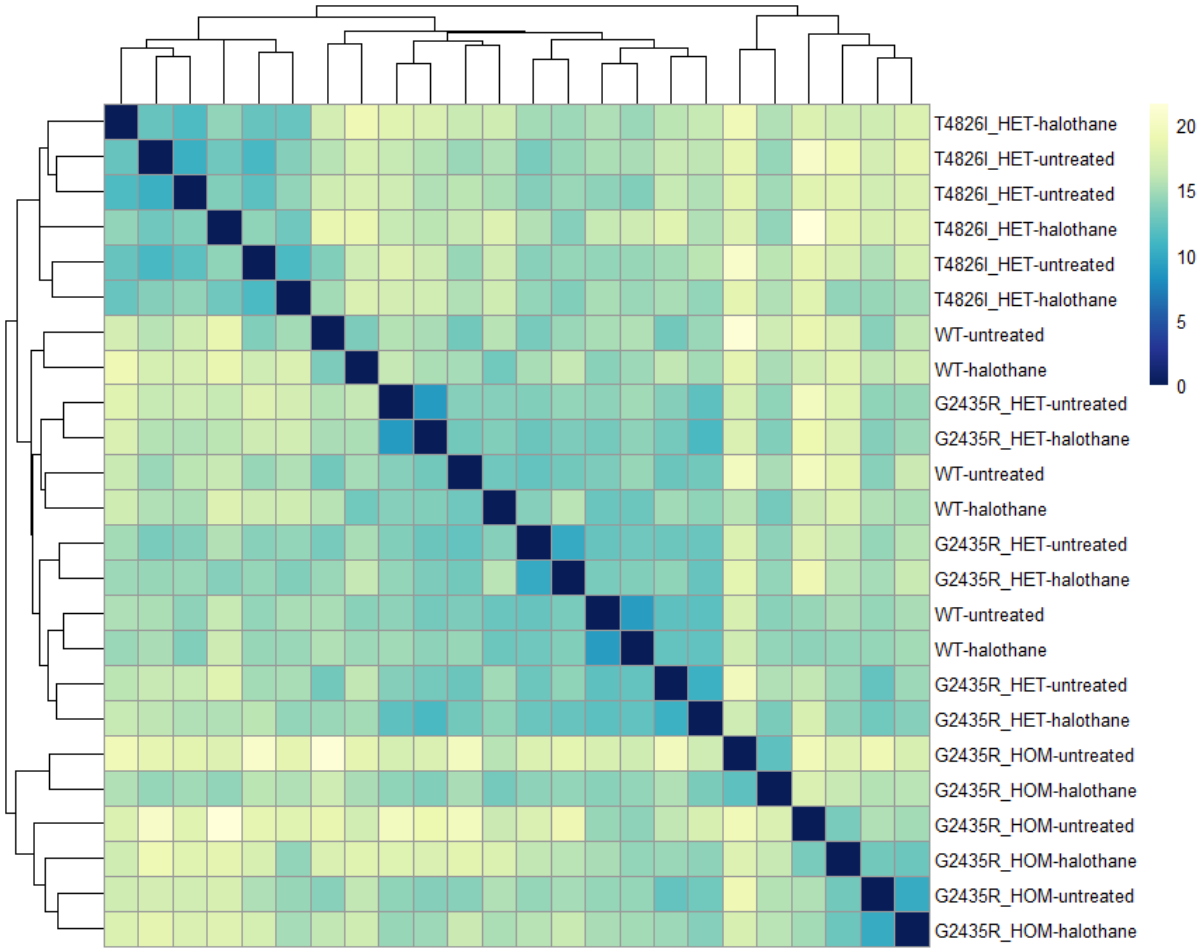

Figure 4.6. Expression heatmap of sample-to-sample distances. The distances between each sample were calculated using variance-stabilising transformation of count data for overall gene expression. All 24 mouse samples are plotted against each other to form relationship clusters represented by the dendrograms at the top and left side of the heatmap. The intensity of the coloured squares reflects the degree of similarity between two samples, ranging from dark blue to pale yellow.

4.4 DISCUSSION

This study aimed to provide an insight into how muscle physiology between RYR1 knock-in mice differs from WT, by investigating differential gene expression at baseline and after halothane exposure. The comparison of transcriptomes, in the absence of MH triggering agents, showed that WT and G2435R-RYR1 HET mice have very similar gene expression profiles, differing in the expression of only one gene (*Blvrb*). In contrast, G2435R-RYR1 HOM and T4826I-RYR1 HET mice had greater variability in gene expression, featuring 393 and 206 differentially expressed genes respectively, in comparison to WT. These results show that different RYR1 genotypes can impact skeletal muscle gene expression in a variant and gene-dose dependent manner, which may account for the variability associated with the MH phenotype.

Studies reporting MH genotype-phenotype correlations have shown that individuals with the human G2435R-RYR1 mutation (G2434R) have weaker phenotypes in comparison to those with the T4826I-RYR1 mutation, who tend to have greater IVCT contracture responses to both caffeine and halothane (Carpenter et al., 2009b). Visual inspection of gene expression data through the MA plot, PCA plot and heatmap showed that global gene expression between WT and G2435R-RYR1 HET mice were almost indistinguishable, which supports the notion of G2435R-RYR1 being a weak mutation. Mice with HOM expression of the G2435R-RYR1 mutation had more divergent gene expression profiles in comparison to the HET equivalent, which may reflect a more severe phenotype. Functional characterisation of this mouse model by Lopez et al., found that HOM mice had increased phenotype severity over HET mice, based on their responses during MH reactions (Lopez et al., 2018). On that basis, it is possible that greater differences in baseline gene expression may contribute to an increased severity of the MH phenotype.

Although rare, a few cases of human MH have been reported with autosomal recessive inheritance of RYR1 mutations (Lynch et al., 1997; Rueffert et al., 2001; Monnier et al., 2002; Wolak et al., 2014). One of the first studies described an MHS proband carrying two mutant alleles of the RYR1 Cys35Arg mutation, arising from consanguineous parents, both of whom were MHS (Lynch et al., 1997). In this study a large pedigree of 18 individuals were investigated, in which two were found to be recessive carriers. IVCT muscle contracture strengths in response to 2 mM caffeine were significantly higher in these two individuals, but

responses to halothane were indistinguishable from MHS family members carrying one mutation (Lynch et al., 1997). This was similar to the observations made in another MHS pedigree where individuals with recessive inheritance of the RYR1 Arg614Cys mutation, had stronger IVCT contracture strengths in response to both drugs (Rueffert et al., 2001). These findings present some evidence of increased IVCT phenotype severity in relation to RYR1 gene-dose but due to low sample size and limited data from human cases, definitive conclusions on this feature cannot be made.

To identify genes in common across comparisons (WT vs G2435R-RYR1 HET, WT vs G2435R-RYR1 HOM and WT vs T4826I-RYR1 HET), each list of differentially expressed genes was contrasted against one another to reveal 17 genes that were differentially expressed in more than one comparison. Among these genes, *Blvrb* was the only transcript upregulated in all three RYR1 knock-ins tested. *Blvrb* encodes for the enzyme biliverdin reductase B (BLVRB), which has a role in heme metabolism and redox regulation (Paukovich et al., 2018; Shalloe et al., 1996). A recent study showed that induced pluripotent stem cells infected with lentiviruses expressing BLVRB, have enhanced redox activity and reduced ROS accumulation (Wu et al., 2016). The increase in *Blvrb* gene expression observed in this study may reflect a cytoprotective response to help reduce ROS accumulation in these MH mice, as increased oxidative stress has been reported in multiple RYR1 knock-in mouse models (Durham et al., 2008; Boncompagni et al., 2009; Canato et al., 2019; Giulivi et al., 2011). With regards to the G2435R-RYR1 mouse model specifically, a colleague within the Leeds MH Unit, Dr Xiaochen Liu, has recently found evidence of elevated ROS production and altered redox regulation within this mouse line which supports this hypothesis (Chang et al., 2020)(discussed in more detail in chapter 5, section 5.4).

Functional annotation of gene lists found that most downregulated genes in both G2435R-RYR1 HOM and T4826I-RYR1 HET mice encoded proteins localised within mitochondria. Many of these genes were responsible for regulating fatty acid metabolism which is an important source of energy in skeletal muscle. Free fatty acids (FFA) are metabolised by first undergoing β-oxidation to generate acetyl coenzyme A (CoA), which is a substrate for the Krebs cycle in the mitochondrial matrix (Turner et al., 2014). Impairment of fatty acid oxidation and transport leads to an accumulation of FFA in skeletal muscle causing lipotoxicity - associated with insulin resistance, oxidative stress, and mitochondrial dysfunction (Turner et al., 2014; Wajner and Amaral, 2015; Vishwanath, 2016). Based on the gene

expression profiles generated, a deficiency in fatty acid β-oxidation may be present in the G2435R-RYR1 HOM and T4826I-RYR1 HET mouse genotypes (Figure 4.7).

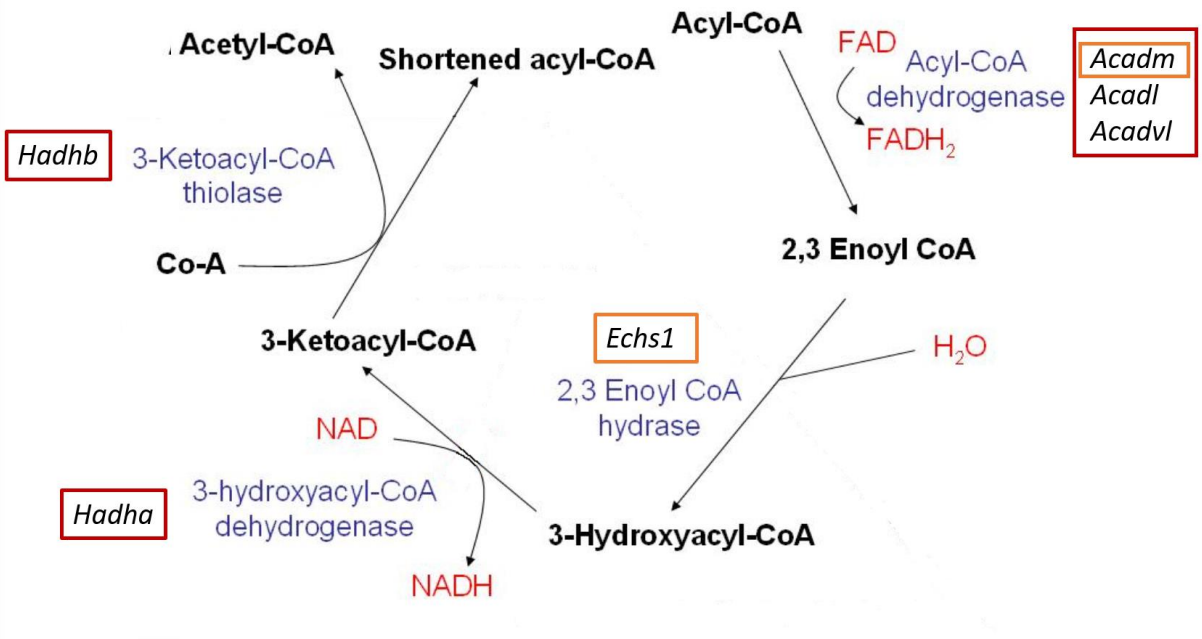

Figure 4.7. Schematic diagram of the fatty acid β-oxidation pathway. Genes encoding enzymes within the pathway, were found downregulated in G2435R-RYR1 HOM (highlighted by the red box) and T4826I-RYR1 HET mice (highlighted by the orange box). The genes *Acadm*, *Acadl* and *Acadvl* encode for medium-chain, long-chain, and very long-chain acyl-CoA dehydrogenase respectively (MCAD, LCAD and VLCAD), which target fatty acids of various lengths. These enzymes catalyse the first step of fatty acid β-oxidation which involves the dehydrogenation of acyl-CoA to trans-2,3-enoyl-CoA (Houten et al., 2016). *Echs1* encodes the short-chain enoyl-CoA hydratase, which catalyses the second step, generating 3-hydroxyacyl-CoA through hydration (Kanazawa et al., 1993). This is subsequently followed by dehydrogenation to form 3-ketoacyl-CoA, catalysed by 3-hydroxyacyl-CoA dehydrogenase (encoded by *Hadha*). Finally, 2-ketoacyl-CoA thiolase (encoded by *Hadhb*) cleaves the 3-ketoacyl-CoA to form an acetyl-CoA and a shortened acyl-CoA (Houten et al., 2016). This image was taken and modified from Wikimedia Commons, made available under the terms of the Creative Commons Attribution-Share Alike 3.0 Unported (https://creativecommons.org/licenses/by-sa/3.0/deed.en).

Several genes encoding enzymes within the fatty acid β-oxidation pathway were downregulated in G2435R-RYR1 HOM mice whilst only two were differentially expressed in T4826I-RYR1 HET mice. Furthermore, carnitine palmitoyltransferases 1b (CPT1B) and 2 (CPT2) (encoded by *Cpt1b* and *Cpt2* respectively), which facilitate the transport of fatty acids into mitochondria through the carnithine cycle, were downregulated in G2435R-RYR1 HOM mice only (Longo et al., 2006). These differences between genotype suggest that fatty acid metabolism in G2435R-RYR1 HOM mice is more severely impaired in comparison to T4826I-RYR1 HET mice.

In humans, mutations in many of the genes discussed (*Acadm, Acadvl, Hadha, Hadhb, Cpt2* and *Echs1*) cause enzyme deficiencies which are associated with fatty acid oxidation disorders (FAOD) (Merritt et al., 2018). FAOD can be asymptomatic or rapidly fatal and often manifest during infancy, with an autosomal recessive mode of inheritance. Examples of FAOD related to genes of interest include: MCAD deficiency (mutations in *Acadm*), VLCAD deficiency (mutations in *Acadvl*), Long-chain 3-hydroxy acyl-CoA dehydrogenase deficiency (mutations in *Hadha*), trifunctional protein deficiency (mutations in *Hadha* and/or *Hadhb*), CPT2 deficiency (mutations in *Cpt2*) and Leigh syndrome (mutations in *Echs1*) (Zschocke et al., 2001; Strauss et al., 1995; IJlst et al., 1994; Brackett et al., 1995; Naiki et al., 2014; Elpeleg et al., 2001; Sakai et al., 2015). Common clinical symptoms associated with these FAOD include hypoketotic hypoglycaemia, cardiomyopathy, arrhythmias and conduction defects, myopathy, and rhabdomyolysis (Houten et al., 2016; Merritt et al., 2018).

Connections between FFA and MH pathology were first described in MHS pigs after significantly higher levels of FFA and phospholipase activity were found in mitochondria (Cheah, 1981; Cheah and Cheah, 1981a; Cheah and Cheah, 1981b). Several years later, elevated FFA production in MHS human muscle was linked to increased sensitivity to halothane (Fletcher et al., 1991a; Fletcher and Rosenberg, 1986; Fletcher et al., 1991b). It was hypothesised that FFA and lipid peroxidation contributed to Ca^{2+} dysregulation by inducing Ca^{2+} release from the SR, with potential to modulate the MH phenotype (Rosenberg et al., 2015; Cheah and Cheah, 1981b; Cheah et al., 1989; Duthie et al., 1992). More recently, a study also speculated that mice with the R163C-RYR1 mutation associated with MH had reduced fatty acid oxidation due to observing a lower expression of enzymes regulating this process (Giulivi et al., 2011; Hardie and Pan, 2002). The data generated from this RNAseq experiment suggests that fatty acid oxidation may indeed be deficient in MHS muscle and may contribute towards the MH phenotype, which warrants further investigation.

Follow up work on this study would first involve selecting genes of interest within the fatty acid β-oxidation pathway and validating them using RT-PCR to confirm RNAseq findings. From there, western blotting should be used to quantify the expression levels of the encoded proteins, to see if the downregulation in mRNA corresponds to a downregulation at the protein level. This can be further supplemented with functional studies using skeletal muscle carrying different MH-associated RYR1 mutations. One approach would be to use the Agilent seahorse XF analyser which allows functional testing of mitochondria through cell culture plate formats. Mitochondrial function and fatty acid oxidation can be assessed within myotubes cultured from different RYR1 knock-in mouse genotypes, using the XF Cell Mito Stress test and palmitate-BSA substrate kits developed by Agilent. Any differences found between RYR1 genotypes would support the connection between MH and fatty acid oxidation suggested by the gene expression data presented.

Aside from fatty acid oxidation, other genes of interest include mitochondria-related genes such as *Ndufs1* and *Ndufs2* (encoding subunits of complex I), *Sdha* (encoding subunit A of complex II) and *Uqcrc2* (encoding a subunit of complex III), all of which were downregulated in G2435R-RYR1 HOM mice when compared to WT. The proteins encoded by these genes are involved in OXPHOS and their downregulation implies functional impairment of skeletal muscle at rest. These genes were not downregulated in G2435R-RYR1 HET mice, and only *Uqcrc2* was downregulated in the T4826I-RYR1 HET genotype. Intact myotubes from T4826I-RYR1 HET and HOM mice have been reported with evidence of lower oxygen consumption rates and mitochondrial content in comparison to WT (Barrientos et al., 2012), and this might be related to reduced mitochondrial complex III expression. All RYR1 knock-in mouse models of MH, except for G2435R-RYR1, have had reports of mitochondrial defects (Giulivi et al., 2011; Barrientos et al., 2012; Canato et al., 2019), and these deficiencies may correlate with the downregulation of OXPHOS gene expression. This topic of mitochondrial dysfunctional within RYR1 knock-in mice will be investigated further in Chapter 5 of this thesis.

With regards to treatment effects, gene expression changes in response to halothane exposure were very modest and resulted in surprisingly few changes between genotypes. The experimental conditions for this mouse study were designed to be a simplified version of the IVCT halothane treatment, with fewer confounding variables. Instead of incremental concentrations of halothane, a static concentration of 2 Vol% halothane was used over 30 minutes. This exposure time was thought to be sufficient for gene expression changes to occur,

as many genes were found to be differentially expressed within a similar time frame, in the human RNAseq experiment described in chapter 2, section 2.3.6. The electrical stimulation usually applied to the muscle sample at the start of the IVCT was also removed so that differences in gene expression could be attributed to halothane exposure alone.

Visual inspection of PCA plots and heatmaps showed that halothane-treated samples clustered together with the untreated baseline samples within each genotype, indicating little to no treatment effect. Gene expression in WT and G2435R-RYR1 HOM muscle was unaffected by halothane exposure and the only gene differentially expressed in G2435R-RYR1 HET muscle (*Gm46620*) has not been functionally characterised. In contrast, halothane exposure had the most pronounced effect on T4826I-RYR1 HET mouse gene expression with several genes downregulated after treatment. Genes of interest in this response include *Pygm*, *Pgm1* and *Atp2a1* which have been implicated in metabolic deficiencies and Ca^{2+} regulation (McArdle, 1951; Stojkovic et al., 2009; Zhang et al., 1995).

Pygm encodes myophosphorylase which is an enzyme that catalyses and regulates the breakdown of glycogen to glucose-1-phosphate during glycogenolysis (Gautron et al., 1987). In humans, mutations within this gene are associated with McArdle disease, which is a recessively inherited condition that prevents the breakdown of glycogen in skeletal muscle (McArdle, 1951). Individuals with this condition often exhibit symptoms of fatigue, cramping, muscle stiffness/weakness and exercise intolerance (Di Mauro, 2007). In cases of sustained exercise, more severe symptoms may include myoglobinuria, rhabdomyolysis and acute renal failure (Quinlivan et al., 2010). The inability to breakdown glycogen impairs energy production during exercise which affects glycolysis directly and OXPHOS indirectly through the lack of pyruvate availability.

Three variants (c.148C>T, c.577G>T and c.1279C>T) in *PYGM* (human orthologue of *Pygm*) were recently reported in three individuals with exertional heat illness (EHI) (Gardner et al., 2020), a condition characterised by the inability to thermoregulate during physical activity (American College of Sports et al., 2007). Both EHI and MH have similar pathophysiology, presenting with common symptoms such as hyperthermia, tachycardia, metabolic and respiratory acidosis, muscle cramps, rhabdomyolysis, multiorgan failure, disseminated intravascular coagulation and death (Capacchione et al., 2010). In the study by Gardner et al., the individual carrying the *PYGM* c.148C>T mutation, and two of the three

individuals carrying the *PYGM* c.577G>T mutation were also found to be MHS_h, diagnosed through the IVCT (Gardner et al., 2020).

Pgm1 encodes phosphoglucomutase-1 (PGM1), an enzyme with a role in both glycolysis and gluconeogenesis, catalysing the transfer of phosphate between the 1- and 6-positions of glucose (Putt et al., 1993). Similar to the symptoms of McArdle disease, PGM1 deficiency in adults has been associated with exercise intolerance, rhabdomyolysis, elevated muscle glycogen content, hypoglycaemia and elevated creatine kinase levels (Stojkovic et al., 2009; Morava, 2014). The reduced expression of both these genes after halothane exposure indicates a shift in metabolic regulation which impairs energy production. This would likely contribute to the rapid depletion of ATP from involuntary muscle contractures during fulminant MH reactions which accelerates cell death.

In addition to energy production mechanisms, exposure to halothane appears to alter the expression of genes regulating intracellular Ca^{2+} in T4826I-RYR1 HET muscle. The gene *Atp2a1* encodes SERCA1, which is an enzyme that catalyses the hydrolysis of ATP coupled with the translocation of Ca^{2+} from the cytosol into the SR to replenish Ca^{2+} stores (Zhang et al., 1995). Mutations in *Atp2a1* are associated with the autosomal recessive inheritance of Brody disease, a skeletal muscle disorder characterised by exercise-induced impairment of skeletal muscle relaxation (Brody, 1969). Individuals with Brody disease have reduced expression of SERCA1 and the delay in muscle relaxation is attributed to deficiencies in Ca^{2+} uptake into the SR which results in the increase of intracellular Ca^{2+} levels (Guglielmi et al., 2013). A variant (c.1613C>T) in *ATP2A1* (human orthologue of *Atp2a1*) was also recently reported in an individual with both EHI and MH susceptibility (Gardner et al., 2020). The downregulation of *Atp2a1* in response to halothane may contribute towards the involuntary muscle contractures by further disrupting Ca^{2+} regulation and during MH reactions.

These observations suggest that the method of halothane treatment was not appropriate to elicit changes in gene expression. This may be due to insufficient halothane exposure time or dosage, despite the human RNAseq results (chapter 2, section 2.3.6), used to inform this experimental design. The effects of these variables on gene expression are difficult to address due to the limitations associated with RNAseq experiments. In an ideal scenario, each mouse sample would be treated with multiple different concentrations of halothane over a range of timepoints to assess the effects of both exposure time and drug dose on gene expression.

However, this experimental design would be extremely costly to perform using RNAseq, as many sequencing lanes would be required to achieve appropriate read depth for each sample.

As previously mentioned in chapter 2, section 2.4, this experiment can be refined by first addressing these variables through drug dose response and time course experiments on cultured myotubes. A microplate reader can be used to measure Ca^{2+} flux in myotubes using a Ca^{2+}-sensitive fluorescent dye. The halothane dose which results in the maximum response in Ca^{2+} flux can be chosen and applied over a range of timepoints, before RNA is extracted from each sample. RT-PCR can then be used to measure gene expression levels at each timepoint, and this information can then be used to better inform the RNAseq design. Unlike RNAseq, this strategy requires a pre-selection of specific genes to assess through RT-PCR. Since MH is a condition associated with Ca^{2+} dysregulation in skeletal muscle, genes involved with Ca^{2+} homeostasis may be a good target for this process.

In summary, the results observed in this study have highlighted differences in baseline gene expression between RYR1 knock-in mouse genotypes. Gene expression profiles from G2435R-RYR1 HET mice are virtually indistinguishable from WT at baseline. In contrast, the G2435R-RYR1 HOM and T4826I-RYR1 HET genotypes showed greater disparity in gene expression which may be associated with differences in phenotype severity. Fatty acid metabolism should be studied further in the context of MH as many genes involved in this pathway were downregulated in RYR1 mutant muscle. This suggests that defects in fatty acid oxidation contribute towards the MH phenotype. Further investigations in this area may involve RT-PCR validation of RNAseq results, quantification of associated protein expression, and functional testing of mitochondria using fatty acid substrates. Genes involved with metabolic deficiencies and Ca^{2+} regulation were downregulated after halothane exposure in T4826I-RYR1 HET mice only. This may reflect a genuine lack of gene expression change in the G2435R-RYR1 knock-in model or that the halothane treatment applied was ineffective, which need to be refined. This can be achieved through a combination of dose-response and time course experiments which will help identify optimal conditions required for gene expression change.

5 BIOENERGETIC DEFECTS IN RYR1 KNOCK-IN MICE

5.1 INTRODUCTION

Evidence of mitochondrial defects have been reported in the first three RYR1 knock-in mouse models associated with MH, supporting a link between MH susceptibility and mitochondrial dysfunction (Durham et al., 2008; Boncompagni et al., 2009; Michelucci et al., 2017; Canato et al., 2019; Giulivi et al., 2011; Barrientos et al., 2012; Yuen et al., 2012). These reports have described gross morphological changes in skeletal muscle mitochondria followed by evidence of functional deficiencies either through alterations in ROS homeostasis or oxygen consumption rates.

The first description of mitochondrial defect was in the Y522S-RYR1 mouse model associated with both MH and central core disease (Durham et al., 2008). Examination of muscle fibres from Y522S-RYR1 HET mice showed many damaged mitochondria, characterised by abnormal size and shape, swelling, loss of matrix density, disorganisation of cristae and external membrane disruption (Durham et al., 2008). These observations were supported by Boncompagni et al. who identified signs of mitochondrial damage as early as eight weeks of age, in addition to central cores devoid of mitochondria which increased in size with age (Boncompagni et al., 2009). Similar structural abnormalities have also been reported in the T4826I-RYR1 mouse model, which shows that these features are not exclusive to *Ryr1* variants associated with central core disease (Yuen et al., 2012). Histological examination of *Soleus* muscles from this model identified abnormal distribution of enlarged mitochondria with deeply infolded sarcolemma and increased severity in males, indicating a sex-dependent phenotype (Yuen et al., 2012).

The cause of mitochondrial damage in RYR1 knock-in mice has been attributed to oxidative stress with evidence of increased ROS production reported in multiple studies (Durham et al., 2008; Boncompagni et al., 2009; Canato et al., 2019). It was proposed that the elevated intracellular Ca^{2+} detected in RYR1 mutant myotubes increases ROS output from mitochondria, resulting in cellular damage over time and myopathic traits (Boncompagni et al., 2009). In support of this hypothesis, a study has shown reduced mitochondrial damage in Y522S-RYR1 HET mice after treating their drinking water with antioxidants (Michelucci et al., 2017). Furthermore, increased Ca^{2+} uptake was observed in Y522S-RYR1 mitochondria at

rest and after electrical/caffeine stimulation, in addition to reduced ROS accumulation after MCU silencing – supporting the connection between ROS production and mitochondrial damage (Canato et al., 2019).

Cellular damage due to oxidative stress causes functional impairment of mitochondria which has been demonstrated in both the R163C-RYR1 and T4826I-RYR1 mouse models (Giulivi et al., 2011; Boncompagni et al., 2009). Muscle fibres from R163C-RYR1 HET mice have been shown to have lower OXPHOS capacity in conjunction with lower expression of mitochondrial proteins, believed to be the result of elevated intracellular Ca^{2+} and increased ROS production (Giulivi et al., 2011). Measurements of oxygen consumption in the T4826I-RYR1 HET and HOM genotypes show a similar pattern with lower oxygen consumption rates and reduced mitochondrial number detected in cultured myotubes (Barrientos et al., 2012).

Following the transcriptomic analysis of G2435R-RYR1 knock-in mice (chapter 4), mitochondrial function was investigated using permeabilised muscle fibres. This chapter describes the first investigation into mitochondrial dysfunction within the G2435R-RYR1 mouse model and this was achieved using high resolution respirometry. This technique allows oxygen consumption rates to be measured through specific mitochondrial complexes using permeabilised muscle fibres, providing the highest level of detail achieved in any MH animal study. Three different experiments were conducted, measuring oxygen consumption rates: at baseline, after halothane exposure and at different Ca^{2+} concentrations. HET mice from the T4826I-RYR1 mouse model were used as a comparison to assess whether responses have an *Ryr1* variant-specific effect. The data generated will help to answer the following research questions with respect to G2435R-RYR1 knock-in mouse genotypes:

- Do muscle fibres from RYR1 knock-in mice have different oxygen consumption rates to WT at baseline?
- How does halothane effect oxygen consumption rates within these mouse muscle fibres?
- How does increased [Ca^{2+}] effect oxygen consumption rates within these mouse muscle fibres?
- Do the oxygen consumption rates differ between the two different RYR1 knock-in mouse models?

5.2 METHODS

5.2.1 Animals

Animals were housed in pathogen-free conditions with free access to food, water and 12 hr light-and-dark cycles. All experiments were undertaken with UK Home Office approval, licence number PB2FB5E94. A mixture of male and female mice (approximately 1:1), between the ages of 8-14 weeks old were used for functional respirometry studies.

5.2.2 Muscle sample preparation for respirometry

An adapted SUIT protocol was used to investigate the OXPHOS capacity of individual complexes and respiratory states (Kuznetsov et al., 2008; Pesta and Gnaiger, 2012). WT and RYR1 knock-in mice (age 8-12 weeks) were killed by cervical dislocation and their *Soleus* muscles were rapidly dissected from their hind limbs and placed into 1 ml of ice-cold biopsy preservation buffer, BIOPS (2.77 mM CaK_2EGTA, 7.23 mM K_2EGTA, 5.77 mM Na_2ATP, 6.56 mM $MgCl_2 \cdot 6H2O$, 20 mM taurine, 15 mM Na_2Phosphocreatine, 20 mM imidazole, 0.5 mM dithiothreitol (DTT), and 50 mM MES hydrate, pH 7.1, adjusted with 5 N KOH at 0°C) immediately after collection for storage and transport.

Muscle fibre bundles containing approximately 4-5 fibres each were mechanically separated from the intact muscles using forceps. These fibre bundles were then exposed to chemical permeabilisation in ice cold BIOPS containing saponin (50 $\mu g \cdot ml^{-1}$) for 30 minutes, before being washed with 1 ml respiration medium, Mir05 (0.5 mM EGTA, 3 mM $MgCl_2 \cdot 6H2O$, 60 mM lactobionic acid, 20 mM taurine, 10 mM KH_2PO_4, 20 mM HEPES adjusted to pH 7.1 with KOH at 37 °C, 110 mM D-sucrose, and 1 $g \cdot L^{-1}$ essentially fatty acid free BSA) to remove residual saponin. Muscle fibre bundles from both legs were then blot-dried for 5 seconds, weighed and loaded into a respirometer chambers (1-2 mg in each chamber, left *Soleus* chamber A, right *Soleus* chamber B) containing 2 ml of Mir05. The time between biopsy collection and assay was ~90 – 120 min (Chang et al., 2019; Pesta and Gnaiger, 2012).

5.2.3 High Resolution Respirometry

Oxygen consumption rates was measured using Oroboros respiratory analysers (Oroboros Instruments, Innsbruk, Austria) at two second intervals with polarographic oxygen sensors and expressed as mass-specific oxygen flux (pmol/s*mg). The analyser was calibrated daily in air saturated solution before experimentation. Assays were initiated by injecting oxygen into each chamber to raise the oxygen concentration to >400 nmol/mL prior to starting a SUIT protocol. Re-oxygenation of the chambers was performed to maintain oxygen concentration between 200-500 nmol/mL to prevent limitation due to oxygen diffusion (Pesta and Gnaiger, 2012). Each assay was performed at 37 °C, with chamber stirrers set at 750 rpm.

5.2.4 SUIT protocol

An in-depth description of the SUIT protocol is described in chapter 3 section 3.2.4. In brief, reagents and inhibitors were sequentially added into the reaction chambers in the order displayed (Table 5.1).

Substrates	Final concentration in chamber
Blebbistatin (B)	5 µM
Glutamate (G)	10 mM
Malate (M)	0.5 mM
Pyruvate (P)	5 mM
Adenosine diphosphate (ADP)	2.5 mM
Cytochrome C (CC)	10 µM
Succinate (S)	10 mM
4-(trifluoromethoxy)-phenylhydrazone (FCCP)	0.5 µM additions until max output
Rotenone (R)	1 µM
Antimycin A (AA)	2.5 µM

Table 5.1. Summary of the chemical components in the SUIT protocol. The chemical names are displayed in the order of application with the respective concentrations applied for each assay.

The composition of each respiratory state (in bold) are as follows –

LEAK: (B, G, M, P)

CI$_{(OXPHOS)}$: (LEAK + ADP)

CI+CII$_{(OXPHOS)}$: (**LEAK** + ADP + CC + S)

CI+CII$_{(ETS)}$: (**LEAK** + ADP + CC + S + FCCP)

CII$_{(ETS)}$: (**LEAK** + ADP + CC + S + FCCP + R)

ROX: (**LEAK** + ADP + CC + S + FCCP + R + AA).

The ROX state represented residual oxygen consumption outside of mitochondrial function and is therefore subtracted from the other states to obtain final readings (Perry et al., 2011; Pesta and Gnaiger, 2012; Chang et al., 2019).

5.2.5 Complex IV Assay

Measurement of mass-specific complex IV oxygen flux was used as an alternative proxy marker for estimations of mitochondrial content. Ascorbate (2 mM) and TMPD (0.5 mM) were applied to each sample at the end of the standard SUIT protocol (Larsen et al., 2012). The measurement of $CIV_{(MAX)}$ is taken at the peak of the corresponding trace and residual chemical background is finally removed from this value by applying sodium azide (10 mM) to the sample. Refer to chapter 3, section 3.2.4, Figure 3.1 for a visual summary of the SUIT and complex IV assay protocol.

5.2.6 Halothane treatment

To assess the effects of halothane on oxygen flux, muscle fibre bundles from WT and RYR1-knock in mice were prepared in the same way as described in section 5.2.2. The muscle fibre bundles in chambers A and B were treated as paired samples with samples in chamber A used as a control for the samples in chamber B which were exposed to halothane. 1 mM halothane was applied as treatment prior to the SUIT protocol, from a stock solution prepared in dimethyl sulphoxide (DMSO). In experiments where 1 mM halothane was used, the DMSO

concentration was 0.05%. An equal concentration of DMSO 0.05% (without halothane) was applied into chamber A to function as control. The SUIT protocol described in section 5.2.4 was conducted three minutes after the addition of halothane/DMSO.

5.2.7 Calcium assay

Oxygen flux in WT and RYR1 knock-in mice was measured and compared at 0, 100 and 300 nM concentrations of free Ca^{2+}. A stock solution of calcium carbonate ($CaCO_3$) was prepared in Mir05 and applied to assay chambers using a Hamilton syringe to modify the [Ca^{2+}] in the assay medium. The free [Ca^{2+}] in the assay medium was calculated with the Ca-EGTA Calculator v1.3 using constants from Theo Schoenmakers' Chelator (Schoenmakers et al., 1992). Due to the limitations of the respirometry analyser having only two chambers, the assessment of each [Ca^{2+}] was conducted on separate mice and was therefore analysed as independent samples rather than paired. The SUIT protocol described in section 5.2.4 was conducted three minutes after the addition of $CaCO_3$.

5.2.8 Data handling and analysis (Respirometry)

Data are presented either as oxygen flux per muscle mass (pmol/s*mg) or as FCR normalised for mitochondrial content. Oxygen flux readings were exported from specialised software DatLab5 (Oroboros Instruments, Innsbruk, Austria) into Microsoft Excel before analysis using IBM SPSS statistics v21. Mass-specific oxygen flux and FCR were assessed for normal distribution using the Shapiro Wilk test before statistical testing.

Oxygen consumption rates and FCR data generated from baseline comparisons were not normally distributed and analysed using the non-parametric Kruskall-Wallis H test with post hoc Dunn’s test. Data collected pre vs post halothane treatment were normally distributed and analysed using a two-way mixed analysis of variance (ANOVA). Finally, data from the calcium assay was analysed using a two-way ANOVA. P-values generated from pairwise comparisons were adjusted for multiple testing using the Bonferroni correction.

Figures used to visualise data were created using GraphPad Prism 8. The power calculator software G*Power, version 3.1.9.2 was used to calculate sample sizes for each experiment (Faul et al., 2007). Post hoc power analysis of preliminary baseline mouse data using a total sample size n = 60, achieved 0.97 power, $\alpha = 0.05$, effect size = 0.58. Sample size calculations for halothane and calcium exposure experiments was performed a priori, with the aim of achieving 0.8 power, $\alpha = 0.05$. An effect size of 0.25 was used, defined as a medium size effect, which generated a total sample size n = 48, across four genotypes.

5.3 RESULTS

5.3.1 Baseline comparisons

Baseline oxygen flux was measured from WT (n=16), G2435R-RYR1 HET (n=16), G2435R-RYR1 HOM (n=16) and T2826I-RYR1 HET (n=12) mice. Results showed that oxygen consumption rates significantly differed among RYR1 genotypes in the LEAK ($p<0.001$), $CI+CII_{(ETS)}$ ($p=0.024$) and $CIV_{(MAX)}$ ($p=0.017$) states. Post hoc pairwise comparisons (Figure 5.1) between WT and G2435R-RYR1 HETs showed no significant differences, while the G2435R-RYR1 HOMs differed only in $CIV_{(MAX)}$ with significantly lower output than WT ($p=0.027$). This finding suggests that G2435R-RYR1 HOM skeletal muscle fibres may have a lower mitochondrial content than WT fibres. T4826I-RYR1 HET knock-ins had lower oxygen flux in LEAK ($p<0.01$ against all genotypes) and a greater ETS capacity ($CI+CII_{(ETS)}$) compared to G2435R-RYR1 HOM mice ($p=0.023$).

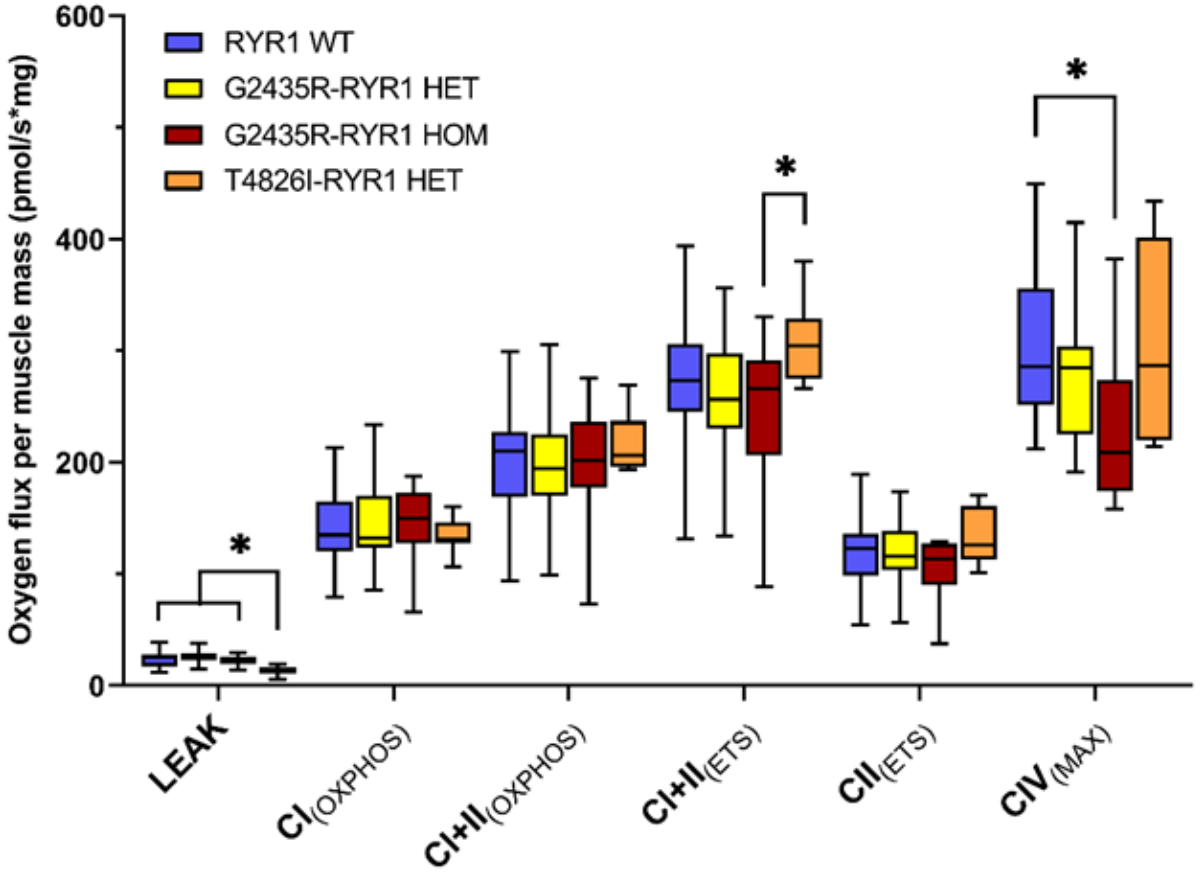

Figure 5.1. Mass-specific oxygen flux in permeabilised *Soleus* muscle across RYR1 mouse genotypes. This figure contains data from WT (n = 16, blue), G2435R-RYR1 HET (n = 16, yellow), G2435R-RYR1 HOM (n = 16, red) and T4826I-RYR1 HET (n = 12, orange) mice. Boxplots show median, IQR and min-max range for each genotype. Statistically significant pairwise comparisons ($p<0.05$) are labelled with an asterisk.

The confounding variable of mitochondrial content was removed in the mass-specific oxygen flux data by normalising to a common reference state, producing FCR (Figure 5.2). FCR provide a measure of function as a proportion of ETS capacity, which is independent of mitochondrial content.

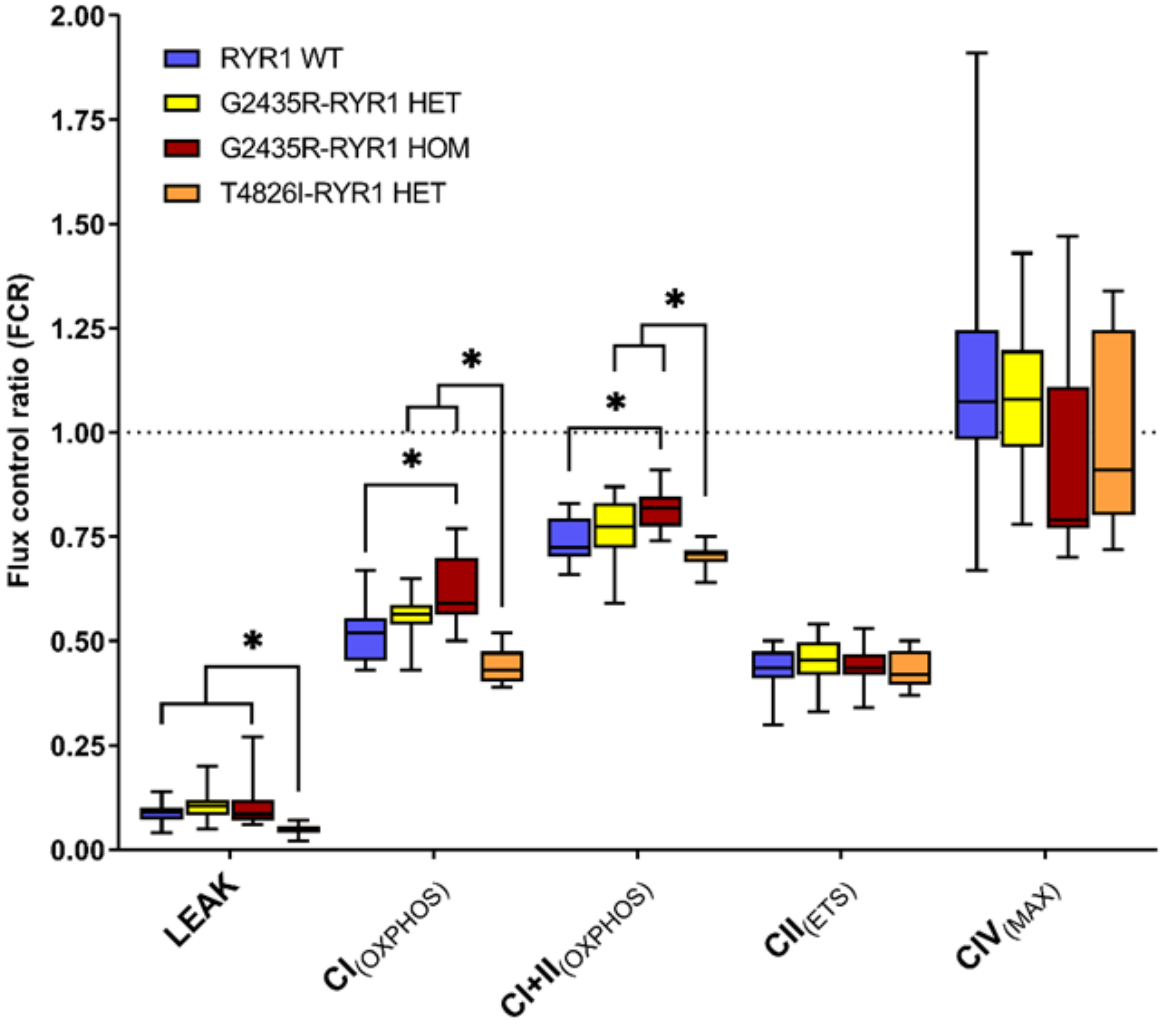

Figure 5.2. Comparison of flux control ratios between RYR1 mouse genotypes. This figure shows normalised data from WT (n = 16, blue), G2435R-RYR1 HET (n = 16, yellow), G2435R-RYR1 HOM (n =16, red) and T4826I-RYR1 HET (n = 12, orange) mice. FCR are generated by internally normalising mass-specific oxygen flux to the $CI+CII_{(ETS)}$ state (indicated by the horizontal dashed line). Boxplots show median, IQR and min-max range for each genotype. Statistically significant pairwise comparisons ($p<0.05$) are labelled with an asterisk.

Comparison of FCR between RYR1 genotypes differed significantly in the LEAK, $CI_{(OXPHOS)}$ and $CI+CII_{(OXPHOS)}$ states (all $p<0.001$). Pairwise FCR comparisons within the LEAK state did not differ from mass-specific oxygen flux after normalisation. However, $CI_{(OXPHOS)}$ FCR showed significantly higher values in G2435R-RYR1 HOM compared to WT ($p=0.014$), suggesting a greater reliance on complex I function as it forms a higher proportion of the ETS capacity. This was also observed in the $CI+CII_{(OXPHOS)}$ combined state which was also significantly higher in G2435R-RYR1 HOM ($p=0.004$), likely due to the differences in complex I. Interestingly, T4826I-RYR1 HET knock-ins showed significantly lower $CI_{(OXPHOS)}$ and $CI+CII_{(OXPHOS)}$ FCR in comparison to G2435R-RYR1 HET and HOM knock-ins which shows that mitochondrial function can differ depending on the *Ryr1* variant present.

5.3.2 Effects of halothane exposure

Oxygen flux was measured with and without exposure to halothane, across all mouse genotypes: RYR1 WT (n =15), G2435R-RYR1 HET (n=15), G2435R-RYR1 HOM (n=14), T4826I-RYR1 HET (n=10). Two-way mixed ANOVAs were conducted for each respiratory state to examine the effects of genotype and halothane on mass-specific oxygen consumption rates (pmol/s*mg). Data is presented as mean ± SE, unless otherwise stated. There was no statistically significant interaction between genotype and halothane exposure on the oxygen consumption rates in any respiratory state. Therefore, analysis of main effects for halothane treatment was performed, which indicated a statistically significant difference in $CI_{(OXPHOS)}$, $CI+CII_{(OXPHOS)}$ and $CI+CII_{(ETS)}$ ($p<0.001$, $p=0.001$ and $p<0.001$ respectively). Pairwise comparisons showed a significant reduction in mean oxygen consumption rates after halothane exposure in $CI_{(OXPHOS)}$ (Pre: 129.2±3.8, Post: 67.8±2.9), $CI+CII_{(OXPHOS)}$ (Pre: 207.4±5.9, Post: 182.6±5.2) and $CI+CII_{(ETS)}$ (Pre: 285.7±8.9, Post: 238.5±7.3).

FCR data showed similar observations with a statistically significant reduction after halothane exposure in $CI_{(OXPHOS)}$ (Pre: 0.458±0.01, Post: 0.246±0.014, $p<0.001$) and $CI+CII_{(OXPHOS)}$ (Pre: 0.730±0.06, Post: 0.662±0.026, $p=0.009$). Additionally, a significant interaction effect between genotype, halothane and FCR was also observed in $CI_{(OXPHOS)}$ ($p=0.037$). This interaction was followed up by assessing the simple main effects of halothane exposure by performing a one-way ANOVA pre and post treatment. The results showed no significant difference in $CI_{(OXPHOS)}$ FCR between genotypes pre halothane exposure ($p=0.248$) but a statistically significant difference was observed post halothane exposure ($p=0.004$).

Pairwise comparisons between genotypes showed that the mean $CI_{(OXPHOS)}$ FCR in T4826I-RYR1 HETs post halothane (0.143±0.06) was significantly lower than all other genotypes (WT: 0.259±0.07, $p=0.039$, G2435R-RYR1 HET: 0.294±0.14, $p=0.004$ and G2435R-RYR1 HOM: 0.287±0.11, $p=0.007$). Pairwise comparisons between the remaining three genotypes showed no significant differences in mean $CI_{(OXPHOS)}$ FCR after halothane exposure. The reduction of $CI_{(OXPHOS)}$ FCR across all genotypes after halothane exposure reflects a normal drug response, but the significantly lower FCR in T4826I-RYR1 HETs suggest that this genotype has heightened sensitivity to halothane. A visual summary of all differences pre vs post halothane can be seen in Figure 5.3, and all raw data is summarised in Table 5.2.

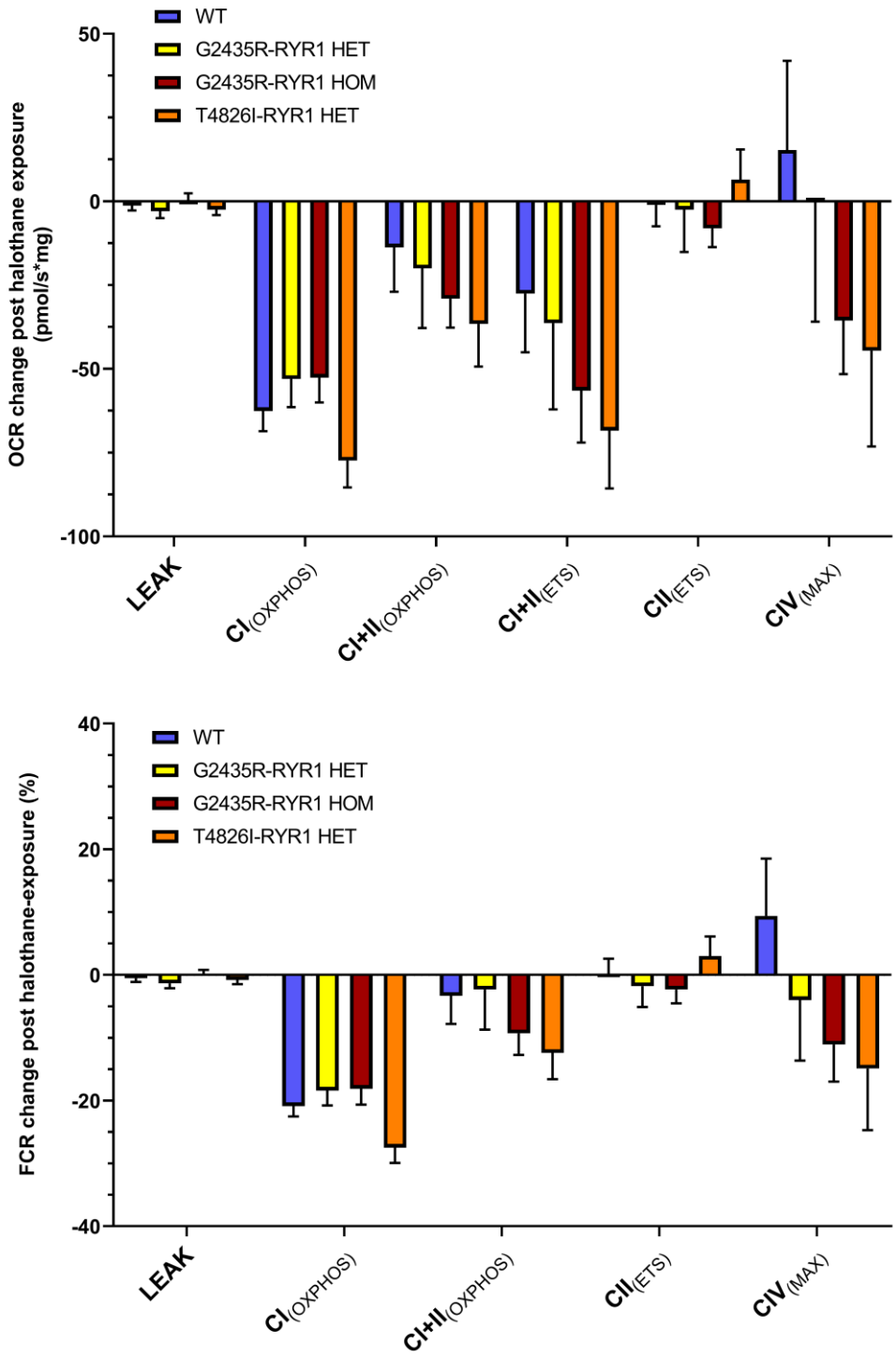

Figure 5.3. Magnitude of responses to halothane exposure across RYR1 knock-in mouse genotypes. The effects of halothane exposure on **A)** oxygen consumption rates (pmol/s*mg) and **B)** FCR (converted to a %) in each respiratory state is illustrated using a bar chart, presenting means ± SE. These plots include data from all samples across the following genotypes: RYR1 WT (n =15, blue), G2435R-RYR1 HET (n=15, yellow), G2435R-RYR1 HOM (n=14, red), T4826I-RYR1 HET (n=10, orange).

Respiratory states (OCR)	WT				G2435R-RYR1 HET				G2435R-RYR1 HOM				T4826I-RYR1 HET			
	OCR (pmol/s*mg) ± SD				OCR (pmol/s*mg) ± SD				OCR (pmol/s*mg) ± SD				OCR (pmol/s*mg) ± SD			
	Control	SD	Post halothane	SD	Control	SD	Post halothane	SD	Control	SD	Post halothane	SD	Control	SD	Post halothane	SD
LEAK	20.6	6.7	19.3	6.9	22.1	8.6	19.2	7.7	19.9	6.8	20.1	10.8	12.7	3.6	10.2	3.5
$CI_{(OXPHOS)}$	138.9	26.5	76.3	22.0	129.5	34.5	76.5	24.9	129.9	18.7	77.3	19.3	118.6	28.2	41.3	16.7
$CI+CII_{(OXPHOS)}$	216.4	35.7	202.7	37.0	201.0	60.2	181.0	44.7	199.9	31.7	170.8	30.9	212.4	34.9	175.7	34.5
$CI+CII_{(ETS)}$	297.6	50.5	270.0	49.6	281.4	89.9	245.0	65.2	281.1	53.2	224.7	42.3	282.8	48.4	214.4	50.0
$CII_{(ETS)}$	123.3	18.4	122.2	22.1	126.6	37.8	124.1	38.1	121.6	19.1	113.5	18.0	125.4	27.0	131.8	25.6
$CIV_{(MAX)}$	370.3	86.4	385.6	104.3	352.2	119.5	352.2	108.9	326.1	52.9	290.5	52.5	354.8	94.3	310.3	99.7
Respiratory states (FCR)	FCR ± SD				FCR ± SD				FCR ± SD				FCR ± SD			
	Control	SD	Post halothane	SD	Control	SD	Post halothane	SD	Control	SD	Post halothane	SD	Control	SD	Post halothane	SD
LEAK	0.07	0.03	0.07	0.03	0.09	0.04	0.07	0.04	0.07	0.03	0.07	0.04	0.04	0.01	0.04	0.01
$CI_{(OXPHOS)}$	0.47	0.05	0.26	0.07	0.48	0.11	0.29	0.14	0.47	0.06	0.29	0.11	0.42	0.06	0.14	0.06
$CI+CII_{(OXPHOS)}$	0.73	0.05	0.70	0.17	0.72	0.04	0.70	0.26	0.72	0.05	0.62	0.15	0.75	0.05	0.63	0.13
$CII_{(ETS)}$	0.42	0.08	0.43	0.12	0.46	0.08	0.48	0.21	0.44	0.04	0.41	0.08	0.44	0.04	0.47	0.10
$CIV_{(MAX)}$	1.25	0.26	1.35	0.47	1.25	0.25	1.33	0.55	1.18	0.19	1.07	0.27	1.26	0.31	1.11	0.35

Table 5.2. The effects of halothane exposure on oxygen flux across RYR1 mouse genotypes. A summary of raw oxygen consumption rates and FCR data, is displayed for each genotype (pre vs post halothane exposure), presented as means ± SD.

5.3.3 Effects of calcium concentration on oxygen flux

Three different [Ca^{2+}] of 0, 100 and 300 nM were selected for the Ca^{2+} assay to encompass the range in $[Ca^{2+}]_{rest}$ (mean ± SD) reported in WT (123 ± 3 nM), G2435R-RYR1 HET (156 ± 16 nM), G2435R-RYR1 HOM (265 ± 32 nM) and T4826I-RYR1 HET (278 ± 21 nM) skeletal muscle (Barrientos et al., 2012; Lopez et al., 2018). The effects of Ca^{2+} on oxygen consumption rates and FCR at those concentrations, were assessed across four RYR1 mouse genotypes (WT (0 nM: n = 16; 100 nM: n = 12; 300 nM: n =12); G2435R-RYR1 HET (0 nM: n = 16; 100 nM: n = 16; 300 nM: n =16); G2435R-RYR1 HOM (0 nM: n = 16; 100 nM: n = 16; 300 nM: n =16) and T4826I-RYR1 HET (0 nM: n = 12; 100 nM: n = 16; 300 nM: n =16)).

All data is presented as mean ± SD unless otherwise stated. Starting with mass-specific oxygen consumption rates, results showed that there was a statistically significant interaction effect between [Ca^{2+}], genotype and oxygen consumption rates in the LEAK state ($p=0.03$). Subsequent analysis using one-way ANOVAs showed that LEAK oxygen consumption rates were significantly affected by [Ca^{2+}] in the G2435R-RYR1 HET and HOM genotypes ($p<0.001$ and $p=0.001$ respectively).

Post hoc pairwise comparisons (Table 5.3) revealed that LEAK oxygen consumption rates in G2435R-RYR1 HETs were reduced at 100 nM and 300 nM [Ca^{2+}], in comparison to 0 nM ($p<0.001$ and $p<0.001$, respectively). In the G2435R-RYR1 HOM genotype, the LEAK oxygen consumption rates at 100 nM was significantly lower than WT ($p=0.001$), but the comparison between 0 and 300 nM [Ca^{2+}] was not significantly different. Comparisons between 100nM and 300 nM [Ca^{2+}] was also not significantly different in any genotype.

Genotype	[Ca^{2+}] (nM) 0	100	300	Pairwise comparisons (p-values) 0 vs 100	0 vs 300	100 vs 300
WT	23.5 (7.4)	17.3 (9.1)	20.4 (6.3)	0.054	0.604	0.904
G2435R-RYR1 HET	25.8 (6.0)	13.8 (5.3)	17.1 (7.2)	<0.001	<0.001	0.421
G2435R-RYR1 HOM	22.3 (4.2)	14.3 (6.3)	18.2 (5.7)	0.001	0.207	0.241
T4826I-RYR1 HET	13.7 (4.1)	13.2 (6.5)	12.6 (5.6)	1.000	1.000	1.000

Table 5.3. Raw data for LEAK oxygen consumption rates in the Ca^{2+} assay. Raw oxygen consumption rates data is presented as means (SD) for each genotype across all [Ca^{2+}]. Pairwise comparisons are also displayed with p-values adjusted with Bonferroni correction ($p<0.05$ is significant).

In contrast, no statistically significant interaction effect between [Ca^{2+}], genotype and oxygen consumption rates were observed in $CI_{(OXPHOS)}$, $CI+CII_{(OXPHOS)}$, $CI+CII_{(ETS)}$, $CII_{(ETS)}$ and $CIV_{(MAX)}$. On that basis, data from each genotype was combined and one-way ANOVAs were used to see how different respiratory states were affected by [Ca^{2+}]. The results of this showed that $CI_{(OXPHOS)}$ and $CII_{(ETS)}$ were significantly different between different [Ca^{2+}] ($p<0.001$ and $p=0.002$). The mean $CI_{(OXPHOS)}$ oxygen consumption rates at 0, 100 and 300 nM [Ca^{2+}] were 141.6 ± 30.0, 119.1 ± 34.9 and 109.4 ± 39.8, respectively. Pairwise comparisons showed that $CI_{(OXPHOS)}$ oxygen consumption rates at 100 and 300 nM [Ca^{2+}] was significantly lower than at 0 nM [Ca^{2+}] ($p=0.004$ and $p<0.001$). The mean $CII_{(ETS)}$ oxygen consumption rates at 0, 100 and 300 nM [Ca^{2+}] were 117.4 ± 29.7, 102.8 ± 26.5 and 101.9 ± 26.3, respectively. Pairwise comparisons showed that $CII_{(ETS)}$ oxygen consumption rates at 100 and 300 nM [Ca^{2+}] were significantly lower than at 0 nM [Ca^{2+}] ($p=0.012$ and $p=0.003$).

Following the analysis of oxygen consumption rates data, the same procedure was performed using FCR data, to address the confounding factor of mitochondrial content. Results showed that the interaction effect previously found in the LEAK state was not statistically significant after normalisation. However, when data across all genotypes were combined, a statistically significant main effect for [Ca^{2+}] in the LEAK state was found ($p=0.005$). Pairwise comparisons showed that the mean LEAK FCR at 100 nM [Ca^{2+}] (0.062 ± 0.033) was significantly lower than at 0 nM [Ca^{2+}] (0.089 ± 0.042, $p=0.003$).

Instead of the LEAK state, FCR data showed a significant interaction effect between $[Ca^{2+}]$, genotype and FCR in $CI_{(OXPHOS)}$ state (p=0.001). Subsequent analysis using one-way ANOVAs showed that $CI_{(OXPHOS)}$ FCR in G2435R-RYR1 HET and HOM genotypes were significantly affected by differences in $[Ca^{2+}]$ (p=0.025 and p<0.001, respectively). Post hoc pairwise comparisons (Table 5.4) showed that $CI_{(OXPHOS)}$ FCR in G2435R-RYR1 HETs was significantly reduced at 300 nM $[Ca^{2+}]$ in comparison to 0 nM $[Ca^{2+}]$ (p=0.024). In G2435R-RYR1 HOMs, $CI_{(OXPHOS)}$ FCR at 100 nM $[Ca^{2+}]$ and 300 nM $[Ca^{2+}]$ was significantly reduced in comparison to 0 nM $[Ca^{2+}]$ (p<0.001 and p=0.001). Comparisons between 100 and 300 nM $[Ca^{2+}]$ was not significant different in any genotype.

	$[Ca^{2+}]$ (nM)			**Pairwise comparisons (p-values)**		
Genotype	**0**	**100**	**300**	**0 vs 100**	**0 vs 300**	**100 vs 300**
WT	0.52 (0.07)	0.49 (0.09)	0.42 (0.14)	1.000	0.100	0.541
G2435R-RYR1 HET	0.56 (0.06)	0.48 (0.08)	0.44 (0.18)	0.218	0.024	1.000
G2435R-RYR1 HOM	0.62 (0.09)	0.44 (0.06)	0.45 (0.12)	<0.001	0.001	1.000
T4826I-RYR1 HET	0.44 (0.04)	0.5 (0.08)	0.54 (0.27)	0.619	0.140	1.000

Table 5.4. Raw data for $CI_{(OXPHOS)}$ FCR in the calcium assay. Raw FCR data is presented as means (SD) for each genotype across all $[Ca^{2+}]$. Pairwise comparisons are also displayed with p-values adjusted with Bonferroni correction (p<0.05 is significant).

These results show that oxygen flux through complex I can be altered by both genotype and increasing $[Ca^{2+}]$ (Figure 5.4). The G2435R-RYR1 knock-in also presents evidence of a gene-dose dependent effect with the G2435R-RYR1 HOM genotype being the most sensitive to changes in $[Ca^{2+}]$ out of the four genotypes studied.

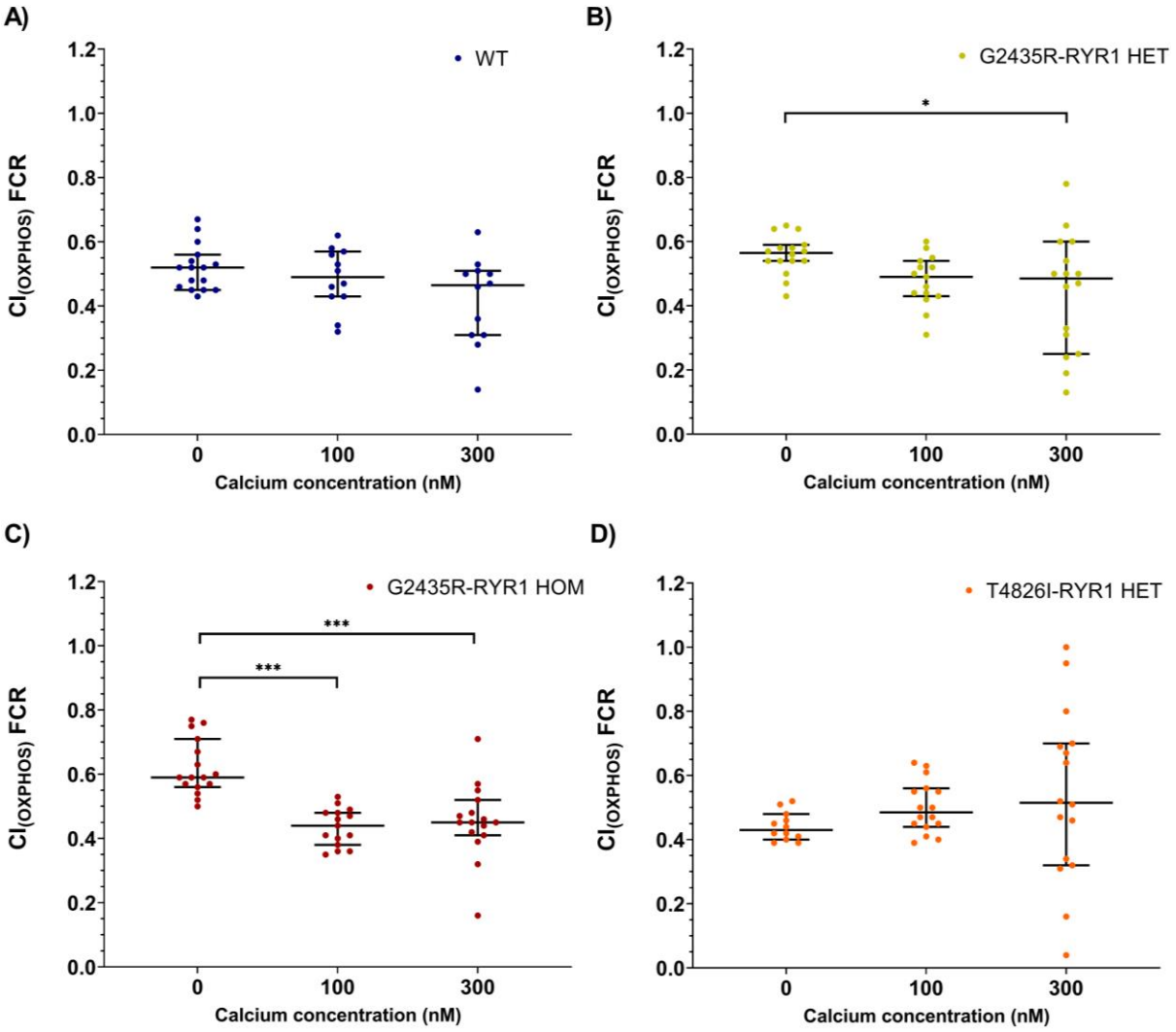

Figure 5.4. $CI_{(OXPHOS)}$ response to increasing concentrations of Ca^{2+}. This scatterplot illustrates the directional change of $CI_{(OXPHOS)}$ FCR at three different concentrations of Ca^{2+} (0, 100 and 300 nM). This data includes samples from four RYR1 mouse genotypes: **A)** WT (0 nM: n = 16; 100 nM: n = 12; 300 nM: n =12), **B)** G2435R-RYR1 HET (0 nM: n = 16; 100 nM: n = 16; 300 nM: n =16), **C)** G2435R-RYR1 HOM (0 nM: n = 16; 100 nM: n = 16; 300 nM: n =16) and **D)** T4826I-RYR1 HET mice (0 nM: n = 12; 100 nM: n = 16; 300 nM: n =16). Error bars present the median and 95% CI. Statistically significant pairwise comparisons are annotated by asterisks ($p<0.05$*, $p<0.01$***).

5.4 DISCUSSION

The data presented in this chapter provides the first evidence of altered mitochondrial bioenergetics in the G2435R-RYR1 knock-in mouse model of MH, supporting the association between mitochondrial dysfunction and MH susceptibility. Overall, mass-specific respiration rates between G2435R-RYR1 HOM, G2435R-RYR1 HET and WT mice were indistinguishable at baseline, except for complex IV. Mass-specific respiration through complex IV, adopted as the mitochondrial biomarker, was significantly lower in G2435R-RYR1 HOM muscle fibres in comparison to WT. This presents evidence of lower mitochondrial content which was not observed in G2435R-RYR1 HET mice.

The mitochondria from G2435R-RYR1 HOM mice also showed evidence of increased electron flow through the ETC, as the maximum OXPHOS capacity was significantly higher than WT. One explanation could be that muscle from G2435R-RYR1 HOM mice have adapted to having less mitochondrial content by increasing electron flow to compensate and meet the energy demands of the muscle. This adaptation may be attributed to an increase in complex I-facilitated OXPHOS, indicated by the elevated $CI_{(OXPHOS)}$ FCR which was also observed in the G2435R-RYR1 HOM genotype. Furthermore, complex II function was unaltered between genotypes which shows that G2435R-RYR1 HOM mice are more dependent on complex I function to satisfy bioenergetic requirements.

In contrast to the G2435R-RYR1 mouse line, baseline data from T4826I-RYR1 HET mice showed evidence of improved coupling efficiency, indicated by the significantly lower LEAK FCR values. The LEAK FCR can be an index of ETS uncoupling, reflecting the proportion of ETS capacity related to non-phosphorylating respiration. This finding was unexpected as MHS muscle has previously been associated with mitochondrial uncoupling at rest, which would imply a less efficient system (Giulivi et al., 2011; Chang et al., 2019; Cheah et al., 1989). Previous study on T4826I-RYR1 HET myotubes reported lower basal respiration, lower ETS capacity and reduced mitochondrial content compared to WT (Barrientos et al., 2012). These features were not observed in this dataset and these contrasting results may be due to differences in sample type, as this study used permeabilised muscle fibres which are a more accurate representation of muscle physiology over cultured myotubes.

With regards to the halothane response, there was no evidence of a hypermetabolic reaction in any mouse genotype after halothane exposure. This was unexpected as the similar

study described in chapter 3 (section 3.3.2), demonstrated elevated oxygen flux in human MHS muscle following IVCT halothane exposure, typical of a hypermetabolic response (Chang et al., 2019). Instead, this mouse study showed a significant decrease in OXPHOS and ETS capacity after halothane treatment across all mouse genotypes. This was attributed to a halothane-induced reduction in complex I-facilitated OXPHOS as no effect was seen in complex II.

As mentioned in the chapter 3 discussion (section 3.4), the inhibition of mitochondrial complex I after halothane exposure has been reported in numerous studies and supports a normal pharmacological response, unrelated to the MH phenotype (Britt et al., 1975; Gronert and Heffron, 1979; Falk et al., 2006; Kayser et al., 2004; Hanley et al., 2002). The inhibition effect was detected in this present mouse study but not in the human study and this may be due to the time delay between drug application and data collection. In this mouse study, oxygen flux was measured shortly after the addition of halothane (three minutes) whilst the human study featured a 90-120 minute time delay before measurements were taken after IVCT. This reinforces the idea that halothane-induced complex I inhibition is an acute effect which reverses over time (Chang et al., 2019; Hanley et al., 2002).

Furthermore, there was evidence of an interaction effect between halothane, genotype and complex I-facilitated OXPHOS after normalising for mitochondrial content. The G2435R-RYR1 mouse line was reported to have a gene-dose dependent increase in halothane sensitivity (Lopez et al., 2018), but this was not demonstrated in this present study. Results showed that T4826I-RYR1 HET muscle was more severely affected by halothane in comparison to WT and both G2435R-RYR1 genotypes. This suggests that the mitochondria from the T4826I-RYR1 mouse line have greater sensitivity to halothane which may contribute to a more severe phenotype over the G2435R-RYR1 mutation. This is supported by the MH genotype-phenotype correlation data generated from human MHS muscle, which showed individuals carrying the T4826I-RYR1 mutation having greater IVCT contracture strengths after exposure to halothane, in comparison to the human G2435R-RYR1 mutation (Carpenter et al., 2009b).

Following the halothane experiments, an investigation into the effects of Ca^{2+} on mitochondrial respiration rates was carried out by modifying the $[Ca^{2+}]$ in the assay media. Increasing the $[Ca^{2+}]$ helped mimic the normal muscle physiology between genotypes, as MHS muscle is associated with elevated $[Ca^{2+}]_{rest}$ due to mutant RYR1 channels leaking Ca^{2+} from the SR. The concentrations chosen for this study were 0, 100 and 300 nM, which covers the

range in mean intracellular [Ca^{2+}] reported in the G2435R-RYR1 mouse line (156 nM in HET mice and 265 nM in HOM mice) (Lopez et al., 2018). This range was also appropriate for the T4826I-RYR1 mouse line, in which the HET myotubes were reported to have a mean [Ca^{2+}] of 278 nM (Barrientos et al., 2012).

Results showed that the modification of assay [Ca^{2+}] only impacted the function of complex I-facilitated OXPHOS across the G2435R-RYR1 mouse line, as WT and T4826I-RYR1 mice were unaffected. The output through complex I was significantly reduced in G2435R-RYR1 HET mice at 300 nM [Ca^{2+}], and a similar effect was seen in HOM mice at as low as 100 nM [Ca^{2+}]. These results show a gene-dose dependent effect, with G2435R-RYR1 HOM mice being the most sensitive to changes in intracellular Ca^{2+}, possibly due to differences in mitochondrial Ca^{2+} uptake. This inhibition effect was surprising since Ca^{2+} is generally regarded as a positive regulator of mitochondrial function, primarily through the upregulation of intra-mitochondrial dehydrogenase enzymes which increases the supply of NADH (Denton, 2009; Panov and Scaduto, 1995). However, a study using submitochondrial particles prepared from rat heart reported a similar inhibition of complex I by Ca^{2+}, in which the inactivation was specific to complex I with no alterations in the rest of the ETS (Matsuzaki and Szweda, 2007). These contrasting reports highlight further complexity in the relationship between mitochondria and Ca^{2+}.

Mitochondrial Ca^{2+} uptake into the matrix is dictated by the MCU, which functions at a threshold of >500 nM [Ca^{2+}], preventing mitochondrial stimulation in the presence of small fluctuations in Ca^{2+} (Csordas et al., 2013). The fact that mitochondrial function was altered in both G2435R-RYR1 HET and HOM mice at 300 nM and 100 nM [Ca^{2+}] respectively, suggests that Ca^{2+} was able to bypass the MCU threshold and enter the mitochondrial matrix. One possible explanation would be that that the MCU threshold is lower in the G2435R-RYR1 mouse line, allowing Ca^{2+} to enter the mitochondrial matrix at a lower $[Ca^{2+}]_{rest}$. Alternatively, it is possible that another means of Ca^{2+} transport independent of MCU may be available which can be accessed at a lower $[Ca^{2+}]_{rest}$. The existence of alternative Ca^{2+} uptake methods is still a subject of debate within the field and challenges the dogma of MCU being the single mode of Ca^{2+} transport into mitochondria (De Stefani et al., 2015). Two other proposed means of mitochondrial Ca^{2+} import are rapid mode of uptake (RaM), in which Ca^{2+} uptake is mediated through cytosolic Ca^{2+} pulses (Bazil and Dash, 2011; Buntinas et al., 2001; Sparagna et al., 1995) and mitochondrial RYR1, which was reported to be in rat heart mitochondria (Beutner et al., 2005; Altschafl et al., 2007). Despite conflicts of opinion, all three methods of Ca^{2+}

transport may exist, as the study by Bondarenko et al. identified three distinct Ca^{2+} currents with different sensitivities from electrophysiological recordings of mitoplasts (Bondarenko et al., 2013).

The consequences of a lower MCU threshold or Ca^{2+} overload in mitochondria presents the risk of MPTP activation which leads to mitochondrial swelling and cell death, in addition to an increase in oxidative stress through constant stimulation of the ETS (Rasola and Bernardi, 2011). Researchers using muscle from the Y522S-RYR1 mouse model, observed both those features which lead to a hypothesis outlining a destructive feed-forward cycle within skeletal muscle. This hypothesis is based around the consequences of SR Ca^{2+} leaks, which elevate $[Ca^{2+}]_{rest}$ and ROS production, contributing to increased oxidative stress and mitochondrial dysfunction over time (Yuen et al., 2012; Boncompagni et al., 2009). This proposed mechanism may be present in the G2435R-RYR1 mouse line, as similar features have been observed.

A colleague within the Leeds MH Unit, Dr Xiaochen Liu, conducted an oxidative stress study on the G2435R-RYR1 mouse line to address this hypothesis (Chang et al., 2020). Liu and colleagues measured the protein expression of two major oxidative stress proteins, NADPH oxidase 2 (NOX2) and superoxide dismutase 1 (SOD1), using western blots, and adopted a fluorescent dye (CellROX Green) to measure ROS production in adult muscle fibres. NOX2 is a producer of ROS in skeletal muscle (Ferreira and Laitano, 2016), and was found to be expressed at a significantly higher level in G2435R-RYR1 HOM mice in comparison to WT. In contrast, SOD1 is an antioxidative enzyme (Powers et al., 2011), which was expressed at a significantly lower level in G2435R-RYR1 HOM mice compared to WT, suggesting a deficiency in ROS regulation. Furthermore, the CellROX green assay using adult muscle fibres, showed that G2435R-RYR1 knock-in mice have a gene-dose dependent elevation of ROS production in response to H_2O_2 induced oxidative stress. Collectively, the data from Liu and colleagues provide evidence of elevated oxidative stress in G2435R-RYR1 knock-in mice (Chang et al., 2020), consistent with observations reported in other MHS RYR1 knock-in mice (Durham et al., 2008; Giulivi et al., 2011; Yuen et al., 2012; Michelucci et al., 2017). The elevated level of oxidative stress identified by Dr Liu, may coincide with the alterations in complex I function observed in this study, since it is one of the main sources of ROS production in mitochondria (Murphy, 2009b; Grivennikova and Vinogradov, 2006).

In summary, the G2435R-RYR1 mouse model for MH has shown some evidence of mitochondrial dysfunction which appears to occur in a gene-dose dependent manner.

Individuals with the equivalent c.7300G>A human MH variant are generally associated with weaker clinical phenotypes and the lack of differences seen between WT and G2435R-RYR1 HET mice reflect this statement. The muscle from G2435R-RYR1 HOM mice has shown evidence of increased electron flow through complex I which is thought to be a compensation mechanism for reduced mitochondrial content. Both the G2435R-RYR1 HET and HOM muscle had increased sensitivity to intracellular Ca^{2+} which may be due to a reduction in MCU threshold. The observations from the T4826I-RYR1 HETs provide evidence of improved coupling efficiency and increased sensitivity to halothane exposure. The differences in mitochondrial bioenergetics across RYR1 knock-in genotypes may correspond with differences in phenotype severity by affecting skeletal muscle sensitivity to both halothane and caffeine. These outcomes are thought to have been perpetuated by elevated $[Ca^{2+}]_{rest}$ and increased oxidative stress.

6 GENERAL DISCUSSION

MH has traditionally been regarded as an autosomal dominant disorder, but evidence now supports a more complex 'multifactorial' model of inheritance, which includes the involvement of additional genetic/non-genetic factors contributing to MH susceptibility. The aim of this thesis was to identify potential modifiers of, and contributors to, the MH phenotype. This was achieved by investigating differential gene expression and mitochondrial function in MHN and MHS skeletal muscle, before (baseline) and after drug exposure. In this final discussion chapter, the main findings from each results chapter will be summarised with comparisons between human MHS and RYR1 knock-in mouse muscle. The limitations of these studies will be outlined and ideas for future research development will be discussed.

6.1 DIFFERENTIAL GENE EXPRESSION BETWEEN MHN AND MHS SKELETAL MUSCLE

The results from both human and mouse RNAseq experiments identified a downregulation in mitochondria-related gene expression at baseline. In the human RNAseq study, many genes involved in the OXPHOS pathway had reduced expression in MHS muscle biopsies, with an emphasis on those encoding mitochondrial complex I. OXPHOS gene expression was reduced when human muscle biopsies were exposed to halothane through IVCT, but this was only observed in MHN muscle. This reduction of OXPHOS gene expression reflects a negative shift in metabolic activity which is perhaps a normal pharmacological response to anaesthesia that is absent in MHS muscle.

Studies have shown that mitochondria are a direct target of volatile anaesthetics, and complex I is known to be selectively inhibited upon exposure (Hanley et al., 2002; Kayser et al., 2004). This interaction effect is not specific to skeletal muscle and has also been demonstrated in mitochondria from the heart, brain, liver, and nervous tissues (Hanley et al., 2002; Zimin et al., 2018; Zimin et al., 2016; Harris et al., 1971). It has been proposed that mitochondrial complex I may modulate the anaesthetic response as research has shown that complex I-deficient organisms (*C. elegans* and knock-out mice) have heightened sensitivity to volatile anaesthetics (Falk et al., 2006; Quintana et al., 2012; Zimin et al., 2018). This feature

may extend to MHS humans since complex I-encoding gene expression was reduced, which needs to be confirmed at the protein level.

With regards to MHS mice, only a few genes encoding ETC complexes were downregulated in G2435R-RYR1 HOM (*Ndufs1*, *Ndufs2*, *Sdha* and *Uqcrc2*) and T4826I-RYR1 HET (*Uqcrc2*) genotypes at baseline. This suggests that potential deficiencies in the ETC expression are less marked in MHS mice. Most of the genes downregulated in RYR1 knock-in mice were involved in fatty acid oxidation and transport, which affects OXPHOS indirectly. This was observed in both G2435R-RYR1 HOM and T4826I-RYR1 HET mice, but absent in G2435R-RYR1 HETs, indicating a gene-dose dependent effect within the G2435R-RYR1 model, and an *Ryr1* variant-specific effect between HET genotypes. Fatty acid oxidation was also among the top 10 downregulated pathways in MHS humans, but only five genes within the pathway had reduced expression.

Defects in fatty acid metabolism were first associated with MH susceptibility, after an accumulation of FFA was detected in the mitochondria of MHS pigs (Cheah, 1981; Cheah and Cheah, 1981a; Cheah and Cheah, 1981b). A similar feature was also observed in studies using human MHS muscle which proposed that halothane sensitivity in MHS muscle was associated with elevated levels of FFA (Fletcher et al., 1991a; Fletcher and Rosenberg, 1986; Fletcher et al., 1991b). Aside from MHS pigs and humans, evidence of lowered fatty acid oxidation was also observed in the R163C-RYR1 mouse model of MH (Giulivi et al., 2011). In support of those findings, the baseline data from mouse, and to a lesser extent human, RNAseq experiments suggest that fatty acid oxidation may be deficient in MHS muscle which may contribute towards the MH phenotype.

The G2435R-RYR1 HET mice, represent the most common genotype found in MHS humans (c.7300G>A) within the UK (Lopez et al., 2018; Miller et al., 2018). The c.7300G>A variant is considered a weak mutation based on IVCT contracture strengths (Carpenter et al., 2009b), and this is reflected by the transcriptome profiles from G2435R-RYR1 HET mice, which were indistinguishable from WT, before and after exposure to halothane. Unlike the human RNAseq data, the method of halothane exposure applied to RYR1 knock-in mouse muscle resulted in almost no change to gene expression across all genotypes. This was surprising since OXPHOS gene expression was downregulated in human MHN muscle after IVCT halothane exposure, and a similar observation was expected to occur in WT mice. These

findings suggest that the method of halothane exposure may not have been appropriate for this study and further experiments are needed to address the shortcomings in design.

6.2 MITOCHONDRIAL FUNCTION BETWEEN MHN AND MHS SKELETAL MUSCLE

Consistent with RNAseq data, functional testing of MHS skeletal muscle revealed evidence of mitochondrial dysfunction in both human and RYR1 knock-in mouse muscle at baseline. However, some discrepancies were identified between species. Firstly, the functional biomarker for mitochondrial content (mass-specific $CIV_{(MAX)}$) suggested an upregulation of mitochondrial content in human MHS muscle, which was not observed in RYR1 knock-in mice. The mitochondrial biomarker only differed in G2435R-RYR1 HOM mice, which was found to be significantly lower than WT. This HOM mouse genotype is not a model for human MH, since very few cases of human MHS are recessive carriers of the RYR1 mutation. However, the HOM mouse genotype does give insight into how RYR1 mutations affect biological systems with increased gene dosage. The concept of human MHS muscle having higher mitochondrial content, contradicts the mouse literature as studies on the Y522S-RYR1, T4826I-RYR1 and R163C-RYR1 variants, have all reported evidence of reduced mitochondrial content (Boncompagni et al., 2009; Giulivi et al., 2011; Barrientos et al., 2012). These conflicting data may be due to differences in muscle fibre type composition which will be discussed in section 6.3.

Human respirometry data normalised for mitochondrial content, showed evidence of reduced OXPHOS capacity and CII deficiency in MHS mitochondria. This indicates functional impairment, which aligns with the study by Thompson et al. describing impaired aerobic metabolism and reduced ATP production in MHS individuals (Thompson et al., 2017). No deficiency in complex I activity was observed, despite the downregulation of complex I-encoding gene expression identified in RNAseq data. In contrast, none of these observations were present in RYR1 knock-in mice. MHS humans typically do not exhibit clinical phenotypes in absence of anaesthetic triggers but some cases have reported muscle-related symptoms such as weakness, exercise intolerance and exercise-induced rhabdomyolysis (Timmins et al., 2015; Wappler et al., 2001; Litman et al., 2018). Certain *RYR1* variants, such as those associated with central core disease, are known to result in central cores and

diminished oxidative metabolism. On that basis, it is possible that specific MH-associated *RYR1* variants, confer varying degrees of influence on mitochondrial function and these myopathic features may only be associated with 'stronger' *RYR1* variants.

This hypothesis was supported in the mouse respirometry data, as mitochondrial function differed between each RYR1 knock-in genotype. Mitochondrial function at baseline, between G2435R-RYR1 HET (weak mutation) and WT mice was indistinguishable whilst, a lower LEAK respiration rate was detected in the T4826I-RYR1 HET genotype (strong mutation) (Carpenter et al., 2009b), providing evidence of *Ryr1* variant-dependent effects on mitochondrial function. Mitochondrial dysfunction from the G2435R-RYR1 mouse model was detected primarily in the HOM genotype, showing evidence of increased complex I dependence and reduced mitochondrial content in permeabilised muscle fibres.

With regards to treatment effects, mitochondria from human MHS muscle biopsies experienced elevated respiration rates after IVCT halothane exposure, with increased severity in MHS_{hc} individuals. This increase in activity is indicative of a hypermetabolic response which is typical of an MH reaction, but contradicts the complex I inhibition effect associated with volatile anaesthetics (Hanley et al., 2002; Zimin et al., 2018; Zimin et al., 2016; Harris et al., 1971). This lack of inhibition has been attributed to the time delay (~90-120 min) between IVCT treatment and respirometry measurements as this effect is known to be reversible. It was speculated that the complex I inhibition was initiated upon first exposure to IVCT halothane but was reversed at the time of respirometry data collection.

This information was used to modify the method of halothane exposure for mouse respirometry experiments and the data generated supported that hypothesis. Halothane was dissolved in DMSO and directly applied to each respirometry chamber to avoid the time delay experienced using human samples, and consequently the halothane-induced complex I inhibition was detected. Direct application of halothane inhibited complex I respiration across all mouse genotypes, but the effect was significantly greater in T4826I-RYR1 HET mice. The mitochondria from RYR1 knock-in mice did not show evidence of the hypermetabolic response demonstrated using human MHS muscle which implies that the MH reaction was not triggered using this method of halothane exposure.

Finally, in addition to halothane treatment, the mouse respirometry experiments assessed the effect of Ca^{2+} on MHS mitochondrial function, since MHS muscle is associated with elevated $[Ca^{2+}]_{rest}$ at baseline (Barrientos et al., 2012; Lopez et al., 2018). A $[Ca^{2+}]$ range

(0 – 300 nM) was chosen to mimic physiological conditions in both MHN and MHS muscle and subsequent exposure to these [Ca^{2+}] caused complex I inhibition in G2435R-RYR1 knock-in mice only. This Ca^{2+}-induced complex I inhibition also showed a gene-dose dependent effect, as G2435R-RYR1 HOM mice were more sensitive to [Ca^{2+}] changes than HET counterparts. This inhibition effect was unexpected since Ca^{2+} is known to be a positive regulator of mitochondrial function (Denton, 2009), and these data may reflect further complexity in the relationship between Ca^{2+} and mitochondria. Furthermore, these results suggest that mitochondrial complex I deficiency is in fact present in G2435R-RYR1 knock-in mice at baseline, but only in the presence of physiologically relevant $[Ca^{2+}]_{rest}$, which needs to be considered in future MH research.

6.3 LIMITATIONS

The four studies described in this thesis all utilised skeletal muscle biopsies which are subject to a similar set of limitations with respect to muscle architecture and quality. These limitations must be taken into consideration when comparing results between studies. Firstly, skeletal muscle is highly plastic and muscle fibre type distribution vary between samples. The quadriceps of untrained individuals is composed of predominantly oxidative fibres (~41% type I slow-twitch oxidative, ~31% type IIA fast-twitch oxidative) (Staron et al., 2000), and a similar proportion has been reported in *Soleus* muscles from mice (~37% type I slow-twitch oxidative, ~39% type II fast-twitch oxidative fibres) (Augusto et al., 2004).

Due to lifestyle diversity, muscle fibre type composition in the human samples can vary significantly as a result of differences in fitness level and adaptations from physical training (e.g. type I slow-twitch oxidative bias from distance running and type IIB fast-twitch glycolytic bias from sprinting). Data on individual fitness level and fibre type composition was not collected and may account for some of the variability seen in human studies. For instance, measurements of mitochondrial content from the human respirometry study may have been influenced by individuals with a higher proportion of type I slow-twitch oxidative fibres, which are rich in mitochondria. This would therefore inflate the results of the mitochondrial biomarker, which should be considered before drawing conclusions. With respect to mouse studies, differences in fibre type composition is thought to be negligible, as all subjects were

exposed to the same living environment so any muscle fibre adaptation will have been shared across genotypes.

In addition to muscle fibre type, another limitation of the human studies is the variety in *RYR1* variants. Due to the opportunistic nature of sample availability, experiments on fresh muscle do not enable us to explore the effects of individual variants. The human MHS samples used in RNAseq, all contained different *RYR1* variants which may confer different strengths in phenotype (Carpenter et al., 2009b). The data generated from mouse RNAseq illustrate how different RYR1 genotypes can alter muscle gene expression and mitochondrial function in different ways which will no doubt contribute to variability in human studies. Likewise, the human MHS samples assessed by high-resolution respirometry included 18 different *RYR1* variants, of which only one (c.1021G>A) was functionally characterised. The *RYR1* c.1021G>A is a weak variant based on IVCT contracture data (Carpenter et al., 2009b), but the relative strengths of the remaining 17 variants are unknown. These uncharacterised *RYR1* variants may be strong mutations, resulting in more overt defects in skeletal muscle - a variable which could not be factored into the analysis.

Aside from inherent limitations within sampling, the methods of drug application in each study was restricted and may not have triggered the appropriate responses in MHS muscle. With regards to both human studies, the IVCT procedure used to administer halothane was complex, involving additional variables (muscle stretching, electrical stimulation, incremental drug dosage) that could have influenced gene expression outside of halothane-induced effects. There is also the issue of whether the halothane exposure time/dosage applied during the IVCT, is sufficient to trigger changes in gene expression and mitochondrial function associated with an MH reaction. These variables could not be altered as all human muscle biopsies were required to undergo IVCT for diagnostic purposes prior to research usage.

The use of RYR1 knock-in mouse models, allowed greater flexibility over experimental conditions since halothane application was not restricted by the IVCT. The method of halothane exposure used for mouse RNAseq resembled the IVCT procedure, but the additional variables (muscle stretching, electrical stimulation, incremental drug dosage) were removed. Surprisingly, this modified application of halothane had almost no effect on muscle gene expression across all RYR1 knock-in mouse genotypes. This showed that the methodology needed to be amended through additional experiments to deduce whether this lack of response is a result of drug dose/ exposure time or additional variables not yet considered.

In an ideal scenario, a dose-response curve and time course experiment should have been conducted prior to RNAseq to optimise experimental factors. The most effective way to achieve this is through *in vitro* experiments using cultured myotubes. The use of fresh muscle biopsies provide a more accurate representation of muscle physiology, but cultured myotubes provide several advantages for experimental design. Myotubes can be prepared from the muscle samples of select individuals who are of similar age and fitness, carrying specific RYR1 genotypes. Drugs can also be incorporated into culture media in a plate format to allow flexibility over drug exposure time and drug concentrations, all of which would be impossible to replicate *in vivo*.

A dose response experiment can be conducted with cultured myotubes using a microplate reader measuring Ca^{2+} flux. A range of halothane concentrations can be assessed with this method to identify the dose which elicits a maximum response, indicated by Ca^{2+} flux. Once the ideal drug concentration is identified, the effect of halothane exposure time on gene expression can be assessed in a time course experiment. The optimal halothane dose can be applied to myotubes over a duration spanning 0 to 24-hours, before mRNA is extracted at multiple time points and prepared for RNAseq. Analysis of gene expression at each time point will reveal the optimal time point required for halothane-induced gene expression to occur.

This same information can be used to inform the method of halothane application used in mouse respirometry. As previously mentioned, halothane exposure reversibly inhibits mitochondrial complex I, which was not detected in the human respirometry study. This was attributed to the time delay between treatment and assay. The direct application of halothane (dissolved in DMSO) in mouse respirometry, avoided this time delay, and caused a significant downregulation of complex I which aligns with the halothane-mitochondria interactions reported in literature. However, the mouse experiment failed to trigger the hypermetabolic response observed in the human respirometry data, indicating that the MH reaction was not triggered in RYR1 knock-in mouse muscle. Again, this may be due to insufficient halothane dosage or exposure time which can be addressed through the dose-response and time course experiments discussed above.

6.4 FUTURE DEVELOPMENT

Despite the limitations, these studies have provided valuable insight into MH pathophysiology, which can now be used inform future MH research. Each study within this thesis has showed evidence of mitochondrial defect in MHS muscle, highlighting its relevance within MH susceptibility. This area of research should be pursued further to clarify its contribution towards MH. Possibilities for further development include:

- **Investigations into potential modifier loci.** With regards to the human gene expression data, three OXPHOS genes of interest (*ATP5MD*, *NDUFC2*, *COQ6*) have already been validated using RT-PCR and followed up using bioinformatic resources. These genes were found to be regulated by a common set of TFs that bind to enhancer regions local to the genes of interest. A list of SNPs, capable of influencing gene expression, were subsequently identified within each enhancer using eQTL information available on the GTEx database. Since these OXPHOS genes are regulated by the same TFs, a SNP within an enhancer, could affect TF binding and influence the expression of the genes of interest. These SNPs therefore represent potential modifier loci capable of influencing the MH phenotype, which can be investigated through SNP genotyping experiments on wider populations of MHS individuals. The Leeds MH Unit has access to 6276 DNA samples (1961 MHS, 3339 MHN, 976 unknown phenotype) with the largest population of MHS individuals worldwide. 780 MHS DNA samples have been prepared on screening plates and are now available for screening. Successful association of these SNPs with the wider MHS population, will provide evidence of these loci contributing towards the MHS phenotype and demonstrate the importance of mitochondrial function within MH susceptibility.

- **Glycolytic metabolism in MHS skeletal muscle.** The studies performed in this thesis have utilised MHS muscles from the quadriceps and *Soleus* which are composed primarily of type I and IIA muscle fibres favouring oxidative metabolism. It will be useful to gain insight into anaerobic metabolism for a comprehensive view of MHS muscle metabolism. This could be achieved by performing similar experiments using muscle groups composed primarily of type II fast-twitch fibres favouring glycolytic metabolism (such as the *Extensor digitorum longus*). Alternatively, glycolytic function could be assessed in cultured myotubes using the XF Glycolysis Stress Test Kit

available on the Agilent Seahorse XF Analyser. Previous respirometry experiments have been carried out using the Oroboros Analyser which allows detailed analyses of individual samples, but it is not suitable for high throughput analyses e.g. testing multiple cell lines. The Agilent Seahorse XF Analysers can measure oxygen consumption rates and extracellular acidification rate in cell culture plate formats, allowing different MHN and MHS cell lines to be assessed simultaneously.

- **Fatty acid metabolism in MHS skeletal muscle.** Fatty acid metabolism should be investigated further in the context of MH as many genes in this pathway were downregulated in RYR1 knock-in mice. Follow up investigations would first involve selecting genes of interest within the fatty acid β-oxidation pathway and validating them using RT-PCR to confirm RNAseq findings. Once validated, western blotting could be used to confirm whether gene expression differences are consistent at the protein level before moving onto functional assays for fatty acid metabolism. Mitochondrial function and fatty acid oxidation can be assessed within myotubes cultured from RYR1 knock-in mouse or MHS human genotypes, using the XF Cell Mito Stress test and palmitate-BSA substrate kits developed for the Agilent Seahorse XF Analyser. Any fatty acid oxidation deficiency found in MHS samples will support the connection between MH and fatty acid oxidation suggested by the gene expression data presented.

- ***Ryr1* variant-specific effects on muscle function.** The RYR1 knock-in mouse data has demonstrated evidence of mutation-specific effects on mitochondrial function. This can be investigated in both MHS humans and RYR1 knock-in mice, by comparing functional differences between cultured myotubes carrying different *Ryr1* variants. The Leeds MH Unit has myoblasts from three RYR1 knock-in mouse lines (R163C, G2435R and T4826I) and human myoblasts from the analogous R163C (5 patients), G2434R (12 patients) and T4826I (1 patient). These samples can be used in the glycolytic and fatty acid metabolism experiments described above, to investigate *Ryr1* variant-specific effects as a secondary objective.

6.5 CONCLUSION

This thesis contains a comprehensive account of differential gene expression and mitochondrial function in MHN and MHS skeletal muscle, before and after halothane exposure. Transcriptome analysis of human and mouse MHS muscle have both shown a downregulation of OXPHOS-related gene expression which is a sign of metabolic defect. This is supported by the functional assessment of MHS muscle using high resolution respirometry, which has also demonstrated evidence of functional deficiency within mitochondria. Investigations using MH mouse models showed differing results between RYR1 knock-in mouse genotypes, demonstrating a gene-dose and variant-dependent effect on mitochondrial function. Together, these data provide a framework for future MH research and has highlighted the importance of mitochondrial function, a potential contributor of phenotype variability within MH.

7 REFERENCES

ALEMAN, M., RIEHL, J., ALDRIDGE, B. M., LECOUTEUR, R. A., STOTT, J. L. & PESSAH, I. N. 2004. Association of a mutation in the ryanodine receptor 1 gene with equine malignant hyperthermia. *Muscle Nerve,* 30**,** 356-65.

ALTSCHAFL, B. A., BEUTNER, G., SHARMA, V. K., SHEU, S. S. & VALDIVIA, H. H. 2007. The mitochondrial ryanodine receptor in rat heart: a pharmaco-kinetic profile. *Biochim Biophys Acta,* 1768**,** 1784-95.

AMERICAN COLLEGE OF SPORTS, M., ARMSTRONG, L. E., CASA, D. J., MILLARD-STAFFORD, M., MORAN, D. S., PYNE, S. W. & ROBERTS, W. O. 2007. American College of Sports Medicine position stand. Exertional heat illness during training and competition. *Med Sci Sports Exerc,* 39**,** 556-72.

ANDERSON, S., BANKIER, A. T., BARRELL, B. G., DE BRUIJN, M. H., COULSON, A. R., DROUIN, J., EPERON, I. C., NIERLICH, D. P., ROE, B. A., SANGER, F., SCHREIER, P. H., SMITH, A. J., STADEN, R. & YOUNG, I. G. 1981. Sequence and organization of the human mitochondrial genome. *Nature,* 290**,** 457-65.

AO, S. I., YIP, K., NG, M., CHEUNG, D., FONG, P. Y., MELHADO, I. & SHAM, P. C. 2005. CLUSTAG: hierarchical clustering and graph methods for selecting tag SNPs. *Bioinformatics,* 21**,** 1735-6.

AUGUSTO, V., PADOVANI, C. R. & CAMPOS, G. E. R. 2004. Skeletal muscle fiber types in C57Bl6J mice. *Brazil Journal of Morphology Science,* 21**,** 89-94.

BANNISTER, R. A. 2013. Dantrolene-induced inhibition of skeletal L-type Ca2+ current requires RyR1 expression. *Biomed Res Int,* 2013**,** 390493.

BANNISTER, R. A., ESTEVE, E., ELTIT, J. M., PESSAH, I. N., ALLEN, P. D., LOPEZ, J. R. & BEAM, K. G. 2010. A malignant hyperthermia-inducing mutation in RYR1 (R163C): consequent alterations in the functional properties of DHPR channels. *J Gen Physiol,* 135**,** 629-40.

BARBAGALLO, M. & DOMINGUEZ, L. J. 2015. Magnesium and type 2 diabetes. *World J Diabetes,* 6**,** 1152-7.

BARBIERI, E. & SESTILI, P. 2012. Reactive oxygen species in skeletal muscle signaling. *J Signal Transduct,* 2012**,** 982794.

BARCA, E., GANETZKY, R. D., POTLURI, P., JUANOLA-FALGARONA, M., GAI, X., LI, D., JALAS, C., HIRSCH, Y., EMMANUELE, V., TADESSE, S., ZIOSI, M., AKMAN, H. O., CHUNG, W. K., TANJI, K., MCCORMICK, E. M., PLACE, E., CONSUGAR, M., PIERCE, E. A., HAKONARSON, H., WALLACE, D. C., HIRANO, M. & FALK, M. J. 2018. USMG5 Ashkenazi Jewish founder mutation impairs mitochondrial complex V dimerization and ATP synthesis. *Hum Mol Genet,* 27**,** 3305-3312.

BARRIENTOS, G. C., FENG, W., TRUONG, K., MATTHAEI, K. I., YANG, T., ALLEN, P. D., LOPEZ, J. R. & PESSAH, I. N. 2012. Gene dose influences cellular and calcium channel dysregulation in heterozygous and homozygous T4826I-RYR1 malignant hyperthermia-susceptible muscle. *J Biol Chem,* 287**,** 2863-76.

BARTLETT, J. R., FRIEDMAN, K. J., LING, S. C., PACE, R. G., BELL, S. C., BOURKE, B., CASTALDO, G., CASTELLANI, C., CIPOLLI, M., COLOMBO, C., COLOMBO, J. L., DEBRAY, D., FERNANDEZ, A., LACAILLE, F., MACEK, M., JR., ROWLAND, M., SALVATORE, F., TAYLOR, C. J., WAINWRIGHT, C., WILSCHANSKI, M., ZEMKOVA, D., HANNAH, W. B., PHILLIPS, M. J., COREY, M., ZIELENSKI, J., DORFMAN, R., WANG, Y., ZOU, F., SILVERMAN, L. M.,

DRUMM, M. L., WRIGHT, F. A., LANGE, E. M., DURIE, P. R., KNOWLES, M. R. & GENE MODIFIER STUDY, G. 2009. Genetic modifiers of liver disease in cystic fibrosis. *JAMA,* 302**,** 1076-83.

BAZIL, J. N. & DASH, R. K. 2011. A minimal model for the mitochondrial rapid mode of Ca(2)+ uptake mechanism. *PLoS One,* 6**,** e21324.

BENJAMINI, Y. & HOCHBERG, Y. 1995. Controlling the False Discovery Rate: A Practical and Powerful Approach to Multiple Testing. *Journal of the Royal Statistical Society. Series B (Methodological),* 57**,** 289-300.

BERG, J. M., TYMOCZKO, J. L. & STRYER, L. 2002. *Biochemistry,* New York, W H Freeman.

BEUTNER, G., SHARMA, V. K., LIN, L., RYU, S. Y., DIRKSEN, R. T. & SHEU, S. S. 2005. Type 1 ryanodine receptor in cardiac mitochondria: transducer of excitation-metabolism coupling. *Biochim Biophys Acta,* 1717**,** 1-10.

BEZAWORK-GELETA, A., ROHLENA, J., DONG, L., PACAK, K. & NEUZIL, J. 2017. Mitochondrial Complex II: At the Crossroads. *Trends Biochem Sci,* 42**,** 312-325.

BLACKMAN, S. M., HSU, S., RITTER, S. E., NAUGHTON, K. M., WRIGHT, F. A., DRUMM, M. L., KNOWLES, M. R. & CUTTING, G. R. 2009. A susceptibility gene for type 2 diabetes confers substantial risk for diabetes complicating cystic fibrosis. *Diabetologia,* 52**,** 1858-65.

BONCOMPAGNI, S., ROSSI, A. E., MICARONI, M., HAMILTON, S. L., DIRKSEN, R. T., FRANZINI-ARMSTRONG, C. & PROTASI, F. 2009. Characterization and temporal development of cores in a mouse model of malignant hyperthermia. *Proc Natl Acad Sci U S A,* 106**,** 21996-2001.

BONDARENKO, A. I., JEAN-QUARTIER, C., MALLI, R. & GRAIER, W. F. 2013. Characterization of distinct single-channel properties of Ca(2)(+) inward currents in mitochondria. *Pflugers Arch,* 465**,** 997-1010.

BRACKETT, J. C., SIMS, H. F., RINALDO, P., SHAPIRO, S., POWELL, C. K., BENNETT, M. J. & STRAUSS, A. W. 1995. Two alpha subunit donor splice site mutations cause human trifunctional protein deficiency. *J Clin Invest,* 95**,** 2076-82.

BRANDOM, B. W., BINA, S., WONG, C. A., WALLACE, T., VISOIU, M., ISACKSON, P. J., VLADUTIU, G. D., SAMBUUGHIN, N. & MULDOON, S. M. 2013. Ryanodine receptor type 1 gene variants in the malignant hyperthermia-susceptible population of the United States. *Anesth Analg,* 116**,** 1078-86.

BRISTON, T., ROBERTS, M., LEWIS, S., POWNEY, B., J, M. S., SZABADKAI, G. & DUCHEN, M. R. 2017. Mitochondrial permeability transition pore: sensitivity to opening and mechanistic dependence on substrate availability. *Sci Rep,* 7**,** 10492.

BRITT, B. A., ENDRENYI, L., CADMAN, D. L., FAN, H. M. & FUNG, H. Y. 1975. Porcine malignant hyperthermia: effects of halothane on mitochondrial respiration and calcium accumulation. *Anesthesiology,* 42**,** 292-300.

BRITT, B. A., KALOW, W., GORDON, A., HUMPHREY, J. G. & REWCASTLE, N. B. 1973. Malignant hyperthermia: an investigation of five patients. *Can Anaesth Soc J,* 20**,** 431-67.

BRODY, I. A. 1969. Muscle contracture induced by exercise. A syndrome attributable to decreased relaxing factor. *N Engl J Med,* 281**,** 187-92.

BROWN, R. L., POLLOCK, A. N., COUCHMAN, K. G., HODGES, M., HUTCHINSON, D. O., WAAKA, R., LYNCH, P., MCCARTHY, T. V. & STOWELL, K. M. 2000. A novel ryanodine receptor mutation and genotype-phenotype correlation in a large malignant hyperthermia New Zealand Maori pedigree. *Hum Mol Genet,* 9**,** 1515-24.

BUA, E., JOHNSON, J., HERBST, A., DELONG, B., MCKENZIE, D., SALAMAT, S. & AIKEN, J. M. 2006. Mitochondrial DNA-deletion mutations accumulate intracellularly

to detrimental levels in aged human skeletal muscle fibers. *Am J Hum Genet,* 79**,** 469-80.
BUNTINAS, L., GUNTER, K. K., SPARAGNA, G. C. & GUNTER, T. E. 2001. The rapid mode of calcium uptake into heart mitochondria (RaM): comparison to RaM in liver mitochondria. *Biochim Biophys Acta,* 1504**,** 248-61.
BURKMAN, J. M., POSNER, K. L. & DOMINO, K. B. 2007. Analysis of the clinical variables associated with recrudescence after malignant hyperthermia reactions. *Anesthesiology,* 106**,** 901-6; quiz 1077-8.
CALDERON, J. C., BOLANOS, P. & CAPUTO, C. 2014. The excitation-contraction coupling mechanism in skeletal muscle. *Biophys Rev,* 6**,** 133-160.
CANATO, M., CAPITANIO, P., CANCELLARA, L., LEANZA, L., RAFFAELLO, A., REANE, D. V., MARCUCCI, L., MICHELUCCI, A., PROTASI, F. & REGGIANI, C. 2019. Excessive Accumulation of Ca(2 +) in Mitochondria of Y522S-RYR1 Knock-in Mice: A Link Between Leak From the Sarcoplasmic Reticulum and Altered Redox State. *Front Physiol,* 10**,** 1142.
CAPACCHIONE, J. F., SAMBUUGHIN, N., BINA, S., MULLIGAN, L. P., LAWSON, T. D. & MULDOON, S. M. 2010. Exertional rhabdomyolysis and malignant hyperthermia in a patient with ryanodine receptor type 1 gene, L-type calcium channel alpha-1 subunit gene, and calsequestrin-1 gene polymorphisms. *Anesthesiology,* 112**,** 239-44.
CARPENTER, D., RINGROSE, C., LEO, V., MORRIS, A., ROBINSON, R. L., HALSALL, P. J., HOPKINS, P. M. & SHAW, M. A. 2009a. The role of CACNA1S in predisposition to malignant hyperthermia. *BMC Med Genet,* 10**,** 104.
CARPENTER, D., ROBINSON, R. L., QUINNELL, R. J., RINGROSE, C., HOGG, M., CASSON, F., BOOMS, P., ILES, D. E., HALSALL, P. J., STEELE, D. S., SHAW, M. A. & HOPKINS, P. M. 2009b. Genetic variation in RYR1 and malignant hyperthermia phenotypes. *Br J Anaesth,* 103**,** 538-48.
CARSANA, A. 2013. Exercise-induced rhabdomyolysis and stress-induced malignant hyperthermia events, association with malignant hyperthermia susceptibility, and RYR1 gene sequence variations. *ScientificWorldJournal,* 2013**,** 531465.
CHABAN, Y., BOEKEMA, E. J. & DUDKINA, N. V. 2014. Structures of mitochondrial oxidative phosphorylation supercomplexes and mechanisms for their stabilisation. *Biochim Biophys Acta,* 1837**,** 418-26.
CHANG, L., DALY, C., MILLER, D. M., ALLEN, P. D., BOYLE, J. P., HOPKINS, P. M. & SHAW, M. A. 2019. Permeabilised skeletal muscle reveals mitochondrial deficiency in malignant hyperthermia-susceptible individuals. *Br J Anaesth,* 122**,** 613-621.
CHANG, L., LIU, X., DIGGLE, C. P., BOYLE, J. P., HOPKINS, P. M., SHAW, M. A. & ALLEN, P. D. 2020. Bioenergetic defects in muscle fibers of RYR1 mutant knock-in mice associated with malignant hyperthermia. *J Biol Chem*.
CHEAH, A. M. 1981. Effect of long chain unsaturated fatty acids on the calcium transport of sarcoplasmic reticulum. *Biochim Biophys Acta,* 648**,** 113-9.
CHEAH, K. S. & CHEAH, A. M. 1981a. Mitochondrial calcium transport and calcium-activated phospholipase in porcine malignant hyperthermia. *Biochim Biophys Acta,* 634**,** 70-84.
CHEAH, K. S. & CHEAH, A. M. 1981b. Skeletal muscle mitochondrial phospholipase A2 and the interaction of mitochondria and sarcoplasmic reticulum in porcine malignant hyperthermia. *Biochim Biophys Acta,* 638**,** 40-9.
CHEAH, K. S., CHEAH, A. M., FLETCHER, J. E. & ROSENBERG, H. 1989. Skeletal muscle mitochondrial respiration of malignant hyperthermia-susceptible patients. Ca2+-induced uncoupling and free fatty acids. *Int J Biochem,* 21**,** 913-20.

CHELU, M. G., GOONASEKERA, S. A., DURHAM, W. J., TANG, W., LUECK, J. D., RIEHL, J., PESSAH, I. N., ZHANG, P., BHATTACHARJEE, M. B., DIRKSEN, R. T. & HAMILTON, S. L. 2006. Heat- and anesthesia-induced malignant hyperthermia in an RyR1 knock-in mouse. *FASEB J,* 20**,** 329-30.

CHEN, E. Y., TAN, C. M., KOU, Y., DUAN, Q., WANG, Z., MEIRELLES, G. V., CLARK, N. R. & MA'AYAN, A. 2013. Enrichr: interactive and collaborative HTML5 gene list enrichment analysis tool. *BMC Bioinformatics,* 14**,** 128.

CHEREDNICHENKO, G., WARD, C. W., FENG, W., CABRALES, E., MICHAELSON, L., SAMSO, M., LOPEZ, J. R., ALLEN, P. D. & PESSAH, I. N. 2008. Enhanced excitation-coupled calcium entry in myotubes expressing malignant hyperthermia mutation R163C is attenuated by dantrolene. *Mol Pharmacol,* 73**,** 1203-12.

CHINENOV, Y. & KERPPOLA, T. K. 2001. Close encounters of many kinds: Fos-Jun interactions that mediate transcription regulatory specificity. *Oncogene,* 20**,** 2438-52.

CHO, C. H., WOO, J. S., PEREZ, C. F. & LEE, E. H. 2017. A focus on extracellular Ca(2+) entry into skeletal muscle. *Exp Mol Med,* 49**,** e378.

CITINO, S. B., BUSH, M. & PHILLIPS, L. G. 1984. Dystocia and fatal hyperthermic episode in a giraffe. *J Am Vet Med Assoc,* 185**,** 1440-2.

COCK, P. J., FIELDS, C. J., GOTO, N., HEUER, M. L. & RICE, P. M. 2010. The Sanger FASTQ file format for sequences with quality scores, and the Solexa/Illumina FASTQ variants. *Nucleic Acids Res,* 38**,** 1767-71.

CONSORTIUM, G. T. 2013. The Genotype-Tissue Expression (GTEx) project. *Nat Genet,* 45**,** 580-5.

CONTRERAS, L., DRAGO, I., ZAMPESE, E. & POZZAN, T. 2010. Mitochondria: the calcium connection. *Biochim Biophys Acta,* 1797**,** 607-18.

CSORDAS, G., GOLENAR, T., SEIFERT, E. L., KAMER, K. J., SANCAK, Y., PEROCCHI, F., MOFFAT, C., WEAVER, D., DE LA FUENTE PEREZ, S., BOGORAD, R., KOTELIANSKY, V., ADIJANTO, J., MOOTHA, V. K. & HAJNOCZKY, G. 2013. MICU1 controls both the threshold and cooperative activation of the mitochondrial Ca(2)(+) uniporter. *Cell Metab,* 17**,** 976-87.

DARRAH, R., MCKONE, E., O'CONNOR, C., RODGERS, C., GENATOSSIO, A., MCNAMARA, S., GIBSON, R., STUART ELBORN, J., ENNIS, M., GALLAGHER, C. G., KALSHEKER, N., AITKEN, M., WIESE, D., DUNN, J., SMITH, P., PACE, R., LONDONO, D., GODDARD, K. A., KNOWLES, M. R. & DRUMM, M. L. 2010. EDNRA variants associate with smooth muscle mRNA levels, cell proliferation rates, and cystic fibrosis pulmonary disease severity. *Physiol Genomics,* 41**,** 71-7.

DE MAGALHAES, J. P., CURADO, J. & CHURCH, G. M. 2009. Meta-analysis of age-related gene expression profiles identifies common signatures of aging. *Bioinformatics,* 25**,** 875-81.

DE STEFANI, D., PATRON, M. & RIZZUTO, R. 2015. Structure and function of the mitochondrial calcium uniporter complex. *Biochim Biophys Acta,* 1853**,** 2006-11.

DEBIGARE, R., MARQUIS, K., COTE, C. H., TREMBLAY, R. R., MICHAUD, A., LEBLANC, P. & MALTAIS, F. 2003. Catabolic/anabolic balance and muscle wasting in patients with COPD. *Chest,* 124**,** 83-9.

DENBOROUGH, M. A., DENNETT, X. & ANDERSON, R. M. 1973. Central-core disease and malignant hyperpyrexia. *Br Med J,* 1**,** 272-3.

DENBOROUGH, M. A., FORSTER, J. F., LOVELL, R. R., MAPLESTONE, P. A. & VILLIERS, J. D. 1962. Anaesthetic deaths in a family. *Br J Anaesth,* 34**,** 395-6.

DENBOROUGH, M. A., WARNE, G. L., MOULDS, R. F. & MARTIN, F. I. 1974. Insulin secretion in malignant hyperpyrexia. *Br Med J,* 3**,** 493-5.

DENTON, R. M. 2009. Regulation of mitochondrial dehydrogenases by calcium ions. *Biochim Biophys Acta,* 1787**,** 1309-16.

DES GEORGES, A., CLARKE, O. B., ZALK, R., YUAN, Q., CONDON, K. J., GRASSUCCI, R. A., HENDRICKSON, W. A., MARKS, A. R. & FRANK, J. 2016. Structural Basis for Gating and Activation of RyR1. *Cell,* 167**,** 145-157 e17.

DEUFEL, T., SUDBRAK, R., FEIST, Y., RUBSAM, B., DU CHESNE, I., SCHAFER, K. L., ROEWER, N., GRIMM, T., LEHMANN-HORN, F., HARTUNG, E. J. & ET AL. 1995. Discordance, in a malignant hyperthermia pedigree, between in vitro contracture-test phenotypes and haplotypes for the MHS1 region on chromosome 19q12-13.2, comprising the C1840T transition in the RYR1 gene. *Am J Hum Genet,* 56**,** 1334-42.

DI MAURO, S. 2007. Muscle glycogenoses: an overview. *Acta Myol,* 26**,** 35-41.

DIAZ-SYLVESTER, P. L., PORTA, M. & COPELLO, J. A. 2008. Halothane modulation of skeletal muscle ryanodine receptors: dependence on Ca2+, Mg2+, and ATP. *Am J Physiol Cell Physiol,* 294**,** C1103-12.

DIXON, A. L., LIANG, L., MOFFATT, M. F., CHEN, W., HEATH, S., WONG, K. C., TAYLOR, J., BURNETT, E., GUT, I., FARRALL, M., LATHROP, G. M., ABECASIS, G. R. & COOKSON, W. O. 2007. A genome-wide association study of global gene expression. *Nat Genet,* 39**,** 1202-7.

DOBIN, A., DAVIS, C. A., SCHLESINGER, F., DRENKOW, J., ZALESKI, C., JHA, S., BATUT, P., CHAISSON, M. & GINGERAS, T. R. 2013. STAR: ultrafast universal RNA-seq aligner. *Bioinformatics,* 29**,** 15-21.

DURHAM, W. J., ARACENA-PARKS, P., LONG, C., ROSSI, A. E., GOONASEKERA, S. A., BONCOMPAGNI, S., GALVAN, D. L., GILMAN, C. P., BAKER, M. R., SHIROKOVA, N., PROTASI, F., DIRKSEN, R. & HAMILTON, S. L. 2008. RyR1 S-nitrosylation underlies environmental heat stroke and sudden death in Y522S RyR1 knockin mice. *Cell,* 133**,** 53-65.

DUTHIE, G. G., WAHLE, K. W., HARRIS, C. I., ARTHUR, J. R. & MORRICE, P. C. 1992. Lipid peroxidation, antioxidant concentrations, and fatty acid contents of muscle tissue from malignant hyperthermia-susceptible swine. *Arch Biochem Biophys,* 296**,** 592-6.

EDGERTON, V. R., SMITH, J. L. & SIMPSON, D. R. 1975. Muscle fibre type populations of human leg muscles. *Histochem J,* 7**,** 259-66.

EIKELENBOOM, G. & VAN DEN BERGH, S. G. 1973. Mitochondrial metabolism in stress-susceptible pigs. *J Anim Sci,* 37**,** 692-6.

EISNER, V., CSORDAS, G. & HAJNOCZKY, G. 2013. Interactions between sarco-endoplasmic reticulum and mitochondria in cardiac and skeletal muscle - pivotal roles in Ca(2)(+) and reactive oxygen species signaling. *J Cell Sci,* 126**,** 2965-78.

ELPELEG, O. N., HAMMERMAN, C., SAADA, A., SHAAG, A., GOLZAND, E., HOCHNER-CELNIKIER, D., BERGER, I. & NADJARI, M. 2001. Antenatal presentation of carnitine palmitoyltransferase II deficiency. *Am J Med Genet,* 102**,** 183-7.

EMHG 1984. A protocol for the investigation of malignant hyperpyrexia (MH) susceptibility. The European Malignant Hyperpyrexia Group. *Br J Anaesth,* 56**,** 1267-9.

ESTEVE, E., ELTIT, J. M., BANNISTER, R. A., LIU, K., PESSAH, I. N., BEAM, K. G., ALLEN, P. D. & LOPEZ, J. R. 2010. A malignant hyperthermia-inducing mutation in RYR1 (R163C): alterations in Ca2+ entry, release, and retrograde signaling to the DHPR. *J Gen Physiol,* 135**,** 619-28.

FAGERLUND, T. H., ISLANDER, G., RANKLEV TWETMAN, E. & BERG, K. 1997. Malignant hyperthermia susceptibility, an autosomal dominant disorder? *Clin Genet,* 51**,** 365-9.

FALK, M. J., KAYSER, E. B., MORGAN, P. G. & SEDENSKY, M. M. 2006. Mitochondrial complex I function modulates volatile anesthetic sensitivity in C. elegans. *Curr Biol,* 16**,** 1641-5.

FAUL, F., ERDFELDER, E., LANG, A. G. & BUCHNER, A. 2007. G*Power 3: a flexible statistical power analysis program for the social, behavioral, and biomedical sciences. *Behav Res Methods,* 39**,** 175-91.

FENG, W., BARRIENTOS, G. C., CHEREDNICHENKO, G., YANG, T., PADILLA, I. T., TRUONG, K., ALLEN, P. D., LOPEZ, J. R. & PESSAH, I. N. 2011. Functional and biochemical properties of ryanodine receptor type 1 channels from heterozygous R163C malignant hyperthermia-susceptible mice. *Mol Pharmacol,* 79**,** 420-31.

FERNANDEZ-VERDEJO, R., VANWYNSBERGHE, A. M., ESSAGHIR, A., DEMOULIN, J. B., HAI, T., DELDICQUE, L. & FRANCAUX, M. 2017. Activating transcription factor 3 attenuates chemokine and cytokine expression in mouse skeletal muscle after exercise and facilitates molecular adaptation to endurance training. *FASEB J,* 31**,** 840-851.

FERREIRA, L. F. & LAITANO, O. 2016. Regulation of NADPH oxidases in skeletal muscle. *Free Radic Biol Med,* 98**,** 18-28.

FIEGE, M., WAPPLER, F., WEISSHORN, R., ULRICH GERBERSHAGEN, M., STEINFATH, M. & SCHULTE AM ESCH, J. 2002. Results of contracture tests with halothane, caffeine, and ryanodine depend on different malignant hyperthermia-associated ryanodine receptor gene mutations. *Anesthesiology,* 97**,** 345-50.

FIGUEROA, L., KRAEVA, N., MANNO, C., TORO, S., RIOS, E. & RIAZI, S. 2019. Abnormal calcium signalling and the caffeine-halothane contracture test. *Br J Anaesth,* 122**,** 32-41.

FISHILEVICH, S., NUDEL, R., RAPPAPORT, N., HADAR, R., PLASCHKES, I., INY STEIN, T., ROSEN, N., KOHN, A., TWIK, M., SAFRAN, M., LANCET, D. & COHEN, D. 2017. GeneHancer: genome-wide integration of enhancers and target genes in GeneCards. *Database (Oxford),* 2017.

FISZER, D., SHAW, M. A., FISHER, N. A., CARR, I. M., GUPTA, P. K., WATKINS, E. J., ROIZ DE SA, D., KIM, J. H. & HOPKINS, P. M. 2015. Next-generation Sequencing of RYR1 and CACNA1S in Malignant Hyperthermia and Exertional Heat Illness. *Anesthesiology,* 122**,** 1033-46.

FJELD, C. C., BIRDSONG, W. T. & GOODMAN, R. H. 2003. Differential binding of NAD+ and NADH allows the transcriptional corepressor carboxyl-terminal binding protein to serve as a metabolic sensor. *Proc Natl Acad Sci U S A,* 100**,** 9202-7.

FLETCHER, J. E., CALVO, P. A. & ROSENBERG, H. 1993. Phenotypes associated with malignant hyperthermia susceptibility in swine genotyped as homozygous or heterozygous for the ryanodine receptor mutation. *Br J Anaesth,* 71**,** 410-7.

FLETCHER, J. E., MAYERBERGER, S., TRIPOLITIS, L., YUDKOWSKY, M. & ROSENBERG, H. 1991a. Fatty acids markedly lower the threshold for halothane-induced calcium release from the terminal cisternae in human and porcine normal and malignant hyperthermia susceptible skeletal muscle. *Life Sci,* 49**,** 1651-7.

FLETCHER, J. E. & ROSENBERG, H. 1986. In vitro muscle contractures induced by halothane and suxamethonium. II: Human skeletal muscle from normal and malignant hyperthermia susceptible patients. *Br J Anaesth,* 58**,** 1433-9.

FLETCHER, J. E., ROSENBERG, H. & BEECH, J. 1991b. Interactions of fatty acids with the calcium release channel in malignant hyperthermia. *Adv Exp Med Biol,* 301**,** 57-69.

FLETCHER, J. E., TRIPOLITIS, L., ERWIN, K., HANSON, S., ROSENBERG, H., CONTI, P. A. & BEECH, J. 1990. Fatty acids modulate calcium-induced calcium release from

skeletal muscle heavy sarcoplasmic reticulum fractions: implications for malignant hyperthermia. *Biochem Cell Biol,* 68**,** 1195-201.

FORTUNATO, G., CARSANA, A., TINTO, N., BRANCADORO, V., CANFORA, G. & SALVATORE, F. 1999. A case of discordance between genotype and phenotype in a malignant hyperthermia family. *Eur J Hum Genet,* 7**,** 415-20.

FRANZINI-ARMSTRONG, C. & JORGENSEN, A. O. 1994. Structure and development of E-C coupling units in skeletal muscle. *Annu Rev Physiol,* 56**,** 509-34.

FRONTERA, W. R. & OCHALA, J. 2015. Skeletal muscle: a brief review of structure and function. *Calcif Tissue Int,* 96**,** 183-95.

FUJII, J., OTSU, K., ZORZATO, F., DE LEON, S., KHANNA, V. K., WEILER, J. E., O'BRIEN, P. J. & MACLENNAN, D. H. 1991. Identification of a mutation in porcine ryanodine receptor associated with malignant hyperthermia. *Science,* 253**,** 448-51.

FULCO, M., SCHILTZ, R. L., IEZZI, S., KING, M. T., ZHAO, P., KASHIWAYA, Y., HOFFMAN, E., VEECH, R. L. & SARTORELLI, V. 2003. Sir2 regulates skeletal muscle differentiation as a potential sensor of the redox state. *Mol Cell,* 12**,** 51-62.

GARCES DE LOS FAYOS ALONSO, I., LIANG, H. C., TURNER, S. D., LAGGER, S., MERKEL, O. & KENNER, L. 2018. The Role of Activator Protein-1 (AP-1) Family Members in CD30-Positive Lymphomas. *Cancers (Basel),* 10.

GARDNER, L., MILLER, D. M., DALY, C., GUPTA, P. K., HOUSE, C., ROIZ DE SA, D., SHAW, M. A. & HOPKINS, P. M. 2020. Investigating the genetic susceptibility to exertional heat illness. *J Med Genet*.

GARIERI, M., DELANEAU, O., SANTONI, F., FISH, R. J., MULL, D., CARNINCI, P., DERMITZAKIS, E. T., ANTONARAKIS, S. E. & FORT, A. 2017. The effect of genetic variation on promoter usage and enhancer activity. *Nat Commun,* 8**,** 1358.

GATZ, E. E. & JONES, J. R. 1969. Effects of six general anesthetics upon mitochondrial phosphorylation. *Federation proceedings,* 28.

GAUTRON, S., DAEGELEN, D., MENNECIER, F., DUBOCQ, D., KAHN, A. & DREYFUS, J. C. 1987. Molecular mechanisms of McArdle's disease (muscle glycogen phosphorylase deficiency). RNA and DNA analysis. *J Clin Invest,* 79**,** 275-81.

GEHLERT, S., BLOCH, W. & SUHR, F. 2015. Ca2+-dependent regulations and signaling in skeletal muscle: from electro-mechanical coupling to adaptation. *Int J Mol Sci,* 16**,** 1066-95.

GIULIVI, C., ROSS-INTA, C., OMANSKA-KLUSEK, A., NAPOLI, E., SAKAGUCHI, D., BARRIENTOS, G., ALLEN, P. D. & PESSAH, I. N. 2011. Basal bioenergetic abnormalities in skeletal muscle from ryanodine receptor malignant hyperthermia-susceptible R163C knock-in mice. *J Biol Chem,* 286**,** 99-113.

GLAHN, K. P., ELLIS, F. R., HALSALL, P. J., MULLER, C. R., SNOECK, M. M., URWYLER, A., WAPPLER, F. & EUROPEAN MALIGNANT HYPERTHERMIA, G. 2010. Recognizing and managing a malignant hyperthermia crisis: guidelines from the European Malignant Hyperthermia Group. *Br J Anaesth,* 105**,** 417-20.

GORLACH, A., BERTRAM, K., HUDECOVA, S. & KRIZANOVA, O. 2015. Calcium and ROS: A mutual interplay. *Redox Biol,* 6**,** 260-271.

GOSKER, H. R., ZEEGERS, M. P., WOUTERS, E. F. & SCHOLS, A. M. 2007. Muscle fibre type shifting in the vastus lateralis of patients with COPD is associated with disease severity: a systematic review and meta-analysis. *Thorax,* 62**,** 944-9.

GOTTSCHALK, A., VAN AKEN, H., ZENZ, M. & STANDL, T. 2011. Is anesthesia dangerous? *Dtsch Arztebl Int,* 108**,** 469-74.

GRIFFITHS, E. J. & RUTTER, G. A. 2009. Mitochondrial calcium as a key regulator of mitochondrial ATP production in mammalian cells. *Biochim Biophys Acta,* 1787**,** 1324-33.

GRIVENNIKOVA, V. G. & VINOGRADOV, A. D. 2006. Generation of superoxide by the mitochondrial Complex I. *Biochim Biophys Acta,* 1757**,** 553-61.

GRONERT, G. A. & HEFFRON, J. J. 1979. Skeletal muscle mitochondria in porcine malignant hyperthermia: respiratory activity, calcium functions, and depression by halothane. *Anesth Analg,* 58**,** 76-81.

GRONERT, G. A., THOMPSON, R. L. & ONOFRIO, B. M. 1980. Human malignant hyperthermia: awake episodes and correction by dantrolene. *Anesth Analg,* 59**,** 377-8.

GROOM, L., MULDOON, S. M., TANG, Z. Z., BRANDOM, B. W., BAYARSAIKHAN, M., BINA, S., LEE, H. S., QIU, X., SAMBUUGHIN, N. & DIRKSEN, R. T. 2011. Identical de novo mutation in the type 1 ryanodine receptor gene associated with fatal, stress-induced malignant hyperthermia in two unrelated families. *Anesthesiology,* 115**,** 938-45.

GU, Y., HARLEY, I. T., HENDERSON, L. B., ARONOW, B. J., VIETOR, I., HUBER, L. A., HARLEY, J. B., KILPATRICK, J. R., LANGEFELD, C. D., WILLIAMS, A. H., JEGGA, A. G., CHEN, J., WILLS-KARP, M., ARSHAD, S. H., EWART, S. L., THIO, C. L., FLICK, L. M., FILIPPI, M. D., GRIMES, H. L., DRUMM, M. L., CUTTING, G. R., KNOWLES, M. R. & KARP, C. L. 2009. Identification of IFRD1 as a modifier gene for cystic fibrosis lung disease. *Nature,* 458**,** 1039-42.

GUGLIELMI, V., VATTEMI, G., GUALANDI, F., VOERMANS, N. C., MARINI, M., SCOTTON, C., PEGORARO, E., OOSTERHOF, A., KOSA, M., ZADOR, E., VALENTE, E. M., DE GRANDIS, D., NERI, M., CODEMO, V., NOVELLI, A., VAN KUPPEVELT, T. H., DALLAPICCOLA, B., VAN ENGELEN, B. G., FERLINI, A. & TOMELLERI, G. 2013. SERCA1 protein expression in muscle of patients with Brody disease and Brody syndrome and in cultured human muscle fibers. *Mol Genet Metab,* 110**,** 162-9.

GUPTA, P. K. & HOPKINS, P. M. 2017. Diagnosis and management of malignant hyperthermia. *BJA Education,* 17**,** 249-254.

GUZY, R. D., SHARMA, B., BELL, E., CHANDEL, N. S. & SCHUMACKER, P. T. 2008. Loss of the SdhB, but Not the SdhA, subunit of complex II triggers reactive oxygen species-dependent hypoxia-inducible factor activation and tumorigenesis. *Mol Cell Biol,* 28**,** 718-31.

HAI, T. & HARTMAN, M. G. 2001. The molecular biology and nomenclature of the activating transcription factor/cAMP responsive element binding family of transcription factors: activating transcription factor proteins and homeostasis. *Gene,* 273**,** 1-11.

HAI, T., WOLFGANG, C. D., MARSEE, D. K., ALLEN, A. E. & SIVAPRASAD, U. 1999. ATF3 and stress responses. *Gene Expr,* 7**,** 321-35.

HAKAMATA, Y., NAKAI, J., TAKESHIMA, H. & IMOTO, K. 1992. Primary structure and distribution of a novel ryanodine receptor/calcium release channel from rabbit brain. *FEBS Lett,* 312**,** 229-35.

HALAZONETIS, T. D., GEORGOPOULOS, K., GREENBERG, M. E. & LEDER, P. 1988. c-Jun dimerizes with itself and with c-Fos, forming complexes of different DNA binding affinities. *Cell,* 55**,** 917-24.

HALDANE, J. B. S. 1941. The relative importance of principal and modifying genes in determining some human diseases. *Journal of Genetics,* 41**,** 149-157.

HALPERIN, E., KIMMEL, G. & SHAMIR, R. 2005. Tag SNP selection in genotype data for maximizing SNP prediction accuracy. *Bioinformatics,* 21 Suppl 1**,** i195-203.

HANLEY, P. J., RAY, J., BRANDT, U. & DAUT, J. 2002. Halothane, isoflurane and sevoflurane inhibit NADH:ubiquinone oxidoreductase (complex I) of cardiac mitochondria. *J Physiol,* 544**,** 687-93.

HARDIE, D. G. & PAN, D. A. 2002. Regulation of fatty acid synthesis and oxidation by the AMP-activated protein kinase. *Biochem Soc Trans,* 30**,** 1064-70.

HARRIS, R. A., MUNROE, J., FARMER, B., KIM, K. C. & JENKINS, P. 1971. Action of halothane upon mitochondrial respiration. *Arch Biochem Biophys,* 142**,** 435-44.

HARRISON, G. G. 1975. Control of the malignant hyperpyrexic syndrome in MHS swine by dantrolene sodium. *Br J Anaesth,* 47**,** 62-5.

HEBERLE, H., MEIRELLES, G. V., DA SILVA, F. R., TELLES, G. P. & MINGHIM, R. 2015. InteractiVenn: a web-based tool for the analysis of sets through Venn diagrams. *BMC Bioinformatics,* 16**,** 169.

HEERINGA, S. F., CHERNIN, G., CHAKI, M., ZHOU, W., SLOAN, A. J., JI, Z., XIE, L. X., SALVIATI, L., HURD, T. W., VEGA-WARNER, V., KILLEN, P. D., RAPHAEL, Y., ASHRAF, S., OVUNC, B., SCHOEB, D. S., MCLAUGHLIN, H. M., AIRIK, R., VLANGOS, C. N., GBADEGESIN, R., HINKES, B., SAISAWAT, P., TREVISSON, E., DOIMO, M., CASARIN, A., PERTEGATO, V., GIORGI, G., PROKISCH, H., ROTIG, A., NURNBERG, G., BECKER, C., WANG, S., OZALTIN, F., TOPALOGLU, R., BAKKALOGLU, A., BAKKALOGLU, S. A., MULLER, D., BEISSERT, A., MIR, S., BERDELI, A., VARPIZEN, S., ZENKER, M., MATEJAS, V., SANTOS-OCANA, C., NAVAS, P., KUSAKABE, T., KISPERT, A., AKMAN, S., SOLIMAN, N. A., KRICK, S., MUNDEL, P., REISER, J., NURNBERG, P., CLARKE, C. F., WIGGINS, R. C., FAUL, C. & HILDEBRANDT, F. 2011. COQ6 mutations in human patients produce nephrotic syndrome with sensorineural deafness. *J Clin Invest,* 121**,** 2013-24.

HERNANDEZ-OCHOA, E. O., PRATT, S. J., LOVERING, R. M. & SCHNEIDER, M. F. 2015. Critical Role of Intracellular RyR1 Calcium Release Channels in Skeletal Muscle Function and Disease. *Front Physiol,* 6**,** 420.

HEYTENS, L. 2007. Molecular genetic detection of susceptibility to malignant hyperthermia in Belgian families. *Acta Anaesthesiol Belg,* 58**,** 113-8.

HILLIAN, A. D., LONDONO, D., DUNN, J. M., GODDARD, K. A., PACE, R. G., KNOWLES, M. R., DRUMM, M. L. & GROUP, C. F. G. M. S. 2008. Modulation of cystic fibrosis lung disease by variants in interleukin-8. *Genes Immun,* 9**,** 501-8.

HONG, J., KIM, B. W., CHOO, H. J., PARK, J. J., YI, J. S., YU, D. M., LEE, H., YOON, G. S., LEE, J. S. & KO, Y. G. 2014. Mitochondrial complex I deficiency enhances skeletal myogenesis but impairs insulin signaling through SIRT1 inactivation. *J Biol Chem,* 289**,** 20012-25.

HOPKINS, P. M. 2011. Malignant hyperthermia: pharmacology of triggering. *Br J Anaesth,* 107**,** 48-56.

HOPKINS, P. M., RUFFERT, H., SNOECK, M. M., GIRARD, T., GLAHN, K. P., ELLIS, F. R., MULLER, C. R., URWYLER, A. & EUROPEAN MALIGNANT HYPERTHERMIA, G. 2015. European Malignant Hyperthermia Group guidelines for investigation of malignant hyperthermia susceptibility. *Br J Anaesth,* 115**,** 531-9.

HORSTICK, E. J., LINSLEY, J. W., DOWLING, J. J., HAUSER, M. A., MCDONALD, K. K., ASHLEY-KOCH, A., SAINT-AMANT, L., SATISH, A., CUI, W. W., ZHOU, W., SPRAGUE, S. M., STAMM, D. S., POWELL, C. M., SPEER, M. C., FRANZINI-ARMSTRONG, C., HIRATA, H. & KUWADA, J. Y. 2013. Stac3 is a component of the excitation-contraction coupling machinery and mutated in Native American myopathy. *Nat Commun,* 4**,** 1952.

HOUTEN, S. M., VIOLANTE, S., VENTURA, F. V. & WANDERS, R. J. 2016. The Biochemistry and Physiology of Mitochondrial Fatty Acid beta-Oxidation and Its Genetic Disorders. *Annu Rev Physiol,* 78**,** 23-44.

HU, H., WANG, Z., WEI, R., FAN, G., WANG, Q., ZHANG, K. & YIN, C. C. 2015. The molecular architecture of dihydropyrindine receptor/L-type Ca2+ channel complex. *Sci Rep,* 5**,** 8370.

HUXLEY, A. F. & NIEDERGERKE, R. 1954. Structural changes in muscle during contraction; interference microscopy of living muscle fibres. *Nature,* 173**,** 971-3.

HUXLEY, H. & HANSON, J. 1954. Changes in the cross-striations of muscle during contraction and stretch and their structural interpretation. *Nature,* 173**,** 973-6.

IBARRA MORENO, C. A., HU, S., KRAEVA, N., SCHUSTER, F., JOHANNSEN, S., RUEFFERT, H., KLINGLER, W., HEYTENS, L. & RIAZI, S. 2019. An Assessment of Penetrance and Clinical Expression of Malignant Hyperthermia in Individuals Carrying Diagnostic Ryanodine Receptor 1 Gene Mutations. *Anesthesiology,* 131**,** 983-991.

IJLST, L., WANDERS, R. J., USHIKUBO, S., KAMIJO, T. & HASHIMOTO, T. 1994. Molecular basis of long-chain 3-hydroxyacyl-CoA dehydrogenase deficiency: identification of the major disease-causing mutation in the alpha-subunit of the mitochondrial trifunctional protein. *Biochim Biophys Acta,* 1215**,** 347-50.

IMAGAWA, T., SMITH, J. S., CORONADO, R. & CAMPBELL, K. P. 1987. Purified ryanodine receptor from skeletal muscle sarcoplasmic reticulum is the Ca2+-permeable pore of the calcium release channel. *J Biol Chem,* 262**,** 16636-43.

INUI, M., SAITO, A. & FLEISCHER, S. 1987. Purification of the ryanodine receptor and identity with feet structures of junctional terminal cisternae of sarcoplasmic reticulum from fast skeletal muscle. *J Biol Chem,* 262**,** 1740-7.

ISAACS, H. & HEFFRON, J. J. 1975. Morphological and biochemical defects in muscles of human carriers of the malignant hyperthermia syndrome. *Br J Anaesth,* 47**,** 475-81.

JUNGBLUTH, H. 2007. Central core disease. *Orphanet J Rare Dis,* 2**,** 25.

KANAZAWA, M., OHTAKE, A., ABE, H., YAMAMOTO, S., SATOH, Y., TAKAYANAGI, M., NIIMI, H., MORI, M. & HASHIMOTO, T. 1993. Molecular cloning and sequence analysis of the cDNA for human mitochondrial short-chain enoyl-CoA hydratase. *Enzyme Protein,* 47**,** 9-13.

KAYSER, E. B., MORGAN, P. G. & SEDENSKY, M. M. 2004. Mitochondrial complex I function affects halothane sensitivity in Caenorhabditis elegans. *Anesthesiology,* 101**,** 365-72.

KIM, J. H., JARVIK, G. P., BROWNING, B. L., RAJAGOPALAN, R., GORDON, A. S., RIEDER, M. J., ROBERTSON, P. D., NICKERSON, D. A., FISHER, N. A. & HOPKINS, P. M. 2013. Exome sequencing reveals novel rare variants in the ryanodine receptor and calcium channel genes in malignant hyperthermia families. *Anesthesiology,* 119**,** 1054-65.

KIM, J. H. & YOUN, H. D. 2009. C-terminal binding protein maintains mitochondrial activities. *Cell Death Differ,* 16**,** 584-92.

KIVILUOTO, S., DECUYPERE, J. P., DE SMEDT, H., MISSIAEN, L., PARYS, J. B. & BULTYNCK, G. 2011. STIM1 as a key regulator for Ca2+ homeostasis in skeletal-muscle development and function. *Skelet Muscle,* 1**,** 16.

KONTRO, H., HULMI, J. J., RAHKILA, P. & KAINULAINEN, H. 2012. Cellular and tissue expression of DAPIT, a phylogenetically conserved peptide. *Eur J Histochem,* 56**,** e18.

KRANS, J. L. 2010. The Sliding Filament Theory of Muscle Contraction. *Nature Education,* 3.

KULESHOV, M. V., JONES, M. R., ROUILLARD, A. D., FERNANDEZ, N. F., DUAN, Q., WANG, Z., KOPLEV, S., JENKINS, S. L., JAGODNIK, K. M., LACHMANN, A., MCDERMOTT, M. G., MONTEIRO, C. D., GUNDERSEN, G. W. & MA'AYAN, A.

2016. Enrichr: a comprehensive gene set enrichment analysis web server 2016 update. *Nucleic Acids Res,* 44**,** W90-7.

KUO, I. Y. & EHRLICH, B. E. 2015. Signaling in muscle contraction. *Cold Spring Harb Perspect Biol,* 7**,** a006023.

KUSHNIR, A., WAJSBERG, B. & MARKS, A. R. 2018. Ryanodine receptor dysfunction in human disorders. *Biochim Biophys Acta Mol Cell Res,* 1865**,** 1687-1697.

KUZNETSOV, A. V., VEKSLER, V., GELLERICH, F. N., SAKS, V., MARGREITER, R. & KUNZ, W. S. 2008. Analysis of mitochondrial function in situ in permeabilized muscle fibers, tissues and cells. *Nat Protoc,* 3**,** 965-76.

LABARGE, S., MCDONALD, M., SMITH-POWELL, L., AUWERX, J. & HUSS, J. M. 2014. Estrogen-related receptor-alpha (ERRalpha) deficiency in skeletal muscle impairs regeneration in response to injury. *FASEB J,* 28**,** 1082-97.

LANNER, J. T., GEORGIOU, D. K., JOSHI, A. D. & HAMILTON, S. L. 2010. Ryanodine receptors: structure, expression, molecular details, and function in calcium release. *Cold Spring Harb Perspect Biol,* 2**,** a003996.

LARACH, M. G., BRANDOM, B. W., ALLEN, G. C., GRONERT, G. A. & LEHMAN, E. B. 2008. Cardiac arrests and deaths associated with malignant hyperthermia in north america from 1987 to 2006: a report from the north american malignant hyperthermia registry of the malignant hyperthermia association of the United States. *Anesthesiology,* 108**,** 603-11.

LARSEN, S., NIELSEN, J., HANSEN, C. N., NIELSEN, L. B., WIBRAND, F., STRIDE, N., SCHRODER, H. D., BOUSHEL, R., HELGE, J. W., DELA, F. & HEY-MOGENSEN, M. 2012. Biomarkers of mitochondrial content in skeletal muscle of healthy young human subjects. *J Physiol,* 590**,** 3349-60.

LAVER, D. R., O'NEILL, E. R. & LAMB, G. D. 2004. Luminal Ca2+-regulated Mg2+ inhibition of skeletal RyRs reconstituted as isolated channels or coupled clusters. *J Gen Physiol,* 124**,** 741-58.

LAVORATO, M., GUPTA, P. K., HOPKINS, P. M. & FRANZINI-ARMSTRONG, C. 2016. Skeletal Muscle Microalterations in Patients Carrying Malignant Hyperthermia-Related Mutations of the e-c Coupling Machinery. *Eur J Transl Myol,* 26**,** 6105.

LEMIEUX, H., BLIER, P. U. & GNAIGER, E. 2017. Remodeling pathway control of mitochondrial respiratory capacity by temperature in mouse heart: electron flow through the Q-junction in permeabilized fibers. *Sci Rep,* 7**,** 2840.

LEVANO, S., GONZALEZ, A., SINGER, M., DEMOUGIN, P., RUFFERT, H., URWYLER, A. & GIRARD, T. 2017. Resequencing array for gene variant detection in malignant hyperthermia and butyrylcholinestherase deficiency. *Neuromuscul Disord,* 27**,** 492-499.

LIAO, Y., SMYTH, G. K. & SHI, W. 2014. featureCounts: an efficient general purpose program for assigning sequence reads to genomic features. *Bioinformatics,* 30**,** 923-30.

LING, C., POULSEN, P., SIMONSSON, S., RONN, T., HOLMKVIST, J., ALMGREN, P., HAGERT, P., NILSSON, E., MABEY, A. G., NILSSON, P., VAAG, A. & GROOP, L. 2007. Genetic and epigenetic factors are associated with expression of respiratory chain component NDUFB6 in human skeletal muscle. *J Clin Invest,* 117**,** 3427-35.

LITMAN, R. S., GRIGGS, S. M., DOWLING, J. J. & RIAZI, S. 2018. Malignant Hyperthermia Susceptibility and Related Diseases. *Anesthesiology,* 128**,** 159-167.

LIU, D., SARTOR, M. A., NADER, G. A., GUTMANN, L., TREUTELAAR, M. K., PISTILLI, E. E., IGLAYREGER, H. B., BURANT, C. F., HOFFMAN, E. P. & GORDON, P. M. 2010. Skeletal muscle gene expression in response to resistance exercise: sex specific regulation. *BMC Genomics,* 11**,** 659.

LIVAK, K. J. & SCHMITTGEN, T. D. 2001. Analysis of relative gene expression data using real-time quantitative PCR and the 2(-Delta Delta C(T)) Method. *Methods,* 25**,** 402-8.

LJUBICIC, V., JOSEPH, A. M., SALEEM, A., UGUCCIONI, G., COLLU-MARCHESE, M., LAI, R. Y., NGUYEN, L. M. & HOOD, D. A. 2010. Transcriptional and post-transcriptional regulation of mitochondrial biogenesis in skeletal muscle: effects of exercise and aging. *Biochim Biophys Acta,* 1800**,** 223-34.

LONGO, N., AMAT DI SAN FILIPPO, C. & PASQUALI, M. 2006. Disorders of carnitine transport and the carnitine cycle. *Am J Med Genet C Semin Med Genet,* 142C**,** 77-85.

LOPEZ, J. R., ALAMO, L., CAPUTO, C., WIKINSKI, J. & LEDEZMA, D. 1985. Intracellular ionized calcium concentration in muscles from humans with malignant hyperthermia. *Muscle Nerve,* 8**,** 355-8.

LOPEZ, J. R., ALAMO, L. A., JONES, D. E., PAPP, L., ALLEN, P. D., GERGELY, J. & SRETER, F. A. 1986. [Ca2+]i in muscles of malignant hyperthermia susceptible pigs determined in vivo with Ca2+ selective microelectrodes. *Muscle Nerve,* 9**,** 85-6.

LOPEZ, J. R., ALLEN, P. D., ALAMO, L., JONES, D. & SRETER, F. A. 1988. Myoplasmic free [Ca2+] during a malignant hyperthermia episode in swine. *Muscle Nerve,* 11**,** 82-8.

LOPEZ, J. R., KAURA, V., DIGGLE, C. P., HOPKINS, P. M. & ALLEN, P. D. 2018. Malignant hyperthermia, environmental heat stress, and intracellular calcium dysregulation in a mouse model expressing the p.G2435R variant of RYR1. *Br J Anaesth,* 121**,** 953-961.

LOPEZ, R. J., BYRNE, S., VUKCEVIC, M., SEKULIC-JABLANOVIC, M., XU, L., BRINK, M., ALAMELU, J., VOERMANS, N., SNOECK, M., CLEMENT, E., MUNTONI, F., ZHOU, H., RADUNOVIC, A., MOHAMMED, S., WRAIGE, E., ZORZATO, F., TREVES, S. & JUNGBLUTH, H. 2016. An RYR1 mutation associated with malignant hyperthermia is also associated with bleeding abnormalities. *Sci Signal,* 9**,** ra68.

LOVE, M. I., HUBER, W. & ANDERS, S. 2014. Moderated estimation of fold change and dispersion for RNA-seq data with DESeq2. *Genome Biol,* 15**,** 550.

LUIJSTERBURG, M. S., DE KRIJGER, I., WIEGANT, W. W., SHAH, R. G., SMEENK, G., DE GROOT, A. J. L., PINES, A., VERTEGAAL, A. C. O., JACOBS, J. J. L., SHAH, G. M. & VAN ATTIKUM, H. 2016. PARP1 Links CHD2-Mediated Chromatin Expansion and H3.3 Deposition to DNA Repair by Non-homologous End-Joining. *Mol Cell,* 61**,** 547-562.

LYNCH, P. J., KRIVOSIC-HORBER, R., REYFORD, H., MONNIER, N., QUANE, K., ADNET, P., HAUDECOEUR, G., KRIVOSIC, I., MCCARTHY, T. & LUNARDI, J. 1997. Identification of heterozygous and homozygous individuals with the novel RYR1 mutation Cys35Arg in a large kindred. *Anesthesiology,* 86**,** 620-6.

MACLENNAN, D. H., DUFF, C., ZORZATO, F., FUJII, J., PHILLIPS, M., KORNELUK, R. G., FRODIS, W., BRITT, B. A. & WORTON, R. G. 1990. Ryanodine receptor gene is a candidate for predisposition to malignant hyperthermia. *Nature,* 343**,** 559-61.

MADONNA, R., VITULLI, P., PIERDOMENICO, S. & DE CATERINA, R. 2019. Deficiency of NDUFC2: Cause or bystander in acute coronary syndromes? *Int J Cardiol,* 286**,** 134-135.

MAILLOUX, R. J. & HARPER, M. E. 2011. Uncoupling proteins and the control of mitochondrial reactive oxygen species production. *Free Radic Biol Med,* 51**,** 1106-15.

MANNING, B. M., QUANE, K. A., ORDING, H., URWYLER, A., TEGAZZIN, V., LEHANE, M., O'HALLORAN, J., HARTUNG, E., GIBLIN, L. M., LYNCH, P. J., VAUGHAN, P., CENSIER, K., BENDIXEN, D., COMI, G., HEYTENS, L., MONSIEURS, K., FAGERLUND, T., WOLZ, W., HEFFRON, J. J., MULLER, C. R. & MCCARTHY, T. V. 1998. Identification of novel mutations in the ryanodine-

receptor gene (RYR1) in malignant hyperthermia: genotype-phenotype correlation. *Am J Hum Genet,* 62**,** 599-609.

MANZUR, A. Y., SEWRY, C. A., ZIPRIN, J., DUBOWITZ, V. & MUNTONI, F. 1998. A severe clinical and pathological variant of central core disease with possible autosomal recessive inheritance. *Neuromuscul Disord,* 8**,** 467-73.

MARTIN, M. 2011. Cutadapt removes adapter sequences from high-throughput sequencing reads. *2011,* 17**,** 3.

MATSUZAKI, S. & SZWEDA, L. I. 2007. Inhibition of complex I by Ca2+ reduces electron transport activity and the rate of superoxide anion production in cardiac submitochondrial particles. *Biochemistry,* 46**,** 1350-7.

MCARDLE, B. 1951. Myopathy due to a defect in muscle glycogen breakdown. *Clin Sci,* 10**,** 13-35.

MCCORMACK, J. G. & DENTON, R. M. 1979. The effects of calcium ions and adenine nucleotides on the activity of pig heart 2-oxoglutarate dehydrogenase complex. *Biochem J,* 180**,** 533-44.

MCLEAN, C. S., MIELKE, C., CORDOVA, J. M., LANGLAIS, P. R., BOWEN, B., MIRANDA, D., COLETTA, D. K. & MANDARINO, L. J. 2015. Gene and MicroRNA Expression Responses to Exercise; Relationship with Insulin Sensitivity. *PLoS One,* 10**,** e0127089.

MENSHIKOVA, E. V., RITOV, V. B., TOLEDO, F. G., FERRELL, R. E., GOODPASTER, B. H. & KELLEY, D. E. 2005. Effects of weight loss and physical activity on skeletal muscle mitochondrial function in obesity. *Am J Physiol Endocrinol Metab,* 288**,** E818-25.

MERRITT, J. L., 2ND, NORRIS, M. & KANUNGO, S. 2018. Fatty acid oxidation disorders. *Ann Transl Med,* 6**,** 473.

MEYER, B., WITTIG, I., TRIFILIEFF, E., KARAS, M. & SCHAGGER, H. 2007. Identification of two proteins associated with mammalian ATP synthase. *Mol Cell Proteomics,* 6**,** 1690-9.

MICHELUCCI, A., DE MARCO, A., GUARNIER, F. A., PROTASI, F. & BONCOMPAGNI, S. 2017. Antioxidant Treatment Reduces Formation of Structural Cores and Improves Muscle Function in RYR1(Y522S/WT) Mice. *Oxid Med Cell Longev,* 2017**,** 6792694.

MILLER, D. M., DALY, C., ABOELSAOD, E. M., GARDNER, L., HOBSON, S. J., RIASAT, K., SHEPHERD, S., ROBINSON, R. L., BILMEN, J. G., GUPTA, P. K., SHAW, M. A. & HOPKINS, P. M. 2018. Genetic epidemiology of malignant hyperthermia in the UK. *Br J Anaesth,* 121**,** 944-952.

MISHRA, J., JHUN, B. S., HURST, S., J, O. U., CSORDAS, G. & SHEU, S. S. 2017. The Mitochondrial Ca(2+) Uniporter: Structure, Function, and Pharmacology. *Handb Exp Pharmacol,* 240**,** 129-156.

MITCHELL, G. & HEFFRON, J. J. 1982. Porcine stress syndromes. *Adv Food Res,* 28**,** 167-230.

MITCHELL, P. & MOYLE, J. 1967. Chemiosmotic hypothesis of oxidative phosphorylation. *Nature,* 213**,** 137-9.

MONNIER, N., KRIVOSIC-HORBER, R., PAYEN, J. F., KOZAK-RIBBENS, G., NIVOCHE, Y., ADNET, P., REYFORD, H. & LUNARDI, J. 2002. Presence of two different genetic traits in malignant hyperthermia families: implication for genetic analysis, diagnosis, and incidence of malignant hyperthermia susceptibility. *Anesthesiology,* 97**,** 1067-74.

MONNIER, N., PROCACCIO, V., STIEGLITZ, P. & LUNARDI, J. 1997. Malignant-hyperthermia susceptibility is associated with a mutation of the alpha 1-subunit of the

human dihydropyridine-sensitive L-type voltage-dependent calcium-channel receptor in skeletal muscle. *Am J Hum Genet,* 60**,** 1316-25.

MOOTHA, V. K., LINDGREN, C. M., ERIKSSON, K. F., SUBRAMANIAN, A., SIHAG, S., LEHAR, J., PUIGSERVER, P., CARLSSON, E., RIDDERSTRALE, M., LAURILA, E., HOUSTIS, N., DALY, M. J., PATTERSON, N., MESIROV, J. P., GOLUB, T. R., TAMAYO, P., SPIEGELMAN, B., LANDER, E. S., HIRSCHHORN, J. N., ALTSHULER, D. & GROOP, L. C. 2003. PGC-1alpha-responsive genes involved in oxidative phosphorylation are coordinately downregulated in human diabetes. *Nat Genet,* 34**,** 267-73.

MORAVA, E. 2014. Galactose supplementation in phosphoglucomutase-1 deficiency; review and outlook for a novel treatable CDG. *Mol Genet Metab,* 112**,** 275-9.

MUKUND, K. & SUBRAMANIAM, S. 2020. Skeletal muscle: A review of molecular structure and function, in health and disease. *Wiley Interdiscip Rev Syst Biol Med,* 12**,** e1462.

MURAYAMA, T., OGAWA, H., KUREBAYASHI, N., OHNO, S., HORIE, M. & SAKURAI, T. 2018. A tryptophan residue in the caffeine-binding site of the ryanodine receptor regulates Ca(2+) sensitivity. *Commun Biol,* 1**,** 98.

MURPHY, M. P. 2009b. How mitochondria produce reactive oxygen species. *Biochem J,* 417**,** 1-13.

MURPHY, R. M., LARKINS, N. T., MOLLICA, J. P., BEARD, N. A. & LAMB, G. D. 2009a. Calsequestrin content and SERCA determine normal and maximal Ca2+ storage levels in sarcoplasmic reticulum of fast- and slow-twitch fibres of rat. *J Physiol,* 587**,** 443-60.

NADEAU, J. H. 2001. Modifier genes in mice and humans. *Nat Rev Genet,* 2**,** 165-74.

NAIKI, M., OCHI, N., KATO, Y. S., PUREVSUREN, J., YAMADA, K., KIMURA, R., FUKUSHI, D., HARA, S., YAMADA, Y., KUMAGAI, T., YAMAGUCHI, S. & WAKAMATSU, N. 2014. Mutations in HADHB, which encodes the beta-subunit of mitochondrial trifunctional protein, cause infantile onset hypoparathyroidism and peripheral polyneuropathy. *Am J Med Genet A,* 164A**,** 1180-7.

NELSON, B. R., WU, F., LIU, Y., ANDERSON, D. M., MCANALLY, J., LIN, W., CANNON, S. C., BASSEL-DUBY, R. & OLSON, E. N. 2013. Skeletal muscle-specific T-tubule protein STAC3 mediates voltage-induced Ca2+ release and contractility. *Proc Natl Acad Sci U S A,* 110**,** 11881-6.

NEUBAUER, O., SABAPATHY, S., ASHTON, K. J., DESBROW, B., PEAKE, J. M., LAZARUS, R., WESSNER, B., CAMERON-SMITH, D., WAGNER, K. H., HASELER, L. J. & BULMER, A. C. 2014. Time course-dependent changes in the transcriptome of human skeletal muscle during recovery from endurance exercise: from inflammation to adaptive remodeling. *J Appl Physiol (1985),* 116**,** 274-87.

NGUYEN, J. H., CHUNG, J. D., LYNCH, G. S. & RYALL, J. G. 2019. The Microenvironment Is a Critical Regulator of Muscle Stem Cell Activation and Proliferation. *Front Cell Dev Biol,* 7**,** 254.

NHS. 2018. *General anaesthesia* [Online]. [Accessed 20 May 2020]. Available from: https://www.nhs.uk/conditions/general-anaesthesia/

NICA, A. C. & DERMITZAKIS, E. T. 2013. Expression quantitative trait loci: present and future. *Philos Trans R Soc Lond B Biol Sci,* 368**,** 20120362.

NISHIO, H., SATO, T., FUKUNISHI, S., TAMURA, A., IWATA, M., TSUBOI, K. & SUZUKI, K. 2009. Identification of malignant hyperthermia-susceptible ryanodine receptor type 1 gene (RYR1) mutations in a child who died in a car after exposure to a high environmental temperature. *Leg Med (Tokyo),* 11**,** 142-3.

O'SHEA, E. K., RUTKOWSKI, R. & KIM, P. S. 1992. Mechanism of specificity in the Fos-Jun oncoprotein heterodimer. *Cell,* 68**,** 699-708.

OHSAKAYA, S., FUJIKAWA, M., HISABORI, T. & YOSHIDA, M. 2011. Knockdown of DAPIT (diabetes-associated protein in insulin-sensitive tissue) results in loss of ATP synthase in mitochondria. *J Biol Chem,* 286**,** 20292-6.

ONG, C. T. & CORCES, V. G. 2011. Enhancer function: new insights into the regulation of tissue-specific gene expression. *Nat Rev Genet,* 12**,** 283-93.

OPENSTAX 2013. Anatomy & Physiology. Houston, TX: OpenStax CNX.

OTSU, K., WILLARD, H. F., KHANNA, V. K., ZORZATO, F., GREEN, N. M. & MACLENNAN, D. H. 1990. Molecular cloning of cDNA encoding the Ca2+ release channel (ryanodine receptor) of rabbit cardiac muscle sarcoplasmic reticulum. *J Biol Chem,* 265**,** 13472-83.

PAIVARINNE, H. & KAINULAINEN, H. 2001. DAPIT, a novel protein down-regulated in insulin-sensitive tissues in streptozotocin-induced diabetes. *Acta Diabetol,* 38**,** 83-6.

PALADE, P., DETTBARN, C., BRUNDER, D., STEIN, P. & HALS, G. 1989. Pharmacology of calcium release from sarcoplasmic reticulum. *J Bioenerg Biomembr,* 21**,** 295-320.

PALTY, R., SILVERMAN, W. F., HERSHFINKEL, M., CAPORALE, T., SENSI, S. L., PARNIS, J., NOLTE, C., FISHMAN, D., SHOSHAN-BARMATZ, V., HERRMANN, S., KHANANSHVILI, D. & SEKLER, I. 2010. NCLX is an essential component of mitochondrial Na+/Ca2+ exchange. *Proc Natl Acad Sci U S A,* 107**,** 436-41.

PANOV, A. V. & SCADUTO, R. C., JR. 1995. Influence of calcium on NADH and succinate oxidation by rat heart submitochondrial particles. *Arch Biochem Biophys,* 316**,** 815-20.

PATTI, M. E., BUTTE, A. J., CRUNKHORN, S., CUSI, K., BERRIA, R., KASHYAP, S., MIYAZAKI, Y., KOHANE, I., COSTELLO, M., SACCONE, R., LANDAKER, E. J., GOLDFINE, A. B., MUN, E., DEFRONZO, R., FINLAYSON, J., KAHN, C. R. & MANDARINO, L. J. 2003. Coordinated reduction of genes of oxidative metabolism in humans with insulin resistance and diabetes: Potential role of PGC1 and NRF1. *Proc Natl Acad Sci U S A,* 100**,** 8466-71.

PATTI, M. E. & CORVERA, S. 2010. The role of mitochondria in the pathogenesis of type 2 diabetes. *Endocr Rev,* 31**,** 364-95.

PAUKOVICH, N., XUE, M., ELDER, J. R., REDZIC, J. S., BLUE, A., PIKE, H., MILLER, B. G., PITTS, T. M., POLLOCK, D. D., HANSEN, K., D'ALESSANDRO, A. & EISENMESSER, E. Z. 2018. Biliverdin Reductase B Dynamics Are Coupled to Coenzyme Binding. *J Mol Biol,* 430**,** 3234-3250.

PERRY, C. G., KANE, D. A., HERBST, E. A., MUKAI, K., LARK, D. S., WRIGHT, D. C., HEIGENHAUSER, G. J., NEUFER, P. D., SPRIET, L. L. & HOLLOWAY, G. P. 2012. Mitochondrial creatine kinase activity and phosphate shuttling are acutely regulated by exercise in human skeletal muscle. *J Physiol,* 590**,** 5475-86.

PERRY, C. G., KANE, D. A., LIN, C. T., KOZY, R., CATHEY, B. L., LARK, D. S., KANE, C. L., BROPHY, P. M., GAVIN, T. P., ANDERSON, E. J. & NEUFER, P. D. 2011. Inhibiting myosin-ATPase reveals a dynamic range of mitochondrial respiratory control in skeletal muscle. *Biochem J,* 437**,** 215-22.

PESTA, D. & GNAIGER, E. 2012. High-resolution respirometry: OXPHOS protocols for human cells and permeabilized fibers from small biopsies of human muscle. *Methods Mol Biol,* 810**,** 25-58.

PESTA, D., HOPPEL, F., MACEK, C., MESSNER, H., FAULHABER, M., KOBEL, C., PARSON, W., BURTSCHER, M., SCHOCKE, M. & GNAIGER, E. 2011. Similar qualitative and quantitative changes of mitochondrial respiration following strength and endurance training in normoxia and hypoxia in sedentary humans. *Am J Physiol Regul Integr Comp Physiol,* 301**,** R1078-87.

POLSTER, A., NELSON, B. R., OLSON, E. N. & BEAM, K. G. 2016. Stac3 has a direct role in skeletal muscle-type excitation-contraction coupling that is disrupted by a myopathy-causing mutation. *Proc Natl Acad Sci U S A,* 113**,** 10986-91.

POWERS, S. K., TALBERT, E. E. & ADHIHETTY, P. J. 2011. Reactive oxygen and nitrogen species as intracellular signals in skeletal muscle. *J Physiol,* 589**,** 2129-38.

PTACEK, L. J., TAWIL, R., GRIGGS, R. C., ENGEL, A. G., LAYZER, R. B., KWIECINSKI, H., MCMANIS, P. G., SANTIAGO, L., MOORE, M., FOUAD, G. & ET AL. 1994. Dihydropyridine receptor mutations cause hypokalemic periodic paralysis. *Cell,* 77**,** 863-8.

PUNTSCHART, A., WEY, E., JOSTARNDT, K., VOGT, M., WITTWER, M., WIDMER, H. R., HOPPELER, H. & BILLETER, R. 1998. Expression of fos and jun genes in human skeletal muscle after exercise. *Am J Physiol,* 274**,** C129-37.

PUTT, W., IVES, J. H., HOLLYOAKE, M., HOPKINSON, D. A., WHITEHOUSE, D. B. & EDWARDS, Y. H. 1993. Phosphoglucomutase 1: a gene with two promoters and a duplicated first exon. *Biochem J,* 296 (Pt 2)**,** 417-22.

QUANE, K. A., KEATING, K. E., HEALY, J. M., MANNING, B. M., KRIVOSIC-HORBER, R., KRIVOSIC, I., MONNIER, N., LUNARDI, J. & MCCARTHY, T. V. 1994. Mutation screening of the RYR1 gene in malignant hyperthermia: detection of a novel Tyr to Ser mutation in a pedigree with associated central cores. *Genomics,* 23**,** 236-9.

QUINLAN, C. L., ORR, A. L., PEREVOSHCHIKOVA, I. V., TREBERG, J. R., ACKRELL, B. A. & BRAND, M. D. 2012. Mitochondrial complex II can generate reactive oxygen species at high rates in both the forward and reverse reactions. *J Biol Chem,* 287**,** 27255-64.

QUINLIVAN, R., BUCKLEY, J., JAMES, M., TWIST, A., BALL, S., DUNO, M., VISSING, J., BRUNO, C., CASSANDRINI, D., ROBERTS, M., WINER, J., ROSE, M. & SEWRY, C. 2010. McArdle disease: a clinical review. *J Neurol Neurosurg Psychiatry,* 81**,** 1182-8.

QUINTANA, A., MORGAN, P. G., KRUSE, S. E., PALMITER, R. D. & SEDENSKY, M. M. 2012. Altered anesthetic sensitivity of mice lacking Ndufs4, a subunit of mitochondrial complex I. *PLoS One,* 7**,** e42904.

QUINZII, C. M. & HIRANO, M. 2010. Coenzyme Q and mitochondrial disease. *Dev Disabil Res Rev,* 16**,** 183-8.

RAFFA, S., CHIN, X. L. D., STANZIONE, R., FORTE, M., BIANCHI, F., COTUGNO, M., MARCHITTI, S., MICALONI, A., GALLO, G., SCHIRONE, L., TOCCI, G., VIOLINI, R., TORRISI, M. R., VOLPE, M. & RUBATTU, S. 2019. The reduction of NDUFC2 expression is associated with mitochondrial impairment in circulating mononuclear cells of patients with acute coronary syndrome. *Int J Cardiol,* 286**,** 127-133.

RAFFA, S., SCROFANI, C., VALENTE, S., MICALONI, A., FORTE, M., BIANCHI, F., COLUCCIA, R., GEURTS, A. M., SCIARRETTA, S., VOLPE, M., TORRISI, M. R. & RUBATTU, S. 2017. In vitro characterization of mitochondrial function and structure in rat and human cells with a deficiency of the NADH: ubiquinone oxidoreductase Ndufc2 subunit. *Hum Mol Genet,* 26**,** 4541-4555.

RASOLA, A. & BERNARDI, P. 2007. The mitochondrial permeability transition pore and its involvement in cell death and in disease pathogenesis. *Apoptosis,* 12**,** 815-33.

RASOLA, A. & BERNARDI, P. 2011. Mitochondrial permeability transition in Ca(2+)-dependent apoptosis and necrosis. *Cell Calcium,* 50**,** 222-33.

RIAZI, S., LARACH, M. G., HU, C., WIJEYSUNDERA, D., MASSEY, C. & KRAEVA, N. 2014. Malignant hyperthermia in Canada: characteristics of index anesthetics in 129 malignant hyperthermia susceptible probands. *Anesth Analg,* 118**,** 381-7.

ROBERTS, M. C., MICKELSON, J. R., PATTERSON, E. E., NELSON, T. E., ARMSTRONG, P. J., BRUNSON, D. B. & HOGAN, K. 2001. Autosomal dominant canine malignant hyperthermia is caused by a mutation in the gene encoding the skeletal muscle calcium release channel (RYR1). *Anesthesiology,* 95**,** 716-25.

ROBINSON, R., CARPENTER, D., SHAW, M. A., HALSALL, J. & HOPKINS, P. 2006. Mutations in RYR1 in malignant hyperthermia and central core disease. *Hum Mutat,* 27**,** 977-89.

ROBINSON, R., HOPKINS, P., CARSANA, A., GILLY, H., HALSALL, J., HEYTENS, L., ISLANDER, G., JURKAT-ROTT, K., MULLER, C. & SHAW, M. A. 2003a. Several interacting genes influence the malignant hyperthermia phenotype. *Hum Genet,* 112**,** 217-8.

ROBINSON, R. L., ANETSEDER, M. J., BRANCADORO, V., VAN BROEKHOVEN, C., CARSANA, A., CENSIER, K., FORTUNATO, G., GIRARD, T., HEYTENS, L., HOPKINS, P. M., JURKAT-ROTT, K., KLINGER, W., KOZAK-RIBBENS, G., KRIVOSIC, R., MONNIER, N., NIVOCHE, Y., OLTHOFF, D., RUEFFERT, H., SORRENTINO, V., TEGAZZIN, V. & MUELLER, C. R. 2003b. Recent advances in the diagnosis of malignant hyperthermia susceptibility: how confident can we be of genetic testing? *Eur J Hum Genet,* 11**,** 342-8.

ROBINSON, R. L., BROOKS, C., BROWN, S. L., ELLIS, F. R., HALSALL, P. J., QUINNELL, R. J., SHAW, M. A. & HOPKINS, P. M. 2002. RYR1 mutations causing central core disease are associated with more severe malignant hyperthermia in vitro contracture test phenotypes. *Hum Mutat,* 20**,** 88-97.

ROBINSON, R. L., CARPENTER, D., HALSALL, P. J., ILES, D. E., BOOMS, P., STEELE, D., HOPKINS, P. M. & SHAW, M. A. 2009. Epigenetic allele silencing and variable penetrance of malignant hyperthermia susceptibility. *Br J Anaesth,* 103**,** 220-5.

ROBINSON, R. L., CURRAN, J. L., ELLIS, F. R., HALSALL, P. J., HALL, W. J., HOPKINS, P. M., ILES, D. E., WEST, S. P. & SHAW, M. A. 2000. Multiple interacting gene products may influence susceptibility to malignant hyperthermia. *Ann Hum Genet,* 64**,** 307-20.

RODENBURG, R. J. 2016. Mitochondrial complex I-linked disease. *Biochim Biophys Acta,* 1857**,** 938-45.

RORBACH, J., GAMMAGE, P. A. & MINCZUK, M. 2012. C7orf30 is necessary for biogenesis of the large subunit of the mitochondrial ribosome. *Nucleic Acids Res,* 40**,** 4097-109.

ROSENBERG, H., POLLOCK, N., SCHIEMANN, A., BULGER, T. & STOWELL, K. 2015. Malignant hyperthermia: a review. *Orphanet J Rare Dis,* 10**,** 93.

ROUVIERE, C., CORONA, B. T. & INGALLS, C. P. 2012. Oxidative capacity and fatigability in run-trained malignant hyperthermia-susceptible mice. *Muscle Nerve,* 45**,** 586-96.

RSTUDIO TEAM. 2015. *RStudio: Integrated Development for R* [Online]. Boston, MA: RStudio, Inc. Available: http://www.rstudio.com/ [Accessed].

RUBATTU, S., DI CASTRO, S., SCHULZ, H., GEURTS, A. M., COTUGNO, M., BIANCHI, F., MAATZ, H., HUMMEL, O., FALAK, S., STANZIONE, R., MARCHITTI, S., SCARPINO, S., GIUSTI, B., KURA, A., GENSINI, G. F., PEYVANDI, F., MANNUCCI, P. M., RASURA, M., SCIARRETTA, S., DWINELL, M. R., HUBNER, N. & VOLPE, M. 2016. Ndufc2 Gene Inhibition Is Associated With Mitochondrial Dysfunction and Increased Stroke Susceptibility in an Animal Model of Complex Human Disease. *J Am Heart Assoc,* 5.

RUDOLF, R., MAGALHAES, P. J. & POZZAN, T. 2006. Direct in vivo monitoring of sarcoplasmic reticulum Ca2+ and cytosolic cAMP dynamics in mouse skeletal muscle. *J Cell Biol,* 173**,** 187-93.

RUEFFERT, H., OLTHOFF, D., DEUTRICH, C., THAMM, B. & FROSTER, U. G. 2001. Homozygous and heterozygous Arg614Cys mutations (1840C-->T) in the ryanodine receptor gene co-segregate with malignant hyperthermia susceptibility in a German family. *Br J Anaesth,* 87**,** 240-5.

RUHOY, I. S. & SANETO, R. P. 2014. The genetics of Leigh syndrome and its implications for clinical practice and risk management. *Appl Clin Genet,* 7**,** 221-34.

SAGAI, T., HOSOYA, M., MIZUSHINA, Y., TAMURA, M. & SHIROISHI, T. 2005. Elimination of a long-range cis-regulatory module causes complete loss of limb-specific Shh expression and truncation of the mouse limb. *Development,* 132**,** 797-803.

SAKAI, C., YAMAGUCHI, S., SASAKI, M., MIYAMOTO, Y., MATSUSHIMA, Y. & GOTO, Y. 2015. ECHS1 mutations cause combined respiratory chain deficiency resulting in Leigh syndrome. *Hum Mutat,* 36**,** 232-9.

SAKS, V. A., VEKSLER, V. I., KUZNETSOV, A. V., KAY, L., SIKK, P., TIIVEL, T., TRANQUI, L., OLIVARES, J., WINKLER, K., WIEDEMANN, F. & KUNZ, W. S. 1998. Permeabilized cell and skinned fiber techniques in studies of mitochondrial function in vivo. *Mol Cell Biochem,* 184**,** 81-100.

SALVIATI, L., TREVISSON, E., DOIMO, M. & NAVAS, P. 2017. *Primary Coenzyme Q10 Deficiency,* Seattle (WA), GeneReviews®.

SANCHEZ-CABALLERO, L., GUERRERO-CASTILLO, S. & NIJTMANS, L. 2016. Unraveling the complexity of mitochondrial complex I assembly: A dynamic process. *Biochim Biophys Acta,* 1857**,** 980-90.

SANDOW, A. 1952. Excitation-contraction coupling in muscular response. *Yale J Biol Med,* 25**,** 176-201.

SCHAEFER, A. M., MCFARLAND, R., BLAKELY, E. L., HE, L., WHITTAKER, R. G., TAYLOR, R. W., CHINNERY, P. F. & TURNBULL, D. M. 2008. Prevalence of mitochondrial DNA disease in adults. *Ann Neurol,* 63**,** 35-9.

SCHIAFFINO, S. & REGGIANI, C. 2011. Fiber types in mammalian skeletal muscles. *Physiol Rev,* 91**,** 1447-531.

SCHOENMAKERS, T. J., VISSER, G. J., FLIK, G. & THEUVENET, A. P. 1992. CHELATOR: an improved method for computing metal ion concentrations in physiological solutions. *Biotechniques,* 12**,** 870-4, 876-9.

SCHWEFEL, D., ARASU, B. S., MARINO, S. F., LAMPRECHT, B., KOCHERT, K., ROSENBAUM, E., EICHHORST, J., WIESNER, B., BEHLKE, J., ROCKS, O., MATHAS, S. & DAUMKE, O. 2013. Structural insights into the mechanism of GTPase activation in the GIMAP family. *Structure,* 21**,** 550-9.

SCOTT, W., STEVENS, J. & BINDER-MACLEOD, S. A. 2001. Human skeletal muscle fiber type classifications. *Phys Ther,* 81**,** 1810-6.

SHALLOE, F., ELLIOTT, G., ENNIS, O. & MANTLE, T. J. 1996. Evidence that biliverdin-IX beta reductase and flavin reductase are identical. *Biochem J,* 316 (Pt 2)**,** 385-7.

SHARMA, L. K., LU, J. & BAI, Y. 2009. Mitochondrial respiratory complex I: structure, function and implication in human diseases. *Curr Med Chem,* 16**,** 1266-77.

SHAULIAN, E. & KARIN, M. 2001. AP-1 in cell proliferation and survival. *Oncogene,* 20**,** 2390-400.

SHAULIAN, E. & KARIN, M. 2002. AP-1 as a regulator of cell life and death. *Nat Cell Biol,* 4**,** E131-6.

SHAW, M. A. & HOPKINS, P. M. 2019. Mission Impossible or Mission Futile?: Estimating Penetrance for Malignant Hyperthermia. *Anesthesiology,* 131**,** 957-959.

SICOTTE, H., RIDER, D. N., POLAND, G. A., DHIMAN, N. & KOCHER, J. P. 2011. SNPPicker: high quality tag SNP selection across multiple populations. *BMC Bioinformatics,* 12**,** 129.

SPARAGNA, G. C., GUNTER, K. K., SHEU, S. S. & GUNTER, T. E. 1995. Mitochondrial calcium uptake from physiological-type pulses of calcium. A description of the rapid uptake mode. *J Biol Chem,* 270**,** 27510-5.

SQUIRE, J. M. 2016. Muscle contraction: Sliding filament history, sarcomere dynamics and the two Huxleys. *Glob Cardiol Sci Pract,* 2016**,** e201611.

SREEKUMAR, R., HALVATSIOTIS, P., SCHIMKE, J. C. & NAIR, K. S. 2002. Gene expression profile in skeletal muscle of type 2 diabetes and the effect of insulin treatment. *Diabetes,* 51**,** 1913-20.

STAMMERS, A. N., SUSSER, S. E., HAMM, N. C., HLYNSKY, M. W., KIMBER, D. E., KEHLER, D. S. & DUHAMEL, T. A. 2015. The regulation of sarco(endo)plasmic reticulum calcium-ATPases (SERCA). *Can J Physiol Pharmacol,* 93**,** 843-54.

STARON, R. S., HAGERMAN, F. C., HIKIDA, R. S., MURRAY, T. F., HOSTLER, D. P., CRILL, M. T., RAGG, K. E. & TOMA, K. 2000. Fiber type composition of the vastus lateralis muscle of young men and women. *J Histochem Cytochem,* 48**,** 623-9.

STOJKOVIC, T., VISSING, J., PETIT, F., PIRAUD, M., ORNGREEN, M. C., ANDERSEN, G., CLAEYS, K. G., WARY, C., HOGREL, J. Y. & LAFORET, P. 2009. Muscle glycogenosis due to phosphoglucomutase 1 deficiency. *N Engl J Med,* 361**,** 425-7.

STRAUSS, A. W., POWELL, C. K., HALE, D. E., ANDERSON, M. M., AHUJA, A., BRACKETT, J. C. & SIMS, H. F. 1995. Molecular basis of human mitochondrial very-long-chain acyl-CoA dehydrogenase deficiency causing cardiomyopathy and sudden death in childhood. *Proc Natl Acad Sci U S A,* 92**,** 10496-500.

SUN, W. 2012. A statistical framework for eQTL mapping using RNA-seq data. *Biometrics,* 68**,** 1-11.

TALBOT, J. & MAVES, L. 2016. Skeletal muscle fiber type: using insights from muscle developmental biology to dissect targets for susceptibility and resistance to muscle disease. *Wiley Interdiscip Rev Dev Biol,* 5**,** 518-34.

THOMPSON, S. J., RIAZI, S., KRAEVA, N., NOSEWORTHY, M. D., RAYNER, T. E., SCHNEIDERMAN, J. E., CIFRA, B. & WELLS, G. D. 2017. Skeletal Muscle Metabolic Dysfunction in Patients With Malignant Hyperthermia Susceptibility. *Anesth Analg,* 125**,** 434-441.

TIMMINS, M. A., ROSENBERG, H., LARACH, M. G., STERLING, C., KRAEVA, N. & RIAZI, S. 2015. Malignant hyperthermia testing in probands without adverse anesthetic reaction. *Anesthesiology,* 123**,** 548-56.

TREBAK, M., ZHANG, W., RUHLE, B., HENKEL, M. M., GONZALEZ-COBOS, J. C., MOTIANI, R. K., STOLWIJK, J. A., NEWTON, R. L. & ZHANG, X. 2013. What role for store-operated Ca(2)(+) entry in muscle? *Microcirculation,* 20**,** 330-6.

TROVATO, F. M., IMBESI, R., CONWAY, N. & CASTROGIOVANNI, P. 2016. Morphological and Functional Aspects of Human Skeletal Muscle. *Journal of Functional Morphology and Kinesiology,* 1**,** 289-302.

TURNER, N., COONEY, G. J., KRAEGEN, E. W. & BRUCE, C. R. 2014. Fatty acid metabolism, energy expenditure and insulin resistance in muscle. *J Endocrinol,* 220**,** T61-79.

TURRENS, J. F. 2003. Mitochondrial formation of reactive oxygen species. *J Physiol,* 552**,** 335-44.

URWYLER, A., DEUFEL, T., MCCARTHY, T., WEST, S. & EUROPEAN MALIGNANT HYPERTHERMIA, G. 2001. Guidelines for molecular genetic detection of susceptibility to malignant hyperthermia. *Br J Anaesth,* 86**,** 283-7.

VANDESOMPELE, J., DE PRETER, K., PATTYN, F., POPPE, B., VAN ROY, N., DE PAEPE, A. & SPELEMAN, F. 2002. Accurate normalization of real-time quantitative

RT-PCR data by geometric averaging of multiple internal control genes. *Genome Biol,* 3**,** RESEARCH0034.

VIGUEIRA, P. A., MCCOMMIS, K. S., SCHWEITZER, G. G., REMEDI, M. S., CHAMBERS, K. T., FU, X., MCDONALD, W. G., COLE, S. L., COLCA, J. R., KLETZIEN, R. F., BURGESS, S. C. & FINCK, B. N. 2014. Mitochondrial pyruvate carrier 2 hypomorphism in mice leads to defects in glucose-stimulated insulin secretion. *Cell Rep,* 7**,** 2042-2053.

VISHWANATH, V. A. 2016. Fatty Acid Beta-Oxidation Disorders: A Brief Review. *Ann Neurosci,* 23**,** 51-5.

WAJNER, M. & AMARAL, A. U. 2015. Mitochondrial dysfunction in fatty acid oxidation disorders: insights from human and animal studies. *Biosci Rep,* 36**,** e00281.

WAPPLER, F., FIEGE, M., STEINFATH, M., AGARWAL, K., SCHOLZ, J., SINGH, S., MATSCHKE, J. & SCHULTE AM ESCH, J. 2001. Evidence for susceptibility to malignant hyperthermia in patients with exercise-induced rhabdomyolysis. *Anesthesiology,* 94**,** 95-100.

WEI, L. & DIRKSEN, R. T. 2010. Ryanodinopathies: RyR-Linked Muscle Diseases. *Curr Top Membr,* 66**,** 139-67.

WEIS, J. 1994. Jun, Fos, MyoD1, and myogenin proteins are increased in skeletal muscle fiber nuclei after denervation. *Acta Neuropathol,* 87**,** 63-70.

WEISS, R. G., O'CONNELL, K. M., FLUCHER, B. E., ALLEN, P. D., GRABNER, M. & DIRKSEN, R. T. 2004. Functional analysis of the R1086H malignant hyperthermia mutation in the DHPR reveals an unexpected influence of the III-IV loop on skeletal muscle EC coupling. *Am J Physiol Cell Physiol,* 287**,** C1094-102.

WICKHAM, H. 2016. *ggplot2: Elegant Graphics for Data Analysis,* Springer-Verlag New York.

WIESNER, R. J., RUEGG, J. C. & MORANO, I. 1992. Counting target molecules by exponential polymerase chain reaction: copy number of mitochondrial DNA in rat tissues. *Biochem Biophys Res Commun,* 183**,** 553-9.

WILSON, J. M., LOENNEKE, J. P., JO, E., WILSON, G. J., ZOURDOS, M. C. & KIM, J. S. 2012. The effects of endurance, strength, and power training on muscle fiber type shifting. *J Strength Cond Res,* 26**,** 1724-9.

WILSON, R. D., NICHOLS, R. J., DENT, T. E. & ALLEN, C. R. 1966. Disturbances of the Oxidative Phosphorylation Mechanism as a Possible Aetiological Factor in Sudden Unexplained Hyperthermia. *Anesthesiology,* 27.

WOLAK, S., RUCKER, B., KOHLSCHMIDT, N., DOETSCH, S., BARTSCH, O., ZECHNER, U. & TZANOVA, I. 2014. [Homozygous and compound heterozygous RYR1 mutations. New findings on prevalence and penetrance of malignant hyperthermia]. *Anaesthesist,* 63**,** 643-50.

WU, S., LI, Z., GNATENKO, D. V., ZHANG, B., ZHAO, L., MALONE, L. E., MARKOVA, N., MANTLE, T. J., NESBITT, N. M. & BAHOU, W. F. 2016. BLVRB redox mutation defines heme degradation in a metabolic pathway of enhanced thrombopoiesis in humans. *Blood,* 128**,** 699-709.

WWW.EMHG.ORG. 2020. *Diagnostic MH Mutations* [Online]. [Accessed 11 June 2020]. Available from: https://www.emhg.org/diagnostic-mutations

YAN, Z., BAI, X., YAN, C., WU, J., LI, Z., XIE, T., PENG, W., YIN, C., LI, X., SCHERES, S. H. W., SHI, Y. & YAN, N. 2015. Structure of the rabbit ryanodine receptor RyR1 at near-atomic resolution. *Nature,* 517**,** 50-55.

YANG, T., RIEHL, J., ESTEVE, E., MATTHAEI, K. I., GOTH, S., ALLEN, P. D., PESSAH, I. N. & LOPEZ, J. R. 2006. Pharmacologic and functional characterization of malignant hyperthermia in the R163C RyR1 knock-in mouse. *Anesthesiology,* 105**,** 1164-75.

YASUDA, T., DELBONO, O., WANG, Z. M., MESSI, M. L., GIRARD, T., URWYLER, A., TREVES, S. & ZORZATO, F. 2013. JP-45/JSRP1 variants affect skeletal muscle excitation-contraction coupling by decreasing the sensitivity of the dihydropyridine receptor. *Hum Mutat,* 34**,** 184-90.

YIN, H., PRICE, F. & RUDNICKI, M. A. 2013. Satellite cells and the muscle stem cell niche. *Physiol Rev,* 93**,** 23-67.

YUEN, B., BONCOMPAGNI, S., FENG, W., YANG, T., LOPEZ, J. R., MATTHAEI, K. I., GOTH, S. R., PROTASI, F., FRANZINI-ARMSTRONG, C., ALLEN, P. D. & PESSAH, I. N. 2012. Mice expressing T4826I-RYR1 are viable but exhibit sex- and genotype-dependent susceptibility to malignant hyperthermia and muscle damage. *FASEB J,* 26**,** 1311-22.

ZAHN, J. M., SONU, R., VOGEL, H., CRANE, E., MAZAN-MAMCZARZ, K., RABKIN, R., DAVIS, R. W., BECKER, K. G., OWEN, A. B. & KIM, S. K. 2006. Transcriptional profiling of aging in human muscle reveals a common aging signature. *PLoS Genet,* 2**,** e115.

ZALK, R., CLARKE, O. B., DES GEORGES, A., GRASSUCCI, R. A., REIKEN, S., MANCIA, F., HENDRICKSON, W. A., FRANK, J. & MARKS, A. R. 2015. Structure of a mammalian ryanodine receptor. *Nature,* 517**,** 44-9.

ZHANG, Y., FUJII, J., PHILLIPS, M. S., CHEN, H. S., KARPATI, G., YEE, W. C., SCHRANK, B., CORNBLATH, D. R., BOYLAN, K. B. & MACLENNAN, D. H. 1995. Characterization of cDNA and genomic DNA encoding SERCA1, the Ca(2+)-ATPase of human fast-twitch skeletal muscle sarcoplasmic reticulum, and its elimination as a candidate gene for Brody disease. *Genomics,* 30**,** 415-24.

ZHU, A., IBRAHIM, J. G. & LOVE, M. I. 2019. Heavy-tailed prior distributions for sequence count data: removing the noise and preserving large differences. *Bioinformatics,* 35**,** 2084-2092.

ZIMIN, P. I., WOODS, C. B., KAYSER, E. B., RAMIREZ, J. M., MORGAN, P. G. & SEDENSKY, M. M. 2018. Isoflurane disrupts excitatory neurotransmitter dynamics via inhibition of mitochondrial complex I. *Br J Anaesth,* 120**,** 1019-1032.

ZIMIN, P. I., WOODS, C. B., QUINTANA, A., RAMIREZ, J. M., MORGAN, P. G. & SEDENSKY, M. M. 2016. Glutamatergic Neurotransmission Links Sensitivity to Volatile Anesthetics with Mitochondrial Function. *Curr Biol,* 26**,** 2194-201.

ZOROV, D. B., JUHASZOVA, M. & SOLLOTT, S. J. 2014. Mitochondrial reactive oxygen species (ROS) and ROS-induced ROS release. *Physiol Rev,* 94**,** 909-50.

ZORZATO, F., FUJII, J., OTSU, K., PHILLIPS, M., GREEN, N. M., LAI, F. A., MEISSNER, G. & MACLENNAN, D. H. 1990. Molecular cloning of cDNA encoding human and rabbit forms of the Ca2+ release channel (ryanodine receptor) of skeletal muscle sarcoplasmic reticulum. *J Biol Chem,* 265**,** 2244-56.

ZSCHOCKE, J., SCHULZE, A., LINDNER, M., FIESEL, S., OLGEMOLLER, K., HOFFMANN, G. F., PENZIEN, J., RUITER, J. P., WANDERS, R. J. & MAYATEPEK, E. 2001. Molecular and functional characterisation of mild MCAD deficiency. *Hum Genet,* 108**,** 404-8.

8 APPENDICES

Appendix 1 – Gene ontology analyses for MHN vs MHS (baseline) comparison

	Upregulated terms	Adjusted p-value
(GO_BP) Biological Process	mRNA processing (GO:0006397)	2.32E-04
	RNA splicing, via transesterification reactions with bulged adenosine as nucleophile (GO:0000377)	2.32E-04
	mRNA splicing, via spliceosome (GO:0000398)	2.41E-04
	RNA splicing (GO:0008380)	1.25E-02
	RNA processing (GO:0006396)	2.19E-02
	RNA secondary structure unwinding (GO:0010501)	7.23E-02
	fat cell differentiation (GO:0045444)	1.46E-01
	positive regulation of cellular protein metabolic process (GO:0032270)	1.75E-01
	response to tumor necrosis factor (GO:0034612)	2.19E-01
	regulation of mitotic cell cycle phase transition (GO:1901990)	2.42E-01
(GO_MF) Molecular Function	RNA binding (GO:0003723)	4.41E-08
	mRNA binding (GO:0003729)	4.04E-02
	ATP-dependent helicase activity (GO:0008026)	5.43E-02
	ATPase activity (GO:0016887)	7.01E-02
	ATPase activity, coupled (GO:0042623)	7.52E-02
	RNA-dependent ATPase activity (GO:0008186)	7.81E-02
	ATP-dependent RNA helicase activity (GO:0004004)	8.34E-02
	RNA helicase activity (GO:0003724)	9.72E-02
	nucleoside-triphosphatase activity (GO:0017111)	1.29E-01
	proteasome-activating ATPase activity (GO:0036402)	1.34E-01
(GO_CC) Cellular Component	nucleolus (GO:0005730)	2.58E-07
	spliceosomal complex (GO:0005681)	4.07E-05
	U2-type spliceosomal complex (GO:0005684)	4.50E-02
	nuclear body (GO:0016604)	4.51E-02
	nuclear speck (GO:0016607)	5.24E-02
	preribosome (GO:0030684)	5.42E-02
	spindle pole (GO:0000922)	5.82E-02
	spliceosomal snRNP complex (GO:0097525)	1.19E-01
	nuclear proteasome complex (GO:0031595)	1.28E-01
	trans-Golgi network (GO:0005802)	1.32E-01

Table 1. Gene ontology results using upregulated genes. Top 10 ontology terms for biological process, molecular function and cellular component generated using Enrichr, in order of adjusted p-value.

	Downregulated terms	Adjusted p-value
(GO_BP) Biological Process	respiratory electron transport chain (GO:0022904)	2.84E-16
	mitochondrial ATP synthesis coupled electron transport (GO:0042775)	4.62E-16
	mitochondrial respiratory chain complex assembly (GO:0033108)	1.01E-11
	mitochondrial respiratory chain complex I assembly (GO:0032981)	1.87E-10
	mitochondrial respiratory chain complex I biogenesis (GO:0097031)	2.24E-10
	NADH dehydrogenase complex assembly (GO:0010257)	2.80E-10
	mitochondrial electron transport, NADH to ubiquinone (GO:0006120)	2.32E-08
	mitochondrial translational elongation (GO:0070125)	3.98E-08
	mitochondrial translational termination (GO:0070126)	5.28E-08
	translational elongation (GO:0006414)	1.09E-07
(GO_MF) Molecular Function	NADH dehydrogenase (quinone) activity (GO:0050136)	1.03E-07
	NADH dehydrogenase (ubiquinone) activity (GO:0008137)	2.06E-07
	NADH dehydrogenase activity (GO:0003954)	3.33E-03
	NEDD8 transferase activity (GO:0019788)	1.37E-01
	small ribosomal subunit rRNA binding (GO:0070181)	1.56E-01
	hydrogen ion transmembrane transporter activity (GO:0015078)	1.60E-01
	ubiquinol-cytochrome-c reductase activity (GO:0008121)	1.83E-01
	oxidoreductase activity, acting on diphenols and related substances as donors, cytochrome as acceptor (GO:0016681)	2.09E-01
	clathrin adaptor activity (GO:0035615)	3.01E-01
	endocytic adaptor activity (GO:0098748)	3.34E-01
(GO_CC) Cellular Component	mitochondrion (GO:0005739)	7.71E-30
	mitochondrial inner membrane (GO:0005743)	8.26E-23
	mitochondrial matrix (GO:0005759)	5.97E-11
	mitochondrial respiratory chain complex I (GO:0005747)	8.06E-11
	mitochondrial respiratory chain complex IV (GO:0005751)	9.26E-07
	mitochondrial respiratory chain complex III (GO:0005750)	1.16E-04
	mitochondrial large ribosomal subunit (GO:0005762)	1.19E-03
	integral component of endoplasmic reticulum membrane (GO:0030176)	1.40E-03
	mitochondrial envelope (GO:0005740)	1.60E-03
	mitochondrial small ribosomal subunit (GO:0005763)	4.95E-03

Table 2. Gene ontology results using downregulated genes. Top 10 ontology terms for biological process, molecular function and cellular component generated using Enrichr, in order of adjusted p-value.

Appendix 2 – Pathway analysis for the MHN vs MHS_h comparison (baseline)

Index	Upregulated pathway terms	P-value	Adjusted p-value	Odds Ratio	Combined score
1	mRNA Processing WP411	6.73E-08	3.18E-05	6.16	101.66
2	Translation Factors WP107	3.92E-05	9.25E-03	7.46	75.68
3	Leptin and adiponectin WP3934	1.33E-02	6.97E-01	11.08	47.88
4	Hippo-Yap signaling pathway WP4537	7.90E-03	6.22E-01	7.23	34.98
5	Nanoparticle triggered autophagic cell death WP2509	7.90E-03	7.46E-01	7.23	34.98
6	Parkin-Ubiquitin Proteasomal System pathway WP2359	1.65E-03	2.59E-01	4.75	30.44
7	Cysteine and methionine catabolism WP4504	2.56E-02	1.00E+00	7.91	29
8	Sulindac Metabolic Pathway WP2542	8.71E-02	1.00E+00	11.08	27.05
9	Intraflagellar transport proteins binding to dynein WP4532	1.24E-02	7.30E-01	6.16	27.04
10	Deregulation of Rab and Rab Effector Genes in Bladder Cancer WP2291	3.30E-02	1.00E+00	6.93	23.62

Index	Downregulated pathway terms	P-value	Adjusted p-value	Odds Ratio	Combined score
1	Electron Transport Chain (OXPHOS system in mitochondria) WP111	1.62E-25	7.65E-23	6.84	390.66
2	Oxidative phosphorylation WP623	1.13E-18	1.78E-16	7.65	316.15
3	Nonalcoholic fatty liver disease WP4396	3.71E-19	8.74E-17	4.76	201.99
4	Mitochondrial complex I assembly model OXPHOS system WP4324	3.54E-10	3.34E-08	5.56	121.04
5	Cytoplasmic Ribosomal Proteins WP477	6.48E-11	7.65E-09	4.6	108.03
6	Proteasome Degradation WP183	1.71E-08	1.35E-06	4.76	85.11
7	Regulation of Apoptosis by Parathyroid Hormone-related Protein WP3872	2.34E-04	1.38E-02	5.22	43.61
8	Dual hijack model of Vif in HIV infection WP3300	1.01E-02	2.06E-01	6.15	28.28
9	Apoptosis Modulation and Signaling WP1772	1.13E-04	7.63E-03	2.88	26.19
10	Pyrimidine metabolism WP4022	5.94E-04	3.11E-02	2.7	20.06

Table 1. Pathway analysis for MHN vs MHS_h at baseline. The top 10 pathway terms generated by Enrichr, using upregulated and downregulated gene lists. Upregulated (Top) and downregulated (bottom) pathways are displayed in order of combined score (log of p-value from Fisher's exact test multiplied by z score of deviation from expected rank).

Appendix 3 - Gene ontology analyses for MHN vs MHS_h (baseline) comparison

	Upregulated terms	Adjusted p-value
(GO_BP) Biological Process	mRNA splicing, via spliceosome (GO:0000398)	3.29E-09
	RNA splicing, via transesterification reactions with bulged adenosine as nucleophile (GO:0000377)	4.54E-09
	mRNA processing (GO:0006397)	1.40E-08
	RNA metabolic process (GO:0016070)	7.38E-05
	RNA processing (GO:0006396)	3.84E-04
	RNA splicing (GO:0008380)	2.48E-03
	nucleic acid metabolic process (GO:0090304)	8.81E-03
	RNA secondary structure unwinding (GO:0010501)	9.85E-03
	ribonucleoprotein complex assembly (GO:0022618)	1.31E-02
	Golgi to plasma membrane protein transport (GO:0043001)	2.81E-02
(GO_MF) Molecular Function	RNA binding (GO:0003723)	5.41E-16
	mRNA binding (GO:0003729)	2.85E-07
	translation initiation factor activity (GO:0003743)	1.08E-03
	translation factor activity, RNA binding (GO:0008135)	6.86E-03
	proteasome-activating ATPase activity (GO:0036402)	2.45E-02
	ATP-dependent helicase activity (GO:0008026)	2.56E-02
	RNA-dependent ATPase activity (GO:0008186)	2.56E-02
	ATP-dependent RNA helicase activity (GO:0004004)	2.62E-02
	RNA helicase activity (GO:0003724)	3.00E-02
	ATPase activity (GO:0016887)	3.01E-02
(GO_CC) Cellular Component	nucleolus (GO:0005730)	1.70E-07
	spliceosomal complex (GO:0005681)	3.86E-07
	nuclear body (GO:0016604)	1.04E-04
	nuclear speck (GO:0016607)	7.09E-04
	spindle pole (GO:0000922)	1.86E-03
	U2-type spliceosomal complex (GO:0005684)	6.69E-03
	endoplasmic reticulum tubular network (GO:0071782)	1.23E-02
	RNA polymerase II transcription factor complex (GO:0090575)	1.50E-02
	nuclear proteasome complex (GO:0031595)	1.62E-02
	cytosolic proteasome complex (GO:0031597)	1.92E-02

Table 1. Gene ontology results using upregulated genes. Top 10 ontology terms for biological process, molecular function and cellular component generated using Enrichr, in order of adjusted p-value.

	Downregulated terms	Adjusted p-value
(GO_BP) Biological Process	respiratory electron transport chain (GO:0022904)	1.40E-15
	mitochondrial ATP synthesis coupled electron transport (GO:0042775)	1.63E-15
	mitochondrial respiratory chain complex assembly (GO:0033108)	1.17E-13
	mitochondrial translational elongation (GO:0070125)	1.68E-13
	cellular protein metabolic process (GO:0044267)	3.45E-13
	mitochondrial transport (GO:0006839)	1.90E-12
	mitochondrial translational termination (GO:0070126)	2.00E-12
	translational termination (GO:0006415)	2.02E-12
	translation (GO:0006412)	3.77E-12
	translational elongation (GO:0006414)	4.14E-12
(GO_MF) Molecular Function	NADH dehydrogenase (ubiquinone) activity (GO:0008137)	1.54E-08
	NADH dehydrogenase (quinone) activity (GO:0050136)	7.68E-09
	hydrogen ion transmembrane transporter activity (GO:0015078)	9.77E-06
	NADH dehydrogenase activity (GO:0003954)	2.13E-04
	ATPase activity, coupled to transmembrane movement of ions, rotational mechanism (GO:0044769)	1.94E-04
	RNA binding (GO:0003723)	3.18E-04
	ubiquitin protein ligase binding (GO:0031625)	1.65E-02
	proton-transporting ATPase activity, rotational mechanism (GO:0046961)	3.18E-02
	ubiquitin-like protein ligase binding (GO:0044389)	3.04E-02
	proton-transporting ATP synthase activity, rotational mechanism (GO:0046933)	3.05E-02
(GO_CC) Cellular Component	mitochondrion (GO:0005739)	8.61E-31
	mitochondrial inner membrane (GO:0005743)	1.10E-28
	mitochondrial respiratory chain complex I (GO:0005747)	6.23E-10
	mitochondrial matrix (GO:0005759)	1.37E-08
	mitochondrial large ribosomal subunit (GO:0005762)	4.97E-08
	cytosolic ribosome (GO:0022626)	3.04E-07
	lysosomal membrane (GO:0005765)	9.41E-07
	azurophil granule (GO:0042582)	1.98E-06
	cytosolic part (GO:0044445)	3.65E-06
	lysosome (GO:0005764)	1.32E-05

Table 2. Gene ontology results using downregulated genes. Top 10 ontology terms for biological process, molecular function and cellular component generated using Enrichr, in order of adjusted p-value.

Appendix 4 - Pathway analysis for the MHN vs MHS_{hc} comparison (baseline)

Index	Upregulated pathway terms	P-value	Adjusted p-value	Odds Ratio	Combined score
1	SREBF and miR33 in cholesterol and lipid homeostasis WP2011	3.93E-04	2.32E-02	67.57	529.82
2	Photodynamic therapy-induced NF-kB survival signaling WP3617	3.66E-05	5.76E-03	46.33	473.28
3	Overview of nanoparticle effects WP3287	5.58E-04	2.64E-02	56.9	426.21
4	Adipogenesis WP236	1.32E-07	6.25E-05	24.95	395.13
5	PPAR signaling pathway WP3942	6.99E-06	1.65E-03	32.27	383.1
6	Transcription factor regulation in adipogenesis WP3599	7.52E-04	3.23E-02	49.14	353.49
7	Vitamin B12 Metabolism WP1533	1.08E-04	1.02E-02	32.43	296.34
8	Eicosanoid Synthesis WP167	1.14E-03	4.47E-02	40.04	271.51
9	Composition of Lipid Particles WP3601	1.65E-02	3.12E-01	60.06	246.4
10	Role Altered Glycolysation of MUC1 in Tumour Microenvironment WP4480	1.65E-02	3.00E-01	60.06	246.4

Index	Downregulated pathway terms	P-value	Adjusted p-value	Odds Ratio	Combined score
1	Oxidative phosphorylation WP623	1.97E-03	9.28E-01	30.3	188.83
2	Electron Transport Chain (OXPHOS system in mitochondria) WP111	5.67E-03	1.00E+00	17.65	91.3
3	Target Of Rapamycin (TOR) Signaling WP1471	3.89E-02	1.00E+00	25.25	82
4	Glycolysis and Gluconeogenesis WP534	4.84E-02	1.00E+00	20.2	61.19
5	Selenium Metabolism and Selenoproteins WP28	4.94E-02	1.00E+00	19.76	59.43
6	Calcium Regulation in the Cardiac Cell WP536	1.16E-02	1.00E+00	12.2	54.44
7	TGF-beta Receptor Signaling WP560	5.78E-02	1.00E+00	16.84	48
8	Mitochondrial complex I assembly model OXPHOS system WP4324	5.99E-02	1.00E+00	16.23	45.71
9	Proteasome Degradation WP183	6.61E-02	1.00E+00	14.66	39.84
10	Alzheimers Disease WP2059	8.75E-02	1.00E+00	10.95	26.69

Table 1. Pathway analysis for MHN vs MHS_{hc} at baseline. The top 10 pathway terms generated by Enrichr, using upregulated and downregulated gene lists. Upregulated (Top) and downregulated (bottom) pathways are displayed in order of combined score (log of p-value from Fisher's exact test multiplied by z score of deviation from expected rank).

Appendix 5 - Gene ontology analyses for MHN vs MHS_{hc} (baseline) comparison

	Upregulated terms	Adjusted p-value
(GO_BP) Biological Process	positive regulation of acute inflammatory response (GO:0002675)	3.33E-01
	fat cell differentiation (GO:0045444)	3.36E-01
	regulation of inflammatory response (GO:0050727)	3.73E-01
	regulation of fat cell differentiation (GO:0045598)	3.74E-01
	regulation of vascular associated smooth muscle cell migration (GO:1904752)	4.47E-01
	regulation of vascular endothelial growth factor production (GO:0010574)	7.84E-01
	regulation of macrophage derived foam cell differentiation (GO:0010743)	7.91E-01
	positive regulation of type 2 immune response (GO:0002830)	8.36E-01
	internal protein amino acid acetylation (GO:0006475)	8.42E-01
	regulation of transforming growth factor beta production (GO:0071634)	8.44E-01
(GO_MF) Molecular Function	oxidoreductase activity, acting on single donors with incorporation of molecular oxygen, incorporation of two atoms of oxygen (GO:0016702)	7.45E-01
	manganese ion binding (GO:0030145)	1.00E+00
	clathrin heavy chain binding (GO:0032050)	1.00E+00
	primary amine oxidase activity (GO:0008131)	1.00E+00
	RNA polymerase II core promoter proximal region sequence-specific DNA binding (GO:0000978)	1.00E+00
	interleukin-6 receptor binding (GO:0005138)	1.00E+00
	calcium-dependent phospholipase A2 activity (GO:0047498)	1.00E+00
	phospholipase binding (GO:0043274)	1.00E+00
	core promoter proximal region sequence-specific DNA binding (GO:0000987)	1.00E+00
	transcription factor activity, RNA polymerase II core promoter proximal region sequence-specific binding (GO:0000982)	1.00E+00
(GO_CC) Cellular Component	lipid droplet (GO:0005811)	1.00E+00
	endoplasmic reticulum lumen (GO:0005788)	1.00E+00
	extrinsic component of external side of plasma membrane (GO:0031232)	1.00E+00
	nuclear speck (GO:0016607)	1.00E+00
	nuclear body (GO:0016604)	1.00E+00
	endolysosome membrane (GO:0036020)	1.00E+00
	nucleolus (GO:0005730)	1.00E+00
	endolysosome (GO:0036019)	1.00E+00
	U4/U6 x U5 tri-snRNP complex (GO:0046540)	1.00E+00
	brush border membrane (GO:0031526)	1.00E+00

Table 1. Gene ontology results using upregulated genes. Top 10 ontology terms for biological process, molecular function and cellular component generated using Enrichr, in order of adjusted p-value.

	Downregulated terms	Adjusted p-value
(GO_BP) Biological Process	heart trabecula formation (GO:0060347)	1.00E+00
	membrane invagination (GO:0010324)	1.00E+00
	negative regulation of establishment of protein localization (GO:1904950)	1.00E+00
	SMAD protein complex assembly (GO:0007183)	1.00E+00
	amyloid fibril formation (GO:1990000)	1.00E+00
	regulation of amyloid precursor protein catabolic process (GO:1902991)	1.00E+00
	vacuolar proton-transporting V-type ATPase complex assembly (GO:0070072)	1.00E+00
	negative regulation of phagocytosis (GO:0050765)	1.00E+00
	proton-transporting V-type ATPase complex assembly (GO:0070070)	1.00E+00
	establishment of synaptic vesicle localization (GO:0097480)	1.00E+00
(GO_MF) Molecular Function	FK506 binding (GO:0005528)	1.03E-01
	peptidyl-prolyl cis-trans isomerase activity (GO:0003755)	3.39E-01
	type I transforming growth factor beta receptor binding (GO:0034713)	1.00E+00
	phosphatidylinositol-5-phosphate binding (GO:0010314)	1.00E+00
	activin binding (GO:0048185)	1.00E+00
	proton-transporting ATP synthase activity, rotational mechanism (GO:0046933)	1.00E+00
	phosphatidylinositol-3,5-bisphosphate binding (GO:0080025)	1.00E+00
	phosphatidylinositol-4-phosphate binding (GO:0070273)	1.00E+00
	ATPase activity, coupled to transmembrane movement of ions, rotational mechanism (GO:0044769)	1.00E+00
	calcium channel regulator activity (GO:0005246)	1.00E+00
(GO_CC) Cellular Component	mitochondrial proton-transporting ATP synthase complex (GO:0005753)	8.71E-02
	mitochondrion (GO:0005739)	4.99E-01
	mitochondrial inner membrane (GO:0005743)	5.78E-01
	mitochondrial proton-transporting ATP synthase complex, coupling factor F(o) (GO:0000276)	5.92E-01
	early phagosome (GO:0032009)	7.39E-01
	endoplasmic reticulum subcompartment (GO:0098827)	9.83E-01
	early endosome (GO:0005769)	1.00E+00
	sarcoplasmic reticulum (GO:0016529)	1.00E+00
	intrinsic component of mitochondrial inner membrane (GO:0031304)	1.00E+00
	sarcoplasm (GO:0016528)	1.00E+00

Table 2. Gene ontology results using downregulated genes. Top 10 ontology terms for biological process, molecular function and cellular component generated using Enrichr, in order of adjusted p-value.

Appendix 6 – Gene ontology analysis for MHN pre vs post IVCT (halothane) comparison

	Upregulated terms	Adjusted p-value
(GO_BP) Biological Process	regulation of transcription, DNA-templated (GO:0006355)	1.03E-15
	regulation of transcription from RNA polymerase II promoter (GO:0006357)	1.15E-14
	RNA splicing, via transesterification reactions with bulged adenosine as nucleophile (GO:0000377)	1.27E-14
	mRNA splicing, via spliceosome (GO:0000398)	1.00E-13
	positive regulation of transcription, DNA-templated (GO:0045893)	1.00E-13
	mRNA processing (GO:0006397)	5.97E-13
	transcription from RNA polymerase II promoter (GO:0006366)	1.10E-12
	positive regulation of transcription from RNA polymerase II promoter (GO:0045944)	3.61E-09
	regulation of gene expression (GO:0010468)	7.47E-09
	transcription, DNA-templated (GO:0006351)	7.93E-09
(GO_MF) Molecular Function	RNA binding (GO:0003723)	6.33E-31
	DNA binding (GO:0003677)	1.04E-05
	ATP-dependent helicase activity (GO:0008026)	2.34E-05
	mRNA binding (GO:0003729)	4.26E-05
	purine ribonucleoside triphosphate binding (GO:0035639)	6.77E-05
	transcription regulatory region DNA binding (GO:0044212)	6.85E-05
	ATPase activity, coupled (GO:0042623)	8.51E-05
	ATPase activity (GO:0016887)	8.91E-05
	nucleoside-triphosphatase activity (GO:0017111)	1.10E-04
	nuclear hormone receptor binding (GO:0035257)	1.16E-04
(GO_CC) Cellular Component	nuclear body (GO:0016604)	4.25E-14
	nucleolus (GO:0005730)	5.65E-12
	nuclear speck (GO:0016607)	6.20E-12
	cytoskeleton (GO:0005856)	1.66E-06
	nucleoplasm part (GO:0044451)	1.87E-06
	spliceosomal complex (GO:0005681)	1.38E-05
	microtubule organizing center (GO:0005815)	1.39E-05
	microtubule organizing center part (GO:0044450)	8.70E-05
	actin cytoskeleton (GO:0015629)	8.90E-05
	centrosome (GO:0005813)	9.63E-05

Table 1. Gene ontology results using upregulated genes. Top 10 ontology terms for biological process, molecular function and cellular component generated using Enrichr, in order of adjusted p-value.

	Downregulated terms	Adjusted p-value
(GO_BP) Biological Process	SRP-dependent cotranslational protein targeting to membrane (GO:0006614)	3.53E-31
	protein targeting to ER (GO:0045047)	1.21E-30
	cotranslational protein targeting to membrane (GO:0006613)	4.69E-30
	respiratory electron transport chain (GO:0022904)	6.74E-30
	mitochondrial ATP synthesis coupled electron transport (GO:0042775)	7.46E-30
	peptide biosynthetic process (GO:0043043)	9.43E-30
	translation (GO:0006412)	3.35E-27
	nuclear-transcribed mRNA catabolic process, nonsense-mediated decay (GO:0000184)	2.57E-25
	viral transcription (GO:0019083)	3.93E-24
	viral gene expression (GO:0019080)	4.87E-24
(GO_MF) Molecular Function	NADH dehydrogenase (quinone) activity (GO:0050136)	4.97E-13
	NADH dehydrogenase (ubiquinone) activity (GO:0008137)	9.94E-13
	rRNA binding (GO:0019843)	3.16E-03
	small ribosomal subunit rRNA binding (GO:0070181)	3.63E-03
	ubiquitin conjugating enzyme activity (GO:0061631)	4.58E-03
	NADH dehydrogenase activity (GO:0003954)	6.25E-03
	ubiquitin-like protein conjugating enzyme activity (GO:0061650)	6.56E-03
	ubiquinol-cytochrome-c reductase activity (GO:0008121)	6.56E-03
	oxidoreductase activity, acting on diphenols and related substances as donors, cytochrome as acceptor (GO:0016681)	7.50E-03
	RNA binding (GO:0003723)	2.06E-02
(GO_CC) Cellular Component	mitochondrion (GO:0005739)	1.73E-39
	mitochondrial inner membrane (GO:0005743)	2.44E-30
	cytosolic ribosome (GO:0022626)	2.10E-28
	cytosolic part (GO:0044445)	1.96E-21
	small ribosomal subunit (GO:0015935)	5.04E-18
	cytosolic small ribosomal subunit (GO:0022627)	3.37E-16
	mitochondrial respiratory chain complex I (GO:0005747)	1.54E-15
	ribosome (GO:0005840)	2.47E-14
	large ribosomal subunit (GO:0015934)	1.08E-12
	cytosolic large ribosomal subunit (GO:0022625)	1.47E-12

Table 2. Gene ontology results using downregulated genes. Top 10 ontology terms for biological process, molecular function and cellular component generated using Enrichr, in order of adjusted p-value.

Appendix 7 – Gene ontology analysis for MHS pre vs post IVCT (halothane) comparison

	Upregulated terms	Adjusted p-value
(GO_BP) Biological Process	protein kinase B signaling (GO:0043491)	6.18E-04
	response to unfolded protein (GO:0006986)	6.19E-04
	response to interleukin-1 (GO:0070555)	6.22E-04
	cellular response to tumor necrosis factor (GO:0071356)	6.41E-04
	inflammatory response (GO:0006954)	6.46E-04
	chemokine-mediated signaling pathway (GO:0070098)	7.98E-04
	eosinophil chemotaxis (GO:0048245)	1.07E-03
	negative regulation of extrinsic apoptotic signaling pathway in absence of ligand (GO:2001240)	1.17E-03
	chaperone mediated protein folding requiring cofactor (GO:0051085)	1.17E-03
	response to tumor necrosis factor (GO:0034612)	1.24E-03
(GO_MF) Molecular Function	chemokine receptor binding (GO:0042379)	1.77E-04
	chemokine activity (GO:0008009)	2.26E-04
	cytokine activity (GO:0005125)	6.76E-04
	C3HC4-type RING finger domain binding (GO:0055131)	4.32E-03
	CCR chemokine receptor binding (GO:0048020)	5.64E-03
	transcription corepressor activity (GO:0003714)	2.17E-02
	transcription regulatory region DNA binding (GO:0044212)	3.08E-02
	sequence-specific double-stranded DNA binding (GO:1990837)	8.59E-02
	transcriptional repressor activity, RNA polymerase II transcription regulatory region sequence-specific binding (GO:0001227)	8.77E-02
	ubiquitin protein ligase binding (GO:0031625)	1.07E-01
(GO_CC) Cellular Component	tertiary granule lumen (GO:1904724)	1.83E-01
	ficolin-1-rich granule lumen (GO:1904813)	2.18E-01
	ficolin-1-rich granule (GO:0101002)	2.38E-01
	specific granule (GO:0042581)	3.29E-01
	tertiary granule (GO:0070820)	3.67E-01
	specific granule lumen (GO:0035580)	1.00E+00
	nuclear speck (GO:0016607)	1.00E+00
	nuclear body (GO:0016604)	1.00E+00
	tertiary granule membrane (GO:0070821)	1.00E+00
	specific granule membrane (GO:0035579)	1.00E+00

Table 1. Gene ontology results using upregulated genes. Top 10 ontology terms for biological process, molecular function and cellular component generated using Enrichr, in order of adjusted p-value.

	Downregulated terms	Adjusted p-value
(GO_BP) Biological Process	mitochondrial electron transport, NADH to ubiquinone (GO:0006120)	3.62E-02
	respiratory electron transport chain (GO:0022904)	5.36E-02
	mitochondrial ATP synthesis coupled electron transport (GO:0042775)	6.56E-02
	mitochondrial respiratory chain complex I assembly (GO:0032981)	6.71E-02
	mitochondrial respiratory chain complex I biogenesis (GO:0097031)	8.05E-02
	NADH dehydrogenase complex assembly (GO:0010257)	1.01E-01
	glomerulus vasculature development (GO:0072012)	1.35E-01
	negative regulation of blood coagulation (GO:0030195)	1.80E-01
	mitochondrial respiratory chain complex assembly (GO:0033108)	2.23E-01
	endothelium development (GO:0003158)	2.80E-01
(GO_MF) Molecular Function	NADH dehydrogenase (quinone) activity (GO:0050136)	2.75E-01
	NADH dehydrogenase (ubiquinone) activity (GO:0008137)	5.50E-01
	protein tyrosine/serine/threonine phosphatase activity (GO:0008138)	1.00E+00
	SH3/SH2 adaptor activity (GO:0005070)	1.00E+00
	mitogen-activated protein kinase kinase binding (GO:0031434)	1.00E+00
	chloride ion binding (GO:0031404)	1.00E+00
	MAP kinase tyrosine/serine/threonine phosphatase activity (GO:0017017)	1.00E+00
	ubiquinol-cytochrome-c reductase activity (GO:0008121)	1.00E+00
	bioactive lipid receptor activity (GO:0045125)	1.00E+00
	oxidoreductase activity, acting on diphenols and related substances as donors, cytochrome as acceptor (GO:0016681)	1.00E+00
(GO_CC) Cellular Component	mitochondrial respiratory chain complex I (GO:0005747)	3.52E-01
	mitochondrial inner membrane (GO:0005743)	2.96E-01
	intercalated disc (GO:0014704)	8.04E-01
	platelet alpha granule (GO:0031091)	1.00E+00
	potassium channel complex (GO:0034705)	1.00E+00
	mitochondrial respiratory chain complex III (GO:0005750)	1.00E+00
	platelet alpha granule membrane (GO:0031092)	1.00E+00
	anchored component of external side of plasma membrane (GO:0031362)	1.00E+00
	intrinsic component of external side of plasma membrane (GO:0031233)	1.00E+00
	mitochondrial proton-transporting ATP synthase complex (GO:0005753)	1.00E+00

Table 2. Gene ontology results using downregulated genes. Top 10 ontology terms for biological process, molecular function and cellular component generated using Enrichr, in order of adjusted p-value.

Appendix 8 – Pathway analysis for pre vs post IVCT (caffeine) comparisons

MHN (pre vs post caffeine)

Index	Upregulated pathway terms	P-value	Adjusted p-value	Odds Ratio	Combined score
1	Photodynamic therapy-induced NF-kB survival signaling WP3617	1.59E-13	7.52E-11	10.87	320.36
2	miRNAs involvement in the immune response in sepsis WP4329	1.64E-09	1.93E-07	8.36	169.04
3	mRNA Processing WP411	2.05E-12	4.83E-10	5.1	137.16
4	Spinal Cord Injury WP2431	1.10E-10	1.73E-08	4.84	110.92
5	Photodynamic therapy-induced unfolded protein response WP3613	9.32E-07	4.00E-05	7.93	110.08
6	IL1 and megakaryocytes in obesity WP2865	3.81E-06	1.06E-04	7.93	98.9
7	Lung fibrosis WP3624	3.71E-08	2.92E-06	5.66	96.88
8	Hypertrophy Model WP516	1.09E-05	2.23E-04	8.32	95.13
9	Apoptosis-related network due to altered Notch3 in ovarian cancer WP2864	2.07E-07	1.22E-05	5.83	89.77
10	TNF related weak inducer of apoptosis (TWEAK) Signaling Pathway WP2036	8.81E-07	4.16E-05	6.23	86.84

MHS (pre vs post caffeine)

Index	Name	P-value	Adjusted p-value	Odds Ratio	Combined score
1	miRNAs involvement in the immune response in sepsis WP4329	3.01E-11	1.42E-08	16.56	401.23
2	Photodynamic therapy-induced NF-kB survival signaling WP3617	3.78E-10	8.91E-08	15.92	345.36
3	Cells and Molecules involved in local acute inflammatory response WP4493	3.36E-07	2.27E-05	19.66	293.1
4	Platelet-mediated interactions with vascular and circulating cells WP4462	9.39E-06	3.17E-04	16.39	189.68
5	Photodynamic therapy-induced AP-1 survival signaling. WP3611	2.29E-07	2.16E-05	10.03	153.31
6	Role Altered Glycolysation of MUC1 in Tumour Microenvironment WP4480	4.45E-04	6.17E-03	18.57	143.33
7	Ethanol metabolism resulting in production of ROS by CYP2E1 WP4269	6.27E-04	8.22E-03	16.71	123.26
8	EBV LMP1 signaling WP262	4.67E-05	1.23E-03	12.11	120.76
9	Spinal Cord Injury WP2431	2.71E-08	4.26E-06	6.61	115.17
10	IL1 and megakaryocytes in obesity WP2865	5.82E-05	1.45E-03	11.61	113.19

Table 1. Pathways upregulated pre vs post IVCT caffeine. The top 10 enriched pathway terms generated by Enrichr, using upregulated gene lists. Pathway terms upregulated in MHN (Top) and MHS (bottom) phenotypes are displayed in order of combined score (log of p-value from Fisher's exact test multiplied by z score of deviation from expected rank).

MHN (pre vs post caffeine)

Index	Downregulated pathway terms	P-value	Adjusted p-value	Odds Ratio	Combined score
1	Electron Transport Chain (OXPHOS system in mitochondria) WP111	5.20E-12	2.46E-09	7.07	183.79
2	Oxidative phosphorylation WP623	6.12E-07	9.62E-05	6.68	95.56
3	Nonalcoholic fatty liver disease WP4396	5.32E-08	1.26E-05	4.47	74.79
4	Target Of Rapamycin (TOR) Signaling WP1471	4.72E-05	5.57E-03	7.08	70.55
5	Robo4 and VEGF Signaling Pathways Crosstalk WP3943	1.05E-02	9.90E-01	12.14	55.35
6	TCA Cycle (aka Krebs or citric acid cycle) WP78	1.24E-02	9.71E-01	6.07	26.68
7	Interleukin-1 Induced Activation of NF-kappa-B WP3656	2.93E-02	1.00E+00	7.29	25.73
8	RalA downstream regulated genes WP2290	4.14E-02	1.00E+00	6.07	19.34
9	miR-517 relationship with ARCN1 and USP1 WP3596	1.30E-01	1.00E+00	7.29	14.87
10	Metastatic brain tumor WP2249	1.54E-01	1.00E+00	6.07	11.37

MHS (pre vs post caffeine)

Index	Downregulated pathway terms	P-value	Adjusted p-value	Odds Ratio	Combined score
1	miR-517 relationship with ARCN1 and USP1 WP3596	3.06E-02	1	32.26	112.45
2	exRNA mechanism of action and biogenesis WP2805	3.66E-02	1	26.88	88.89
3	miRNA Biogenesis WP2338	3.66E-02	1	26.88	88.89
4	Robo4 and VEGF Signaling Pathways Crosstalk WP3943	3.66E-02	1	26.88	88.89
5	Hfe effect on hepcidin production WP3924	4.26E-02	1	23.04	72.71
6	DDX1 as a regulatory component of the Drosha microprocessor WP2942	4.26E-02	1	23.04	72.71
7	Dual hijack model of Vif in HIV infection WP3300	4.86E-02	1	20.16	60.99
8	White fat cell differentiation WP4149	1.68E-02	1	10.08	41.22
9	Gene regulatory network modelling somitogenesis WP2854	6.61E-02	1	14.66	39.82
10	Type 2 papillary renal cell carcinoma WP4241	1.88E-02	1	9.49	37.71

Table 2. Pathways downregulated pre vs post IVCT caffeine. The top 10 enriched pathway terms generated by Enrichr, using downregulated gene lists. Pathway terms downregulated in MHN (Top) and MHS (bottom) phenotypes are displayed in order of combined score (log of p-value from Fisher's exact test multiplied by z score of deviation from expected rank).

Appendix 9 – Gene ontology for MHN pre vs post IVCT (caffeine) comparison

	Upregulated terms	Adjusted p-value
(GO_BP) Biological Process	regulation of transcription from RNA polymerase II promoter (GO:0006357)	1.35E-14
	regulation of transcription, DNA-templated (GO:0006355)	1.72E-12
	positive regulation of transcription, DNA-templated (GO:0045893)	2.75E-12
	RNA splicing, via transesterification reactions with bulged adenosine as nucleophile (GO:0000377)	7.86E-11
	cytokine-mediated signaling pathway (GO:0019221)	9.72E-11
	mRNA splicing, via spliceosome (GO:0000398)	2.48E-10
	negative regulation of transcription from RNA polymerase II promoter (GO:0000122)	5.99E-10
	cellular response to cytokine stimulus (GO:0071345)	6.43E-10
	positive regulation of transcription from RNA polymerase II promoter (GO:0045944)	1.44E-09
	mRNA processing (GO:0006397)	3.37E-09
(GO_MF) Molecular Function	RNA binding (GO:0003723)	5.81E-19
	transcription factor activity, RNA polymerase II core promoter proximal region sequence-specific binding (GO:0000982)	3.15E-06
	RNA polymerase II core promoter proximal region sequence-specific DNA binding (GO:0000978)	7.28E-06
	core promoter proximal region sequence-specific DNA binding (GO:0000987)	1.08E-05
	RNA polymerase II regulatory region sequence-specific DNA binding (GO:0000977)	1.10E-05
	transcription regulatory region DNA binding (GO:0044212)	1.30E-05
	DNA binding (GO:0003677)	2.33E-05
	core promoter binding (GO:0001047)	6.93E-05
	purine ribonucleoside triphosphate binding (GO:0035639)	1.06E-04
	transcriptional repressor activity, RNA polymerase II transcription regulatory region sequence-specific binding (GO:0001227)	2.37E-04
(GO_CC) Cellular Component	nuclear body (GO:0016604)	1.61E-08
	nuclear speck (GO:0016607)	9.04E-09
	nucleolus (GO:0005730)	1.69E-08
	cytoskeleton (GO:0005856)	4.43E-05
	actin cytoskeleton (GO:0015629)	7.04E-04
	spliceosomal complex (GO:0005681)	1.91E-03
	focal adhesion (GO:0005925)	3.94E-03
	Cajal body (GO:0015030)	1.02E-02
	fibrillar center (GO:0001650)	9.50E-03
	microtubule cytoskeleton (GO:0015630)	9.37E-03

Table 1. Gene ontology results using upregulated genes. Top 10 ontology terms for biological process, molecular function and cellular component generated using Enrichr, in order of adjusted p-value.

	Downregulated terms	Adjusted p-value
(GO_BP) Biological Process	respiratory electron transport chain (GO:0022904)	1.12E-21
	mitochondrial ATP synthesis coupled electron transport (GO:0042775)	1.47E-21
	mitochondrial electron transport, NADH to ubiquinone (GO:0006120)	3.38E-07
	mitochondrial respiratory chain complex assembly (GO:0033108)	3.92E-07
	mitochondrial electron transport, cytochrome c to oxygen (GO:0006123)	9.04E-07
	cellular respiration (GO:0045333)	7.89E-06
	mitochondrial respiratory chain complex I assembly (GO:0032981)	3.20E-05
	mitochondrial respiratory chain complex I biogenesis (GO:0097031)	3.61E-05
	NADH dehydrogenase complex assembly (GO:0010257)	4.12E-05
	preassembly of GPI anchor in ER membrane (GO:0016254)	2.83E-04
(GO_MF) Molecular Function	NADH dehydrogenase (quinone) activity (GO:0050136)	5.29E-07
	NADH dehydrogenase (ubiquinone) activity (GO:0008137)	1.06E-06
	small ribosomal subunit rRNA binding (GO:0070181)	2.14E-03
	ubiquinol-cytochrome-c reductase activity (GO:0008121)	3.28E-03
	oxidoreductase activity, acting on diphenols and related substances as donors, cytochrome as acceptor (GO:0016681)	4.10E-03
	ubiquitin conjugating enzyme activity (GO:0061631)	5.79E-02
	ubiquitin-like protein conjugating enzyme activity (GO:0061650)	6.66E-02
	rRNA binding (GO:0019843)	1.52E-01
	NADH dehydrogenase activity (GO:0003954)	1.69E-01
	2 iron, 2 sulfur cluster binding (GO:0051537)	1.87E-01
(GO_CC) Cellular Component	mitochondrion (GO:0005739)	4.13E-18
	mitochondrial inner membrane (GO:0005743)	5.51E-18
	mitochondrial respiratory chain complex I (GO:0005747)	1.69E-07
	mitochondrial respiratory chain complex IV (GO:0005751)	1.71E-07
	mitochondrial respiratory chain complex III (GO:0005750)	6.97E-06
	mitochondrial matrix (GO:0005759)	1.03E-02
	mitochondrial small ribosomal subunit (GO:0005763)	1.44E-02
	small ribosomal subunit (GO:0015935)	1.45E-02
	intrinsic component of mitochondrial inner membrane (GO:0031304)	2.06E-02
	signal recognition particle (GO:0048500)	2.70E-02

Table 2. Gene ontology results using downregulated genes. Top 10 ontology terms for biological process, molecular function and cellular component generated using Enrichr, in order of adjusted p-value.

Appendix 10 – Gene ontology for MHS pre vs post IVCT (caffeine) comparison

	Upregulated terms	Adjusted p-value
(GO_BP) Biological Process	response to unfolded protein (GO:0006986)	9.40E-07
	inflammatory response (GO:0006954)	8.34E-05
	cellular response to tumor necrosis factor (GO:0071356)	1.45E-04
	response to tumor necrosis factor (GO:0034612)	2.15E-04
	regulation of NF-kappaB import into nucleus (GO:0042345)	2.83E-04
	negative regulation of cellular process (GO:0048523)	3.88E-04
	regulation of cell proliferation (GO:0042127)	4.16E-04
	positive regulation of transcription, DNA-templated (GO:0045893)	5.71E-04
	PERK-mediated unfolded protein response (GO:0036499)	7.34E-04
	cellular response to heat (GO:0034605)	8.68E-04
(GO_MF) Molecular Function	chemokine receptor binding (GO:0042379)	2.20E-04
	transcription factor activity, RNA polymerase II core promoter proximal region sequence-specific binding (GO:0000982)	4.71E-04
	chemokine activity (GO:0008009)	5.50E-04
	cytokine activity (GO:0005125)	1.34E-03
	transcriptional activator activity, RNA polymerase II transcription regulatory region sequence-specific binding (GO:0001228)	3.75E-03
	CCR chemokine receptor binding (GO:0048020)	1.05E-02
	RNA polymerase II core promoter proximal region sequence-specific DNA binding (GO:0000978)	1.21E-02
	transcriptional activator activity, RNA polymerase II core promoter proximal region sequence-specific binding (GO:0001077)	1.31E-02
	C3HC4-type RING finger domain binding (GO:0055131)	1.41E-02
	core promoter proximal region sequence-specific DNA binding (GO:0000987)	1.87E-02
(GO_CC) Cellular Component	ficolin-1-rich granule lumen (GO:1904813)	1.70E-01
	ficolin-1-rich granule (GO:0101002)	4.15E-01
	specific granule (GO:0042581)	1.00E+00
	tertiary granule (GO:0070820)	1.00E+00
	tertiary granule lumen (GO:1904724)	1.00E+00
	nuclear speck (GO:0016607)	1.00E+00
	specific granule membrane (GO:0035579)	1.00E+00
	endolysosome membrane (GO:0036020)	1.00E+00
	nuclear body (GO:0016604)	1.00E+00
	endocytic vesicle lumen (GO:0071682)	1.00E+00

Table 1. Gene ontology results using upregulated genes. Top 10 ontology terms for biological process, molecular function and cellular component generated using Enrichr, in order of adjusted p-value.

	Downregulated terms	Adjusted p-value
(GO_BP) Biological Process	regulation of nitric oxide biosynthetic process (GO:0045428)	2.26E-01
	negative regulation of cellular biosynthetic process (GO:0031327)	5.21E-01
	regulation of protein tyrosine kinase activity (GO:0061097)	5.22E-01
	regulation of blood coagulation (GO:0030193)	5.33E-01
	negative regulation of nitric oxide biosynthetic process (GO:0045019)	5.72E-01
	negative regulation of binding (GO:0051100)	6.18E-01
	negative regulation of cell activation (GO:0050866)	6.52E-01
	mitochondrial ATP synthesis coupled electron transport (GO:0042775)	6.58E-01
	negative regulation of nitric oxide metabolic process (GO:1904406)	6.67E-01
	regulation of endothelial cell proliferation (GO:0001936)	6.85E-01
(GO_MF) Molecular Function	calcium-activated potassium channel activity (GO:0015269)	1.00E+00
	calcium activated cation channel activity (GO:0005227)	1.00E+00
	potassium channel regulator activity (GO:0015459)	1.00E+00
	NADH dehydrogenase (quinone) activity (GO:0050136)	1.00E+00
	NADH dehydrogenase (ubiquinone) activity (GO:0008137)	1.00E+00
	patched binding (GO:0005113)	1.00E+00
	primary miRNA binding (GO:0070878)	1.00E+00
	chloride ion binding (GO:0031404)	1.00E+00
	MAP kinase tyrosine/serine/threonine phosphatase activity (GO:0017017)	1.00E+00
	calcium-dependent protein serine/threonine phosphatase activity (GO:0004723)	1.00E+00
(GO_CC) Cellular Component	lipid droplet (GO:0005811)	1.00E+00
	mitochondrial respiratory chain complex I (GO:0005747)	1.00E+00
	ruffle membrane (GO:0032587)	1.00E+00
	filopodium (GO:0030175)	1.00E+00
	IkappaB kinase complex (GO:0008385)	1.00E+00
	condensed nuclear chromosome kinetochore (GO:0000778)	1.00E+00
	actin-based cell projection (GO:0098858)	1.00E+00
	nuclear telomere cap complex (GO:0000783)	1.00E+00
	mitochondrial respiratory chain complex III (GO:0005750)	1.00E+00
	perinuclear region of cytoplasm (GO:0048471)	1.00E+00

Table 2. Gene ontology results using downregulated genes. Top 10 ontology terms for biological process, molecular function and cellular component generated using Enrichr, in order of adjusted p-value.

Appendix 11 - Genes overlapping between MHS drug treatment gene lists

Gene lists within each Venn diagram segment	Number of genes	Genes within overlapping segment
MHSh caffeine, MHSh halothane, MHShc caffeine, MHShc halothane	89	*ABRA, ADAMTS4, ATF3, ATP6V1FNB, BCL3, BRD2, CCDC200, CCL2, CD83, CDKN1A, CHIT1, CKS2, CXCL1, CXCL3, DCP1A, DDIT3, DNAJA1, DNAJB1, DNAJB5-DT, DSTNP2, DUSP2, DUSP5, DUSP6, EGFL7, EGR2, ERF, ERRFI1, GASAL1, GEM, GIMAP6, GIMAP8, H2AX, H2BC20P, HEXIM1, HHATL-AS1, HNRNPA1P38, HSPA1A, HSPA1B, ICAM1, ICAM4, ID1, IL1B, ING1, IQCN, IRF1, LFNG, MAFB, MAFF, MIR3153, MT1A, MT-ND6, MT-TA, MT-TC, MT-TE, MT-TF, MT-TK, MT-TM, MT-TN, MT-TQ, MT-TT, MT-TY, PECAM1, PPP1R10, RCAN1, RGS16, RND1, RPL13P5, SAT1, SELE, SERTAD1, SLC20A1, SLC2A14, SLC2A3, SNHG12, SNORA10, SNORD14C, SNORD14D, SNORD14E, SNORD3A, SNORD3B-1, SNORD3B-2, SNORD3C, SNORD3D, SOCS1, SRSF2, SRSF3, TNFAIP3, TNFRSF10D, TNFSF9*
MHSh caffeine, MHShc caffeine, MHShc halothane	37	*AMD1, ARHGEF15, ARID5B, ARL5B, BIRC3, BTG3, CBX4, CCL8, CLDN6, DIPK2B, FAM71A, GJA1, GPR183, ID4, IER3, INSIG1, IVNS1ABP, LINC01004, MT-TV, NABP1, NKX3-1, OLR1, PCF11, PHLDA1, PNP, POLG2, RNU5E-1, SERPINB9, SNORA61, THSD1, TIPARP, TNF, TNFAIP6, TNFAIP8L1, VSIG2, ZC3HAV1, ZNF792*
MHSh caffeine, MHSh halothane, MHShc halothane	4	*LRG1, MIR24-2, MT-TP, S1PR1*
MHSh caffeine, MHSh halothane, MHShc caffeine	9	*EGR4, HSP90AB1, MIR616, MT-TS2, MT-TW, PDE4B, PLEKHO2, SNORD99, TSPYL2*
MHShc caffeine, MHShc halothane	51	*A2M, ABHD5, APCDD1, ARAP3, ARHGAP31, ARL6IP1, C16orf58, CCDC71L, CDH5, CDKN2AIP, CLEC1A, COL15A1, COL4A1, CRNDE, CTC1, DCHS1, DONSON, GCFC2, GJA5, KCNQ1OT1, KLRA1P, LYPLAL1, MGAT4A, MIR222HG, MIR3064, NAE1, NAMPT, NFE2L2, NOVA2, NYNRIN, PAX7, PDGFB, PIK3R3, RASD2, RET, RFX5, RSRP1, SDC3, SFPQ, SMARCD1, SNORA31, TCIM, TCTE3, TDRD6, THUMPD3-AS1, TM4SF1, TRIB3, UGCG, VASH1, ZNF540, ZSCAN32*
MHSh caffeine, MHShc halothane	15	*ARC, BMP2, BTG1, CLK2, CYP1B1, FABP5, HAS2, IER5L, KLF5, NFIL3, RASGEF1B, RND3, S1PR3, SSTR2, USHBP1*
MHSh halothane, MHShc caffeine	2	*CCN2, IFIT5*
MHSh caffeine, MHShc caffeine	28	*ASTL, BAMBI, BCL6, CDH16, CSRP2, DHDH, DNAJA4, FUS, GLA, GTF2B, HAPLN3, HSPA1L, HSPA6, IRX2, KPNA2, LITAF, MTND2P28, MTND5P11, MYLIP, NAMA, NFKBIE, NKX6-3, PRSS42P, PRSS44P, STAG3L2, TUBB3, VCAM1, ZNF331*

Table 1. Genes overlapping between MHS drug treatment gene lists. All genes lists in the MHS pre vs post drug treatment were compared and the genes within each segment of the Venn diagram displayed in Figure 2.12, are presented here. **(continued next page)**

MHSh caffeine, MHSh halothane	86	*APOL3, BTG2, BTN3A3, C11orf91, CAV1, CAV2, CCL3, CDK2, CSRNP1, CYB561D1, DIO3OS, EDN1, EGR3, EIF4A1, EIF4A3, ERFE, ETS2, FABP4, FOSL2, FZD7, GADD45B, GIMAP1, GIMAP4, GIMAP7, GRASP, H2BC19P, H4C14, HBEGF, HEY1, IER5, IL6, JMJD6, KCNJ8, LAG3, LDLR, LRATD2, MEPCE, MIDN, MIR22, MIR23A, MIR8085, MMP19, MT-ND2, MT-TD, MT-TG, MT-TH, MT-TI, NCOA6, NDUFB4P11, NFKBID, NFKBIZ, NLRP3, NOLC1, NR2F2, NR4A1, NR4A3, NRN1, OSGIN1, OTUD1, PER1, PFKFB3, PLAUR, POLR2A, PPP1R15A, PRKCG, RBKS, RNF122, SDC4, SERTAD3, SIK1, SIK1B, SLC16A14, SLC25A25, SMURF1, SNAI1, SNHG9, SNORA64, SNORA67, STK35, TP53INP2, TUBB4B, XIRP1, ZC3H12A, ZFAS1, ZFP36*
MHSh halothane	40	*ACTN1, ANKRD29, ARNT2, ASAP2, ASPN, ATP1A2, BATF2, CNTNAP3B, DNM3OS, GIMAP2, GNG11, GNL3L, ITM2B, JAM2, JRK, KY, LEPR, LINC01578, LIPA, LTC4S, MAN1A1, MAU2, MICAL3, MIR23B, MOB3C, MTND4LP30, N4BP2L2-IT2, NT5C1A, PITPNC1, PPARGC1B, RGCC, RPL7P3, SNAI2, SOCS7, TMEM50A, TMSB4X, TMSB4XP8, ZBTB16, ZNF559, ZNF706*
MHShc halothane	60	*ACOT11, ADCY4, AIF1L, ANKZF1, ARHGAP11A, C5orf51, C6orf120, C6orf47, CADM1, CHRDL2, CLDN12, CREG1, DCK, DNAJC27, FBH1, GDAP2, GLMN, H3-3B, HS6ST2, KCNA5, LINC00672, LSM6, MIR27A, MORC2, MRPL16, MSTO1, MTATP6P1, NDUFA1, NPR1, OSGEP, PCDH1, PCDH12, PKD1L1, PNRC1, POT1, PRNP, PTGR1, RAP1B, RBMS3, RLF, ROBO4, RPS13P2, RYBP, SDCBP, SH2D3C, SHF, SLC19A2, SLC1A7, SPSB2, TBC1D23, TGFB2, TIE1, TMEM165, TMEM167B, UBE2D3, UNG, WDR33, ZBTB21, ZBTB4, ZNF500*
MHSh caffeine	181	*ADAMTS1, AGER, ANKRD1, ANKRD37, AOC2, APOLD1, AREG, ARID5A, ASPRV1, ATP1A1, ATP1B3, B3GNT5, BCDIN3D, BCL2A1, BHLHE40, BTBD19, C11orf96, C1QTNF9, C2CD4B, C4A-AS1, C9orf170, CA4, CARMN, CBX2, CCL3L1, CCL4, CCL4L2, CCND2, CD300LG, CEACAM1, CENPW, CFAP97D1, CGB7, CH25H, CHMP4BP1, CPNE8-AS1, CRTC3, CSF3, CSRNP2, CSTF1, CXCL2, CXCL8, CXCR4, DACT1, DCUN1D3, DLC1, DLG5, DNALI1, DPPA2P4, DUSP8, DYRK3, EGR1, EMP1, ENDOU, EPOP, ETV4, EXOSC6, FAM181A-AS1, FAM72A, FOSL1, FOXC2, FZD5, GADD45A, GAREM1, GCH1, GDNF, GH1, GIPC3, GPIHBP1, GPR4, GPRC5A, H4C15, HARS2, HAS1, HCP5, HELB, HOXD8, HSP90AA2P, IDO1, IL1A, IL1RN, IRF4, IRX4-AS1, ITPKC, ITPRIPL1, JCAD, JUNB, KDM6B, KIAA0040, KLF7, KLHL15, KLHL9, LAD1, LBP, LINC00205, LINC01569, LUCAT1, MAP3K8, MCL1, MECOM, MED28, MIR7975, MSX1, MT-ATP8, MT-ND5, MT-TL1, MYC, NDRG4, NEXN-AS1, NFKB2, NFKBIA, NOCT, NPTX2, NR4A2, NUAK2, NXF1, OLIG1, OR51E1, PEG10, PIGA, PIM1, PIM2, PLAU, PLEKHG2, PPP1R16B, PPP1R35-AS1, PPRC1, PTPN1, RAB15, RASD1, RASSF5, REC8, RGS2, RNF151, RNU2-2P, RNU4ATAC, RRAD,SBK3, SCN3B, SEMA4C, SERPINA3, SERPINB1, SERPINE1, SERPINH1, SESN2, SFT2D3, SLC1A5, SLC9A1, SLC9A3R1, SLCO4A1, SLFN11, SOCS3, SPAAR, SSTR1, STC1, STC2, STX11, TAP1, TCF15, TENT5A, TENT5C, TEX14, TGFB3, THBD, THBS1, TIGD3, TMEM229B, TMEM26, TMEM80, TNFAIP2, TSPAN13, TTYH3, TUSC3, UBE2E1, VAMP1, VMO1, ZNF433-AS1, ZNF442, ZNF486, ZNF580, ZSWIM8-AS1*

Table 1. Continued next page

MHShc caffeine	147	*AGRN, AHNAK, AP5B1, APP, ARHGAP30, ARPIN, ARRB1, ASXL1, ATP2A3, ATP8B4, AXIN2, BAZ2A, BCL9L, C4orf46, CARD6, CASKIN2, CCDC8, CCNH, COL6A3, CXCL10, DIPK1A, DNAJB4, DOK4, DTL, ECE1, EDA, ENPP5, EPAS1, EVC, EZH2, FBXW7, FGD5, FHDC1, FLNA, FLNB, GAS1, GAS2L1, GLI1, GLI2, GNRH1, HBA1, HBB, HMCN2, HSP90AA1, HSPG2, HSPH1, IGFBP5, IGHG2, IGSF3, IL15, IL17RA, IL1RL1, INTS6, IQSEC1, ITGB4, ITPR3, KANK2, KCNC4, KCNE4, KIF21B, KMT2D, LGALSL, LGR5, LINC00467, LINC01355, LRIF1, LRP1, LRRC66, MAGEH1, MALINC1, MAP3K2-DT, MAPK13, MAST3, MED4, METTL5, MICAL2, MTATP8P1, MXRA5, MYO9B, NAV1, NID2, NOTCH1, NOTCH2, NOTCH3, NPTXR, NUDT13, OLFML2A, PDGFRB, PGAM1P8, PHF12, PIGP, PIK3IP1, PLEKHG3, PLK1, PMAIP1, PODXL, PPCS, PPM1F, PPP1R3C, PPP2CA, PPP2R3C, PSMG1, PTPN9, PXDN, RAB11FIP4, REM1, RGP1, SALL2, SCUBE1, SIRT1, SLC30A5, SLC46A1, SLC46A3, SLIT2, SMIM10L1, SMIM3, SNHG1, SPTAN1, SULF2, SVEP1, SYDE1, SYT15, TAF1D, TGFB1I1, TLN1, TMEM131L, TMEM60, TNS1, TPD52L1, TRH, TRIL, TSPYL5, TYW1, UCHL3, VANGL1, WASF2, WDR89, ZBTB39, ZC3H7B, ZMIZ1, ZNF112, ZNF142, ZNF267, ZNF394, ZNF525, ZNF644, ZNF91*

Appendix 12 – Pathway analysis for WT vs G2435R-RYR1 HOM comparison

Index	Upregulated pathway terms	P-value	Adjusted p-value	Odds Ratio	Combined score
1	MAPK Cascade WP251	3.42E-04	6.02E-02	21.87	174.51
2	Notch Signaling Pathway WP29	1.49E-03	5.23E-02	13.31	86.66
3	Novel Jun-Dmp1 Pathway WP3654	7.15E-03	1.57E-01	15.7	77.55
4	Delta-Notch Signaling Pathway WP265	7.41E-04	6.52E-02	9.84	70.89
5	Signaling of Hepatocyte Growth Factor Receptor WP193	1.20E-02	2.35E-01	12	53.06
6	Primary Focal Segmental Glomerulosclerosis FSGS WP2573	5.33E-03	1.56E-01	8.5	44.51
7	Insulin Signaling WP65	1.12E-03	6.55E-02	6.42	43.62
8	MAPK signaling pathway WP493	1.12E-03	4.92E-02	6.42	43.62
9	Osteoclast WP454	6.65E-02	5.57E-01	14.58	39.52
10	Splicing factor NOVA regulated synaptic proteins WP1983	1.80E-02	2.64E-01	9.72	39.03

Index	Downregulated pathway terms	P-value	Adjusted p-value	Odds Ratio	Combined score
1	Fatty Acid Beta Oxidation WP1269	8.44E-16	1.49E-13	25.92	899.71
2	Mitochondrial LC-Fatty Acid Beta-Oxidation WP401	1.44E-09	1.27E-07	29.66	603.77
3	Fatty Acid Biosynthesis WP336	1.45E-05	5.09E-04	15.41	171.71
4	Fatty acid oxidation WP2318	3.53E-04	8.88E-03	20.34	161.68
5	TCA Cycle WP434	5.28E-06	2.32E-04	13.12	159.44
6	PPAR signaling pathway WP2316	3.12E-07	1.83E-05	8.37	125.38
7	Amino Acid metabolism WP662	8.16E-05	2.39E-03	5.71	53.75
8	Retinol metabolism WP1259	2.54E-03	5.59E-02	6.95	41.55
9	Synthesis and Degradation of Ketone Bodies WP543	7.16E-02	6.30E-01	13.56	35.75
10	Acetylcholine Synthesis WP175	9.88E-02	6.96E-01	9.69	22.42

Table 1. Pathway analysis for WT vs G2435R-RYR1 HOM comparison. The top 10 pathway terms generated by Enrichr, using upregulated and downregulated gene lists. Upregulated (Top) and downregulated (bottom) pathways are displayed in order of combined score (log of p-value from Fisher's exact test multiplied by z score of deviation from expected rank).

Appendix 13 - Pathway analysis for WT vs T4826I-RYR1 HET comparison

Index	Upregulated pathway terms	P-value	Adjusted p-value	Odds Ratio	Combined score
1	Glycolysis and Gluconeogenesis WP157	1.20E-03	2.11E-01	14.35	96.49
2	Osteoblast WP238	4.03E-02	1.00E+00	24.39	78.35
3	Osteoclast WP454	5.59E-02	1.00E+00	17.42	50.24
4	Orphan GPCRs WP1398	7.51E-02	1.00E+00	12.84	33.23
5	Calcium Regulation in the Cardiac Cell WP553	2.26E-02	1.00E+00	4.98	18.87
6	One Carbon Metabolism WP435	1.12E-01	1.00E+00	8.41	18.38
7	Wnt Signaling in Kidney Disease WP3857	1.41E-01	1.00E+00	6.59	12.91
8	TNF-alpha NF-kB Signaling Pathway WP246	4.16E-02	1.00E+00	3.91	12.44
9	DNA Replication WP150	1.55E-01	1.00E+00	5.95	11.08
10	IL-7 Signaling Pathway WP297	1.66E-01	1.00E+00	5.54	9.97

Index	Downregulated pathway terms	P-value	Adjusted p-value	Odds Ratio	Combined score
1	Fatty acid oxidation WP2318	1.66E-03	9.74E-02	32.26	206.46
2	Fatty Acid Biosynthesis WP336	3.29E-04	5.78E-02	21.99	176.4
3	Fatty Acid Beta Oxidation WP1269	1.21E-03	1.06E-01	14.23	95.6
4	Heme Biosynthesis WP18	5.45E-02	7.99E-01	17.92	52.16
5	Irinotecan Pathway WP475	6.03E-02	8.17E-01	16.13	45.29
6	TCA Cycle WP434	1.58E-02	6.94E-01	10.41	43.18
7	Toll Like Receptor signaling WP88	1.78E-02	6.25E-01	9.78	39.4
8	Tryptophan metabolism WP79	3.05E-02	6.70E-01	7.33	25.6
9	ErbB signaling pathway WP1261	3.31E-02	6.46E-01	7.01	23.91
10	Mitochondrial LC-Fatty Acid Beta-Oxidation WP401	9.48E-02	1.00E+00	10.08	23.76

Table 1. Pathway analysis for WT vs T4826I-RYR1 HET comparison. The top 10 pathway terms generated by Enrichr, using upregulated and downregulated gene lists. Upregulated (Top) and downregulated (bottom) pathways are displayed in order of combined score (log of p-value from Fisher's exact test multiplied by z score of deviation from expected rank).

Appendix 14 – Gene ontology for WT vs G2435R-RYR1 HOM comparison (upregulated terms only)

	Upregulated terms	Adjusted p-value
(GO_BP) Biological Process	Plasma membrane organization (GO:0007009)	1.89E-01
	Positive regulation of protein autophosphorylation (GO:0031954)	4.72E-01
	Regulation of protein autophosphorylation (GO:0031952)	7.32E-01
	Response to thyroid hormone (GO:0097066)	8.77E-01
	Platelet degranulation (GO:0002576)	8.94E-01
	Transmembrane receptor protein tyrosine kinase signaling pathway (GO:0007169)	9.00E-01
	Positive regulation of actin cytoskeleton reorganization (GO:2000251)	9.08E-01
	Stress-activated MAPK cascade (GO:0051403)	9.09E-01
	Mitotic cytokinesis (GO:0000281)	9.11E-01
	Basement membrane organization (GO:0071711)	9.25E-01
(GO_MF) Molecular Function	Collagen binding (GO:0005518)	1.77E-01
	Vinculin binding (GO:0017166)	6.49E-01
	Hydrolase activity, acting on carbon-nitrogen (but not peptide) bonds, in cyclic amides (GO:0016812)	1.00E+00
	Transforming growth factor beta-activated receptor activity (GO:0005024)	1.00E+00
	Estradiol 17-beta-dehydrogenase activity (GO:0004303)	1.00E+00
	Acetylcholine receptor regulator activity (GO:0030548)	1.00E+00
	Superoxide-generating NADPH oxidase activator activity (GO:0016176)	1.00E+00
	Protein kinase C activity (GO:0004697)	1.00E+00
	Platelet-derived growth factor binding (GO:0048407)	1.00E+00
	Immunoglobulin binding (GO:0019865)	1.00E+00
(GO_CC) Cellular Component	Cytoskeleton (GO:0005856)	1.10E-03
	Cell cortex part (GO:0044448)	1.80E-02
	Secretory granule lumen (GO:0034774)	2.51E-02
	Caveola (GO:0005901)	3.04E-02
	Focal adhesion (GO:0005925)	4.34E-02
	Polymeric cytoskeletal fiber (GO:0099513)	7.22E-02
	Platelet alpha granule (GO:0031091)	7.73E-02
	Septin filament array (GO:0032160)	1.00E-01
	Septin ring (GO:0005940)	1.12E-01
	Septin cytoskeleton (GO:0032156)	1.26E-01

Table 1. Gene ontology analyses for the WT vs G2435R-RYR1 HOM comparison (upregulated terms). Top 10 ontology terms for biological process, molecular function and cellular component generated using Enrichr, in order of adjusted p-value.

Appendix 15 – Gene ontology for WT vs T4826I-RYR1 HET comparison

	Upregulated terms	Adjusted p-value
(GO_BP) Biological Process	Glucose catabolic process to pyruvate (GO:0061718)	3.38E-01
	Canonical glycolysis (GO:0061621)	5.08E-01
	Apoptotic process (GO:0006915)	7.15E-01
	Glycolytic process through glucose-6-phosphate (GO:0061620)	1.00E+00
	Positive regulation of catecholamine secretion (GO:0033605)	1.00E+00
	Cerebral cortex cell migration (GO:0021795)	1.00E+00
	Negative regulation of keratinocyte differentiation (GO:0045617)	1.00E+00
	Regulation of cytokine production involved in immune response (GO:0002718)	1.00E+00
	Peptidyl-proline hydroxylation (GO:0019511)	1.00E+00
	Response to manganese ion (GO:0010042)	1.00E+00
(GO_MF) Molecular Function	MHC class II protein complex binding (GO:0023026)	1.00E+00
	1-phosphatidylinositol-3-kinase regulator activity (GO:0046935)	1.00E+00
	Coreceptor activity involved in Wnt signaling pathway, planar cell polarity pathway (GO:1904929)	1.00E+00
	Calcium:sodium antiporter activity (GO:0005432)	1.00E+00
	C3HC4-type RING finger domain binding (GO:0055131)	1.00E+00
	Ubiquitin-dependent protein binding (GO:0140036)	1.00E+00
	Hydroxymethyl-, formyl- and related transferase activity (GO:0016742)	1.00E+00
	MHC protein complex binding (GO:0023023)	1.00E+00
	Satellite DNA binding (GO:0003696)	1.00E+00
	Wnt-activated receptor activity (GO:0042813)	1.00E+00
(GO_CC) Cellular Component	Flotillin complex (GO:0016600)	1.00E+00
	Clathrin-sculpted gamma-aminobutyric acid transport vesicle membrane (GO:0061202)	1.00E+00
	Perinuclear endoplasmic reticulum (GO:0097038)	1.00E+00
	Clathrin-sculpted gamma-aminobutyric acid transport vesicle (GO:0061200)	1.00E+00
	NpBAF complex (GO:0071564)	1.00E+00
	SWI/SNF complex (GO:0016514)	1.00E+00
	BAF-type complex (GO:0090544)	1.00E+00
	Dendrite membrane (GO:0032590)	1.00E+00
	Intrinsic component of external side of plasma membrane (GO:0031233)	1.00E+00
	Axon (GO:0030424)	1.00E+00

Table 1. Gene ontology analyses for the WT vs T4826I-RYR1 HET comparison (upregulated terms). Top 10 ontology terms for biological process, molecular function and cellular component generated using Enrichr, in order of adjusted p-value.

	Downregulated terms	Adjusted p-value
(GO_BP) Biological Process	Fatty acid catabolic process (GO:0009062)	4.12E-01
	Response to alkaloid (GO:0043279)	8.03E-01
	Cardiolipin acyl-chain remodeling (GO:0035965)	8.38E-01
	Fatty acid beta-oxidation (GO:0006635)	9.62E-01
	Sarcoplasmic reticulum calcium ion transport (GO:0070296)	1.00E+00
	Regulation of acyl-CoA biosynthetic process (GO:0050812)	1.00E+00
	Cardiolipin metabolic process (GO:0032048)	1.00E+00
	Acetyl-CoA metabolic process (GO:0006084)	1.00E+00
	Regulation of acetyl-CoA biosynthetic process from pyruvate (GO:0010510)	1.00E+00
	Fatty acid beta-oxidation using acyl-CoA dehydrogenase (GO:0033539)	1.00E+00
(GO_MF) Molecular Function	Acetylcholine-gated cation-selective channel activity (GO:0022848)	1.00E+00
	CoA hydrolase activity (GO:0016289)	1.00E+00
	1-acylglycerol-3-phosphate O-acyltransferase activity (GO:0003841)	1.00E+00
	Exoribonuclease activity (GO:0004532)	1.00E+00
	Lysophosphatidic acid acyltransferase activity (GO:0042171)	1.00E+00
	Primary miRNA binding (GO:0070878)	1.00E+00
	DEAD/H-box RNA helicase binding (GO:0017151)	1.00E+00
	Leucine binding (GO:0070728)	1.00E+00
	Wnt-activated receptor activity (GO:0042813)	1.00E+00
	NAD binding (GO:0051287)	1.00E+00
(GO_CC) Cellular Component	Mitochondrial matrix (GO:0005759)*	5.23E-04
	Mitochondrion (GO:0005739)	3.18E-01
	Cytoplasmic vesicle membrane (GO:0030659)	6.67E-01
	Acetylcholine-gated channel complex (GO:0005892)	8.43E-01
	NURF complex (GO:0016589)	1.00E+00
	RISC complex (GO:0016442)	1.00E+00
	Junctional sarcoplasmic reticulum membrane (GO:0014701)	1.00E+00
	RNAi effector complex (GO:0031332)	1.00E+00
	Sarcoplasmic reticulum (GO:0016529)	1.00E+00
	Sarcoplasm (GO:0016528)	1.00E+00

Table 2. Gene ontology analyses for the WT vs T4826I-RYR1 HET comparison (downregulated terms). Top 10 ontology terms for biological process, molecular function and cellular component generated using Enrichr, in order of adjusted p-value.